THE EFFECT OF HEAT TREATMENT ON THE MICROSTRUCTURE EVOLUTION AND MECHANICAL PROPERTIES OF Ti-5Al-5V-5Mo-3Cr, AND ITS POTENTIAL APPLICATIONS IN LANDING GEARS.

THE EFFECT OF HEAT TREATMENT ON THE MICROSTRUCTURE EVOLUTION AND MECHANICAL PROPERTIES OF Ti-5Al-5V-5Mo-3Cr, AND ITS POTENTIAL APPLICATIONS IN LANDING GEARS.

By

ROQUE PANZA-GIOSA, B.A.Sc., M.Eng.

A Thesis Submitted to the
School of Graduate Studies in
Partial Fulfillment of the
Requirements for the Degree of
Doctor of Philosophy

McMaster University

DOCTOR OF PHILOSOPHY (2009)   McMaster University, Hamilton, Ontario
(Materials Science and Engineering)

TITLE: The Effect of Heat Treatment on the Microstructure Evolution and Mechanical Properties of Ti-5Al-5V-5Mo-3Cr, and Its Potential Application in Landing Gears.

AUTHOR: Roque Panza-Giosa, B.A.Sc., M.Eng. (University of Toronto)

SUPERVISOR: Professor   Dr. J. D. Embury

CO-SUPERVISOR: Professor   Dr. Z. Wang (University of Toronto, Materials Science and Engineering)

NUMBER OF PAGES: 197

ABSTRACT

The properties and microstructure of Ti-5Al-5V-5Mo-3Cr were characterized under various stress states after the following heat treatments: 1) annealing above the β transus, followed by cooling at various rates and ageing for different times; 2) solution heat treatment in the α-β range, fan-cooling and ageing for various temperatures and times.

Heat treatment above the β transus temperature causes complete recrystallization of the as-forged microstructure. The as-cooled microstructure consists of equiaxed β grains with an average grain size of 200μm. Water quenching from above the β transus results in precipitation of a dispersion of nano-sized ω phase; while the fan-cooled microstructure contains nano-sized ω and α precipitates. Ageing of the fan-cooled microstructure at 790°C or 600°C precipitates sub micron acicular α throughout the β grains. The tensile properties of this condition could not be determined using standard tensile specimens due to brittle failure at the grips.

Controlled cooling from above the β transus to the ageing temperature at slower rates produces a coarser α+β microstructure. Acicular α laths are produced with cooling rates of 1°C/min, while lamellar α develops at cooling rates of 3.4°C/min. The β annealed and fan-cooled condition is characterized by relatively low strength (~850MPa) and low ductility (~6% elong.).The fracture mode is by intensely localized slip and the creation of transgranular cracks. Localization of slip is attributed to shearing of the nano-scale ω precipitates by dislocations. A linear relationship between the grain size, $d^{-1/2}$, and the yield and fracture stresses was established, as described by the Hall-Petch relation. With controlled cooling, the strength and ductility improve by precipitation of lamellar α within the β matrix. Improvements in ductility and strength are achieved by reducing the slip length.

Solution heat treatment below the β transus and fan-cooling results in complete dissolution of the as-forged acicular α phase. Solutionizing at 50°C below the β transus yields a volume fraction of 16.5% primary α in a matrix of retained β. Low angle grain boundaries and globular primary α, each measuring 2-4μm average in diameter, are uniformly distributed throughout the retained β matrix. The tensile strength in this condition is relatively low, i.e. (~ 900MPa) and the ductility relatively high (~ 16% elong.). With ageing in the 500°C to 600°C temperature range, precipitation of α within the retained β begins within 5 minutes of the start of ageing. Precipitating is heterogeneously nucleated at dislocations and grain boundaries. The yield and ultimate tensile strengths reach values of roughly 1200 and 1300MPa, respectively, and remain relatively constant for up 48 hours ageing
The fracture stresses for the solution treated condition and for material subsequently aged at 500°C and 600°C are quite similar in magnitude. This similarity is due to the fact that the fracture mechanism, which controls the fracture stress, is the same for all these conditions. The fracture mechanism for all the solution treated conditions begins with shear decohesion of the primary α/β interfaces.

For each condition, the damage mechanisms and final fracture modes were evaluated and rationalized on the basis of microstructural features. The yield and fracture stresses for the various conditions were calculated and plotted on a two-principal stress axis coordinate system, thus creating the failure envelope for Ti-5553. For the β annealed and fan cooled and for the α-β solution heat treated and aged conditions the yield and fracture envelopes are two concentric ellipses in good agreement with the shear strain energy (von Mises) model for failure.

The fracture toughness and stress corrosion cracking behaviour for the STA condition were evaluated and compared against other β titanium alloys.

ACKNOWLEDGEMENTS

This thesis is dedicated to my family who supported me and encouraged me at every step of this work. To my mother Angela, who through love and sacrifice raised two doctors as a single mother. To my sister Rosalia who inspired me with her example, generosity and kindness. To my wife and my love Lynn - who patiently supported me through the years, and late nights, and week ends of thesis work. To my children Gabriela and Michael whose hugs and smiles gave me the strength to persevere.

Sincere thanks to Dr. Dave Embury and Dr. Zhirui Wang for their invaluable guidance, patience and open mindedness. I know that deviating from the usual academic approach to an industrial thesis was not easy. From them I learned much more than science.

I would like to also acknowledge the steadfast support of Mr. Gerry Kouverianos and Mr. Neil Harris of Goodrich Landing Gear, who made it possible to dream of achieving a higher academic degree.

Finally, I would like to acknowledge the support and early guidance of the late Dr. George Weatherly who inspired and encouraged me to pursue higher knowledge.

My deep gratitude to Dr. Mike Mei (U of T) and Dr. Zhang Wang (Mc Master) for their invaluable assistance on the TEM work and interpretation of results.

Many thanks to: Glenn Forbes, Tom Zolis, Ellie Cochien, Marilea Manzini, Ben Evans, Mirko Zdero, Keith Williamson, George Hall, Bob Bianco, Paul Vanderpol, Brad Baird and Karthik Narayan for their assistance and support at Goodrich Landing Gear. Special thanks to Karen Andrews for giving this document a professional look.

Sincere thanks for the assistance, materials and advice to: Mike Loretto, Jim Cotton, Rod Boyer, Srini Rajagopalan, Jim Williams, Gary Purdy, Dmitry Malakhov, Joe McDermid, Gianluigi Botton, Chris Butcher, Pascal Jacques and hid group, John Fanning, Megan Harper, Alexi Shibanov and Igor Levin.

TABLE OF CONTENTS

LIST OF FIGURES

LIST OF DIAGRAMS

LIST OF TABLES

1.0   INTRODUCTION

Since the early beginnings of the aircraft industry, there has been a continuous drive to reduce component weight for both airframes and engines.
Although every major element in an aircraft structure is considered critical, the landing gears structural components are perhaps the only areas where designers would consider using certain materials deemed cutting edge. This tendency has to do with the notion that although indispensable to the safe operation of an aircraft, the landing gears are considered a weight burden since they do not directly assist flight.

Amongst the most widely accepted work in materials selection is that by Dr. M.F. Ashby *[1]*, who published a series of materials selection charts illustrating the ranking of various materials according to their properties. The advantage of titanium alloys for structural components subject to tensile strength and density considerations is highlighted in Figure 1.1. In this chart, titanium and aluminum alloys offer an advantage over steel, due to their higher strength to density ratio. Another important criterion for aircraft structures is the fracture toughness, which represents the ability of a material to tolerate internal flaws or damage. Figure 1.2 presents the fracture toughness versus strength for various materials. In this chart, titanium alloys and steels rate amongst the highest, with steels offering a slight advantage.

Despite their relatively low fracture toughness, ultra-high strength steels and β-titanium alloys continue to make up the majority of a landing gear's structural members. Materials considered to be an unacceptable risk for other airframe applications, such 300M steels and peak-strength aged Ti-10V-2Fe-3Al, are the materials of choice for landing gear designs. The refinement of stress analysis tools such as finite element analysis, and the ability to create three dimensional models of the structural members, have revolutionized the ability to predict stresses and reduce component weight. On the downside, the higher level of accuracy provided by these tools can sometimes result in a less cautious approach to the analysis. This is because the input loads are almost always estimated and must be confirmed during flight testing. However, the evolution of the tools for analysis has not been accompanied by a commensurate increase in the understanding of material behaviour. The conservatism inherent in factors of safety, which accounted for some of the gaps in the knowledge are being eroded. It is for these reasons that a fundamental understanding of the material mechanical properties and in particular its yield and fracture behaviour are crucial to the safe design of aircraft structures and landing gears. This understanding is intrinsically linked to the evolution and control of the alloy's microstructure. The primary aim of this thesis is to shed light on the mechanical behaviour of a novel β-titanium alloy based on a more thorough understanding of its microstructure and response to heat treatment.
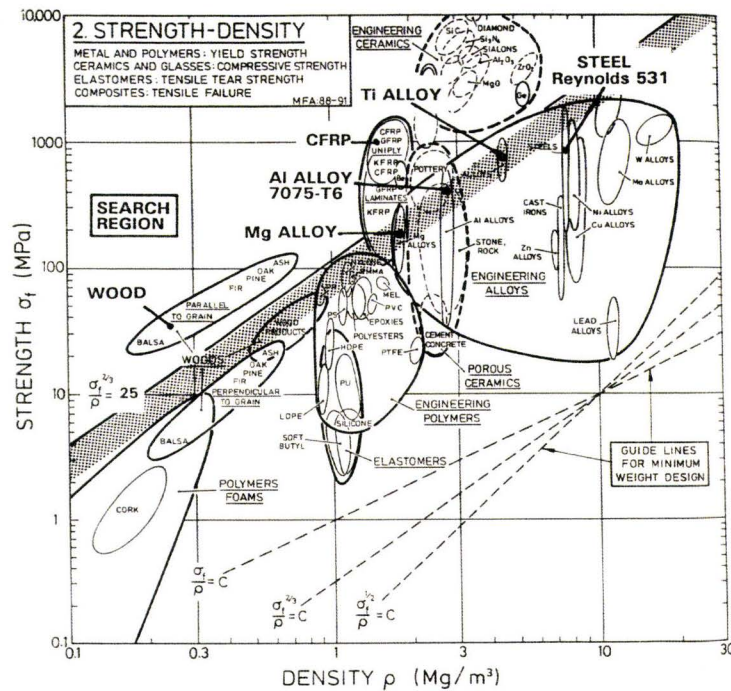
Figure 1.1: Chart showing relative ranking of materials according to their Strength and Density. [1]
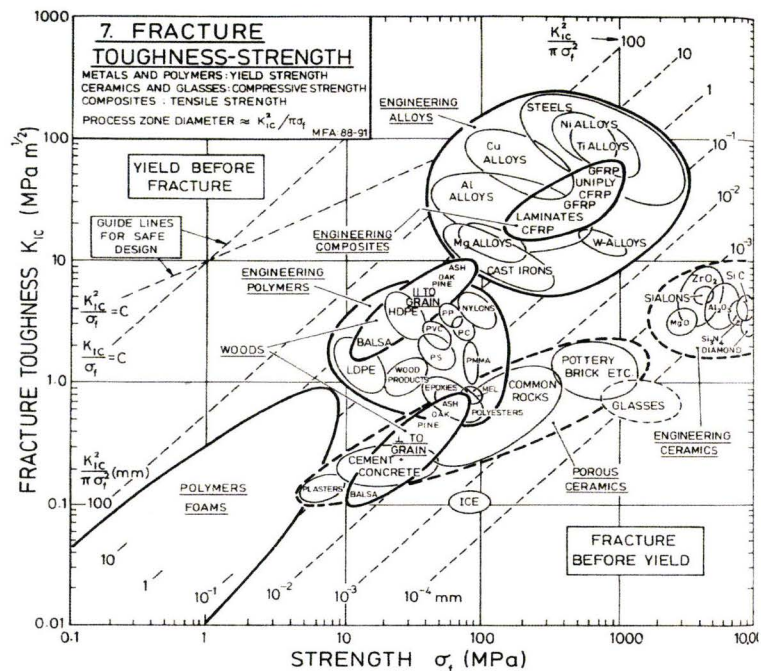
Figure 1.2: Chart showing relative ranking of materials according to their Fracture Toughness and Strength. [1]

1.1 A Short History of β Alloys in Aerospace Applications

Shortly after World War II, titanium alloys were recognized for their combination of desirable properties and their strategic advantage for aeronautical applications. Among these desirable properties are: high strength to weight ratio, high temperature capabilities, resistance to environmental degradation, and relatively good fatigue properties [1]. Development of titanium alloys has been dominated by the military sector, where the development and acquisition costs have been justified by performance advantages. In the context of landing gear applications, military proven titanium alloys have slowly been introduced to the more conservative commercial sector justified by weight saving potential. Acceptance of titanium alloys in commercial aircraft design has been accompanied by intense scrutiny and cost benefit analysis. The reluctance surrounding the wider acceptance of titanium has been to due to the volatile nature of the titanium market. More recently, a lot of research has been devoted by titanium manufacturers into cost effective production of titanium concentrates from oxide ores and single melt processes such as plasma hearth and "skull" melting.[2][3] These efforts are aimed at reducing the high cost of titanium and stabilizing the market. Even though the price of titanium remains comparatively high, the use of titanium alloys has increased steadily with every new design. In recent years, development of airframe alloys is sometimes lead by the commercial sector. More specifically to landing gear applications, early designs made use of α-β alloy Ti-6Al-4V, for structural and "shock strut" internal components, but were subsequently replaced by Ti-6Al-6V-2Sn, and later by higher strength β alloys such as Ti-10V-2Fe-3Al.[4], [5] High pressure hydraulic tubing, traditionally made of corrosion resistant steels, have been converted almost entirely to Ti 3Al-2.5V, in the commercial and military sectors. Other β-titanium alloys have also found other niche applications such as springs, where Ti-3Al-8V-6Cr-4M0-4Zr has become the alloy of choice

Historically, a separation in the development of titanium alloys existed between the west (USA, Europe and Japan) and the east (predominantly in the former Soviet Union). This has lead to the development of independent alloy systems.

With the onset of globalization and dissolution of the former Soviet Union, Russian alloys are now available in the west.[6] The most interesting for the landing gear application has been Ti-5Al-5V-5Mo-3Cr, based on the Russian alloy system termed VT22 (BT22). The most common alloy currently used for commercial sector landing gears is Ti-10V-2Fe-3Al. This β alloy is somewhat difficult to melt and its mechanical properties decrease with increasing thickness. Recently, Ti-5Al-5V-5Mo-3Cr has gained significant interest, as it has been shown to have higher tensile strength capabilities for larger thickness (200mm) than Ti-10V-2Fe-3Al.

The two most important criteria driving the selection of titanium alloys in aerospace applications are the combination of high strength-to-density ratio, and resistance to environmental degradation. Depending on the specific application, resistance to fatigue is sometimes as important as static strength in modern aircraft designs. However, the compelling reasons for selecting β titanium alloys in landing gear design remain their high static strength/density ratio and their extremely high corrosion resistance. Among the corrosion related factors considered are the resistance to general corrosion and to stress corrosion cracking. Except in the high temperature areas of an aircraft, all titanium alloys are considered immune to general corrosion and degradation in the environments typical of aircraft operation. In fact, the vast majority of titanium components spend their service life without any surface treatment or corrosion protection. Hence, from a corrosion standpoint, the only critical attribute considered is the alloy's stress threshold to avoid fracture due to stress corrosion cracking.

From a static strength perspective, Ti-5Al-5V-5Mo-3Cr has a higher tensile strength/density ratio when compared to the incumbent landing gear alloys. For components or sections of components designed by static strength, this results in lighter designs. Figure 1.3 presents a comparison of the strength/density ratio and fracture toughness, for the alloys of choice used in landing gear design. Depending on the size and service duty expected, aluminum alloy 7175 in the T7451 temper or ultrahigh strength steel 300M heat treated to a minimum tensile strength of 1930MPa, are the most common landing gear alloys. However, these alloys often experience corrosion degradation and must be overhauled periodically. To prevent in-service corrosion, the titanium alloy of choice is Ti-10V-2Fe-3Cr in the solution treated and aged (STA) condition. Although titanium components are typically lighter and do not require maintenance due to corrosion, their acquisition cost is typically 10-15 times that of equivalent components made from ultra high strength steels. Considering the strength-to-density ratio in the design of a component using titanium alloy Ti-5Al-5V-5Mo-3Cr against 300M steel, would result in a advantage of more than 4%; such significant advantage often justifies the additional expense. Note that the fracture toughness for all these alloys is relatively low, and would be considered unacceptable for design of aircraft structural members other then landing gears.
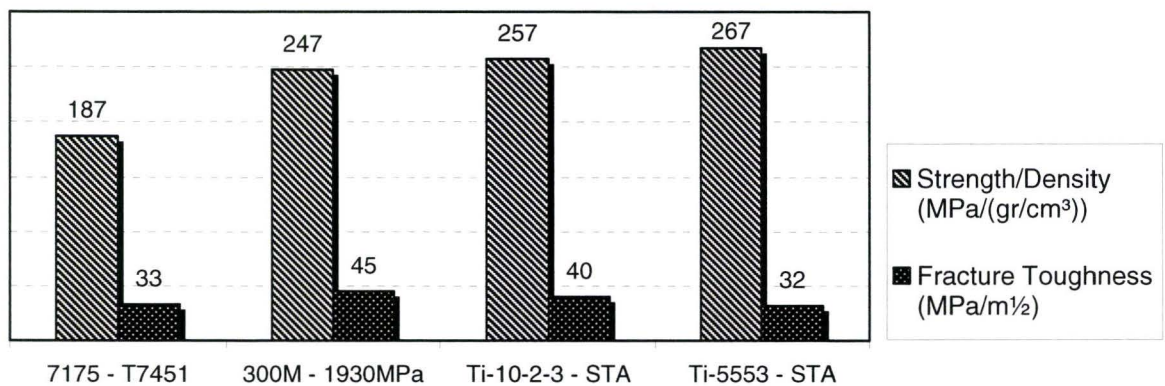
Figure 1.3: Comparison of Strength/Density and Fracture Toughness for common Landing Gear alloys against Ti-5553. Note: STA refers to Solution Treated and Aged corresponding to the "peak strength" condition.

Characterization and understanding of the microstructure and mechanical properties of this alloy would be of great interest to the landing gear design community. It is expected that this alloy would become the replacement for Ti-10V-2Fe-3Al and result in lighter, more efficient landing gear designs.

1.2   Background on Titanium Alloy VT22 and Engineering Problem

As the tensile properties of titanium alloys are lower than those for the so called "ultra high strength steels" (300M, etc.), the dimension and cross sections of structural landing gear components made from titanium are proportionally larger. For very large landing gears, the sections exceed the maximum hardenability achievable with water quench alloys such as Ti-10V-2Fe-3Al. Figure 1.4 is a isometric diagram of a Bogie Beam for a very large airliner manufactured from Ti-10-2-3. This forging weighs in excess of 3,200 kg, has a length of over 4.2 m and a maximum cross section of 560X670mm.

1 m
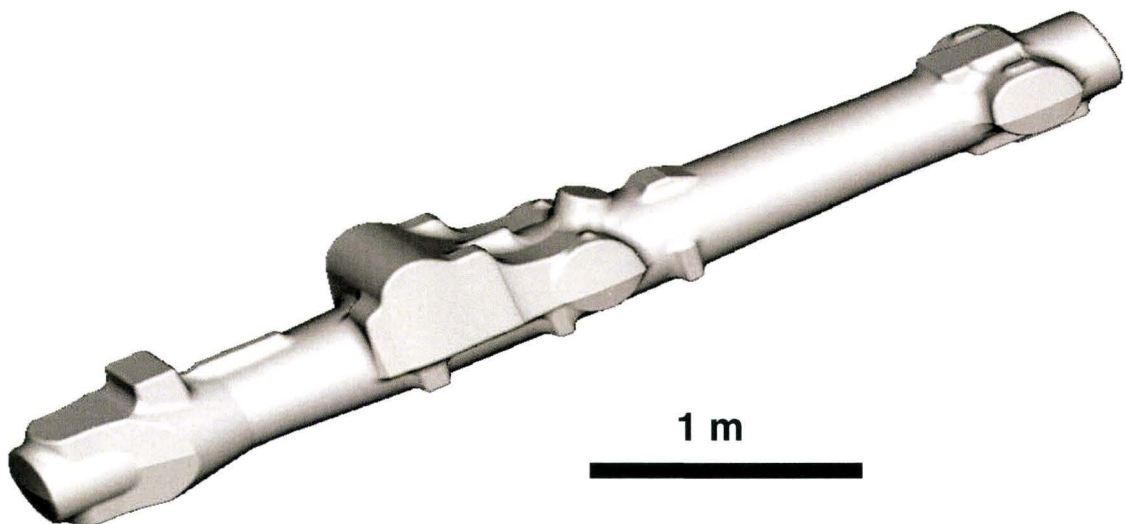
Figure 1.4: Three Dimensional Model of Bogie Beam Forging for a Large Airliner.

Prior to heat treatment, the forging must be extensively machined to reduce the section thickness. Quench distortion is often a concern with heat treatment of such large, slender components, which complicates the manufacturing process.

Air "quench" alloys such as Ti-5Al-5V-5Mo-3Cr are capable of higher tensile properties in much larger cross sectional sizes. Furthermore, this alloy can be through hardened as a forging without the need for prior machining, eliminating manufacturing steps and the risk of distortion. This alloy is an improved derivative of a Russian titanium alloy termed VT22, which has a nominal composition of Ti-5Al-5V-5Mo-1Cr-1Fe. VT 22 was used extensively in Russian airframe applications for the Ilyushin, Tupolev, Antonov, and Yakovlev aircraft. [8]
Another similar alloy often referred to as VT22-1, having a nominal composition Ti-5Al-5V-5Mo-3Cr-1Zr, is also being investigated in Europe. This system of alloys, and in particular Ti-5Al-5V-5Mo-3Cr (Ti-5553), is not well understood in the West.

Although the potential benefit of using this new alloy in landing gear designs has attracted a great deal of interest, there is an equal hesitation to adopt this alloy until its microstructure-property relationship is better understood.

2.0   OBJECTIVES

The objective of this thesis is to characterize the microstructural changes occurring in Ti-5Al-5V-5Mo-3Cr upon heat treatment, and to gain a fundamental understanding of the relationship between the microstructure and mechanical properties. The outcome of the mechanical property response will be assessed against minimum property requirements for industrial consideration of this alloy.

In this context, the evolution of the microstructure will be studied using industry based heat treatment processes. These practices necessitate heat treatment in air furnaces and involve complications such as adsorption of oxygen at the surface. Additionally, the scale of the cross sections intended for Ti-5553 dictate cooling rates which are much slower than those possible in a laboratory setting.

Analysis of the mechanical response for this alloy will consider the elastic, plastic and final fracture behaviours for each heat treatment condition. Since the fracture process in industrial components involves more than tensile stresses, deformation and fracture evaluation will involve tension, compression and shear stress states.

Moreover, other properties such as fracture toughness and stress corrosion cracking, deemed essential for alloy consideration in component design, will be evaluated against currently used alloys.

The knowledge of critical plasticity and fracture properties will aid structural analysis and reduce the risk of component failure. It is hoped that with a better understanding of this alloy, manufacturing processes and heat treatment can be optimized and the properties tailored for use in new landing gear designs.
As the great majority of structural components for landing gears are manufactured from forgings, this work will utilize forged product forms manufactured to the current industry practice.

The approach taken to accomplish the outlined goals is as follows:

i)   Characterization of the microstructural evolution as a function of heat treatment

ii)   Study of the mechanical properties and strengthening mechanisms operative for this alloy

iii)   Analysis of the deformation and fracture under various stress states

iv)   Evaluation of the fracture toughness and stress corrosion cracking behaviours

v)   Discussion of the important features pertinent to Ti-5553 microstructure and properties

vi)   Conclusions, Practical Recommendations and Future Work

3.0   LITERATURE REVIEW

The following is a brief summary of the usual classification of titanium alloys with the aim of introducing the basic properties and the terminology common in the literature. The basic concepts of phase stability of the α and β phases are discussed, the classification of α, $\alpha+\beta$ and β alloys are presented for the purpose of placing Ti-5553 in a comparative scale with other β alloys. The equilibrium and non-equilibrium transformations possible are introduced with emphasis on the metastable phases which are likely to appear in the heat treatment of Ti-5553. Recent work on phase transformations of Ti-5553 is reviewed. A brief consideration of the mechanical properties of β titanium alloys with emphasis on the representation of the stress strain behaviour is presented. Finally, the general theories of elastic failure are introduced and the concept of yield and fracture envelopes discussed.

3.1.   Classification of Titanium Alloys

Titanium is an allotropic element; in its pure form it undergoes a phase transition from hexagonal close packed (α phase) to body centered cubic (β phase) when heated above 882.5°C. [56]. Unalloyed titanium is very ductile but has relatively low strength. Alloying elements dissolved in titanium can raise the transition temperature (α stabilizers), lower it, (β stabilizers) or have little effect (neutral additions).[7]

Alpha Stabilizers: These elements are soluble in the α- phase and increase the β-transus temperature with increasing concentration. It is customary to further subdivide α stabilizers into substitutional or interstitial.

Beta stabilizers: These are mostly transition metals in the periodic table, they lower the β transus temperature and expand the range over which the β phase is stable within the equilibrium phase diagram. To further simplify classification of β stabilized systems, β stabilizers are subdivided into β-isomorphous and β-eutectoid.

Beta Isomorphous: These elements have restricted α, but extensive β solubility ranges. The literature often refers to these elements as completely soluble in the β phase. Increasing the solute content decreases the β transus, but the decomposition reaction of β into α + eutectoid products does not occur, even under equilibrium conditions.

Beta Eutectoid: These elements stabilize the beta phase, whereby the β phase has a limited solubility range. Upon cooling, β decomposes into α + intermetallic compound.

Alpha-Beta Isomorphous (Neutral Additions): These elements show complete mutual solubility with titanium in the α and β phases, and do not strongly promote phase stability. Additions of these elements are made to both α and β alloys, as strengthening agents and to slow down reaction kinetics - Zr and Sn are examples.

A summary of the major alloying elements for titanium and respective classification as described above is presented in Table 3.1.

Table 3.1:   Classification of the major alloying elements in titanium

α - Stabilizing	β - Isomorphous	β - Eutectoid	Neutral
Aluminum Gallium Germanium Lanthanum Cerium Oxygen Nitrogen Carbon	Vanadium Niobium Tantalum Molybdenum Rhenium	Copper Silver Gold Indium Lead Bismuth Chromium Tungsten Manganese Iron Cobalt Nickel Hydrogen Silicon	Zirconium Hafnium Tin

A list of the alloying elements and their effect on yield strength is presented in Table 3.2. Additions of α stabilizers such as Aluminum and even 0.1% Nitrogen double the yield strength of pure titanium, while additions of a few percent of β stabilizers such as Iron and Chromium have an even higher effect on yield strength. Note that additions of Zirconium and Tin have a very small effect on yield strength.

Table 3.2:   Effect of alloying additions on Yield Strength of titanium [30]

Element	Addition to Base %	Yield Strength Annealed* MPa	Annealed* ksi	Heat Treated* MPa	Heat Treated* ksi
Base Ti		241	35	...	...
Alpha-stabilizer:					
N	0.1	483	70	...	...
O	0.1	365	53	...	...
C	0.1	324	47	...	...
Al	4	496	72	...	...
Neutral stabilizer:					
Zr	4	331	48	...	...
Sn	4	310	45	...	...
Beta-stabilizer:					
Fe	4	593	86	703	102
Cr	4	510	74	655	95
Mn	4	503	73	634	92
Mo	4	490	71	620	90
W	4	483	70	572	83
V	4	400	58	496	72
Nb	4	310	45	324	47
H	0.1	241	35**	...	...
Si	1	448	65	.	..

*Annealed-[Beta transus - 93°C (200°F)] - FC to 482°C (900°F) - AC
Heat Treated - [Beta transus - 38°C (100°F)] - 1/2 hr - WQ, 538°C (1000°F)-2 Hr-AC
**Strengthening has been noted in α + β and some α alloys
Note: FC = Furnace-cooled
      AC = Air-cooled
      WQ = Water-quenched

3.1.1. Multicomponent Titanium Alloys

Multicomponent alloys are generally made up of α and β stabilizers. Several classification schemes have been proposed in the literature based on relative amounts of stabilizers; the most accepted in North America is the "US Technical Multicomponent" system, which subdivides titanium alloys into α, β and $\alpha + \beta$ alloys. The $\alpha + \beta$ alloys are further classified as near α, and near β alloys. According to this scheme, Ti-5Al-5V-5Mo-3Cr is classified as a β alloy, more precisely a metastable β alloy, see Figure 3.1. The metastable term is due to relatively unstable nature of the beta phase following quenching from the beta phase field. The other characteristic of the metastable β alloys is that the martensite start (Ms) temperature is suppressed below room temperature.

An alternate scheme to alloy classification was formulated by Nishimura [4], which places the US Technical Multicomponent alloys along the abscissa of a β-isomorphous pseudo-binary phase diagram, see Figure 3.1. This scheme places the alloys according to the relative abundance of α and β stabilizing additions. This relative rating is best-expressed in terms of α and β stabilizer equivalencies.
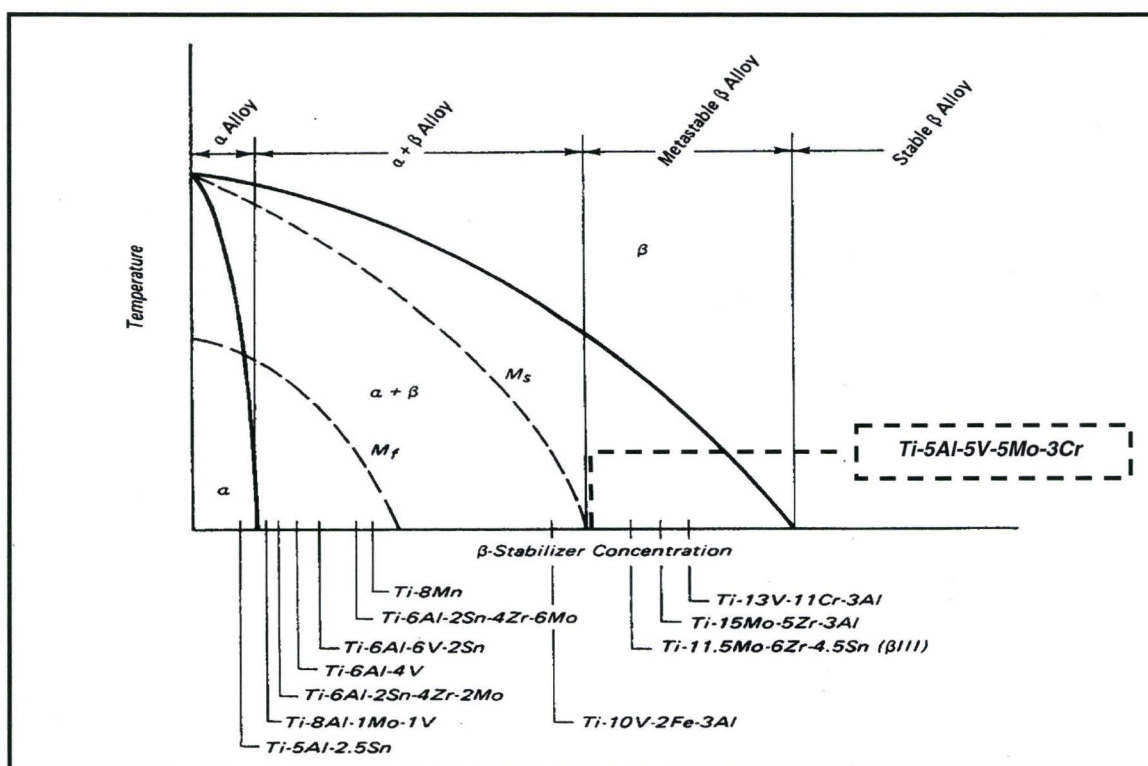
Figure 3.1: Compositions of multicomponent alloys mapped onto a pseudo-binary β-isomorphous phase diagram, including location of Ti-5Al-5V-5Mo-3Cr. *[4]*

The concept of stabilizing equivalency utilizes Aluminum and Molybdenum as the prototypical α and β stabilizing components respectively.
Rosembergh,[43] devised an Aluminum equivalency formula, based on weight percent concentrations of Aluminum, Zirconium, Tin and Oxygen.

[Al]eq = [Al] + 1/6[Zr] + 1/3[Sn] + 10[O]

The influence of additions of β stabilizers (transition elements) to titanium can be expressed by how much they lower the martensite start temperature and the degree by which they retain the β-phase at room temperature. Molchanova [9], expressed this Molybdenum equivalency as follows:

[Mo]eq = [Mo] + 1/5[Ta] + 1/3.6[Nb] + 1/2.5[W] + 1/1.5[V] + 1.25[Cr] + 1.25[Ni] + 1.7[Mn] + 1.7[Co] + 2.5[Fe]

A minimum [Mo]eq of 10 is required to retain the β-phase at room temperature; the [Mo]eq for Ti-5Al-5V-5Mo-3Cr is approximately 13 while for Ti-10V-2Fe-3Al this value is closer to 12.

Converting a multicomponent alloy Al and Mo equivalencies provides a rationalization for different alloys characteristics and assists in predicting its properties. Figure 3.2 presents the classification of selected β titanium alloys with Al and Mo equivalencies, Ti-6Al-4V is included as a baseline for comparison. Note the position of Ti-5Al-5V-5Mo-3Cr, which has a higher [Mo]eq than Ti-10V-2Fe-3Al, and higher [Al]eq and [Mo]eq than VT22.
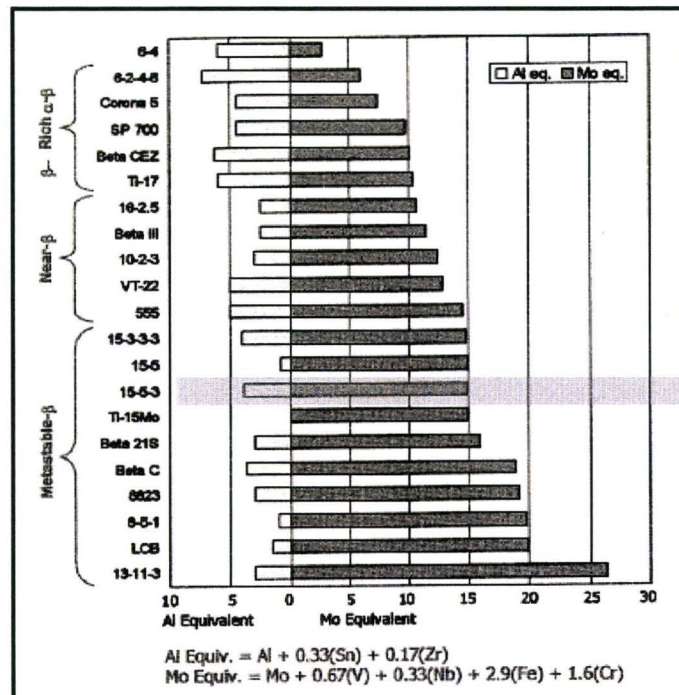
Figure 3.2: Classification of selected β titanium alloys with Al and Mo equivalencies shown. [10]

3.1.2. Comments on Phase Stability in Titanium

Study of the factors governing phase stability in titanium and titanium alloys has received considerable attention in the literature and is beyond the scope this thesis. However, the following is a synopsis of the basis for phase stability in titanium alloys, as summarized by E.W. Collings *[56]*. Mc Quilan, presented a thermodynamic explanation based on the relatively more open BCC (β) structure, which has higher vibrational entropy than the close-packed HCP (α) structure. Upon heating, the free energy of the HCP lattice will decrease more slowly than that of the imaginary BCC lattice. With continued heating, there will be a temperature above which the lattice will transform from HCP to the more thermodynamically favourable BCC structure. At an atomistic level, Jaffe and coworkers concluded that although size factors play a role, phase stabilization mechanisms in titanium alloys are electronic in nature. Before a specific discussion of the phase stability and decomposition of the β phase in Ti-5Al-5V-5Mo-3Cr can take place, a general discussion of the equilibrium and non-equilibrium reactions is warranted.

3.2. Equilibrium Phases

For an alloy such a Ti-5553, an understanding of the equilibrium phases would require a quintenary diagram, which is at present not available. Nonetheless, a review of the pertinent binary phase diagrams would provide insight into the anticipated reactions. The following pages are devoted to introducing the equilibrium phases expected in terms of the binary phase diagrams for the main alloying elements Aluminum, Molybdenum, Vanadium, Chromium and Iron.

3.2.1. Ti-Al System

The Ti-Al equilibrium phase diagram has been considered to be representative of α stabilized titanium alloys. Although several diagrams for this system are available in the literature, a great deal of discussion has been centered on discrepancies in the absolute locations of phase boundaries; one of the earliest phase diagrams being that of Molchanova [9]. Figure 3.3 presents a binary Ti-Al phase diagram taken from *Alloy Phase Diagrams* - ASM Handbook, and attributed to J. L. Murray 1987. The most important features of this diagram is the presence of the ordered intermetallic compounds Ti$_3$Al (*hP*8) and TiAl (*tP*4). These compounds are important because of their brittle intermetallic nature at high aluminum concentrations ~25 at.% (Ti$_3$Al), 50 at.% (TiAl), and ~70 at.% (TiAl$_3$). However, these ordered intermetallic compounds are not present in the great majority of commercial titanium alloys.
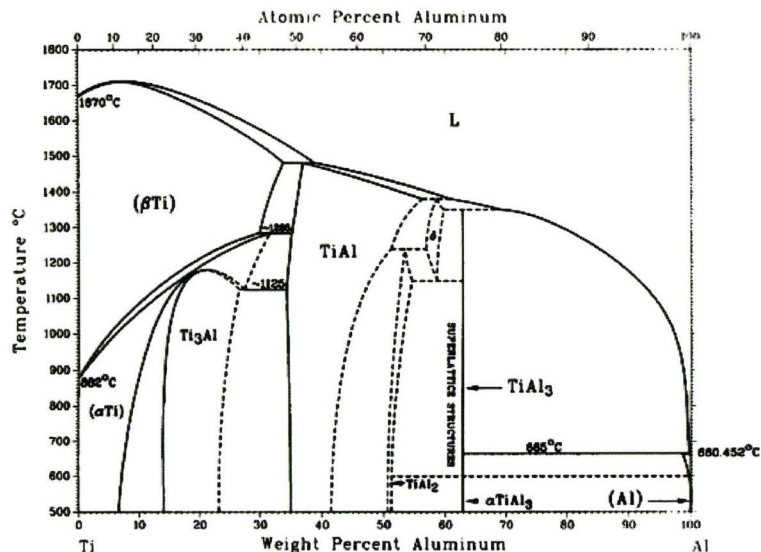
Figure 3.3: Ti-Al equilibrium phase Diagram. *[11]*

3.2.2.   Ti-Mo – The β-Isomorphous System

As expressed earlier, Ti-Mo is the system considered representative of β-isomorphous additions and is characterized by an almost linear decrease in the β transus with increasing Molybdenum content to ~21 weight %, Figure 3.4. Similarly, the Ti-V diagram shows a decrease in the β transus with increasing Vanadium concentration up to a composition of ~19 weight %. However, as shown in Figure 3.5, Vanadium is significantly more soluble than Molybdenum in the α phase.
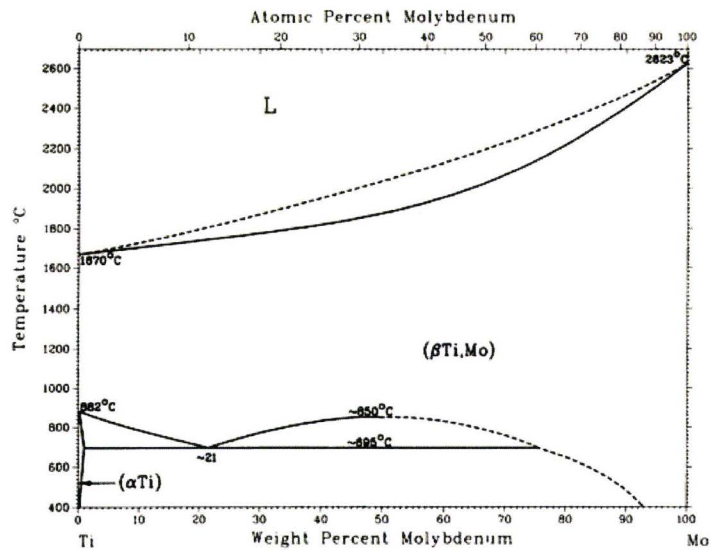
Figure 3.4   Ti-Mo equilibrium phase Diagram *[11]*
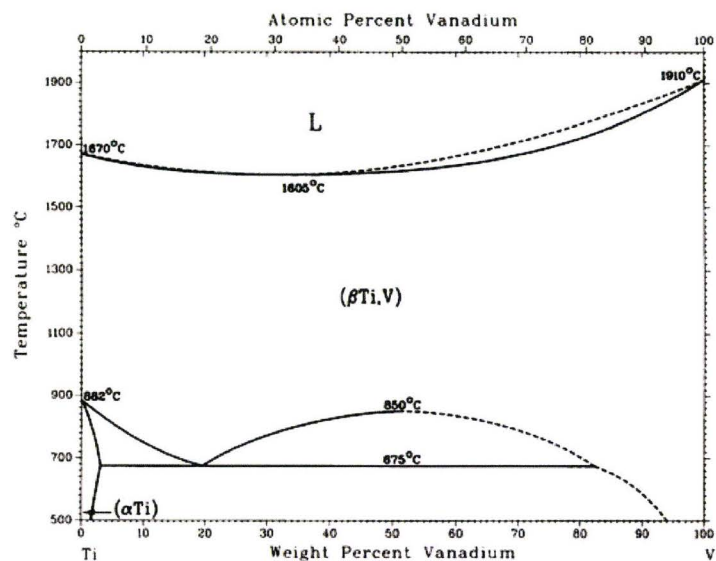
Figure 3.5: Ti-V equilibrium phase Diagram *[11]*

3.2.3   Ti-Cr – The β Eutectoid System

The Ti-Cr binary diagram, shown in Figure 3.6, is characterized by the presence of the intermetallic compound $TiCr_2$, which is allotropic (α $TiCr_2$, $cF24$, β$TiCr_2$, $hP12$ and γ$TiCr_2$, $hP24$) within a narrow composition range (65-68 weight %). Similarly, the Ti-Fe diagram is shown in Figure 3.9 and has an intermetallic, TiFe ($cP2$) at approximately 51-54 weight % Fe. Fe is much less soluble than Cr in the α phase, with a maximum solubility of 0.047%. Additionally, Fe is a more potent β stabilizer, reducing the β transus more rapidly and, the eutectoid temperature being 595°C. Both these elements are considered sluggish eutectoid formers; hence, the presence of intermetallic compounds in commercial alloys such as Ti-5553 would not be expected.
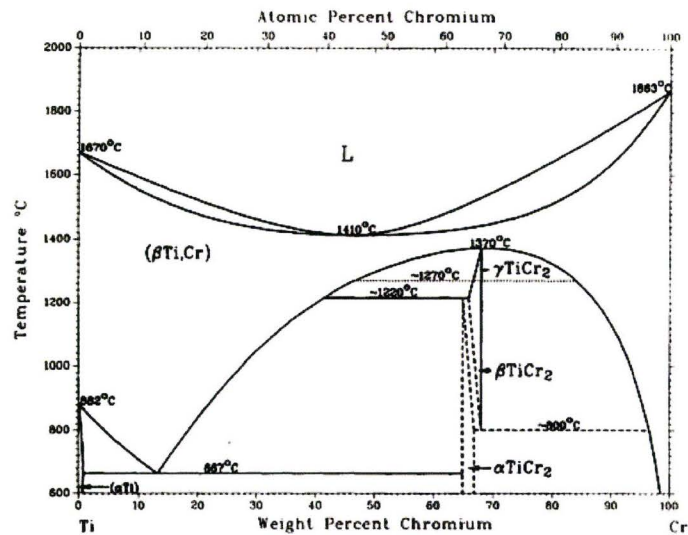
Figure 3.6: Ti-Cr equilibrium phase Diagram *[11]*
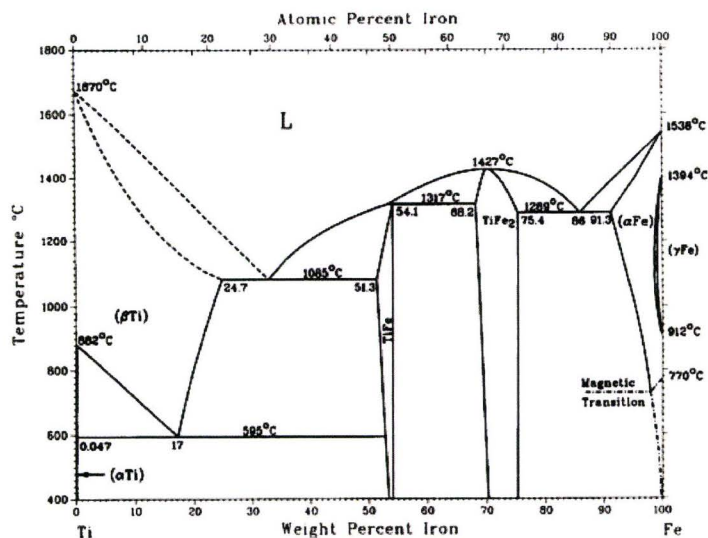
Figure 3.7: Ti-Fe equilibrium phase Diagram *[11]*

3.3. Metastable Phases and Phase Transformations

The preceding section presented the equilibrium phases for binaries of titanium and the alloying elements in Ti-5553; however, in commercial practice, equilibrium states are impractical and rarely achieved. In fact, it is often desired to "quench in" some non equilibrium state or affect a non equilibrium transformation. In α and commercially pure titanium, the transformation of the BCC β phase to the HCP α phase can take place by diffusion controlled nucleation and growth processes or martensitically, depending on α alloy composition and cooling rates. Studies of the transformation of in zirconium by Burgers [33], established that the crystallographic relationship between the β phase and the α phase is the following:

$$(110)\beta \parallel (0002)\alpha$$
$$[1\bar{1}1]\beta \parallel [11\bar{2}0]\alpha$$

Both, the diffusion controlled and martensitic forms of the α phase are found to closely obey the Burgers relationship, and can transform into 12 different variants with respect to the parent β crystal. A more detailed explanation of these variants is presented later in this chapter. For near α and $\alpha+\beta$ Ti alloys rapidly quenched from the β field, the resulting structure is martensitic, and referred to as α' or α''. [56] [13] [14] However when cooling in a less rapid fashion and allowing time for alpha nucleation and growth, a coarser structure known as Widmanstätten α develops. This process is illustrated in Figure 3.8:
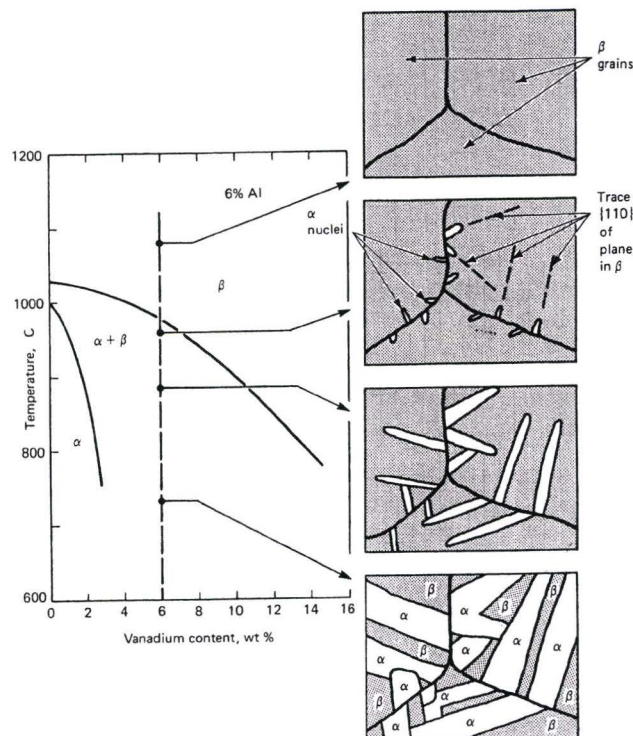
Figure 3.8: Schematic representation of the formation of the Widmanstätten structure in Ti-6Al-4V by cooling slowly from above the β transus, final microstructure consists of α plates (white), separated by β phase (gray). [12]

If however, the material is allowed to stabilize at some high temperature in the $\alpha+\beta$ field and then rapidly quenched, the resulting structure will be the "quenched in" structure present at this temperature and the transformation products of the rapid cooling. Of course, because the transformation times are relatively short, both of these scenarios result in metastable phases; the possible phases are discussed in more detail on the following sections.

3.3.1. Martensitic Transformation in Titanium Alloys

The martensitic transformation is a shear driven process involving the collective movement of atoms from the BCC structure to the hexagonal crystal structure over a certain volume. As shown in the pseudo-binary sketch in Figure 3.1, below an M_s temperature, the BCC structure is unstable and, two types of martensite α' and α'' are known to form. The shape of the transformed volume is disk shaped for most titanium alloys, but in two dimensions, the shape is described as plate-like. For dilute α stabilized systems, the α' martensite (HCP structure) prevails. On systems which are β stabilized and depending on compositions exceeding certain limits, transformation to the α'' martensite (orthorhombic) is favoured. The shear transformation process is complicated but can be simplified as the activation of the following shear systems:

$$[2\bar{1}\bar{1}3]\alpha\ (\bar{2}112)\alpha \ \text{ and } \ [2\bar{1}\bar{1}3]\alpha\ (\bar{1}011)\alpha.\text{[35]}$$

The orientation relationship of the β phase and the α' is: [13] [14]

$$(110)\beta\ \|\ (0002)\alpha'$$
$$[1\bar{1}1]\beta\ \|\ [11\bar{2}0]\alpha'$$

The α'' formation is strongly dependent on composition and, as determined for the Ti-Nb system, has a the following crystallographic relationship to the parent β:[56]

$$[100]\alpha''\ 2° \text{ from } \langle001\rangle\beta$$
$$[010]\alpha''\ 2° \text{ from } \langle110\rangle\beta$$
$$[001]\alpha''\ \|\langle1\bar{1}0\rangle\beta$$

Two morphologies of the α' martensite have been reported: the so called "massive" or packet martensite and the "acicular" martensite. The massive martensite occurs in pure or solute lean titanium alloys and consists of large (50-100µm), irregular regions with no optically resolvable internal features. However, at high magnifications, these regions contain sub-micron packets of parallel plates or α laths of the same Burgers relationship variant.

Acicular martensite consists of adjacent α plates, each having a different variant of the Burgers relationship. The morphology of the massive and acicular martensites is presented in Figure 3.9, and 3.10, respectively. This determination is possible as the higher solute content prevents a complete transformation to α phase, thus leaving β phase trapped between the acicular α plates. With the small β phase present, determination of the habit plane is possible.

The acicular α phase formation is analogous to the Widmanstätten plate formation presented as part of the diffusion controlled transformations. This comparison serves to illustrate that although the ideal martensite decomposition is a diffusionless process, depending on alloy composition and cooling rates, a competition between the diffusional and martensite transformation processes exist during quenching.
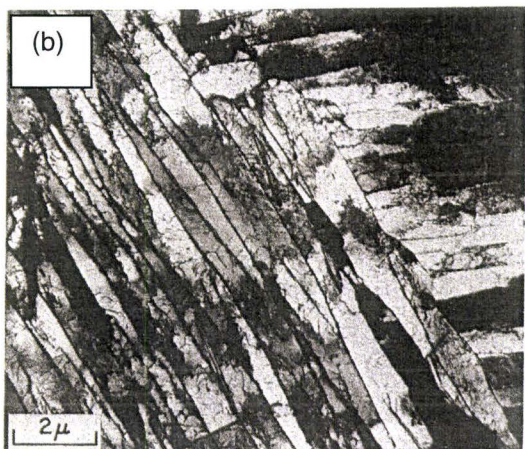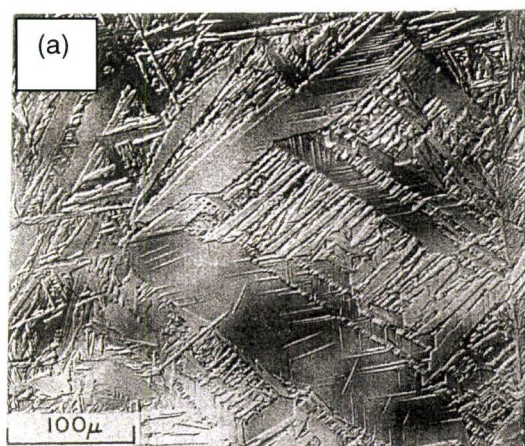
Figure 3.9: Massive martensite in Ti-1.78%Cu quenched from 900°C, (a) Optical, (b) TEM [37]
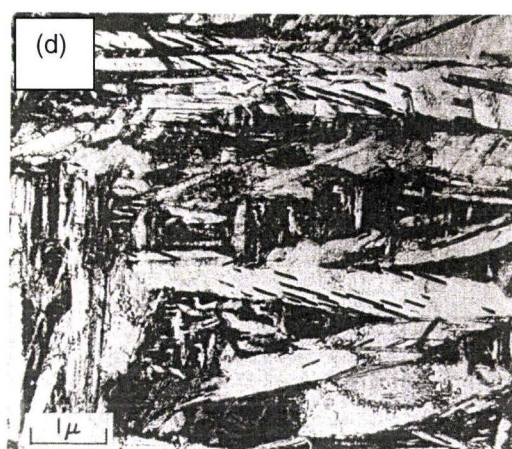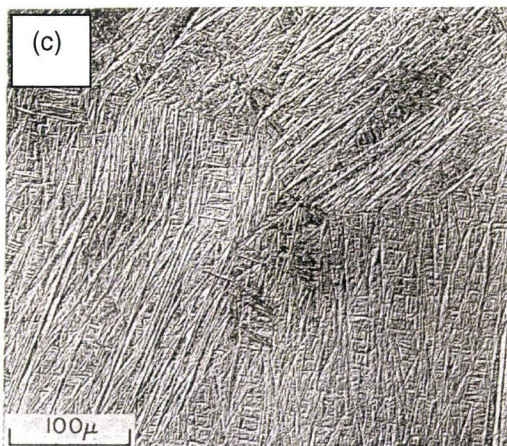
Figure 3.10: Acicular martensite in Ti-1.2%V quenched from 900°C, (c) Optical, (d) TEM [37]

For alloys with increased solute content, the hexagonal martensite becomes distorted, and can no longer be described as hexagonal, hence the crystallographic structure of this martensite is orthorhombic and identified as α". The boundary of the α'/α" in terms of the transition metal content has been determined by Bagariatskii and co-workers in the former USSR and varies greatly from one binary system to another. [4]

Nonetheless, the higher the solute content the trend points to a less ordered hexagonal structure giving way to an orthorhombic arrangement.

Another possible martensite formation mechanism is the stress induced martensite, which can take place in solute lean β alloys. Duerig, Terlinde and Williams [36], have shown that

stress assisted α" martensite can form in β and α-β annealed Ti-10V-2Fe-3Al alloy upon cold working. A small amount of mechanical twinning of the {112} $\langle 111 \rangle$ type was also observed, these twins being indistinguishable from the α" martensite.

It is important to note that for some alloys in which the martensitic reaction is suppressed, decomposition of the β phase occurs by means of the athermal ω phase. The athermal ω phase is thought to be a precursor of the martensite reaction as its formation involves the shear displacement in the <111> direction of the β lattice. A more detailed discussion of the ω phase formation and differences from titanium martensites follow in next section.

3.3.2. The Athermal and Isothermal ω Phase

When α+β or β stabilized alloys are quenched rapidly from the β phase field, a fine precipitate known as athermal omega (ω_a) can form for some compositions. These compositions contain sufficient β stabilizing elements to suppress the martensite finish temperature below room temperature. It is generally accepted that ω_a phase forms without a change in composition, and it cannot be suppressed by quenching, at least at rates of 11,000°C/sec. *[37]* Hence, the ω_a phase was originally thought to form by a martensitic transformation, primarily because it could not be suppressed by quenching.

The ω phase is metastable; it was first discovered by X-ray diffraction and later confirmed by electron microscopy.*[56]* Determination of the structure of the ω phase has been characterized by controversy, nonetheless, it is well accepted that in weakly alloyed systems the ω phase is hexagonal, and in more highly alloyed systems its structure is trigonal. *[16]* The above is applicable for the athermal and isothermal ω phases, regardless of their morphology. Isothermal omega (ω_i) is formed during ageing of the retained β phase (or β + ω_a) in the 200-500°C range. Nucleation of ω is accepted to be a homogeneous transformation.

The ideal hexagonal structure is that of AlB_2 arrangement, which can be visualized by forming an ABABAB... stacking sequence. Since there is no preferential segregation of solute and titanium to the A or B planes, there is conflict between the purely metallic to metallic bonds in the Ti-solute (ω), versus the mixed metallic-covalent bonding between Aluminum and Boron (AlB_2). Consequently, in the ω phase arrangement, the distance in the B plane must be 7% shorter than that of the A plane, and 14% shorter than the shortest AB distance. This provides for the highly unusual packing in the ω phase structure. *[16]*

The orientation between the β and ω phases have been found to be as follows: *[16][17]*

$$[111]\beta \parallel [0001]\omega$$
$$(110)\beta \parallel (11\bar{2}0)\omega$$

This results in four variants of ω with respect to β. An illustration of this relationship looking along the [111]β is shown in Fig. 3.11.
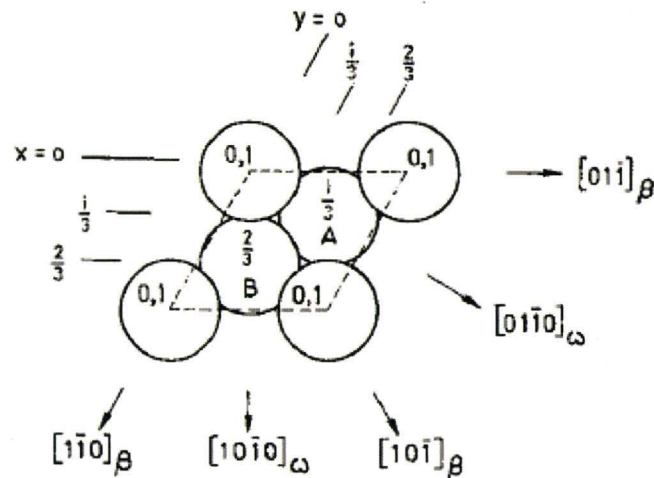
Figure 3.11:   BCC atomic arrangement looking along the [111]β direction, numbers within atoms are Z-coordinates. *[16]*

The mechanism of ω formation is accepted to be by collapse of the pair of (110)β planes leaving the adjacent planes unaltered, as depicted in Figure 3.12.
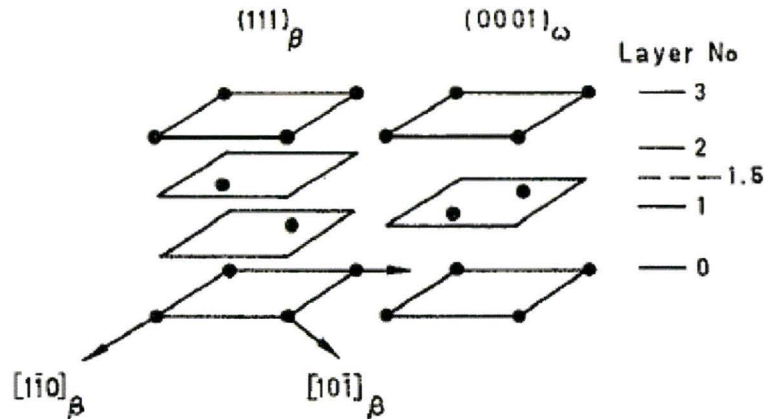
Figure 3.12:   ⟨111⟩ plane collapse model. (111) planes in β become (0001) in ω phase with central atoms moving from layers 1 and 2 to layer 1.5. *[16]*

This requires a longitudinal displacement wave $2/3\langle 111\rangle\beta$ to the BCC lattice (Figure 3.13 (a)). Another way to visualize this is by application of a pair of equal and opposite shears to the (110)β planes in the ⟨111⟩β direction, through distances ~1/6 of the ⟨111⟩β plane separation, as shown in Figure 3.13.

The ω phase is extremely fine scale (20 - 40Å), hence it can not be resolved optically but can unequivocally be identified by SAD in the TEM. An example of ω_a from a brine-quenched Ti-5%Mo alloy identified by TEM is shown in Figure 3.14. Omega phase manifests itself by the appearance of additional diffracted intensities at $1/3\langle 112\rangle$, $2/3\langle 111\rangle$.... positions in the diffraction patterns of the β phase.

(a)

(b)
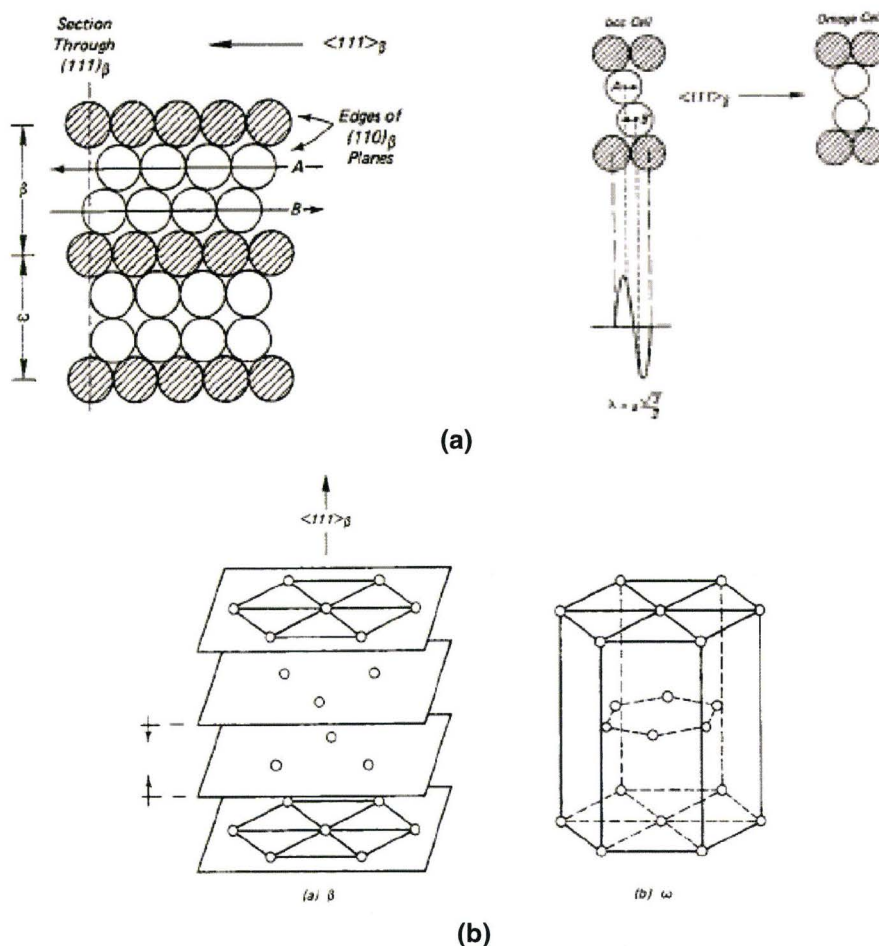
Figure 3.13: Transformation of β to ω two different views: (a) along the <111>β; (b) side view of the ω hexagonal lattice. [4]
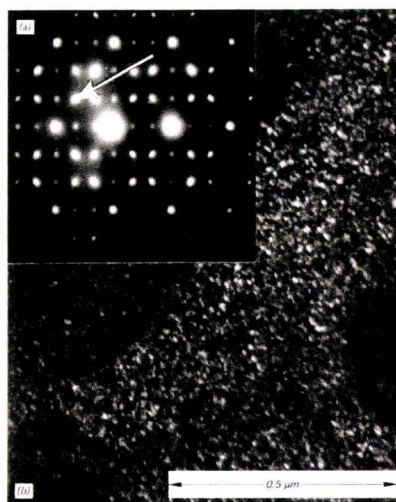
Figure 3.14: Transmission electron micrographs of Ti-Mo (5 at.%). (a) SAD pattern of omega; dark field image of spot indicated by arrow is shown in (b). [56]

Figure 3.15(a) presents the relative stability ranges for α', α'' and the mechanically unstable retained β in terms of a pseudo binary phase diagram. This diagram is helpful in visualizing the different martensitic transformation ranges, in particular, it presents a fine dotted line corresponding to a martensite start for deformation induced martensite (α''_D). Furthermore, this diagram predicts that with increasing solute content, α'' can form directly from retained β or as the result of deformation.

As shown in Figure 3.15(b), the ω_a range of composition is close to the α''. The composition of the ω_a phase is very similar to that of the quenched alloy, but for the ω_i, there is a shift in the lattice parameters of the β phase occurring during ageing. This points to an enrichment of solute in the retained β, and depletion of solute in the ω phase. [16] Occurrence of the ω_a in close proximity to the α'' phase boundary suggests that the formation mechanism of these phases are closely related. However, the absence of a habit plane precludes characterization of the formation of ω_a as martensitic.[56] The ω_a and α'' formation have been shown to occur due to a common electronic mechanism and have a narrow but distinct electron/atom range ratios. In alloys such as Ti-10V-2Fe-3Al, a somewhat similar alloy to Ti-5553, which is known to exhibit ω_a after quenching, the ω_a and α'' martensite are believed to compete, hence the as-quench structure will contain both. Moreover, the formation of stress induced α'', for the β solution treated Ti-10-2-3 containing ω_a has been reported by several researchers, more notably Duerig and Williams. [36]
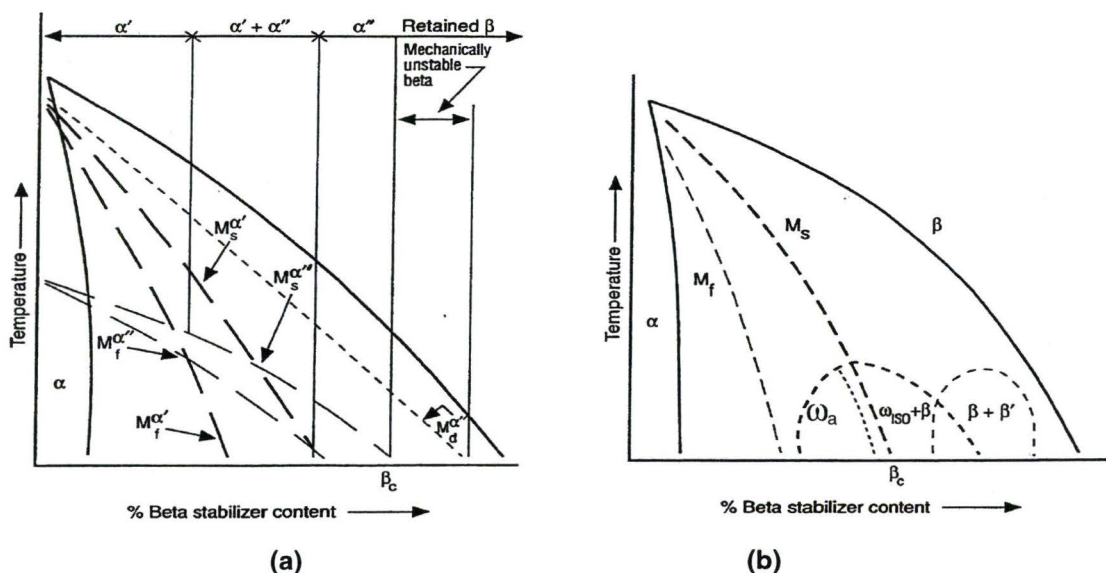
Figure 3.15: **Pseudo-binary phase diagram depicting the relative stability ranges for α', α'', ω_a and ω_i.** [38]

The volume fraction of ω_a depends on alloy chemistry but it is usually low, hence, it has little effect on as-quenched properties. A great deal of attention has been given to the effect of ω on tensile properties due to its association with embrittlement problems. It has generally been shown that embrittlement occurs for volume fractions of ω greater than 50%. For intermediate volume fractions 25-45%, ω can lead to effective strengthening. However, the presence of ω_a and α'' are of considerable importance during subsequent ageing treatments.

The morphology and mechanism of the ω_I phase precipitation has been investigated by Williams and also Hickman *[39]*, and has been shown to form as ellipsoids or cubes depending on the elements involved. In the Ti-Mo system misfits are small and the shape of the ω particles is predicated on minimization of the surface energy; hence the particles resemble ellipses with the major axis parallel to the <111>β. For the Ti-V system, the misfit is large and ω particle shape is dictated by minimization of the elastic strain in the matrix; consequently, the particles are cuboidal with the cube faces parallel to the <100>β. In general, for Ti-V, Ti-Cr, Ti-Mn and Ti-Fe, ω forms as cubes while for Ti-Nb and Ti-Mo alloys, ω forms as ellipsoids, see Figure 3.16 (a) and (b), respectively. The lattice misfit to particle shape relationship has been reported as linear; with misfits of <0.5% the ω is ellipsoidal, while for higher misfits it is cuboidal.

(a)   (b)
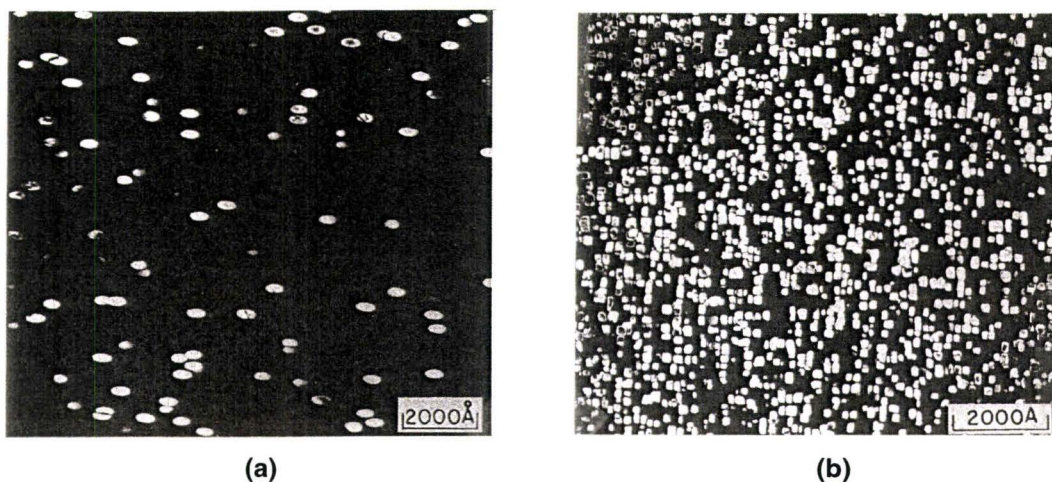
Figure 3.16:   Transmission electron dark field images of ellipsoidal (a) and cuboidal (b) ω-phase. *[37]*

The stability range of the ω_I phase is relatively small and varies with temperature and alloy composition. The maximum temperature at which ω_I is stable for at least a few minutes is ~550°C.

During the early stages of precipitation, the ω phase is coherent with the β matrix, as no misfit dislocations have been reported. As the particles grow, the misfits increase and lattice parameters changes have been interpreted as coherency strains. This increase in misfit strains have been used to explain changes is ω particle size and subsequent nucleation of the α phase. *[37]*

Nucleation of the ω-phase is generally believed to be homogeneous, although for some systems such as - Ti-Mo-Si, heterogeneous nucleation due to the presence of silicon has been reported. Nonetheless, the large volume fractions of extremely fine scale, coherent ω particles, suggest that for most Ti-alloy systems, the energy barrier for ω nucleation is very low.

3.3.3.   The β phase separation - β' phase

With compositions higher in β stabilizers the martensite and ω occurrence are suppressed, and the metastable retained β phase can undergo a phase separation β+β' upon ageing. Both phases have BCC structure but the β' phase is leaner in solute. *[56]* This phase separation occurs at temperatures between 200-500°C in the form very fine scale precipitates that can only be resolved by thin foil transmission electron microscopy; Figure 3.17 shows an example of β' precipitation. The relative stability range for the β' phase with relation to temperature and composition is shown in Figure 3.15 (b). The β+β' phase separation is a clustering reaction characteristic of alloys with positive heat of mixing. There seems to be disagreement on whether the β+β' phase separation can be considered an equilibrium or metastable reaction. Nonetheless, the reaction has characteristics akin to spinodal decomposition.
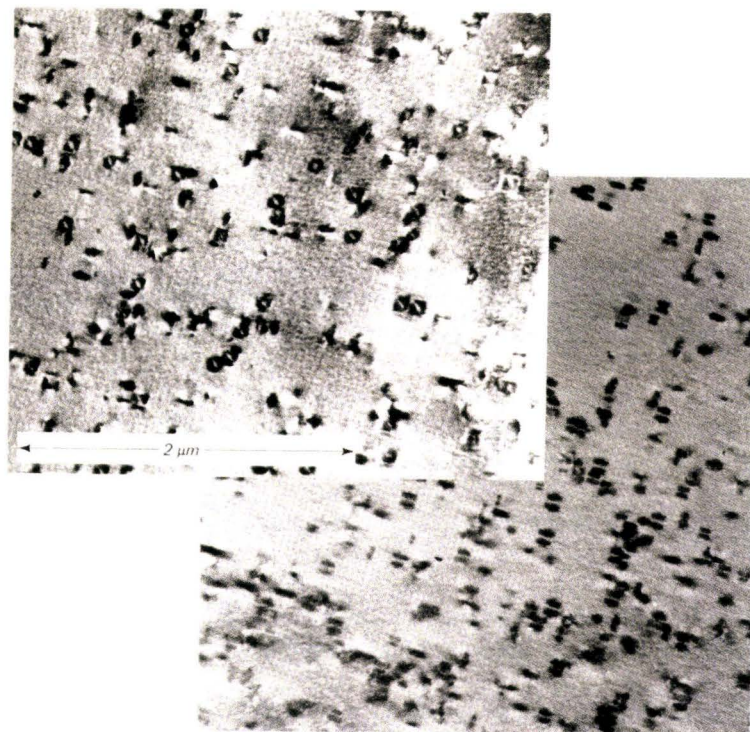
Figure 3.17:   Example of β' precipitates in a matrix of β. *[1.]*

Similarly to the ω-phase, the β' phase forms as a coherent, uniformly distributed zones within the β matrix,. The morphology of β' zones varies with alloy composition and misfit between the solute rich and lean BCC phases. *[37]* Like the ω phase, β' provides a nucleation path for alpha precipitation during ageing. Decomposition of the metastable β phase by means of the phase separation has been observed in a number of more heavily stabilized titanium alloys for which the ω phase is suppressed. Accordingly, the β+β' reaction can be characterized as the kinetically favoured decomposition route for alloys in which ω-phase formation is not possible and the equilibrium α formation is too sluggish.

3.4.   Ageing Reactions and Formation of the α Phase

Following solution heat treatment and quenching from either the β or α+β phase fields, the structure of a α+β or β titanium alloy will consist of some amount of retained β. This β is metastable and will decompose during ageing to the equilibrium β + α, or β + compound. Depending on composition and temperature the transformation of retained β can take various paths upon ageing. If we concentrate on alloys which composition does not allow for the formation of martensite, i.e. alloys with compositions to the right of the M_s line in Figure 3.15(b), only the ω and β' phases need to be considered. When ageing at relatively low temperatures, the transformation sequence is either:

$$\beta \rightarrow \beta + \omega \rightarrow \beta + \omega + \alpha \rightarrow \beta + \alpha$$
$$\text{or}$$
$$\beta \rightarrow \beta + \beta' \rightarrow \beta + \beta' + \alpha \rightarrow \beta + \alpha$$
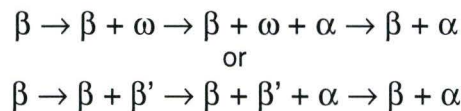
When ageing at higher temperatures a direct precipitation of α from β will occur:

$$\beta \rightarrow \beta + \alpha$$
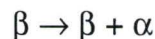
When either the ω or β' phases are involved, nucleation of alpha from these can result in an extremely fine and uniform coherent precipitate. However, the resulting dispersions are so fine that these precipitates are cut by dislocations and there is very limited plastic ductility; low temperature ageing cycles have little industrial acceptance. [13] [20] Commercial alloys are typically aged at higher temperatures in order to precipitate incoherent α particles nucleated at the ω or β' particles. Step ageing, consisting of a low temperature cycle aimed at nucleating a fine α dispersion at ω or β' sites, followed by a higher temperature cycle are more common. The β alloys Ti-3Al-8V-6Cr-4Mo-4Zr (Beta C), is often step aged to increase tensile strength and reduce ageing times.

Direct precipitation of α from the retained β phase which results from ageing at higher temperatures where ω or β' are unstable, generally leads to coarser α + β dispersions.

Similarly to the α + β alloys, two types of α phase have been reported for β alloys; that which obeys the Burgers orientation relationship and one that does not obey the Burgers relationship, which forms in a complex and not entirely understood manner. [18] The Burgers relationship between the BCC β matrix and the HCP α phase is presented in Figure 3.18, with an illustration of this relationship for an α/β colony provided at leftt, and the distortion associated with the α and β lattices at right.

$\{110\}\beta \parallel \{0001\}\alpha$
$\langle 111 \rangle \beta \parallel \langle 1120 \rangle \alpha$
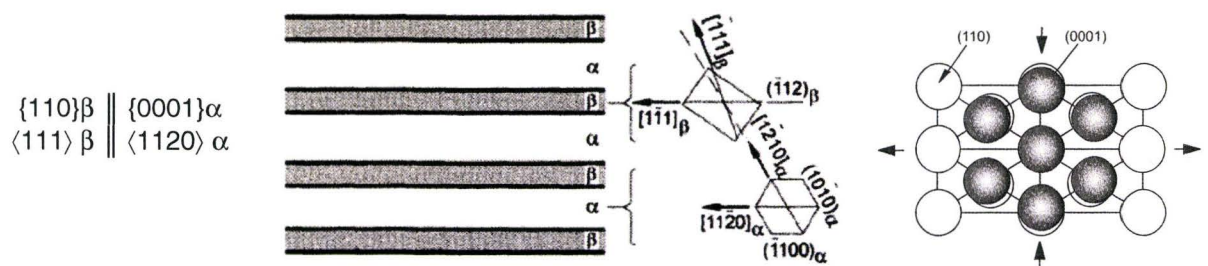
Figure 3.18: Diagram depicting the Burgers relationship on a α/β colony (left) [18], and distortion associated with the α and β lattices (right) [45].

A total of 36 variants of the Burgers relationship are possible between the β and α phases; however, only 24 variants are distinguishable in terms of atomic configuration. From these, two of each variant have the same primitive hexagonal lattice and can not be distinguished in terms of electron diffraction. This implies that a BCC crystal can transform to 12 HCP variants each with a different orientation to the parent β crystal. [40]

For alloys lean in β stabilizers or with significant amounts of Aluminum, the typical β decomposition involves the formation of Widmastätten α plates, with the long axis of the plates parallel to the $\{110\}\beta$. In these alloys, each Widmastätten α plate forms as a single variant of the Burgers relationship. Slow cooled Ti-6Al-4V provides an example of this type of β decomposition, see Figure 3.8.

The other type of direct β-to-α phase precipitation is characteristic of alloys richer in β stabilizers. This type of α forms as aggregates of very small α particles, with two distinct morphologies: (1) long lenticular regions and (2) clusters or "rafts" of α phase. When viewed under the TEM, the lenticular regions appear to contain internal structure, ostensibly related to the boundaries between the α particles and some small volume of untransformed β phase. With continued ageing, the regions containing α phase seem to grow at the expense of the retained β phase with no apparent coarsening of the individual α particles. Once the volume fraction of α reaches equilibrium, continued ageing results in coarsening of the individual particles and disappearance of the internal structure. Selected area diffraction patterns of these areas suggest that the Burgers orientation relationship is not strictly followed, furthermore, observations under dark field conditions suggest these particles conform to more than one variant. [37] This mechanism of β decomposition has been described as "sympathetic nucleation" similar to that of α-iron at α/matrix interphase boundaries studied by Aaronson [41] for steels. Nucleation and growth of variants of α at α/β boundaries has been characterized by Menon and Aaronson in terms of edge to edge and edge to face sympathetic nucleation in titanium alloys.[42]. Williams [37] reported that during the initial stages of ageing, the deviation of α to β phases from the Burgers relationship is relatively large, possibly due to strains involved. Nonetheless, the resulting α precipitates are fine, incoherent and act as effective strengtheners during ageing.

Ageing in the high temperature regime results in relatively coarse α precipitates, some nucleated at the grain boundaries and with a non-uniform distribution within the grains. The ensuing microstructure consists of relatively large regions of retained β and coarse α platelets, which results in low ductility. Titanium alloy Beta C (Ti-3Al-8V-6Cr-4Mo-4Zr) exhibits this behaviour; this is depicted in Figure 3.19. When aged directly from the solution treated condition at 510°C, large areas of retained β remain with the grains - Figure 3.19(a). However, if the bar is "ramp" aged, i.e. gradually heated at a rate of 100°C/ hour and then aged for the same time at 510°C, the α dispersions are much more dense and uniform - Figure 3.19(b). In this case, the slower heating rate provided for metastable precipitates known to form in this alloy (ω_a and possibly β'), to provide additional nucleation sites to the α precipitation.

To improve the mechanical properties, introduction of additional α nucleation sites by means of cold work prior to ageing has proven effective for β titanium alloys. The effect of cold work on the precipitation is illustrated in Figure 3.20 for cold rolled Beta C bar. After aging, the micrograph shows a dense distribution of fine α precipitates, near the edge of the bar, which has received the bulk of the plastic deformation. Away from the edge, the precipitated α becomes gradually coarser and less dense. This example also highlights the limitations of trying to increase the density and homogeneity of α precipitates by cold working of thick β titanium products.

(a) **(b)**
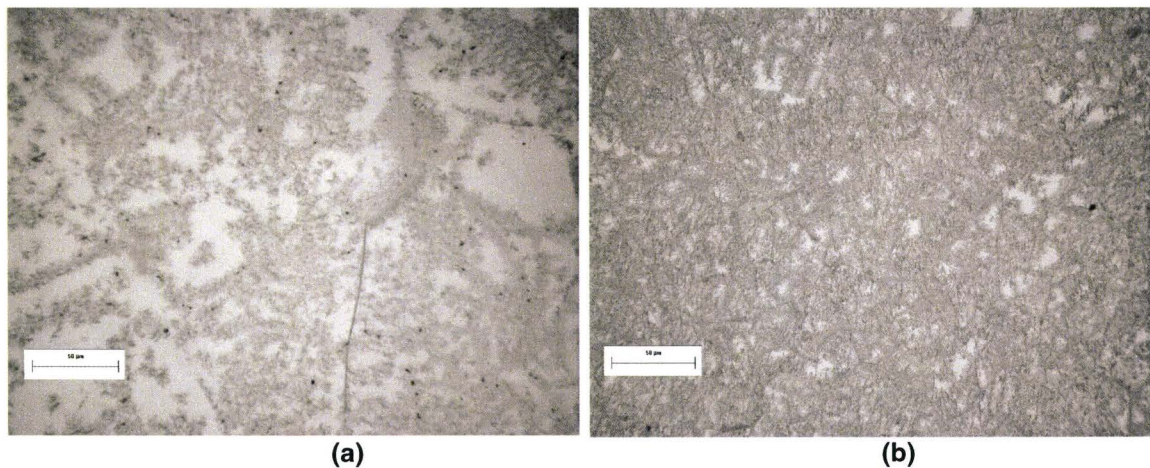
Figure 3.19: Optical micrographs of Alloy Beta C; (a) aged at 510°C for 24hrs. (b) "ramp" aged at 100°C/hr followed by 24hrs at 510°C. Etched in RMI reagent.
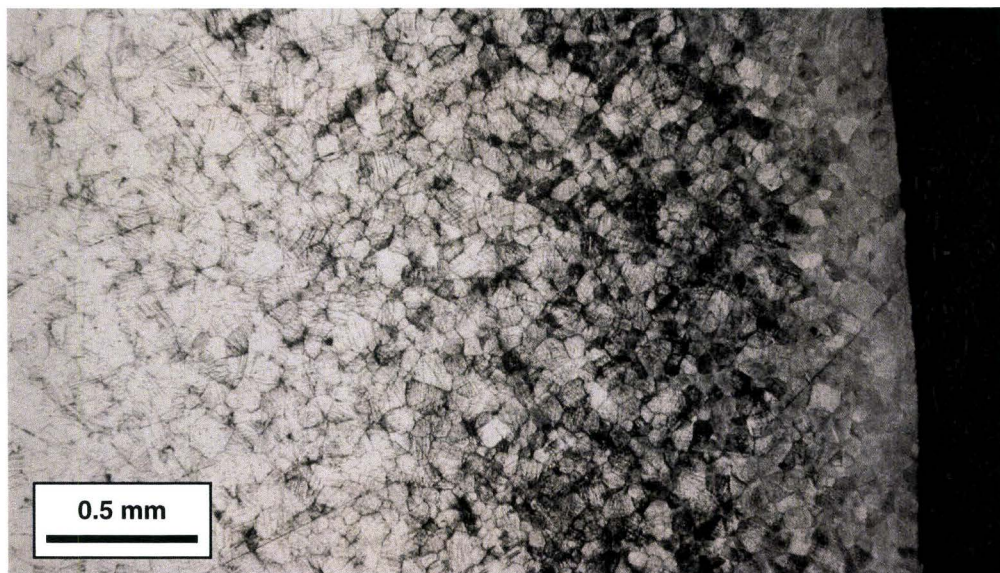
Figure 3.20: Optical micrograph illustrating ageing response for solution treated and cold rolled Beta C bar after aging at 510°C for 30 minutes. Etched in RMI reagent.

The descriptions of possible β decomposition paths highlight that a vast variety of α phase precipitates are possible even within the same system and a narrow temperature range. Because of the profound effect that the mechanism of α phase nucleation and growth have on mechanical properties, one of the more important aspects of this work will be to establish whether martensite, or metastable phases such as ω or β' are part of the precipitation process in Ti-5553.

3.4.1. Intermetallic Precipitates in the β Phase

Precipitation of intermetallic compounds in the β phase has not been studied extensively; however, a comprehensive review has been provided by Williams *[37]* and is a summarized as follows.

Several alloys systems exhibit precipitation of ordered intermetallic compounds; perhaps the most relevant to Ti-5553 is the Ti-Mo-Al system. For this system, formation of the β_2 (Ti$_2$Mo Al) compound, having the CsCl crystal structure, has been observed. Furthermore, it has been shown that the β_2 phase can form on quenching from the β phase and that this phase can be in equilibrium with the α and β after low temperature ageing. At elevated temperatures, the compound α_2 (Ti$_3$Al) has been shown to be in equilibrium with the β phase. As the α_2 and β_2 phases occur as very fine uniformly distributed precipitates, they offer the potential to provide a microstructure with high strength and reasonable ductility.

Other system for which fine precipitates have been known to form in the β phase involve Silicon, some examples are Ti-V-Si, Ti-Mo-Si and Ti-Mo-Zr-Si. The silicide phase which precipitates throughout as an unshearble dispersion, has the potential to enhance the high temperature strengthening capabilities of these alloys. Ankem and co-workers at RMI Titanium, reported Silicides formation in alloy Beta C.*[46]* Continuous precipitation of this phase along grain boundaries was found to cause intergranular fracture and be detrimental to tensile properties. However, thermal and thermo-mechanical means to avoid this continuous precipitate were identified.

Although Ti-5553 contains the significant concentrations of V and Mo prerequisite for silicide formation, the composition limit for silicon is only 0.15 wt% maximum. Consequently, significant amounts of silicides would not be expected for this alloy.
A more in depth prediction of the equilibrium phases possible for Ti-5553 using Thermo-Calc Software will follow in Chapter 5.

3.5. Phase Transformations in Ti-5553

Notwithstanding the keen interest in Ti-5553 over recent years, the published literature on phase transformations for this alloy remains limited. Work available on Russian alloy VT22 remains inaccessible to the western world mainly due to language barriers. Ishunkina and Rodinov, reported the presence of ω phase and provided a TTT diagrams for alloy VT22 (BT22). Other work by Popov et. al. on VT22 reported only the homogeneous and heterogeneous precipitation of α, but no ω phase was reported β decomposition.
Clément, Lenain and Jacques *[44]* reported the formation of ω phase in Ti-5553 upon quenching from the β phase. However, unlike the strong crystallographic evidence of ω_a found for other titanium alloys of similar Mo$_{eq}$, selected area diffraction (SAD) patterns revealed only faint streaks corresponding to the ω reflections. These streaks can be interpreted as diffused scattering from the ω precursor. They concluded that for Ti-5553, the extent of ω_a phase formation is somewhat lower than that of alloys with similar Mo$_{eq.}$ content, and suggested that the relatively higher Al$_{eq.}$ content may suppress ω_a formation. The difficulty in detecting the ω phase may account for the apparent discrepancy in the Russian work. Clément et.al., also conducted ageing experiments at

800°C, 700°C and 500°C following β annealing. The microstructure aged at 800°C consisted of sparsely distributed pairs of equiaxed α; although not reported as such, these α precipitates appear to be sympathetically nucleated. The low volume fraction of these precipitates is due to the ageing temperature being only 70°C below the β-transus for the heat of material studied. Ageing at 700°C resulted in continuous films of α at the grain boundaries, and relatively large α plates (1μm thick by 20μm long) growing intragranularly. A network of fine α plates in a β matrix was reported for the material aged at 500°C; nucleation was said to be homogeneous throughout the β grains. An even finer α dispersion was reported for ageing at lower temperatures.

Earlier work by Harper and co-workers at Ohio State University [23] [47] reported the presence of ω_a after oil quenching from above the β transus and the coexistence of ω and α when ageing the quenched material at 350°C. Nucleation of the α precipitates at the ω sites was confirmed. An example of such nucleation is presented in Figure 3.21.
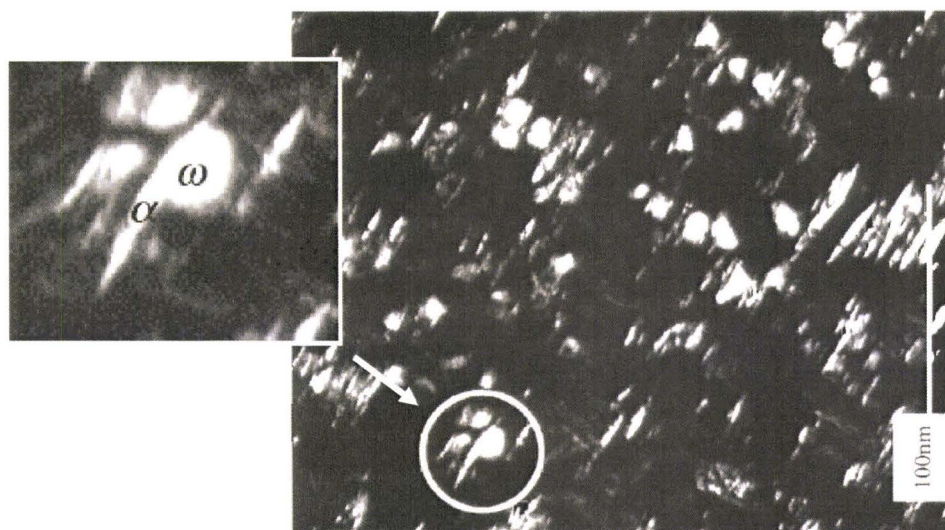
Figure 3.20:   Dark field TEM image showing precipitation of α needle at a ω particle. *[47]*

Slow cooling from above the β transus resulted in a sluggish precipitation of α, with complete transformation of the retained β after 4 hours. The morphology of the slow cooled α was elongated and much coarser than the ω-nucleated α. Bi-modal microstructures consisting of globular primary α and fine precipitated α laths was reported when solution heat treating and ageing below the β transus.

Cotton and coworkers at the Boeing Company [31] studied the microstructural transformations in Ti-5553 upon cooling from above and below the β transus. Slow cooling from above the β transus followed by ageing in the 540-600°C range produced a microstructure of relatively course α-β lamellae and grain boundary α. The above heat treatment is referred to as Beta Annealed Slow Cooled and Aged (BASCA) by Boeing and is reported to attain high damage tolerance characteristics. A small amount of α_2 (Ti$_3$Al) precipitates were found within the α lamellae. Through thermodynamic calculations, the stability of the α_2 is expected to increase with oxygen content; the α_2 solvus was placed in the 550-600°C range. They concluded that the microstructural evolution in Ti-5553 is mostly dependent on the diffusional processes associated with the β → α reaction, and hence highly influenced by the cooling rates. In view of the relatively

slow (<0.1°C/sec) cooling rates involved in industrial processes, their work included the development of Continuous Cooling Transformation (CCT) diagrams and Time Temperature Transformation (TTT) diagrams – both were determined by dilatometry. These diagrams are presented in Figures 3.22 and 3.23, respectively. The TTT diagram shows curves determined by cooling from above and below the β transus (888°C and 838°C, respectively). However, the α start and finish lines are essentially indistinguishable; furthermore, within the 600-800°C range, there appears to be little dependence of the time to transformation on temperature.

From the CCT diagram, cooling rates below 0.25°C/sec appear to suppress entirely the transformation to α, while favouring precipitation of the ω_a phase (not shown in diagram). According to the CCT diagram, significant transformation to α occurs at 650°C, which corresponds to a linear cooling rate of 0.05°C and a cooling time of roughly one hour.

This observation is important as it emphasizes the need to control cooling rates in industrial heat treatment processes in order to obtain the desired microstructure on Ti-5553. For large forgings and components containing thick and thin cross sections, it may be necessary to implement additional provisions within the heat treat furnace to affect a prescribed cooling rate; this type of control is not typical of most titanium alloys.
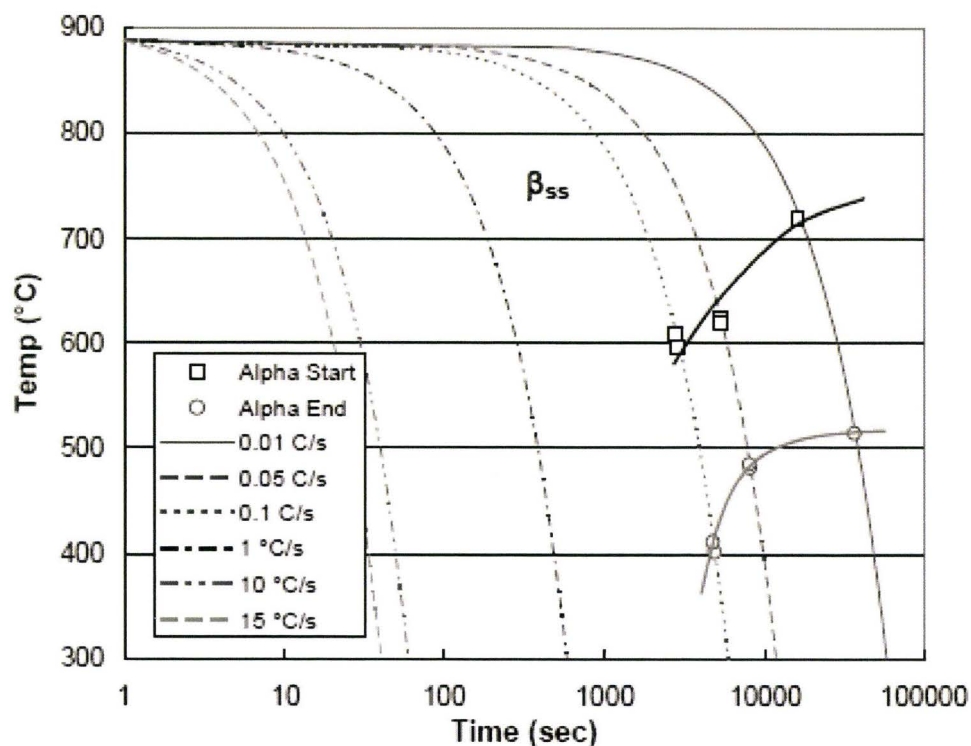
Figure 3.21: CCT diagram for bulk α phase in Ti-5553; specimens were solution treated at 888°C for 60 minutes prior to cooling at the specified rates. [31]
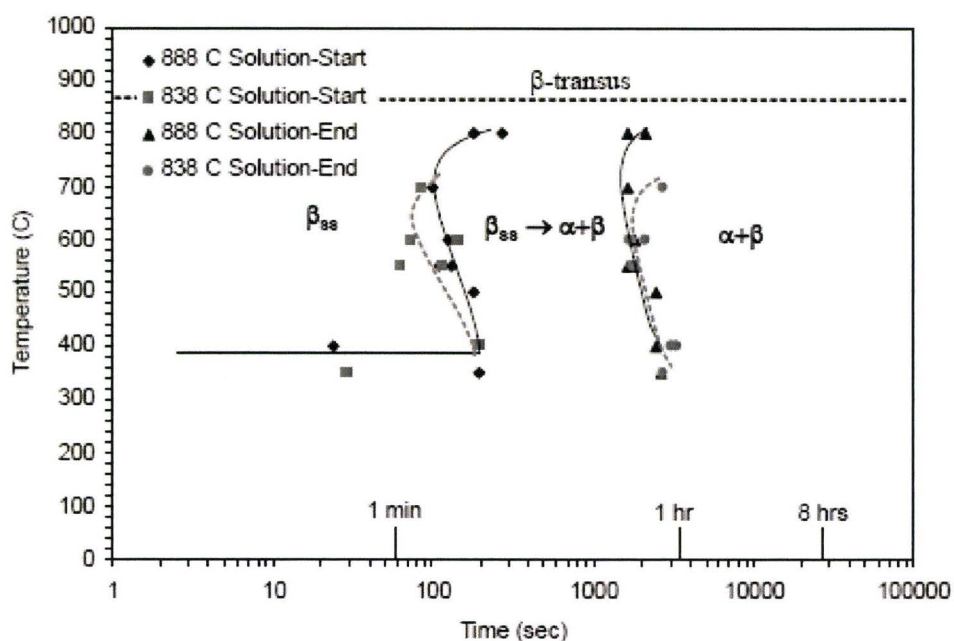
Figure 3.22:   TTT diagram for Ti-5553; cooling was carried out from 838°C and 888°C, as noted. [31]

3.6.   Mechanical Properties of β Titanium Alloys

3.6.1.   Review of Deformation Mechanisms for BCC and HCP Phases in Titanium Alloys

The mechanical response of titanium alloys to an applied tensile (or compressive) stress will vary significantly from one alloy type to another. This elastic and plastic response depends on whether the microstructure consists primarily of α, β, or a combination of α and β phases. In terms of the slip systems which facilitate plastic deformation, the most closely packed planes for the α (HCP) and β (BCC) crystal structures are presented in Figure 3.24. The HCP unit cell also contains the room temperature values for lattice parameters: $a = 0.295nm$ and $c = 0.468nm$. Based on these values, the c/a ratio for pure α titanium is 1.587, which is smaller than that of the ideal HCP structure 1.633. This indicates that the structure of the α phase is somewhat compressed. The more closely packed planes shaded are one of the basal planes (0002), one of the three prismatic planes $\{10\bar{1}0\}$ and one of the six pyramidal planes $\{10\bar{1}1\}$. Three easy slip systems and six twinning modes exist in α titanium. The three close-packed directions a_1, a_2 and a_3 which have the indices $<11\bar{2}0>$ operate parallel to the basal plane. Hence, if a stress acting on the direction of the c axis is applied, there will be no critical resolved shear stress acting on the basal plane. In this case, other slip systems can be activated so that the requirement of having five independent slip systems for general plasticity is satisfied (von-Mises criterion). Consequently, crystallographic texture plays an important role in deformation of α alloys. Figure 3.25 shows the preferred slip systems activated in a case where texture orientation results in the basal plane alignment perpendicular to the forging plane. The preferred slip systems are ranked on the basis of critical resolved shear stresses with respect to stresses acting in the long transfer (forging) direction.

The BCC unit cell depicted in Figure 3.24 shows one of the six most densely packed {110} planes and the close packed <111> directions (cube diagonals). The lattice parameter for the β phase in pure titanium (0.332nm) is provided at a temperature of 900°C, at which the phase is stable.
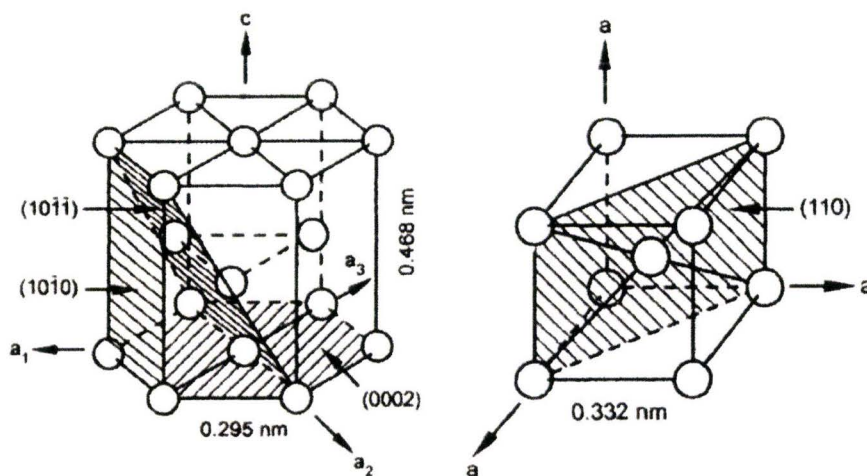
Figure 3.23:   Unit cells for α phase (HCP) and β phase (BCC) for pure titanium. *[18]*
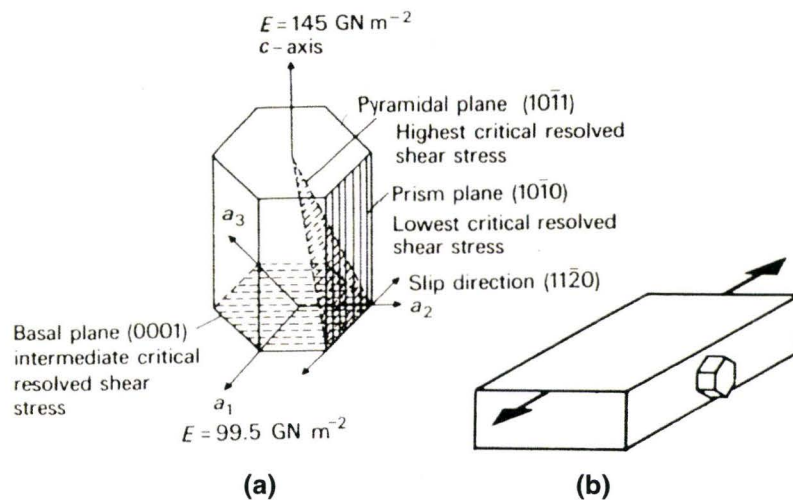
Figure 3.24: **(a) Slip planes in α titanium ranked according to critical resolved shear stress, (b) alignment of HCP unit cell in forged α titanium showing strongly preferred orientation after forging.** *[14]*

Due to the anisotropy associated with the HCP crystal structure, the elastic moduli along the *c*-axis and the *a*-axis in α titanium single crystals varies greatly. As shown in Figure 3.26, the modulus of elasticity varies from 145GPa to 99.5GPa, along and perpendicular to the *c*-axis. *[14]* Although this effect is diminished in polycrystalline α titanium, this variation has important consequences for elastic properties of two phase titanium alloys. Similar variations are observed for the shear modulus of α phase single crystals. For shear stresses applied in the $<11\bar{2}0>$ direction and in the (0002) or $\{10\bar{1}0\}$ planes, the shear modulus ranges from 46GPa to 34GPa. *[18]*
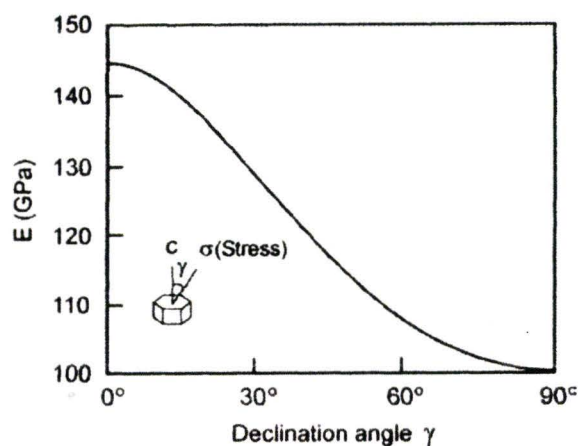
Figure 3.25: **Variation of the elastic modulus with declination angle for α titanium single crystals** *[4].*

Variations in elastic properties will depend strongly in the amount of α phase present in the microstructure and the nature and intensity of crystallographic texture.

The elastic modulus of pure β titanium can not be measured at room temperature as this phase is not stable below the β transus. However, commercial β titanium alloys have a lower elastic modulus than the α and $\alpha+\beta$ alloys. Values of 70-90GPa are reported for commercial β alloys as-quenched from above the β transus. [4]

3.6.2. Representation of Stress-Strain Behaviour for Titanium Alloys

A variety of mathematical expressions have been proposed to model the shape of the stress-strain curve depending on the characteristics of the material being tested. A generalized true stress-true strain curve is presented in Figure 3.27.
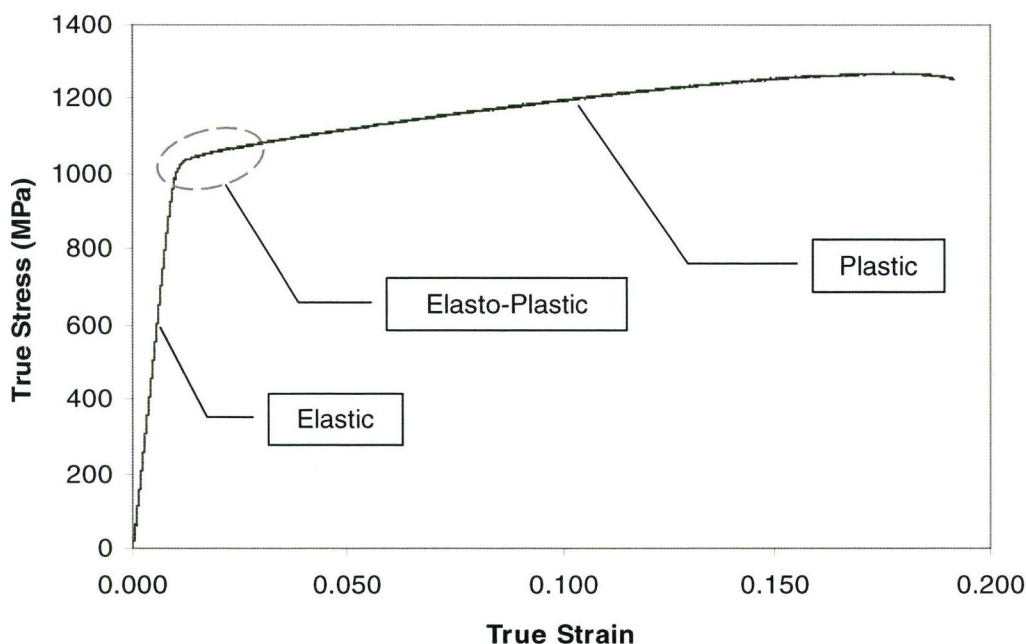
Figure 3.27:   Generalized True Stress-True Strain Plot for an Engineering Alloy.

The curve has been divided into three regions. As depicted in Figure 3.27, the initial linear portion of the curve corresponds to elastic behaviour which follows Hooke's law.

$$\sigma = \varepsilon\, E \qquad \text{eq. (1)}$$

Where: ε = strain; σ = stress; E = Young's modulus.

The region labeled Plastic represents the portion of the curve where plastic deformation of the material is observed; in many cases this portion can be approximated by a simple power law.

$$\sigma = K\varepsilon^{n} \qquad \text{eq. (2)}$$

Where: K = is the strength coefficient and n = strain hardening exponent.

The region between Elastic and Plastic regimes represents the transition from elastic to plastic behaviour and is depicted as Elasto-Plastic. This region is particularly important when considering the deformation behaviour of two phase alloys such as dual phase steels and α-β titanium.

Representation of the strain hardening behaviour on this region can be done by plotting the rate of strain hardening, $d\sigma/d\varepsilon$ versus ε.
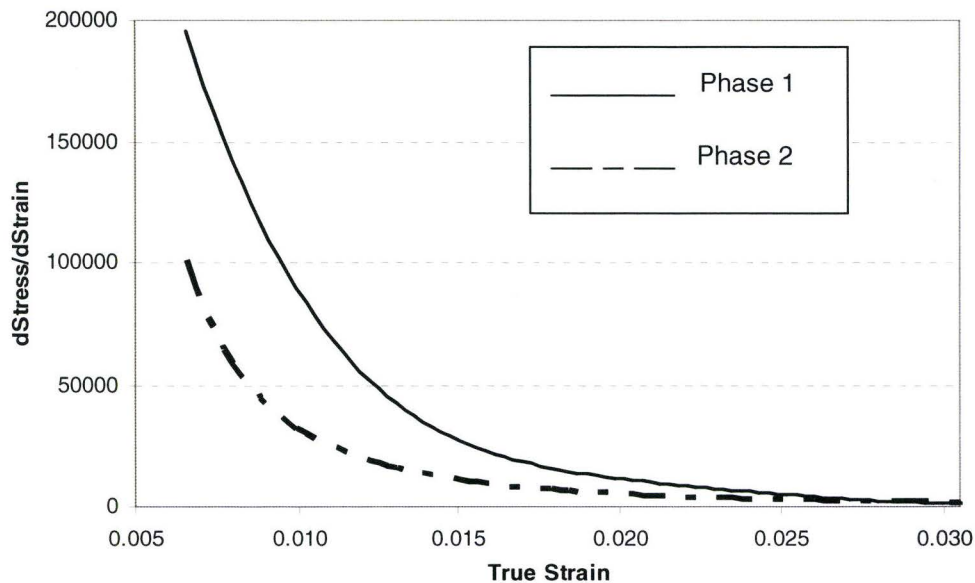
Figure 3.28: **Plot of the Strain Hardening Rate, $d\sigma/d\varepsilon$, Versus True Strain for Each of the Two Phases in a Dual Phase Alloy.**

A plot of the rate of strain hardening for each phase can help visualize the work hardening characteristics after the onset of plasticity. A plot of the strain hardening rate versus true-strain for each of the phases in a two phase alloy is shown in Figure 3.28. Since the plastic behaviour of each phase during deformation of dual phase alloys can be different, plotting the individual strain hardening rates can explain the strain partitioning and the deformation behaviour within the Zone II regime.

3.7. General Theories of Failure

3.7.1 The Concept of Yield and Fracture Surfaces

The uni-axial tensile test is one of the most commonly used tests to determine static properties such as yield and fracture stresses. The strength of materials are not generally known under complex stress states, and designers rely on theoretical models to relate the tensile properties results to the complex stresses encountered in practice. These models are used for determining allowable working stresses to prevent component failure. A number of models have

been developed which provide the theoretical criteria for yielding and fracture of ductile and brittle materials. Below is a summary of some of the more widely accepted models to predict failure: [59]

1)   Maximum principal stress (Rankine)
2)   Maximum shear stress (Guest-Tresca)
3)   Shear strain energy per unit volume (Maxwell-Huber-von Mises)
4)   Mohr's modified shear stress

The Rankine model assumes that elastic failure will occur when the maximum principal stress in the complex stress system, σ_1, exceeds the elastic limit determined by the uniaxial tensile test. Failure could also occur in compression if the least principal stress, σ_3, reaches the yield stress in compression. Hence the failure criterion is: σ_1 or $\sigma_3 = \sigma_y$.

In the "Guest-Tresca" model, failure is assumed to occur when the maximum shear stress in the complex stress system equals that of the yield stress in axial tension test. In terms of principal stresses this can be expressed σ_y as:

$$\sigma_1 - \sigma_3 = \sigma_y, \qquad \text{eq. (3)}$$
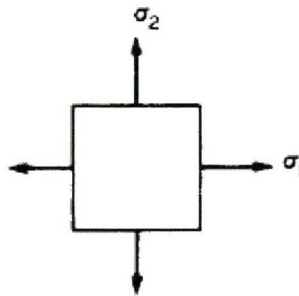
Where σ_3 is algebraically the smallest stress value - and assuming that one stress (σ_2) is zero.

Dividing by σ_y and expressing in terms of σ_1 and σ_2, expression (3) becomes:

$$\sigma_1/\sigma_y - \sigma_2/\sigma_y = 1 \qquad \text{eq. (4)}$$

Figure 3.29(a) is a plot of expression (4), presenting the hexagonal envelope for failure (or yield) when one of the stresses is zero. However, when none of the stresses are zero, the failure locus can be shown to be a regular hexagonal prism with the central axis on the line described by $\sigma_1 = \sigma_2 = \sigma_3$, termed the hydrostatic stress line; Figure 3.29(b).

(a)   (b)
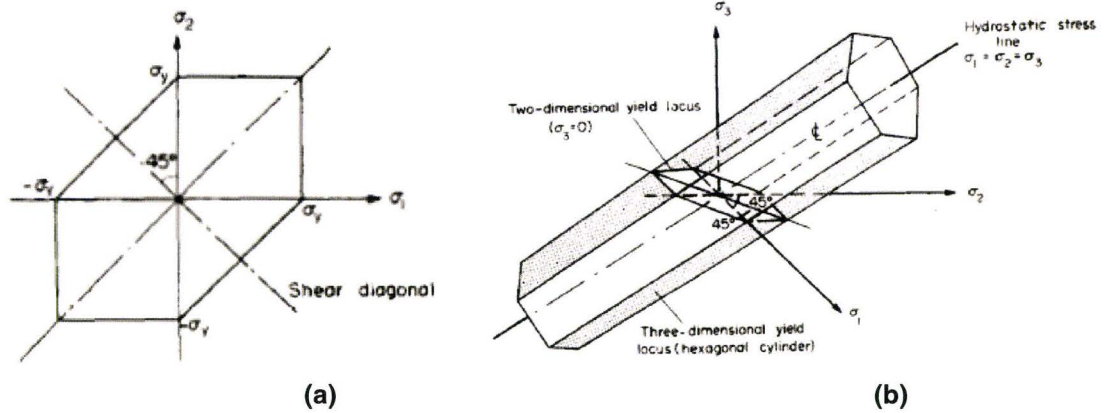
Figure 3.29:   (a) Two dimensional yield envelope and (b) three dimensional yield locus for the maximum shear stress model. [59

Hence, in three dimensional stress, the failure criteria becomes a surface within which component failure (plastic deformation) is not expected.

The shear strain energy per unit volume (Maxwell-von Mises) model, for two dimensional stress results in:

$$(\sigma_1/\sigma_y)^2 + (\sigma_2/\sigma_y)^2 - (\sigma_1/\sigma_y)(\sigma_1/\sigma_y) = 1 \quad \text{eq. (5)}$$

Expression (5) constitutes an ellipse which is presented in Figure 3.30(a). Note that the hexagonal criteria for failure predicted by the Tresca model are contained within this ellipse, making the Tresca criteria more conservative. When none of the stresses are zero, the failure locus becomes the surface of a regular prism of cylindrical cross section, inclined along the hydrostatic stress line, as shown in Figure 3.30(b). It can be shown that hydrostatic stress alone can not cause yielding [59], the Maxwell-von Mises model predicts that stress states within this surface are equally safe. This model has received the greatest level of verification and demonstrated the greatest level of agreement with experimental data. When dealing with ductile materials, the Maxwell-von Mises failure criteria has become the most accepted method for component design.

(a)   (b)
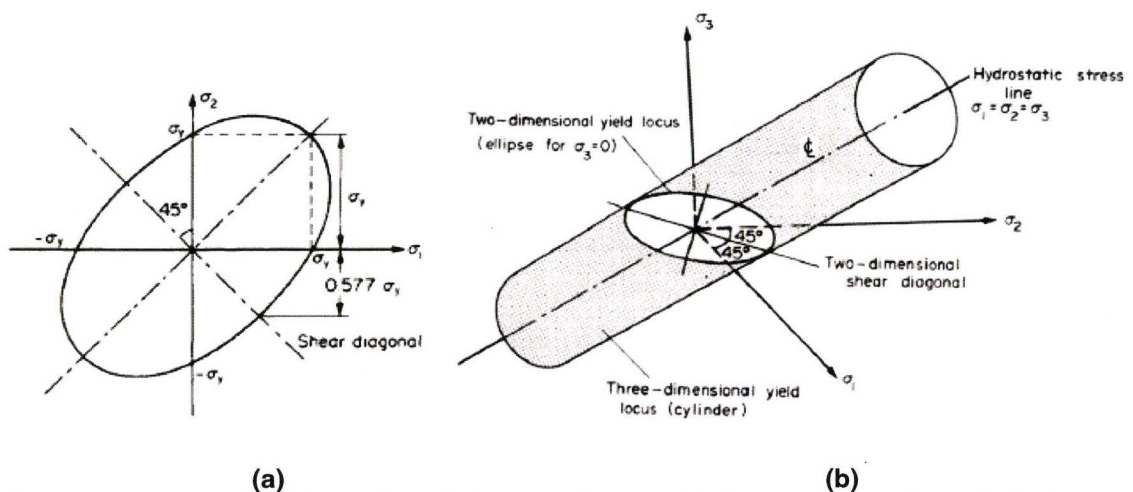
Figure 3.26:   (a) Two dimensional yield envelope and (b) three dimensional yield locus for the shear strain energy per unit volume model. [59]

It is well known that for certain materials such as cast irons and high strength steels, the fracture stress in compression is much higher that in tension. *[59] [60]*. For these materials, the modified Mohr shear stress model is a better predictor of failure.

A representation of this model for a by-axial stress state is presented in Figure 3.31.
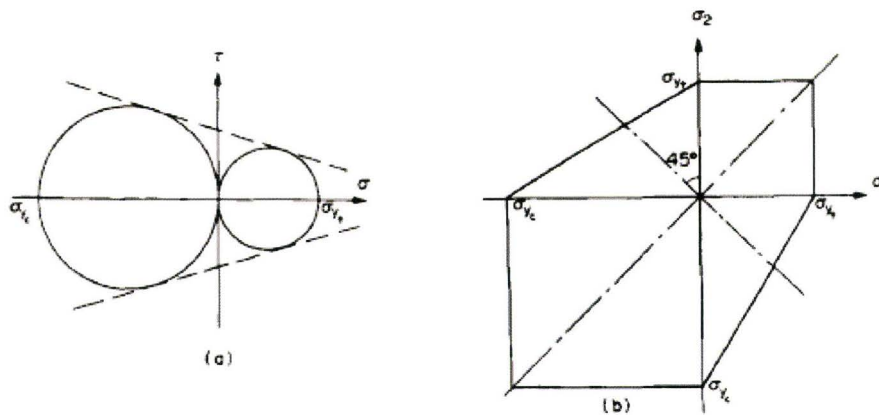
Figure 3.31: **(a) Simplified Mohr model on a σ-τ axes, (b) two dimensional yield envelope for the Mohr's modified shear stress model.** *[59]*

This model is derived from constructing two Mohr circles as shown in Figure 3.31(a), where σ_{yt} and σ_{yc} are respectively the yield stresses in tension and compression. The failure surface is described by expression (6) which is plotted in Figure 3.31(b)

$$\sigma_1 / \sigma_{yt} - \sigma_2 / \sigma_{yc} = 1 \quad \text{eq. (6)}$$

The properties of the material being considered and the stress state have important consequence to the description of failure. Failure in ductile materials is typically ascribed to the onset of plastic deformation, while for very brittle materials, fracture occurs prior to yielding. Many high strength engineering materials have relatively low ductility; for these materials failure is a competition between yield and fracture and is influenced by the state of stress. These materials exhibit a tendency toward a higher fracture stress in compression than that in tension. In these cases, two surfaces, one for yielding and one for fracture must be considered. In three dimensional stress, the fracture surface extends outside of the yield surface. Examples of these surfaces are presented in Figure 3.32.
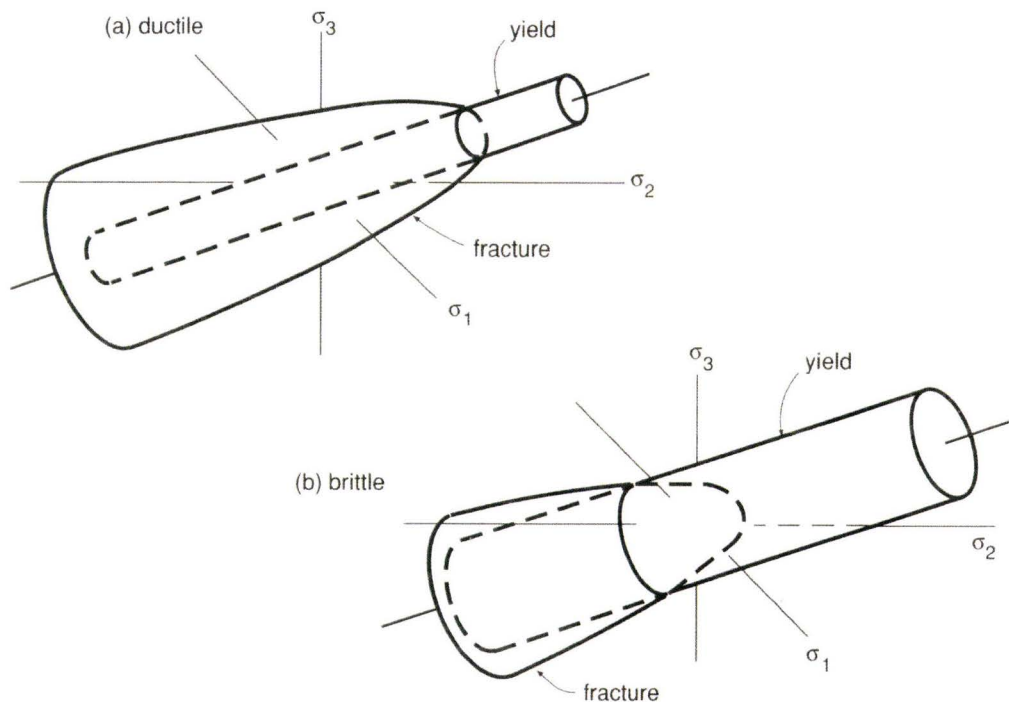
Figure 3.32:   Relationship between the surfaces for yielding and fracture for two materials: (a) material with relatively ductile behaviour and (b) relatively brittle material.[59]

However, it is clear from Figure 3.32 that for certain stress states the yield surface is encountered first, while for others the fracture stress is encountered first. For relatively ductile materials fracture prior to yielding is not encountered except for condition involving large hydrostatic tension. Depending on the amount of hydrostatic compression, the stress may be increased past the yield surface before fracture ensues. For relatively brittle materials, fracture occurs prior to yielding except for stress states involving high hydrostatic compression. It follows that for highly compressive stress states, the predicted fracture stress is much higher that that in tension.

Stress calculations in engineering components often assume that fracture in compression is unlikely due to the higher resistance of the material to damage in compression. In many cases, compressive stresses are ignored and the analysis focuses on preventing fracture under tensile stresses only.

As an introduction to the material which will be presented in this thesis, this Chapter contains a review of relevant elements in the literature to prepare the reader for the thesis results and discussion. This review began with the classification of titanium alloys and the concepts of molybdenum and aluminum equivalents. General phase transformations in titanium alloys were reviewed; furthermore, equilibrium and non-equilibrium phases were discussed. A literature review of recent work in Ti-5553 was presented with emphasis on phase transformations and the microstructure. The mechanical properties of β titanium alloys were briefly discussed, concluding with a concise review of the general theories of elastic failure.

The main objective of the thesis is to provide insight into the microstructural changes upon heat treatment and the effect on properties; for this reason, a broad array of experimental methods will be employed. The techniques used to characterize the microstructure employ optical and electron microscopy, while the mechanical properties will be studied using a variety of standard and customized tests. The following Chapter gives details of the experimental methods which will be used to characterize this alloy.

4.0   EXPERIMENTAL METHODS

4.1.   Composition and History of Ti-5553 Forged Billet

As Ti-5553 is a relatively new alloy, there is still no published Aerospace Material Specification (AMS) for this alloy. An AMS specification has been drafted. At present however, aircraft manufacturers have developed proprietary specifications to control the procurement of the alloy. This alloy was developed by VSMPO (Verkhnaya Salda Metallurgical Production Association), the premier integrated titanium supplier in Russia.

Ti-5553 is based on Russian alloy VT-22 with additions of slow diffusers, primarily Cr, that delay precipitation and inhibit microstructural coarsening [31]. Another improvement is the reduced Fe content which diminishes the likelihood of melt defects such as segregation of β stabilizers, these defects are commonly known as β-flecks. The composition of VT 22 and Ti-5553 are presented in Table 4.1.

Table 4.1:   Nominal Compositions of Alloys VT-22 and Ti-5553.

Alloy	Element	Al	V	Mo	Cr	Fe
VT-22	Weight %	4.4 - 5.7	4.0 - 5.5	4.0 - 5.5	0.5 - 1.5	0.5 - 1.5
Ti-5553	Weight %	4.4 - 5.7	4.0 - 5.5	4.0 - 5.5	2.5 - 3.5	0.3 - 0.5

All experiments were conducted on material melted and forged by VSMPO, heat number 8-42-2034, lot number 4182. The specified control limits and the reported chemical composition for the cast ingot are presented in Table 4.2.

Table 4.2:   Composition limits for Ti-5553 and composition of Heat # 8-42-2034.

Element	Al	V	Fe	Mo	Cr	Si	Zr	O2	H2	C
Weight %	4.4 - 5.7	4.0 - 5.5	0.30 - 0.50	4.0 - 5.5	2.5 - 3.5	0.15 max.	0.30 max	0.18 max.	0.015 max	0.10 max.
Top	5.43	5.18	0.34	5.12	2.86	0.031	0.003	0.148	0.0026	0.007
Bottom	5.34	4.84	0.30	4.96	2.73	0.029	0.008	0.151	0.0011	0.006

The titanium sponge required for the primary melting was produced by AVISMA, a subsidiary of VSMPO, using the Kroll process. The ingot was produced by double vacuum arc re-melting (VAR) process; the electrode was inverted for the second VAR cycle. The β-transus of this ingot was reported to be 838°C for the top and the bottom, which indicates that the ingot was chemically homogeneous. All open die and block forging operations were conducted by VSMPO, the details of ingot to billet conversion sequence are presented in the following section.

4.2   Microstructure and Properties of the Forged Billet - Heat # 8-42-2034

The microstructure and properties of β titanium alloys are closely linked to their thermo-mechanical history and the heat treatment selected. In order to follow the evolution of the microstructure and its effect on properties, it is fundamental to first develop a thorough understanding of the as-forged microstructure and the prior thermo-mechanical work.
Prior to the detailed treatment of the microstructure evolution with various heat treatments, characterization of the material which will be studied through out this work was conducted. It is important to note that this characterization is in the context of practices used for titanium die

forgings, and in line with the methodology used in the aerospace industry. A number of other methods could have been followed to determine the chemical and structural homogeneity of the starting material. However, this approach was followed to remain consistent with the industrial relevance of this work. This characterization involved:

i)   A review of the forging sequence beginning with the cast ingot.
ii)   Assessment of the chemical homogeneity of the forged billet by means of macrostructure and hardness surveys.
iii)   Evaluation of the variation in tensile properties from billet edge to core.

The aim of the above mentioned is twofold: 1) to understand whether this material is representative of typically produced die forgings, and 2) to determine that the forging sequence has produced a billet which is homogeneous and make necessary adjustments to the compensate for texture and anisotropy variations.

4.3   Thermo-mechanical History and Characterization of As-Forged Billet.

Almost all the experiments were conducted on a forged Ti-5553 square cross section billet measuring 0.2 X 0.2 X 2.0 m. The material was supplied in the as-forged condition by the Russian supplier VSMPO. The billet had successfully passed ultrasonic inspection to detect any internal defects. Although the detailed conversion sequence was said to be proprietary, Diagram 4.1 provides is a broad description of the forging sequence followed to convert the ingot into forged billet. The primary purpose of each step is presented in brackets, as surmised from review of the literature [12] [32]. A pseudo-binary diagram for a typical β titanium alloy is provided to illustrate the different steps.

1) β-phase work beginning at 1140°C
Upsetting and Forging - Reduction ratio ~ 5.2
(Ingot Breakdown)

2) α + β phase work at 810°C
Upsetting and Drawing - Reduction ratio ~ 2.5.
(Breakdown of Cast Structure/Grain Refinement)

3) β-phase work at 980°C
 Upsetting and Drawing - Reduction ratio ~ 1.6
(Re-crystallization)

4) α + β phase work at 810°C
Forge to shape - Reduction ratio ~ 4.0
(Grain refinement)

5) Air cooling

Diagram 4.1   Summary of Ingo-to-Billet Conversion Sequence for Characterized Material.

The β-transus for this ingot was reported to be 838°C for the top and the bottom. Reduction ratio is defined as the initial diameter of the billet divided by the final diameter. The terms "upsetting" and "drawing" describe the hot deformation by compression along the ingot's longitudinal and perpendicular axis respectively. These operations are aimed at breaking down the as-cast structure, and are carried out on an open die press. In this context, the term "forging" describes the process of restoring a barreled section to a more uniform shape and to impart certain billet dimensions. The function of the second β-phase work operation is to re-crystallize the material and prevent surface cracking of the billet. [12] [32]

The α+β phase work in step 4) encompasses multiple heating and deformation cycles which are required to achieve the reduction ratio stated. As the shape of the billet is no longer round, the reduction ratio for step 4) is defined as the starting cross sectional area divided by the final area.

The above forging sequence is referred to as "ingot to billet conversion" and would normally be followed by a final forging operation in a closed die. Characterization of a new forging alloy and development of design properties is normally conducted on representative die forgings. Comparing this thermo-mechanical sequence to that of an actual forging, the last step would be followed by a die forging operation within the α+β phase range, in two sets of closed dies, a blocker and finisher die. Consequently, the final reduction ratio for a die forging would vary with part geometry; as thick sections would receive a lower level of reduction than thin areas. Additionally, the grain flow of the forging would follow the contour of the part and would be symmetrical about a parting plane. As a consequence of the final forging operation in the α+β phase range, the material contains a great deal of stored energy due to dislocations. This stored energy leads to partial recovery during subsequent thermal steps and results in fine-scale sub-grains developing throughout the microstructure.

For this work, a forged bar containing additional α+β phase deformation was believed to be more appropriate as the consistency and homogeneity of the billet would be superior to that of a die forging. A confirmation of the homogeneity associated with the forging sequent follows in next section.

4.4   Evaluation of the As-Forged Billet Homogeneity

In addition to the presence of α and β phases within the microstructure, β titanium alloys posses larger scale structure, typically high angle grain boundaries, termed macrostructure. [32]. Macrostructure evaluation provides a qualitative appraisal of the degree of ingot breakdown and uniformity of billet microstructure and properties. Images of a polished and macro-etched slice of the as-forged billet are presented in Figures 4.1 and 4.2. The transverse macrostructure was remarkably uniform across the entire cross section; the grain size at the centre of the billet was found to be slightly finer than that at the corners. The transverse grain size was determined by the line intercept method and found to be in the range of 0.5-0.8 mm in diameter. Since the scale of the grain size is in line with that resulting from β annealing, it appears that the macrostructure evolved from the last β-phase re-crystallization cycle.
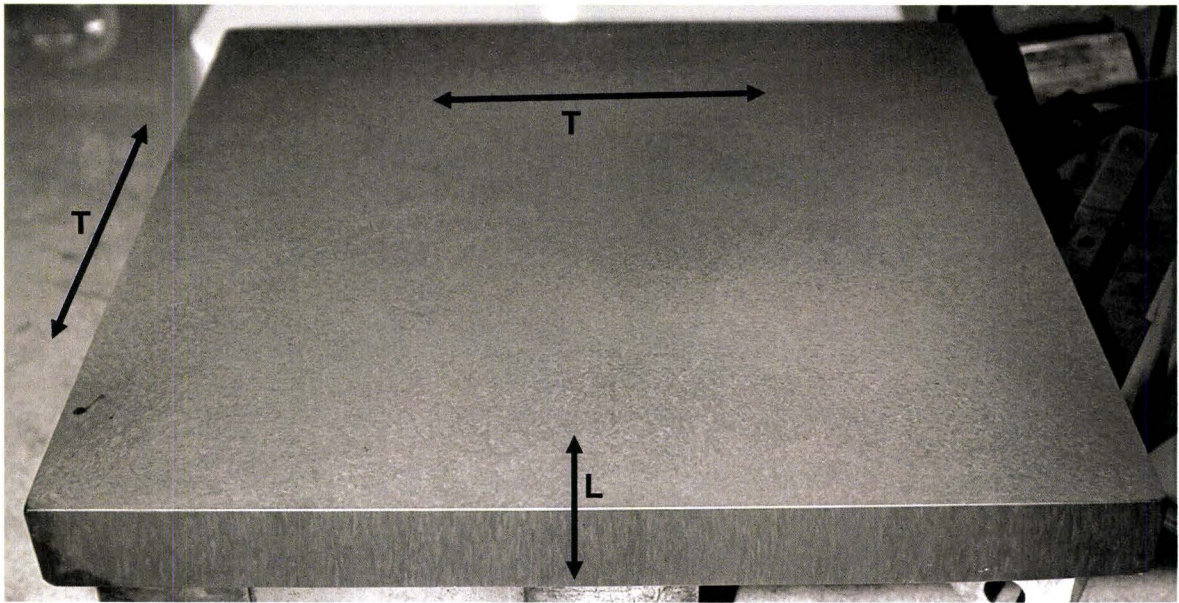
Figure 4.1:. **Photograph of the macrostructure of the as forged billet. Forging directions noted as: L = Longitudinal ; T = Transverse. Etched in 70% Nitric - 8% Hydrofluoric acids.**

2 mm
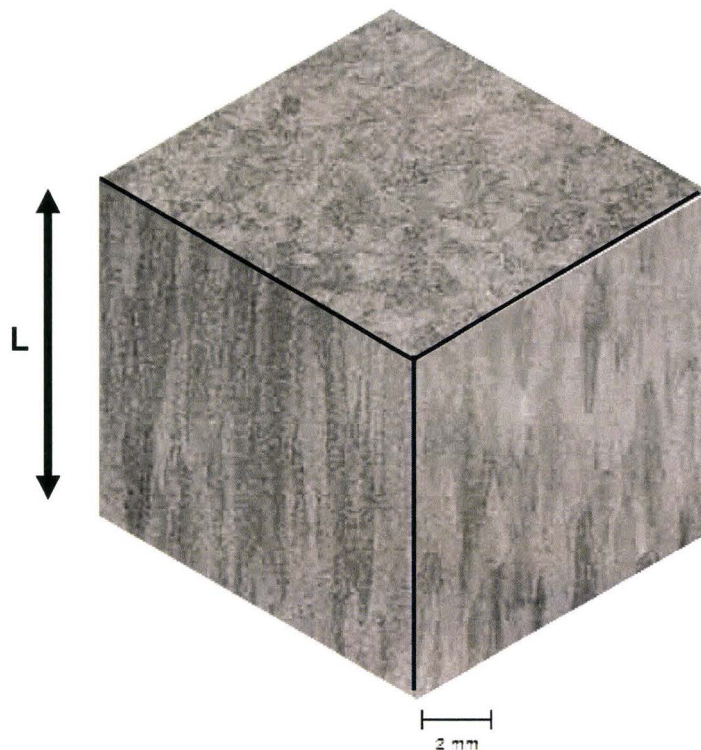
Figure 4.2: **Representation of the macrostructure of the as-forged billet, from sections taken across longitudinal and transverse axis; arrow indicates longitudinal or "drawing" direction during forging.**

The longitudinal grain structure was elongated with an aspect ratio of Ø/L=~0.1. The titanium industry standard for macrostructure rating is AMS 2380, "Approval and Control of Premium-Quality Titanium Alloys". The rating is done by comparing etched cross sections of the material being evaluated against visual standards. The rating scheme consists of 10 levels: level 10 being the finest and level 100 being the coarsest. The billet being evaluated rated finer than level 10 in the transverse direction and level 30 in the longitudinal direction. Comparing these values to conventional die forgings, we can conclude that the billet's macrostructure was finer than typical, in line with thinner forging sections that have received very large reductions. Consequently, the resulting properties are expected to be homogeneous.

Longitudinal and transverse sections of the as-forged billet were excised from the billet, mounted and polished to reveal the microstructure. Figure 4.3 shows the as-forged microstructure for the two directions; the microstructure consisted of uniformly distributed globular primary alpha regions, in a matrix of aged β. In the transverse direction, the primary α phase is consistently round and approximately 2-6µm in diameter. The longitudinal direction contained regions of elongated primary α, refer to Figure 4.3 (a), aligned along the drawing direction.

10µm	10µm
(a)	(b)
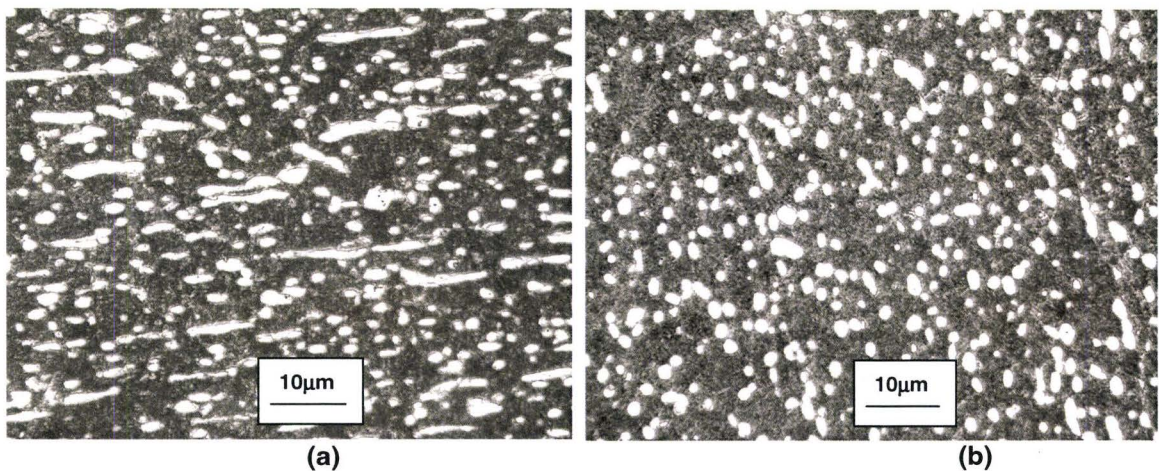
Figure 4.3: Microstructure of as-forged billet in the longitudinal (a) and transverse (b) directions, the microstructure consists of globular primary α (light phase) in a matrix of transformed β (dark etching matrix). Etched in Krolls.

Aside from the obvious anisotropy expected due to the difference in aspect ratio, the primary α volume fraction would play a role on the tensile properties of the alloy. Fanning, J.C. 2005, [2] reported an increase in tensile strengths and a decrease in ductility, with a decrease in the primary α volume fraction. The average primary α volume fraction was 16.5%, and 19.2% for the transverse and longitudinal directions respectively, with and error of ± 1.3%. These values are considered accurate as the primary α volume fraction evaluations were conducted in 10 fields per specimen, in accordance with the method described later in this Chapter . The percent error was assessed by adjusting the digital images within the contrast range allowed by the software and conducting area counts at either side of the range.

Although an incomplete appraisal of the billet's texture, differences in grain structure and primary α volume fractions between the longitudinal and transverse directions are likely to give rise to anisotropy of properties. To avoid this problem, all specimens for mechanical property evaluations were oriented in the transverse direction.

4.5   Hardness Evaluation of As-forged Billet

To provide a more quantitative assessment of the billet's homogeneity, a thorough survey of the variation in hardness was conducted. A slice of the as-forged billet approximately 200 X 200 X 25 mm was excised from the billet, machined flat and polished. A grid pattern was drawn covering the entire surface with squares 20 X 20 mm, hardness measurements were taken at the centre of each square. For reference, each column of the grid was labeled sequentially from A to J, while the rows were labeled 1 to 10. The hardness was also evaluated along the edge of the slice, at intervals of 20 mm. The Rockwell C hardness results are presented in Tables 4.3 and 4.4; the average hardness is HRC 44.4, with a standard deviation of 0.72. The hardness was found to be remarkably uniform across the section except for squares, G9 and G10, which were almost 3 points below the average. The billet corners were slightly above the average, but no significant variation between edge and core was evident.

Table 4.3: Rockwell C hardness across billet slice. Squares G9 and G10 (gray) had the lowest hardness.

COL/ROW	A	B	C	D	E	F	G	H	I	J	AVERAGE
1	45.6	45.3	44.3	44.3	44.5	43.7	44.4	44.1	44.7	45	44.6
2	44.1	44.5	44.6	46	44.5	43.2	44.6	43.3	45.5	45.1	44.5
3	43.9	44.5	44.2	44.2	44.4	44	44.5	44.3	44.7	44.8	44.4
4	44.1	44	43.9	44.5	42.6	44.2	43.9	43.7	44.2	44.7	44.0
5	44.3	43.4	43.5	44.4	44.4	44.5	44.5	43.8	43.9	43.4	44.0
6	44.9	44.9	43.9	44.8	44.9	44.5	44.3	44.4	44.1	45.6	44.6
7	43.9	44.6	44	44.9	44.3	44.1	44.3	44.8	45	45	44.5
8	43.7	44.6	45	44.5	43.9	45.2	44.4	44.1	44.7	44.8	44.5
9	45.2	44.9	45	44.4	44.3	43.3	41.8	44.5	44.3	45.5	44.3
10	45.5	44.7	44.1	44.5	43.4	43.3	41.6	45.1	45.1	45.7	44.3
AVERAGE	44.5	44.5	44.3	44.7	44.1	44.0	43.8	44.2	44.6	45.0	44.4

Table 4.4: Rockwell C hardness along edge of slice (along 'drawing' direction).

Location	A	B	C	D	E	F	G	H	I	J	AVERAGE
Hardness	43.5	43.7	44.5	43.6	43.9	44	45.6	45.5	44.6	45.2	44.4

Based on the consistent hardness and the fine, uniform grain size in the transverse direction, it is clear that billet properties will not be strongly influenced by inhomogeneities in the grain structure from edge to core.

4.6   As-Forged Tensile Properties

Although the microstructure and hardness surveys suggest uniform properties across the billet, tensile properties provide quantitative validation of this notion. Transverse tensile properties for the edge and centre of the billet are presented in Table 4.5.

Table 4.5:   Tensile properties of the as-forged billet – transverse direction.

Location	UTS (MPa)	YS (MPa)	% Elongation	% RA
Edge 1	1379.0	1289.3	3.0	12.0
Edge 2	1379.0	1296.2	5.0	9.0
Core 1	1420.3	1337.6	Broke at grip	Broke at grip
Core 2	1420.3	1337.6	5.0	11.0

As expected from the hardness results, the tensile strength of the as-forged condition is deemed to be very high for a titanium alloy. In itself, the as-forged properties provide insight into the strength level capability of this alloy; furthermore, since the billet was 200mm by 200mm in cross section, the high depth of hardenability anticipated is also confirmed.

The material ductility was relatively low, with elongations of less than 5% and reduction of area values of approximately 10%. A very small difference in the ultimate and yield strengths were evident between edge and core specimens, with the core having the slightly higher values. However, the slight difference confirms the homogeneity predicted from the hardness survey.

Evaluation of the as-forged billet can be summarized as follows:

i)   The degree of ingot breakdown was extensive and consistent with a well developed thermo-mechanical work sequence. The resulting macrostructure of the billet was fine and uniform.

ii)   The microstructure showed an appreciable difference between the longitudinal (drawing) and transverse directions. In the longitudinal direction, the primary α was elongated while the transverse direction presented a uniform dispersion of globular primary α.

iii)   Hardness surveys and tensile properties revealed that the billet's properties were uniform from edge to core.

From the above, the following conclusions can be drawn:

- The billet was uniform in chemical and processing attributes and deemed representative of a typical die forging. A similar conclusion can be made about the billet's tensile properties from edge to core. Hence, the billet was judged suitable for a comprehensive characterization of forged Ti-5553.

- Mechanical property evaluations must consider the effect of the volume fraction, shape and distribution of the primary α phase. To address anisotropy concerns, it was decided that all mechanical property specimens be oriented in the transverse direction.

All of the experiments involving Ti-5553 were conducted on material excised from the above forged billet; however, a few comparative tests were conducted on forged Ti-10V-2Fe-3Al (Ti-10-2-3). In every case, the Ti-10-2-3 material was excised from forging prolongations of landing gear components.

4.7 Metallographic Specimen Preparation and Etching

A number of polishing techniques were attempted; results varied widely depending on the sample's heat treat condition. The most successful results were obtained with a semi-automatic Struers polishing machine using progressively finer media as recommended for titanium. The last polishing step was done using a 0.5µm diamond suspension in a 10/90 solution of hydrogen peroxide/distilled water.
The majority of the specimens were etched in Kroll's reagent # 2 per ASTM E407, solution # 192; the optimum etching time for the aged conditions was determined to be 7 seconds, longer times were used for the α-β solution treated and β annealed conditions.

Although Kroll's reagent was adequate for most conditions, better control over the etching response was achieved in some cases by using a solution of:

$$5 \text{ ml } HNO_3$$
$$5 \text{ ml } HF$$
$$15 \text{ ml Lactic Acid}$$
$$65 \text{ ml } H_2O$$

This etchant was recommended by RMI titanium and is noted on each figure as RMI reagent.

Macro etched sections were wet polished with 600 grit emery paper to a fine finish and etched by swabbing with a solution of:

$$70 \text{ ml } HNO_3$$
$$9 \text{ ml } HF$$
$$22 \text{ ml } H_2O$$

Increased contrast was obtained by allowing the solution to remain on the surface for 20-30 seconds prior to rinsing with distilled water; an example is shown below:

4.8   Optical and Scanning Electron Microscopy

Optical microscopy was done using a Nikon Optiphot-2 microscope with dry lenses capable of magnifications 50 – 1000 X. All photographs were taken with a digital camera and enhanced through the Image Pro+ software.

Grain size measurements were carried out by the intercept method, following ASTM E112.

Fracture surfaces for SEM observation were cleaned in an ultrasonic bath with 50% methyl alcohol – 50% acetone solutions. The SEM employed was a HITACHI S3700N, equipped with an Oxford, INCA X-act EDS system or a Philips 515. General fractographic analysis in the SEM was conducted on specimens which were polished and etched as described earlier. However, when optimum edge retention was required, the fractured specimens were coated with a thin layer of electroless nickel. As the adhesion of nickel to titanium is often poor, and surface preparation could not employ strong acid etch steps, several pre-cleaning and plating processes were attempted. A process involving two nickel deposition steps was found to yield very successful results. The procedure involved the deposition of a nano-layer of electrolytic nickel, so called "nickel strike", followed by deposition of the 15μm of electroless nickel. The procedure details are outlined below:

- Immerse in a bath of Oakite 90 solution (alkaline cleaner) at 80-90°C for 2-4 minutes at 6volts.
- Rinse with distilled water at for ~1 minute.
- Immerse in a bath of 5% HCl solution at room temperature for 2 minutes.
- Rinse with distilled water for 1 minute.
- Immerse in a mixture of HNO_3 (500g/l)-HF (30g/l max.) at ambient temp. for 15-30 seconds.
- Rinse with distilled water for 1 minute.
- Reverse etch at 50-100 Amps per square foot within Nickel strike bath for ~3 minutes.
- Nickel strike at room temperature for ~3 minutes at 6 volts.
- Hot distilled water rinse for 1 minute.
- Electroless Nickel Plate to a thickness of 10-20 μm.

Prior to plating the specimens, an attempt to measure the amount of material removed by the pre-cleaning (etching) steps was conducted. Adhesion was measured by means of a bend test over a 12mm mandrel. This analysis revealed that although much less than 1μm of the surface was removed during pre-cleaning, acceptable plating adhesion could be achieved. Figure 4.4 is an SEM image of a fractured tensile specimen which had been electroless nickel plated. The excellent edge retention achieved with nickel plating allowed for observation of fine detail along the fracture path.
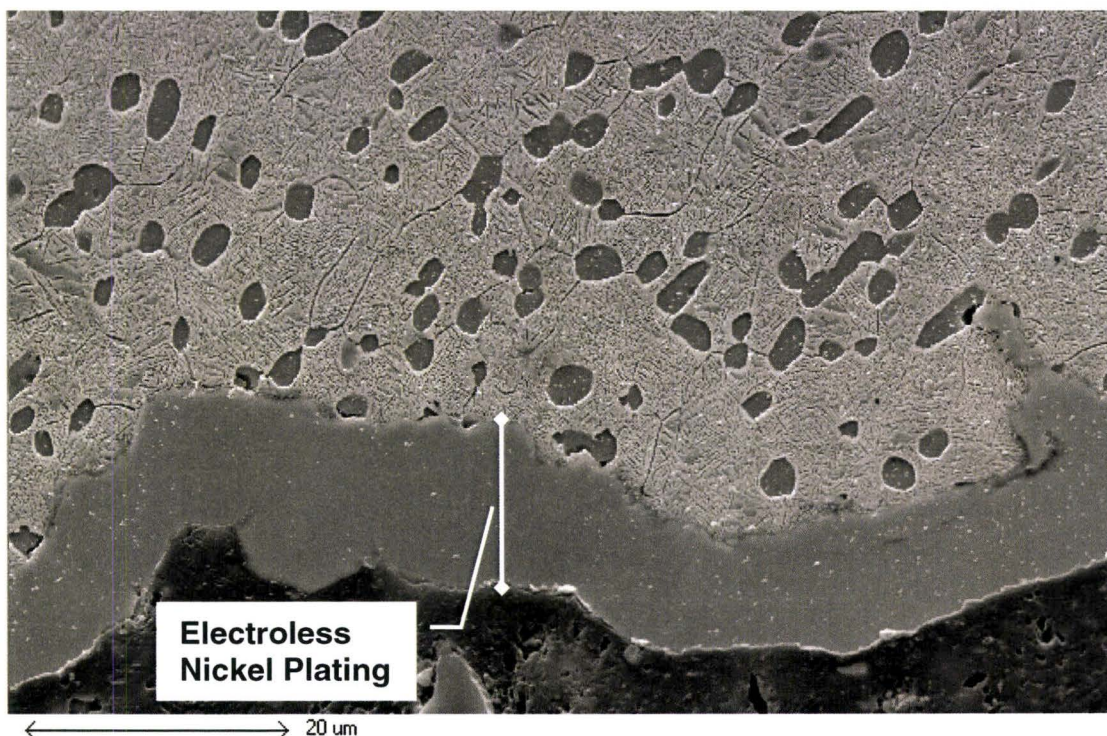
Figure 4.4: SEM image of fractured tensile specimen, with a layer of electroless nickel plating approximately 10-15μm thick.

4.9   Measurements of the Primary α Volume Fractions

Primary α volume fractions were determined from images of the etched microstructure. A total of 10 images, corresponding to 10 fields of observation for every metallographic mount, were analyzed for each reported value. The reported volume fractions are the averages of the 10 measurements. The digital enhancement is done by creating light objects (primary α) and darkening the matrix (transformed β), as illustrated in Figure 4.5. By this technique, the average primary α volume fraction was determined with an error of ± 1.3%.
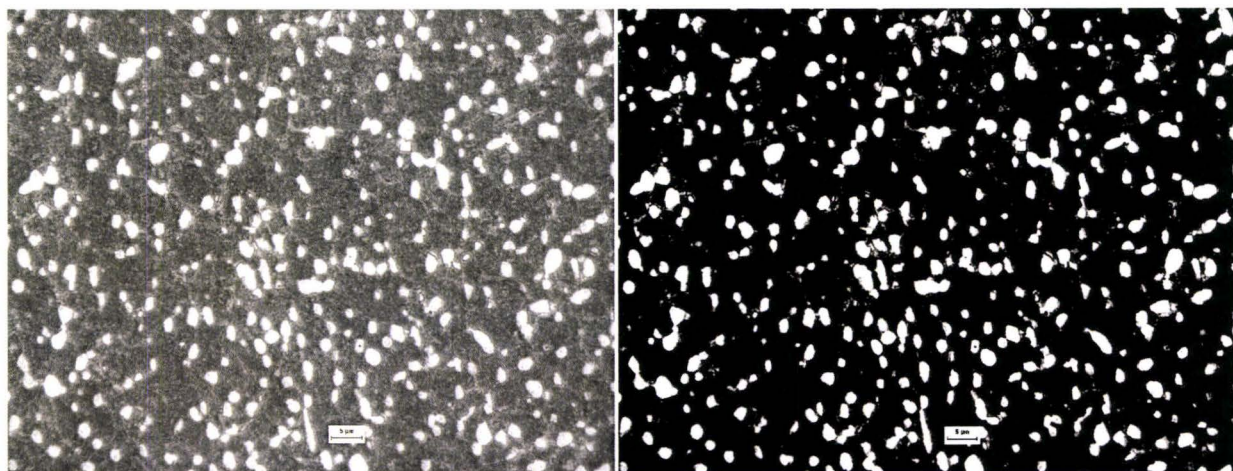
Figure 4.5: Illustration of digital manipulation used to calculate the volume fraction of primary α.; right image is a digital enhancement of left image to facilitate counting.

4.10   Preparation of Foils and Transmission Electron Microscopy

Throughout this work several heat treatment conditions were investigated by transmission electron microscopy (TEM). Depending on the prevalent microstructural phases and properties, some foil preparation techniques were found to be more successful than others. For example, jet polishing parameters had to be drastically changed between α-β solution treated and β annealed materials; ion beam thinning was used in some cases. Furthermore, some of the early TEM work was carried out at University of Toronto under the guidance of Dr. Mike Mei, while the latter work was done at McMaster University under the guidance of Dr. Xiang Wang. Regardless of the specific foil thinning technique all specimens were first excised from bulk samples using a precision wafering saw equipped with a 0.37mm thick diamond blade. The wafer specimens were mechanically thinned to a thickness of about 50-80µm by polishing with fine SiC paper - 400 grit down to 1200 grit. Once deemed sufficiently thin, several disks approximately 3mm in diameter were punched out from each wafer. The disks were electrolytically thinned by a twin-jet polishing device until perforation occurred; this resulted in electron transparent thickness around the perforation.

The solution used for jet polishing at University of Toronto was as follows:

> 180 ml Butyl Alcohol
> 300 ml Methyl Alcohol
> 30 ml Perchloric Acid

Optimization of conditions to achieve specimens suitable for observation was conducted by varying temperature and voltage. The temperature maintained during electropolishing ranged between -35 and $-50°C$, and the voltage used ranged between 20 and 40 Volts. Adequate results were achieved at 22Volts and $-45°C$, with resulting currents of 10-12 mA. Electropolishing was found to be inadequate for specimen thinning of the peak-aged condition, where preferential etching of the alpha phase occurred. Ion beam thinning using the Gatan precision ion polishing system was used for these specimens.

TEM foils prepared at McMaster University were prepared as follows. Thin slices were first cut from all samples. After mechanical grinding (both sides) down to approximately a thickness of 100 µm, 3 mm diameter discs were punched followed by twin-jet electropolishing in a solution of 10 pct. perchloric acid and 90 pct. methanol, at -35°C and 15V. TenuPol-5 equipment made by Struers was used for jet-polishing.

TEM images and corresponding selected area diffraction patterns (SADP) of specimens characterized at University or Toronto were obtained at 200 kV in a Philips Tecnai G-20 electron microscope equipped with a LaB6 source. The images were recorded using CCD slow-scan camera and then analyzed by the Digital Micrograph software.

At McMaster, a PHILIPS CM12 transmission electron microscopy, operated at 120 kV, was used to characterize the microstructure of samples subjected to different heat treatment conditions.

4.11   Electron Backscatter Diffraction Analysis

Characterization of the grain structure using Electron Backscatter Diffraction (EBSD) technique was carried on the material solution heat treated below the β transus and fan-cooled. The scanning electron microscope used was a JEOL 7000F, field emission SEM, equipped with a Nordlys II EBSD detector with no forescatter detector to capture the diffraction patterns. The system uses Oxford HKL CHANNEL5 acquisition software, the Flamenco program was used to index and analyze the patterns. More specifically, the Tango software package was used to process the maps. The specimen was polished to a very fine finish as recommended in the literature with a final polishing step using 0.5µm alumina suspension in a solution of 10% hydrogen peroxide - 90% water. All diffraction patterns were collected in the SEM with an accelerating voltage of 20KV at a current of ~86µA and a tilt angle of 70°. The step size was 0.2µm and the spot size always less than the spot size.

4.12   Heat Treatments

All heat treatments were conducted in air, as is the industrial practice. Titanium is a very reactive metal at high temperatures, consequently, heat treatment in air results in absorption of oxygen at the surface. As oxygen is an α-stabilizer, the oxygen rich outer layer is commonly known as α-case. The depth of the α-case varies with temperature and soak time. A typical example of α-case resulting from β solution heat treatment at 900°C for 75 minutes, followed by ageing at 600°C for 3 hours is presented in Figure 4.6 (a). Figure 4.6 (b) provides another example of α-case resulting from solution heat treatment in air of alloy Ti-3Al-8V-6Cr-4Mo-4Zr (Beta C) at 790°C for 60 minutes. In both cases, the depth of the α-case is approximately 50µm. To eliminate any adverse effects due to oxygen pick up at the surface all specimens were machined from the core of the heat treated bars allowing for several millimeters of metal removal.

(a)   **(b)**
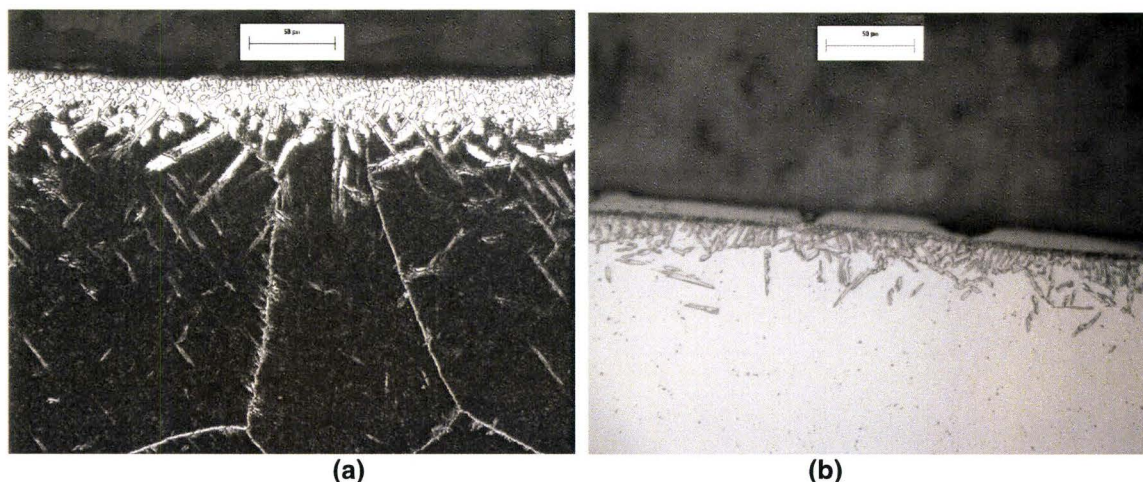
Figure 4.6: Examples of α-case observed in: (a) Ti-5553 after β-annealing and aging; (b) Beta-C after solution treatment. (a) Etched in Krolls; (b) Etched in RMI reagent.

The furnace was capable of controlling temperature to within $\pm$ 5°C, but actual deviation from set temperature was $\pm$ 3°C for all cycles. The heat treatments conducted can be subdivided into three types, β annealing, α-β solution heat treatments and ageing cycles. The β transus

temperature for the characterized billet was 838°C, hence the β annealing cycle was conducted at 900°C for 75 minutes followed by fan cooling. The soaking time was selected to allow sufficient time to achieve a complete transformation to the β phase. Harper, et.al [47]. 2002, reported that at 910°C, the microstructure of forged Ti-5553 fully re-crystallizes to β phase within 20 minutes. The cooling times from the solutionizing temperature to ambient were measured by means of a thermocouple at mid-section of a 20mm thick plate. The cooling curve obtained is presented in Figure 3-7. In terms of linear cooling rate for the critical transformation range, i.e. from 850 to 300°C, this rate is of the order of 1.7°C/sec, while the overall cooling rate is closer to 0.8°C/sec.
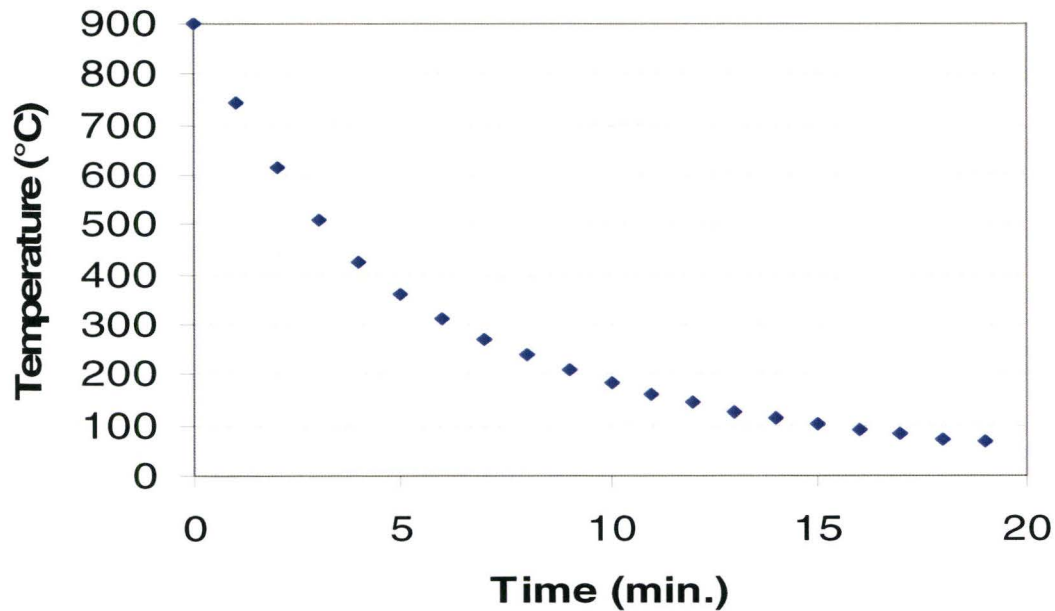
Figure 4.7: Cooling curve for a fan-cooled 20mm thick plate.

The temperature selected for the α-β solution heat treatment was 790°C ± 5°C, which is approximately 50°C below β-transus, followed by fan-cooling. This temperature was selected on the basis of a mechanical property optimization study which is discussed in more detail in Chapter 6. The soak time was 3 hours which is consistent with industrial practice.

Various ageing temperatures and times were used, but in every case the furnace variation was within ± 5°C of the set temperature. The actual thermal cycle is referenced with the pertinent results.

4.13   Determination of Mechanical Properties

The mechanical properties determined in this work included hardness, tensile, compression, shear, fracture toughness and stress corrosion cracking (SCC) tests; all properties were determined at room temperature. The majority of the tensile, compression and shear testing was carried at Cambridge Materials Testing, in Cambridge, Ontario. The fracture toughness and SCC tests were carried at Westmoreland Mechanical Testing and Research, in Youngstown Pennsylvania. Some of the compression and shear tests were done at Goodrich Landing Gear, using a calibrated, refurbished Tinius-Olsen servo-hydraulic test frame. All tensile, fracture toughness and SCC specimens were machined at the respective testing laboratories.
All compression and shear specimens were machined at Goodrich Landing Gear.

4.14   Tensile and Compression Tests

Tensile testing was carried out in accordance with ASTM E8-04 and ASTM B348-06a, while compression testing was carried out using the testing apparatus outlined in ASTM E9-89a at a test speed of 0.13 mm/minute to yield and then at 1.3 mm/minute to fracture.
The tensile specimens were cylindrical "dog bone" type with a diameter of 6.3mm and a gage length of 25.4mm. A diagram of the specimen is presented in Figure 4.8, note that the measurements are in inches.
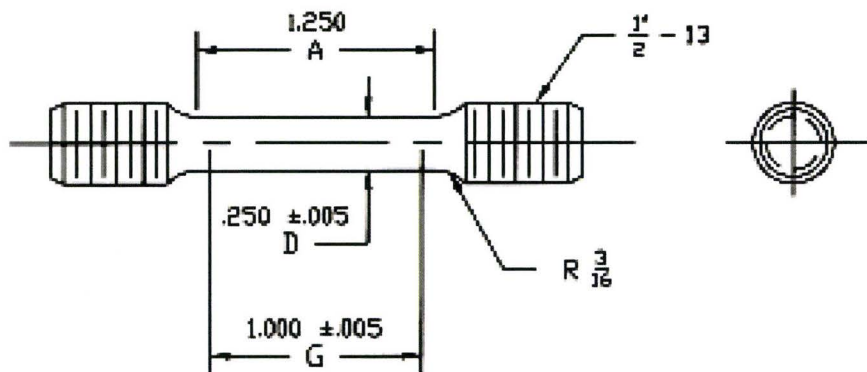
Figure 4.8: Standard test specimen configuration used for all tensile tests, G= gage length, A= length or reduced section, min., D= diameter, R= transition radius, min.

Compression specimens were cylindrical rods 10.0mm in diameter and 15.0mm in length, as depicted in Figure 4.9.
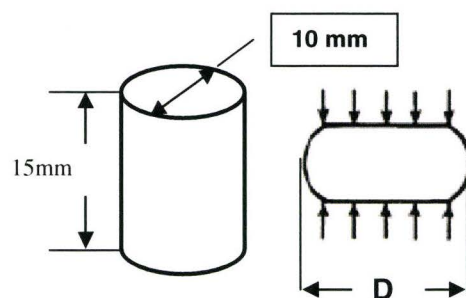
Figure 4.9:   Diagram of cylindrical compression specimen, the area at fracture is determined from the maximum diameter at the "barreled" section labeled D.

Due to the influence of friction at the loading interface of the compression specimen, the ends of the specimen are restricted from free radial expansion. As a consequence, wedge shaped regions of undeformed material are present at either end. This effect is depicted in the Diagram below.
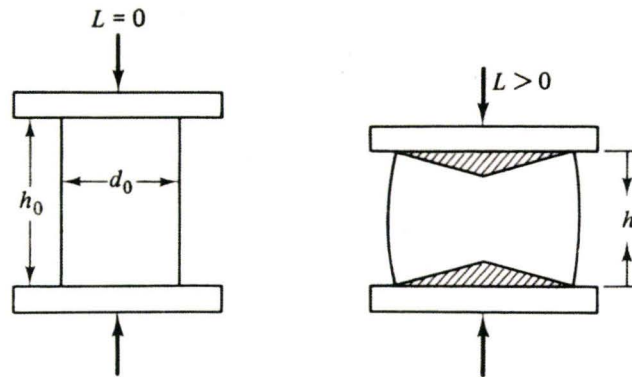
Diagram 4.2   Illustration of the Deformation Expected in a Compression Test; Shaded Areas Represent Undeformed Material.

With continued loading, non- uniform deformation and barreling at the specimen's mid section becomes more pronounced. The area at fracture for the compression tests is calculated by using the dimensions of the barreled diameter **D**.

Determination of the true stress-true strain curves was accomplished by converting the load displacement data into true stress and true strain as follows:

$$\sigma = P/A_o\,(e + 1)$$

where σ is the true stress, P is the load, A_o is the initial area, and e is the engineering strain.

$$\varepsilon = ln\,(e + 1)$$

Note that $e = (L - L_o) / L_o$

where L_o is the initial gage length and L is the instantaneous length.

The true fracture stress in tension was determined from the following expression:

$$\sigma_f = P_f / A_f$$

where P_f is the load at fracture and A_f is the area at fracture determined from:

$$A_f = A_o\,(1\text{-}q)$$

in which q is the reduction in area at fracture.

4.15   Precision and Error

In all the tensile and compression tests, measurements of the instantaneous cross section were not possible as means to measure the cross section beyond uniform deformation were not available. However, determination of the area at fracture and strain at fracture are, ignoring the elastic contribution, deemed accurate. These values are derived from physical measurements of the fractured specimen using a calibrated micrometer with an accuracy of ± 0.001mm. As the instantaneous cross section could not be determined, the portion of the true stress-true strain curve starting at the onset of necking up to the specimen fracture have been plotted as a doted line. An example os such curve is depicted in Figure 4.10.

True Stress-True Strain
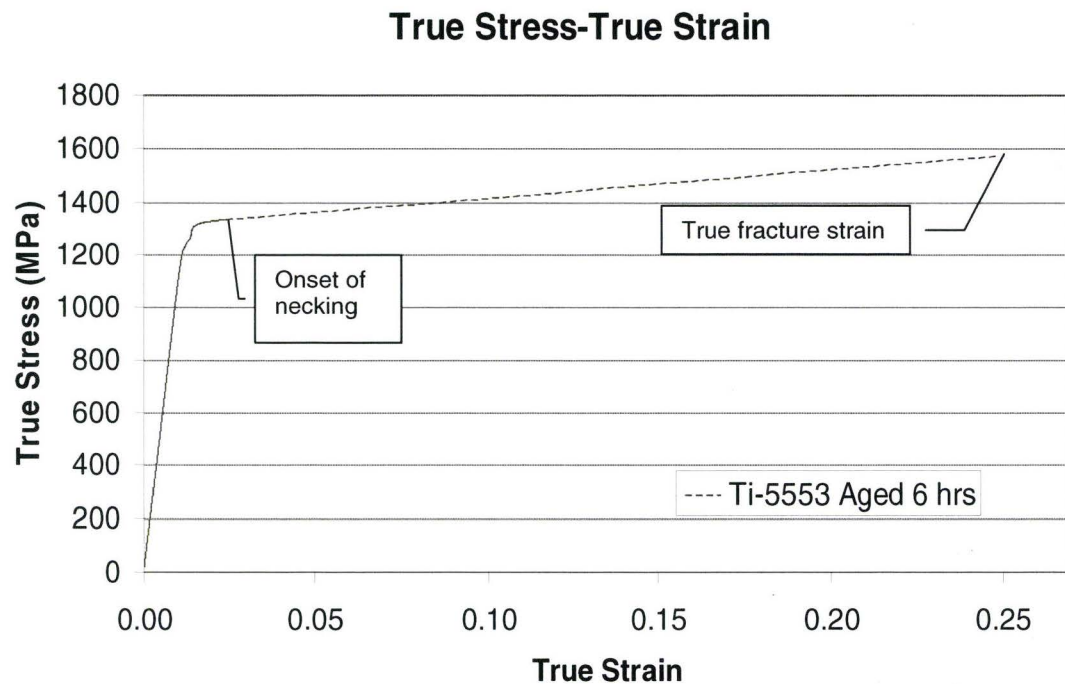
Figure 4.10: Typical true stress - true strain curve, showing extrapolated data with dotted line.

In compression, the true fracture stress was determined in a similar manner as that for tension, with the exception of the area at fracture which was calculated using the diameter of the "barreled" rod measured at the specimen's mid-section, as depicted by **D** in Figure 4.9. The degree of barreling was in the range of 8% to 11%, depending on the heat treat condition tested. In addition, the barreled section was not completely circular and more resembling of an ellipse. This anisotropy of deformation is likely due to texture effects. The difference between the ellipse's major and minor axis was approximately 10% of the original diameter. An average of these two dimensions was taken as the barrel diameter and used to calculate the post-deformation cross sectional area.

4.16   Shear Tests

The shear specimens were of the "top hat" design, with two effective shear planes measuring 2.5 X 10.7mm each. The diagram of the shear specimen configuration is presented in Figure 4.11.
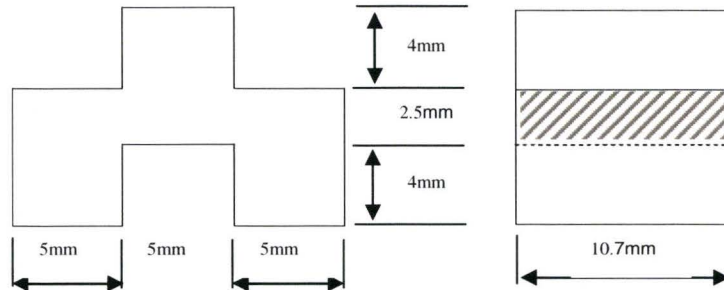
Figure 4.11:   Diagram of shear specimen, front view (left), side view (right), cross hatched area depicts the shear plane.

Determination of the shear strength was calculation by dividing the load at fracture by the shear plane area:

$$\tau = P \: / \: A$$

Where τ is the shear strength, P is the load and A is the total shear plane area.

4.17   Plain-Strain Fracture Toughness Tests

Several specimen configurations are available to determine the plain-strain fracture toughness of metals. The specimen selected was the Compact Specimen C (T) configuration in accordance with ASTM E399. This selection was based on successful prior experience in testing β titanium alloys. The proportions of the specimen are depicted in Figure 4.12, note that all dimensions are in inches, the specimen width, W, was 38.1mm (1.5"), and the thickness, B, was 19.0mm (0.75") which yielded valid K_{IC} results. Determination of K_{IC} was in accordance with ASTM E399, as follows:

$$K_{IC} = P / [(BW)^{\frac{1}{2}}] * f(a/W)$$

Where P is the load, B is the specimen thickness, W is the specimen width, *a* is the fatigue crack length and the term $f(a/W)$, is available from tables in ASTM E399 - for each ratio of *a*/W.
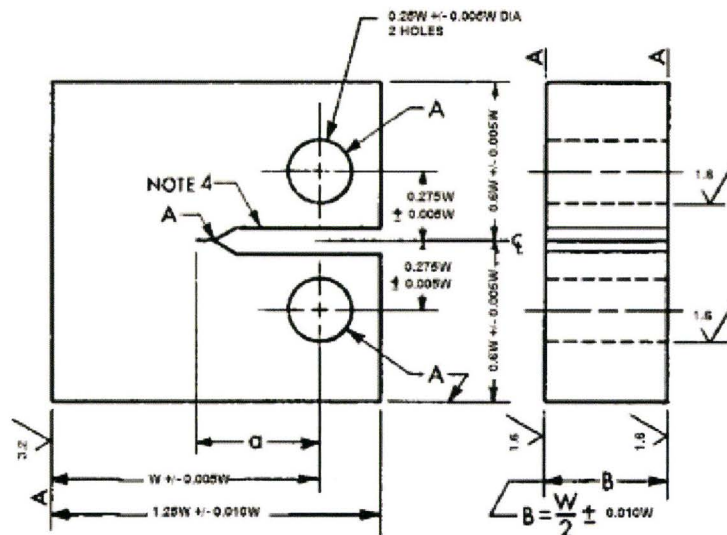
Figure 4.12:   Diagram depicting proportions of Compact Specimen C (T), note that W = 38.1mm (1.5") and B = 19.0mm (0.75").

The material form used in this work was square bar, the convention used to depict the fatigue crack plane identification with respect to bar's longitudinal axis was also in accordance with ASTM E399 and is presented in Figure 4.13. Fracture toughness determinations were made for the C-L and R-C orientations.
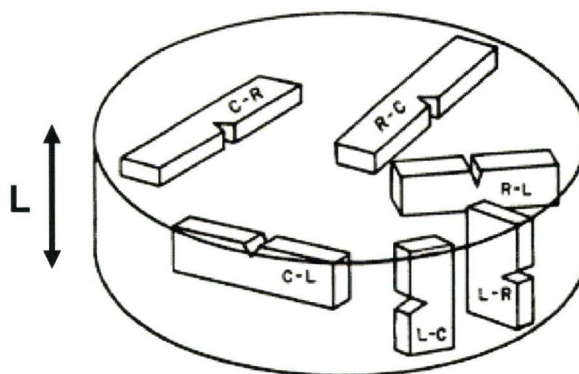
Figure 4.13: **Identification of fatigue crack plane orientation; L.= longitudinal direction of bar.**

4.18   Stress Corrosion Cracking Tests

Customarily, assessment of a materials' resistance to SCC is determined in two ways: initiation of a stress corrosion crack and propagation of an existing flaw under stress corrosion conditions. The latter is known as K_{ISCC}, and is evaluated with a specimen similar to the K_{ISC}. Based on these two assessment methods, two different types of SCC tests were conducted. The specimen used for the onset of SCC was the C ring specimen per ASTM G38, see Figure 4.14; the specimen was excised with its axis oriented perpendicular to the bar's longitudinal direction, i.e. transverse direction. The outside diameter of the specimen was 19.0mm (0.75"), the stress applied was 1090MPa and the test duration was 60 days. The selection of the applied stress, which constitutes 85% of the average yield stress, and the test duration were arbitrary but considered to be severe.
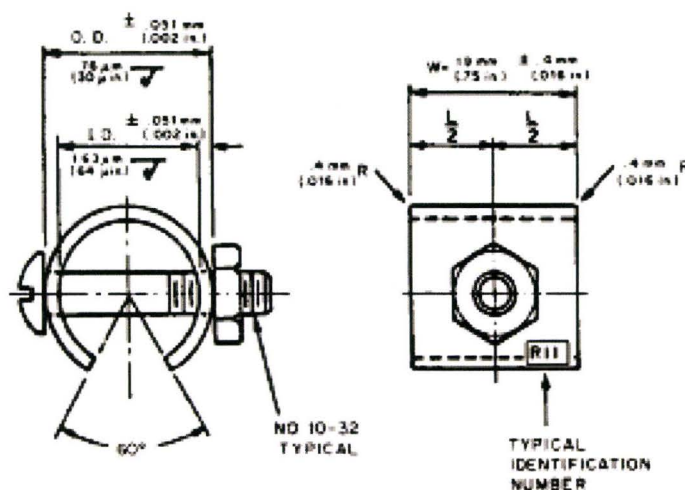
Figure 4.14: **Diagram of C-ring Stress Corrosion specimen, O.D. = 19.0 mm (0.75").**

The test environment was 3.5% NaCl, following the alternate immersion procedure per ASTM G47, which involved 10 minutes immersion in the salt water followed by 50 minutes drying cycles. Examination of the specimens was done daily with the naked eye; a final inspection with a

10X magnifier was done at the conclusion of the 60 days. The absence of any cracking or specimen fracture constitutes a pass.

The resistance to crack propagation by SCC, was determined by means of the 1.000-C(T) Modified WOL K_{ISCC} specimen. This test was done at constant displacement, the load being applied by a fine threaded bolt. The proportions of the specimen are based on it's thickness; a specimen 25.4mm thick was selected for this work based on successful testing of similar alloys. However, the specimen design contains two longitudinal grooves aligned along the crack plane, reducing the effective thickness to 22.8mm. The specimen and test methodology are in line with ASTM E1681-99. A drawing of the actual specimen dimensions is presented in Figure 4.15. The specimens were pre-cracked in fatigue and subjected to stress intensity levels corresponding to 75% of the K_{IC} value, and later increased to higher levels due to the negligible crack growth observed at the initial levels. All specimens were pre-soaked in the 3.5% NaCl solution for at least 10 hours prior to loading. The test time was 100 hrs and the test temperature was 24°C. Determination of K_{ISCC} was in accordance with ASTM E1681 (based on ASTM E399), as follows:

$$K_{ISCC} = P / [(BW)^{\frac{1}{2}}] * f(a/W)$$

Where P is the load, B is the specimen thickness, W is the specimen width, a is the crack length and the term $f(a/W)$, is available from tables in ASTM E399 - for each ratio of a/W.
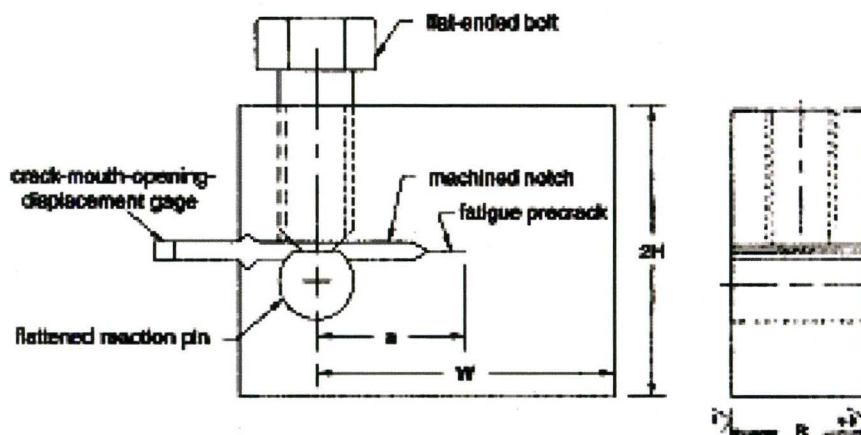
Figure 4.15: Diagram depicting proportions of the 1.000-C(T) Modified WOL K_{ISCC} specimen, note that W = 64.7mm (2.55") and B = 25.4mm (1.0").

5.0 MICROSTRUCTURE EVOLUTION WITH HEAT TREATMENT

All β titanium alloy heat treatments involve a solution heat treatment step conducted either above or below the β transus followed by cooling at a prescribed rate. The aim of the above step is to retain some amount of the metastable β phase for the purpose of hardening the phase by precipitating the α phase at a later ageing step. A schematic diagram illustrating the two types of β titanium heat treatments is provided below.
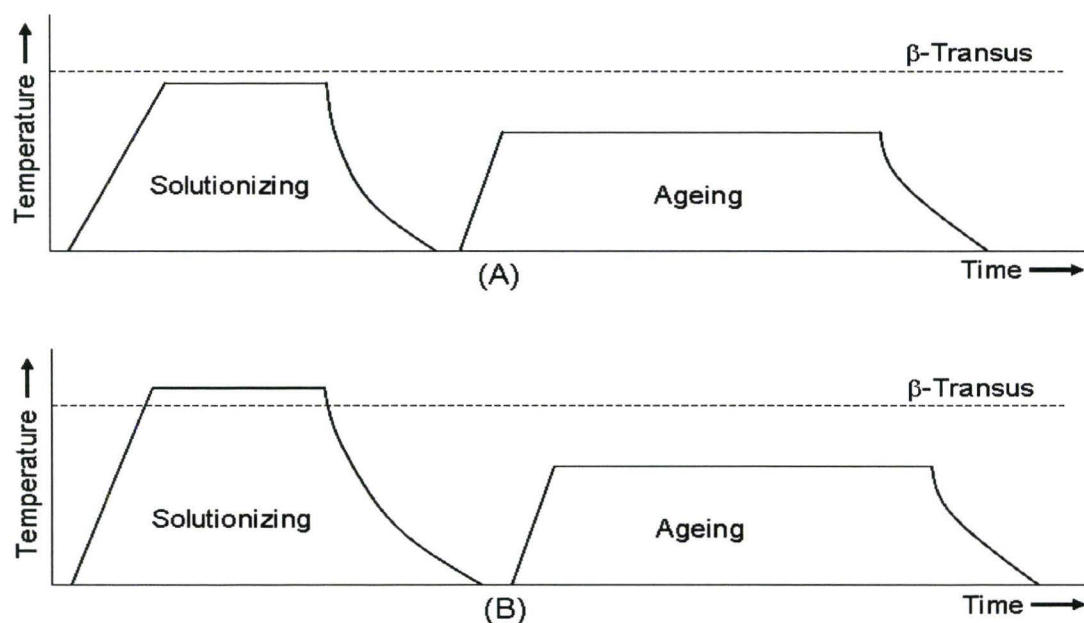
Diagram 5.1: Graphic Illustration of Typical Heat Treatments for β Titanium Alloys:
(A) Solution heat treatment below the β transus
(B) Solution heat treatment above the β transus

In Chapter 1, it was stated that for Ti-5553, the rate of cooling from the solutionizing temperature has significant impact on the kinetics of β decomposition and on the development of metastable phases. The great majority of the work presented herein involved a single cooling rate; this rate is that resulting from "fan cooling" 20mm thick plates, i.e. an average of 1.7°C/sec. However, slower cooling rates, achieved by controlled furnace cooling were used to cool from above the β transus to the ageing temperature. These cooling rates are in line with industrial heat treat practices prescribed for Ti-5553 and are considered practical. In all cases, the starting material was in the as-forged condition, which was already characterized in Chapter 4. It is important to note that variations in the microstructure would be expected from edge to core of the 20mm thick plate. For this reason, analysis of the microstructure, images and descriptions were based on observations made away from the edges and close to the plate's core. As explained earlier, all specimens were oriented to reveal the microstructure in the transverse direction of the forged billet.

Precipitation of α from the retained β phase can follow various paths and involves a variety of metastable phases; however, due to the relatively long times and high temperatures involved this precipitation process is always a diffusion controlled process rather than martensitic one.

This Chapter will explore the microstructures resulting from solution heat treatments conducted above and below the β transus, followed by fan-cooling or controlled furnace cooling and subsequent ageing. The work will involve characterization of the microstructures using the Optical, SEM and TEM; the approach will be as follows:

i)   Microstructure after solution heat treatment above the β transus

    a)   Coexistence of ω and α phases on as-cooled β annealed microstructure

    b)   Characterization of the microstructure as solution-treated and after various ageing steps.

    c)   The effect of cooling rates on microstructure ranging from water quenched to controlled furnace cooled.

ii)   Microstructure after solution heat treatment below the β transus.

    a)   Identification of the metastable ω phase

    b)   Characterization of the microstructures resulting from ageing at 600°C for various times ranging from 5 minutes to 48 hours.

    c)   Confirmation of the heterogeneous nucleation of the α phase.

ii)   Discussion of the microstructure evolution

    a)   Thermodynamic-based equilibrium phase predictions

    b)   Role of the ω phase on α nucleation

    c)   Nucleation and growth of the α phase

    d)   Quantification of microstructural features

    e)   Rationalization of the microstructure evolution

The primary aim of the work reported in this Chapter is to gain an understanding of the microstructural changes which occur during heat treatment of Ti-5553; this knowledge will be used in an attempt to optimize and influence the mechanical properties of this alloy. The scale of the various microstructural features will be quantified in an effort to rationalize the mechanical properties in the next Chapter.

5.1   Microstructure after Solution Heat Treatment above the β Transus

This section will explore the microstructure resulting from annealing above the β transus. The purpose of the solution heat treatment cycle is to convert some portion of the microstructure to a metastable β phase, this phase is normally termed *retained* β. The metastable β is subsequently aged in a controlled manner, resulting in a fine scale mixture of α and β, so called *aged* β. The nomenclature and terminology used to interpret and describe the microstructures throughout this section is in line with guidelines in the literature, namely references [4], [7] and [50]. Annealing above the β transus causes recrystallization and complete disappearance of the α phase. The β annealing cycle consisted in heating the specimens in an air furnace to 903°C, holding at temperature for 75 minutes followed by fan-cooling to room temperature. Below is a schematic representation of the β annealing cycle.
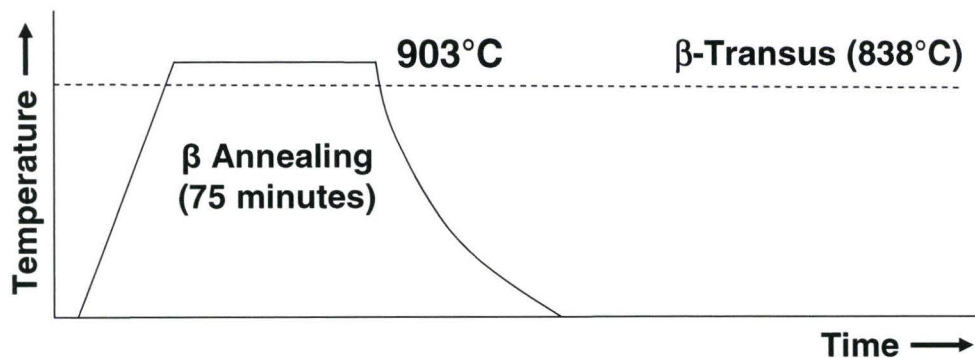
Diagram 5.2:   Graphic Illustration of the β Annealing Cycle.

The microstructure resulting from β annealing and fan-cooling is presented in Figure 5.1, and consists of equiaxed β grains devoid of any optically resolvable features. The grain size was measured by the linear intercept method and found to be 187μm on average.
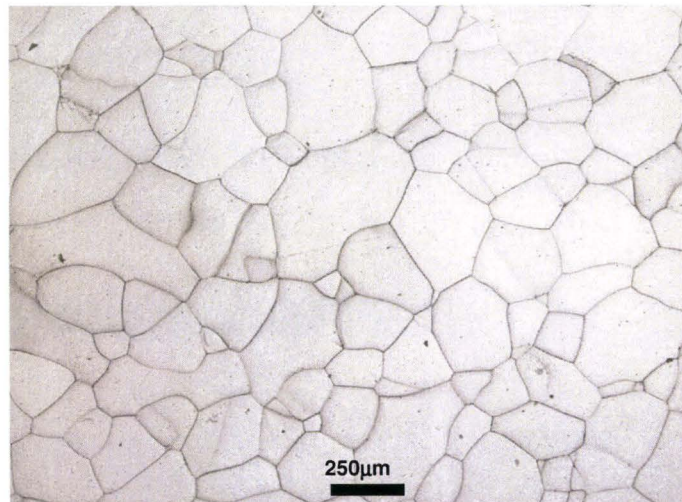
Figure 5.1:   Optical image of β annealed microstructure. Etched in Kroll's Reagent.

As reported in Chapter 4, the cooling time from 904 to 100°C was roughly 20 minutes. More importantly however, the time elapsed through the critical transformation range, i.e. from 850 to 300°C, was approximately 6 minutes. This amounts to a linear cooling rate of roughly 1.5°C/sec. Since the reported transformation times for Ti-5553 are in the order of minutes at similar cooling rates *[31]*, it is essential to establish whether ω or α phases form within these cooling times. Due to the influential role of the ω-phase on subsequent ageing cycles, it is deemed appropriate at this stage in the presentation of results to conclusively identify whether the ω phase is present in the retained β.

The following section deals with the identification of the phases present after cooling from above the β transus temperature using diffraction in and visual evidence and compare this data to other Titanium alloys in the literature.

5.1.1   Identification of nano-precipitates in the fan-cooled, β annealed microstructure.

Aside from the grain boundaries, Optical and SEM examination of the polished and etched specimens did not reveal any other microstructural features. Thin foils were prepared for TEM examination using two methods: by jet polishing and by ion milling - the preparation method is noted for each image. The reason for preparing duplicate specimens by the two thinning techniques was to ascertain that the features observed were not artifacts of the foil preparation method.

Figure 5.2 is a bright field TEM image of a β grain with the associated [110]β zone axis diffraction pattern; this image is typical of many other regions of the specimen. Furthermore, identical images and diffraction patterns were obtained from specimens prepared by jet polishing and from specimens prepared by ion milling. The diffraction patterns present streaks oriented along the diagonals joining the primary β reflections; these streaks correspond to diffused scattering due to the ω phase (a more detailed discussion of the ω phase has been presented in Section 3.3.2).

Observation of the microstructure at high magnification revealed a series of contrast modulations, two such images are presented in Figure 5.3, (a) bright field, (b) dark field. Dark field observation was carried out aligning the electron beam with the diffused scattering regions; thus highlighting the areas of contrast modulation associated with the fine scale ω phase precipitates. As shown in Figure 5.3 (b), the contrast modulations are only a few nanometers in length. This diffused scattering has been referred to as "ω-precursor" or "diffused ω" in the literature, and are said to be characteristic of the initial stage of β → ω transformation. *[16] [31] [44] [48]*

Consequently, there is evidence that the ω phase is present in the β annealed and fan-cooled microstructure, and that the scale of the ω phase is extremely fine (>10nm).

Superimposing the cooling rates realized in this work on the partial TTT diagram due to Cotton, et al.*[31]* , nucleation of α in Ti-5553 is expected within 2-3 minutes of cooling start. However, such α precipitation would be in its very early stages. From review of the literature, the presence of ω phase is expected to aid the nucleation process, thus resulting in copious α phase precipitates. To confirm these predictions, foils were examined at high magnifications and the SAD patterns collected with an emphasis on identifying the α phase.

(a)   (b)
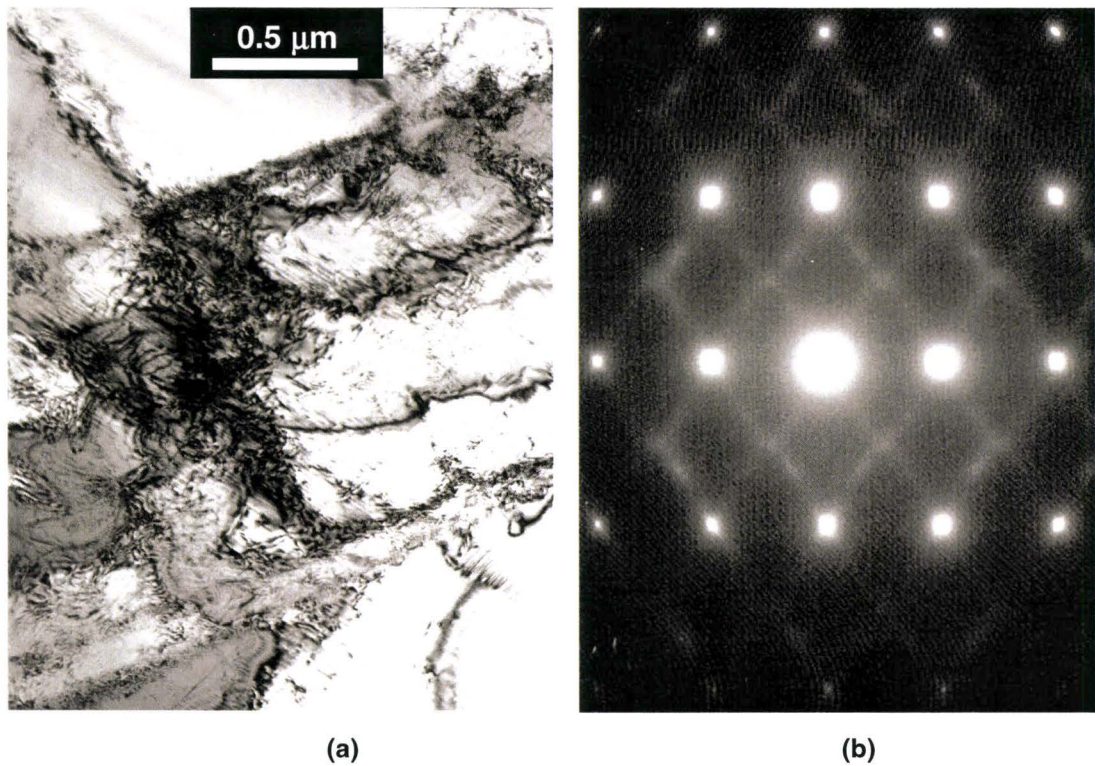
Figure 5.2:   Bright field TEM image of the β phase with associated [110]β zone axis diffraction pattern at right. Foil prepared by jet polishing.

(a)   (b)
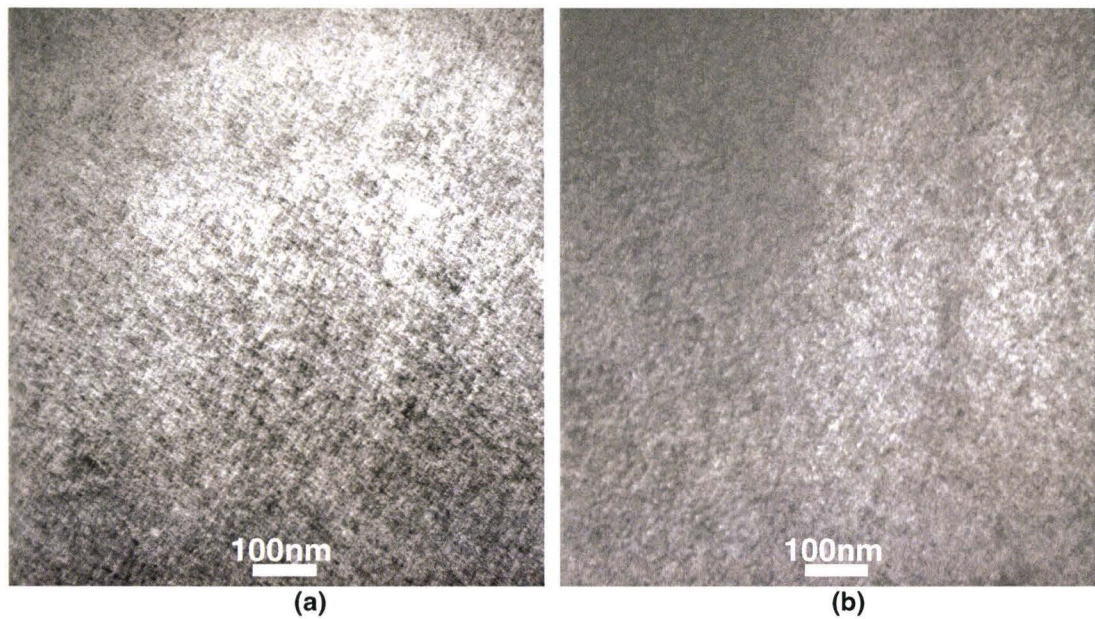
Figure 5.3:   (a) Bright field, (b) Dark field TEM images of the β phase showing very fine-scale precipitate. Foil prepared by ion milling.

Bright and Dark field images of the β annealed microstructure and the associated SAD pattern formed in the [001]β zone axis are presented in Figure 5.4 (a), (b) and (c) respectively. The SAD pattern is quite similar to that reported in the literature for β annealed Ti-14Mo-6Al alloy [49] Figure 5.4 (d), as they both present precipitate reflections which are arced, or curved, rather than streaked in a given crystallographic direction. These reflections are associated with α precipitates which do not obey the Burgers relationship and are termed type 2 α; a more detailed explanation is provided in the Discussion section of this Chapter. The DF image, Figure 5.4 (b), corresponds to the reflection flanking the (110)β and highlights the very fine-scale α precipitates.

(a) BF

(b) DF

(c)

(d)
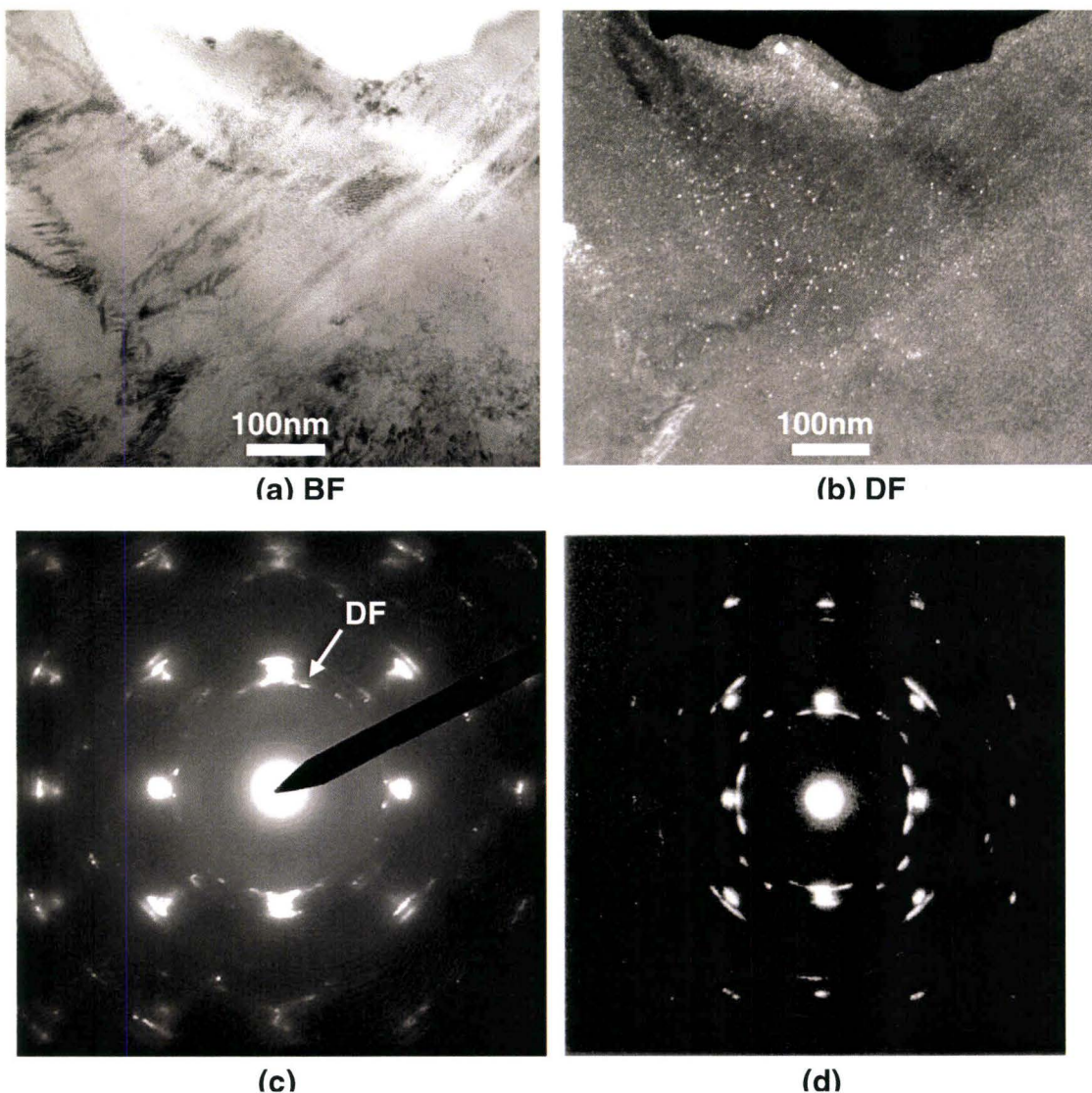
Figure 5.4: **(a) Bright field, (b) Dark field TEM images of the β phase for a Ti-5553 foil prepared by ion milling. (c) and (d) are [001]β zone axis SAD patterns from β annealed Ti-5553 and Ti-14Mo-6Al alloys [49], respectively.**

Based on visual and crystallographic evidence presented, it is concluded that the β annealed and fan-cooled Ti-5553 microstructure contains both, ω and α phases. The scale of these phases is very fine, less than 10nm in size. Having established that the retained β contains these two phases, the impending transformation of the microstructure with ageing was investigated.

5.1.2 Microstructure evolution after various heat treatment cycles.

5.1.2.1 Solution heat treatment and ageing in the α-β temperature range.

The heat treatment cycle performed for the as-forged material, i.e, the ST condition described in Section 4.1 was also performed on the β annealed specimens. This cycle involved re-solution heat treatment in the α-β range at 790°C for 2 hours followed by fan-cooling, as summarized below, a schematic diagram for this cycle is also provided.

- β annealing at 903°C for 75 minutes
- Fan cooling to room temperature
- Solution heat treatment at 790°C for 2 hours
- Fan cooling to room temperature
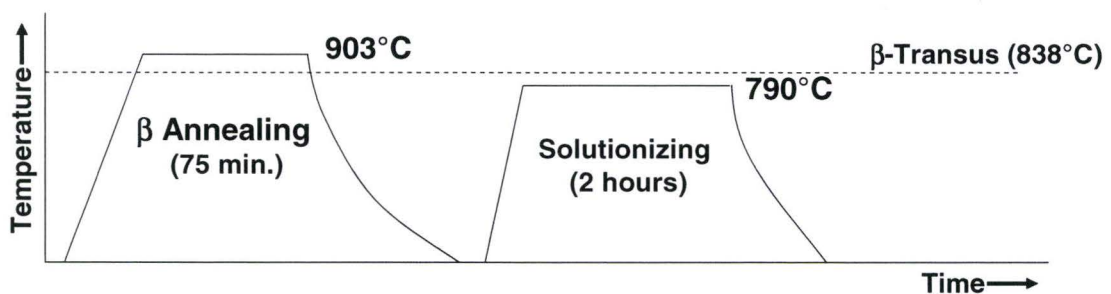
Diagram 5.3: Graphic Illustration of the β Annealing and ST Cycle.

An optical image of the microstructure after etching is shown in Figure 5.5. The etched microstructure consisted of equiaxed grains, with various degrees of darkening within individual grains which could not be resolved optically.

Images of the microstructure, as seen by the SEM are presented in Figures 5.6. The microstructure consisted of sub-micron acicular α, arranged in lath patterns. Individual needles could be resolved near the grain boundaries where the needles were larger; however gradual refining was evident toward the grain interior. The average grain size remained the same as that following the β annealing cycle as the precipitation of the α needles extended throughout the retained β grains.
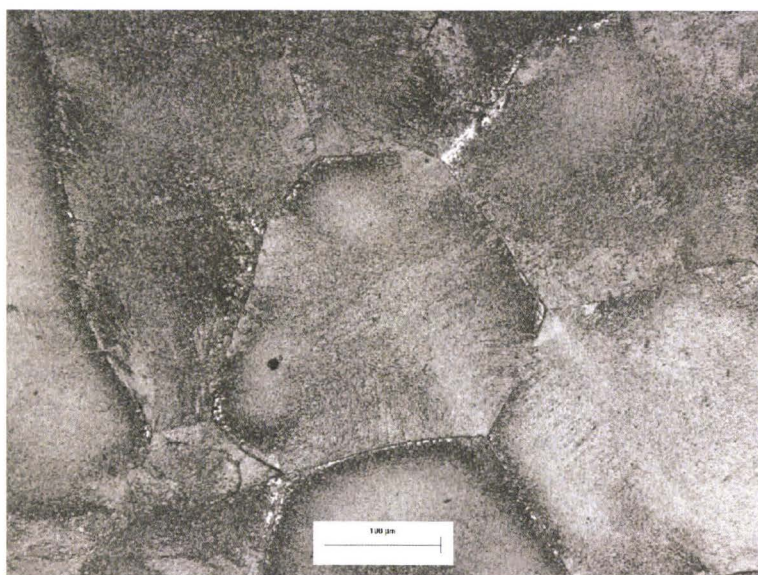
Figure 5.5: Optical image of the microstructure after β annealing at 903°C for 75 minutes, fan-cooling, followed α-β solution treatment at 790°C for 2hrs and fan-cooling. Darkening near the grain boundaries corresponds to coarser α needles. Etched in Kroll's reagent
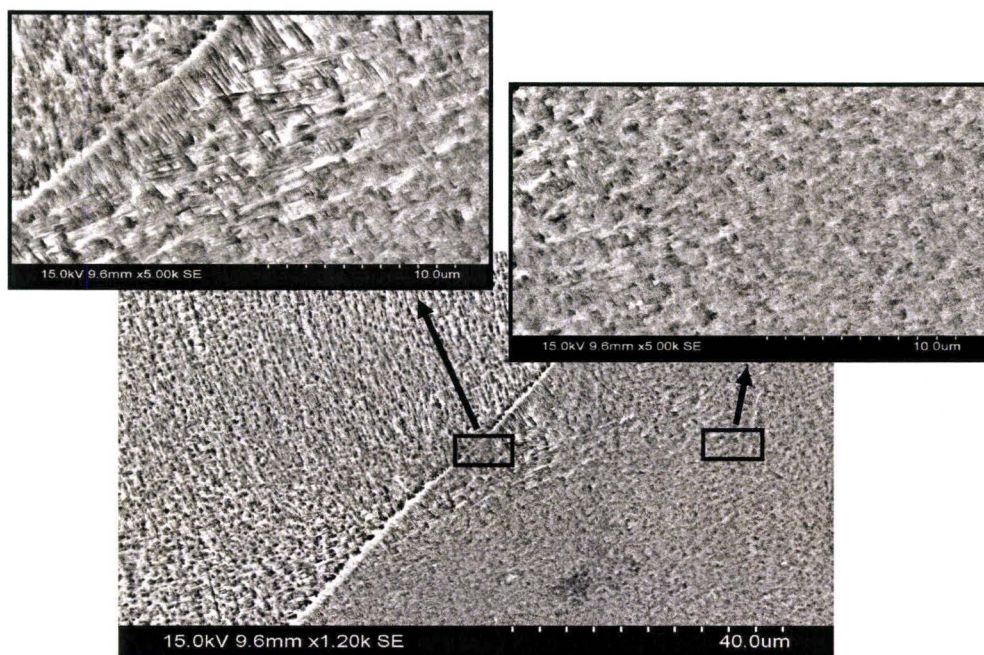
Figure 5.6: SEM image of the microstructure after β annealing at 903°C for 75 minutes, fan-cooling, followed α-β solution treatment at 790°C for 2hrs and fan-cooling. Note the acicular microstructure arranged in fine laths, the needles are coarser in the vicinity of the grain boundaries. Etched in Kroll's reagent

Ageing of specimens heat treated as described above at 600°C for 6 hours did not alter the microstructure significantly. The complete heat treatment cycle is summarized below; a schematic diagram is also provided:

- β annealing at 903°C for 75 minutes
- Fan cooling to room temperature
- Re-solution heat treatment at 790°C for 2 hours
- Ageing at 600°C for 6 hours
- Fan cooling to room temperature
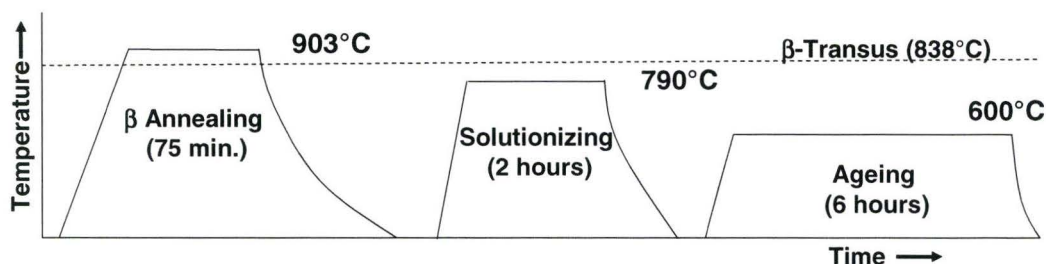
Diagram 5.4:   Graphic Illustration of the β Annealing, ST and Aging Cycle

Optically, the microstructure was very similar to that presented in Figure 5.5, with the exception that the darkening around the grain boundaries was less pronounced. Under the SEM, the microstructure consisted of acicular α, almost indistinguishable from that in Figure 5.6, and is shown at two magnifications in Figure 5.7.
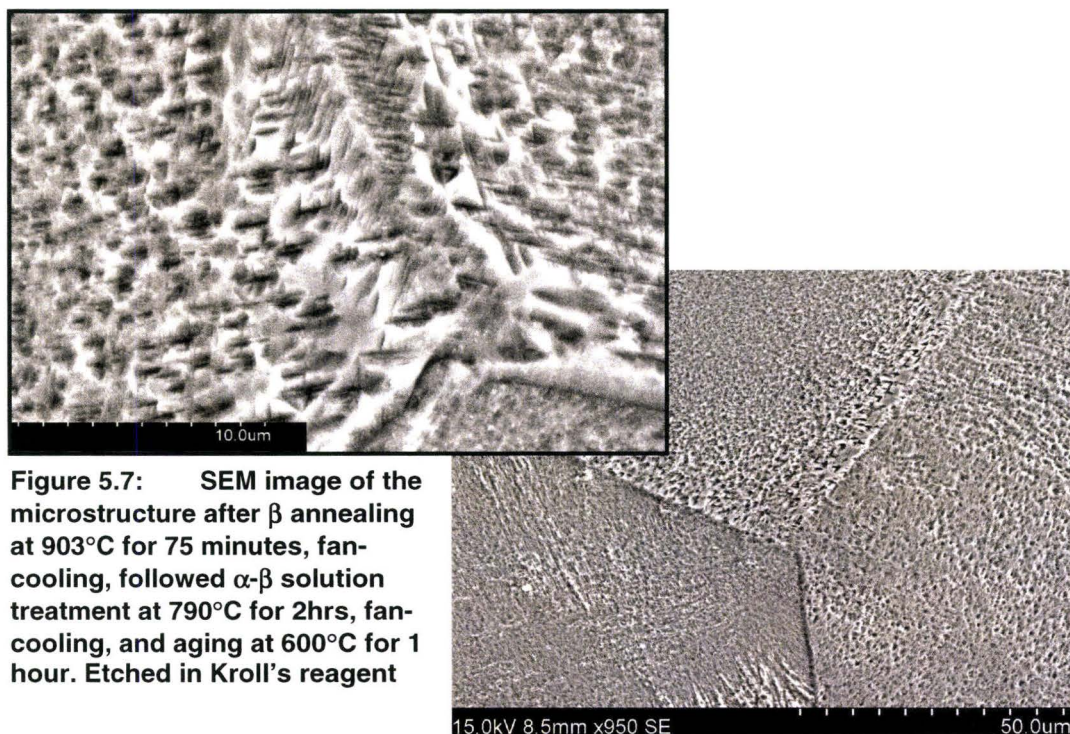
Figure 5.7:   SEM image of the microstructure after β annealing at 903°C for 75 minutes, fan-cooling, followed α-β solution treatment at 790°C for 2hrs, fan-cooling, and aging at 600°C for 1 hour. Etched in Kroll's reagent

To summarize, re-solution treatment of the β annealed microstructure at 790°C and ageing at 600°C results in precipitation of fine scale acicular α. The microstructure is coarsest near the grain boundaries and becomes gradually finer toward the grain interiors. As the entire retained β grains undergo this transformation after the re-solution heat treatment step, the subsequent ageing step did not noticeably alter the microstructure.

5.1.2.2 Rapid cooling from above the β transus and ageing temperature.

In order to avoid formation of the ω phase upon cooling to room temperature, cooling directly to the ageing temperature was conducted: details of the heat treatment and a diagram are provided below:

- β annealing at 903°C for 75 minutes
- Cooling to 600°C in 3 minutes
- Aging at 600°C for 20 minutes and 3 hours
- Air cooling to room temperature
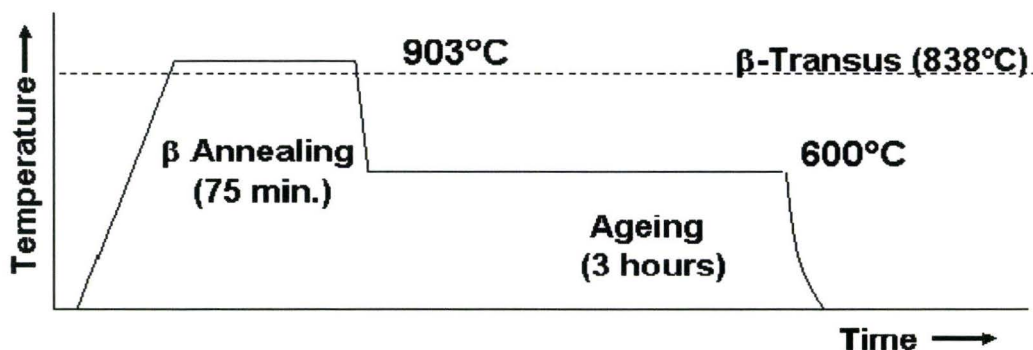
Diagram 5.5:   Graphic Illustration of the β Annealing, and Direct Ageing Cycle.

Cooling to the ageing temperature was achieved by setting the furnace to 600°C and opening the furnace door until the temperature stabilized. The cooling time was roughly 3 minutes, which constitutes an average cooling rate was approximately 100°C/min The microstructure resulting from this heat treatment cycle is presented in Figures 5.8 and 5.9, for optical and SEM images respectively. Specimens aged for 20 minutes and for 3 hours possessed identical microstructures. Acicular α, measuring 3-6μm in length is the dominant feature throughout the specimen, with coarser α precipitates and a precipitate free zone, decorating the grain boundaries. A comparison between the scale of the α precipitates, forming with and without the ω phase as a precursor, is presented later in this Chapter.
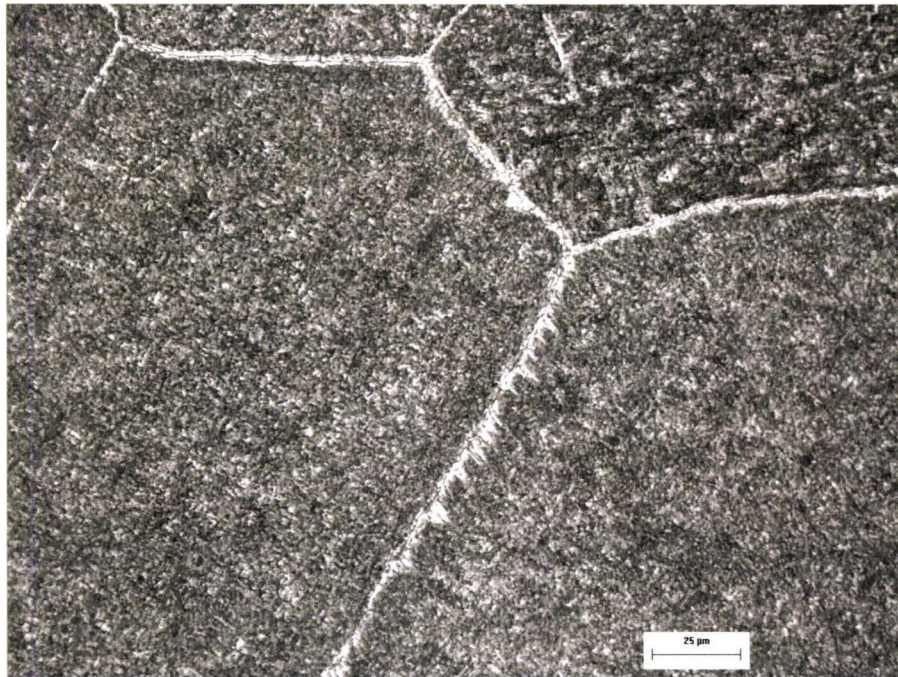
Figure 5.8: Optical image of the microstructure after β annealing at 903°C for 75 minutes, direct cooling to 600°C and ageing for 3 hours. Etched in Kroll's reagent
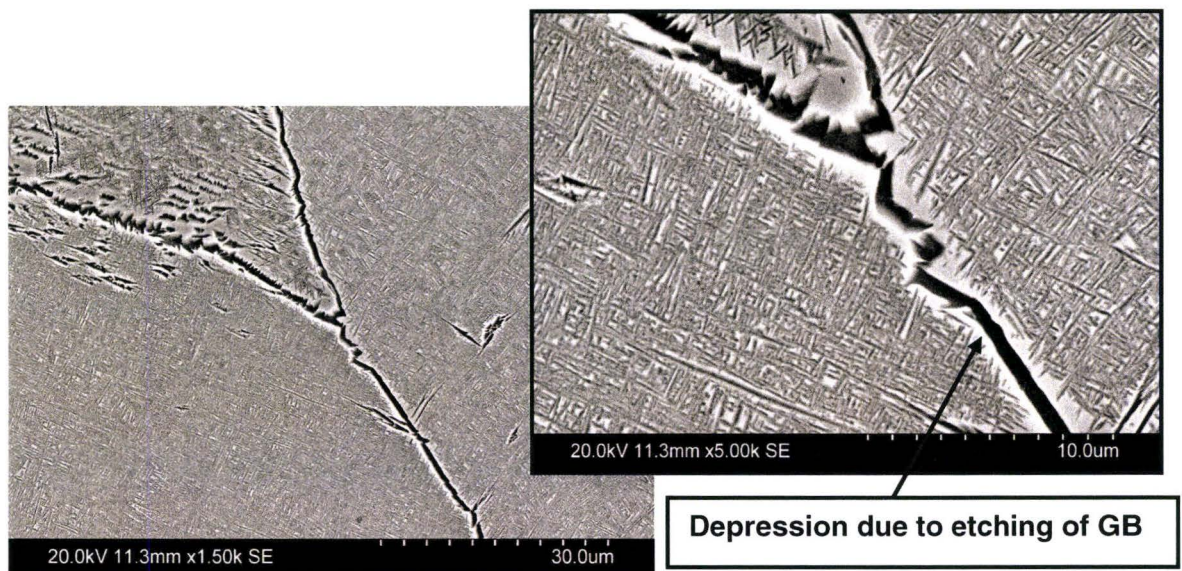
Figure 5.9: SEM image of the microstructure after β annealing at 903°C for 75 minutes, direct cooling to 600°C and ageing for 3 hours

5.1.2.3 Slow cooling from above the β transus and ageing in the α-β temperature range.

The effect of cooling rate on microstructure evolution was investigated by β annealing and slow cooling to the ageing temperature, followed by prolonged ageing. A summary and schematic diagram for this cycle is provided below:

- β annealing at 903°C for 75 minutes
- Furnace cooling to 600°C in 90 minutes
- Aging at 600°C for 8 hours
- Air cooling to room temperature
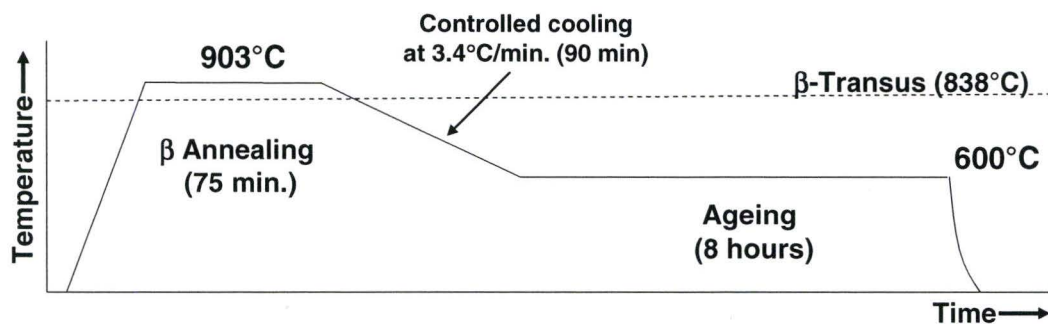
Diagram 5.6: Graphic Illustration of the β Annealing, Controlled Cooled and Aged Cycle.

The above cycle amounted to an average cooling rate of 3.4°C/min which is significantly slower that the fan-cooling rate (1.5°C/sec). Optical images of the microstructure are presented in Figure 5.10, while SEM images are shown in Figure 5.11. The microstructure consists of mostly acicular α in a matrix of retained β. The α is arranged in laths, however these laths are coarser than those discussed in section 5.1.2.2. A network of grain boundary α platelets is evident in the light micrographs, as well as pockets of lamellar α, which are encircled in Figure 5.10.
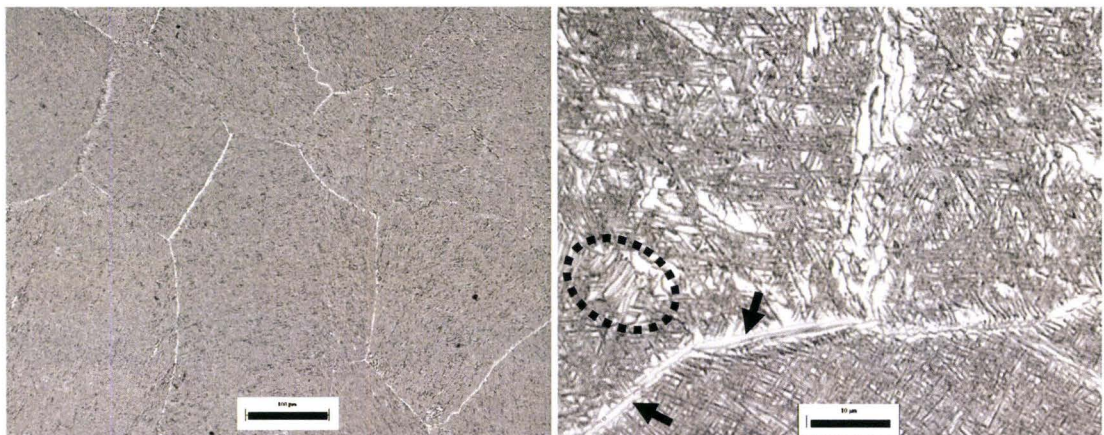
Figure 5.10: Optical images of the microstructure after β annealing at 903°C, controlled cooling at 3.4°C/min. to 600°C and aged at 600°C for 8 hours. Note the grain boundary α (arrows) platelets and pockets of lamellar α within the grains (ellipse). Etched in Kroll's reagent
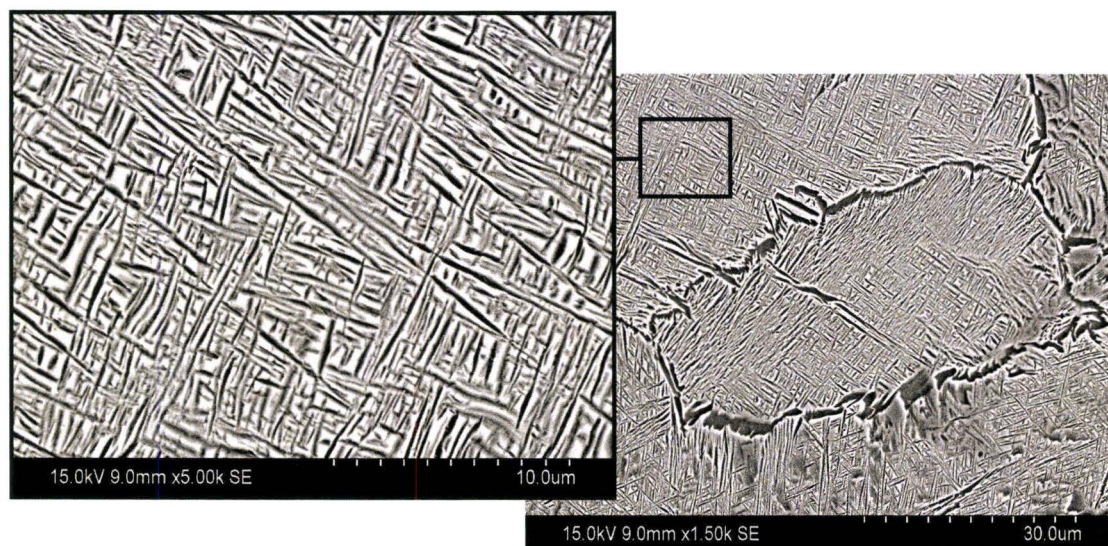
Figure 5.11: SEM images of the microstructure after β annealing at 903°C, controlled cooling at 3.4°C/min. to 600°C and aged at 600°C for 8 hours. Note the jagged grain boundaries due to local protrusion of α needles into adjacent grains. Etched in Kroll's reagent

Another important microstructural change occurring with the slow cooling is that the grain boundaries no longer appear as smooth lines. As depicted in Figure 5.11, there is local re arrangement at the grain boundaries as the growing α needles extend past the boundaries and into adjacent grains. In many cases, an entire colony of needles protrudes into another grain giving the grain boundary a stepped or jagged appearance. The length of the acicular α is of the order of several micrometers. The effect of further slowing the cooling rate on the microstructure was investigated by the heat treatment cycle described below, a schematic diagram is also provided:

- β annealing at 903°C for 75 minutes
- Furnace cooling to 600°C in 5 hours
- Aging at 600°C for 8 hours
- Air cooling to room temperature
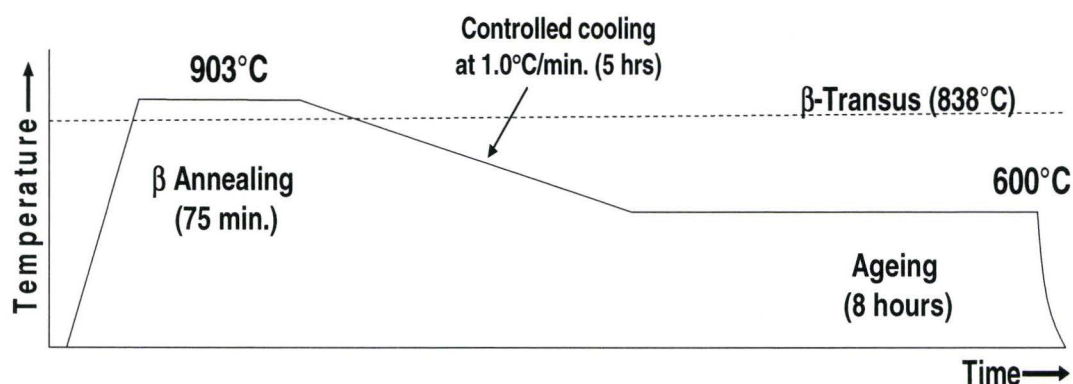
Diagram 5.7: Graphic Illustration of the β Annealing, Controlled Cooled and Aged Cycle.

The above cycle amounted to an average cooling rate of 1.0°C/min., which is in line with the industrially prescribed heat treatment for improved toughness. Optical and SEM images of the resulting microstructure are presented in Figure 5.12 and 5.13, respectively. The microstructure consists of lamellar α in matrix of retained β; the α is coarser than that in the preceding conditions studied. Grain boundary α platelets are evident, as highlighted by arrows in Figure 5.12. Under the SEM, fine acicular α could be resolved amongst lamellar α.
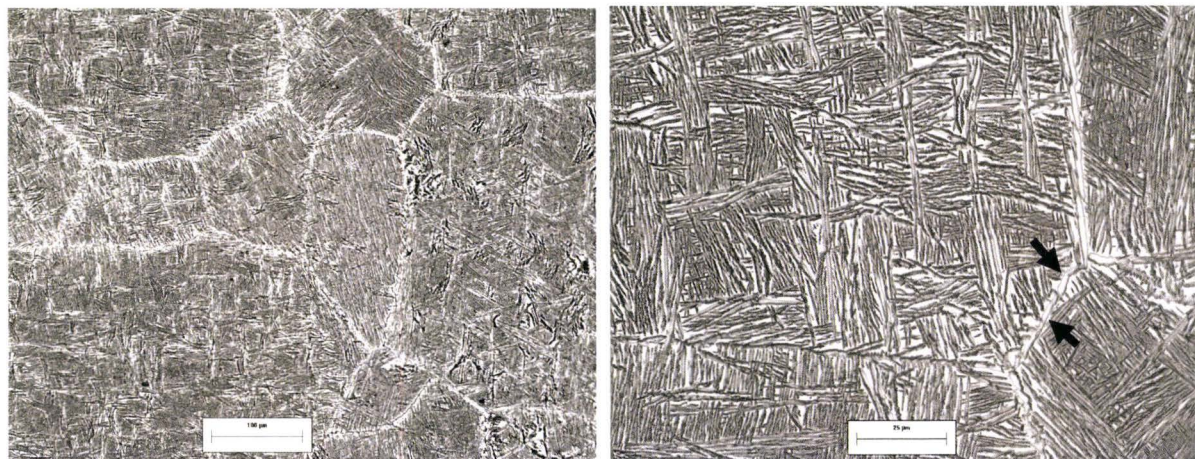
Figure 5.12:   Optical images of the microstructure after β annealing at 900°C, controlled cooling at 1°C/min. to 600°C and aged at 600°C for 8 hours. Note the grain boundary α (arrows) and lamellar α. Etched in Kroll's reagent
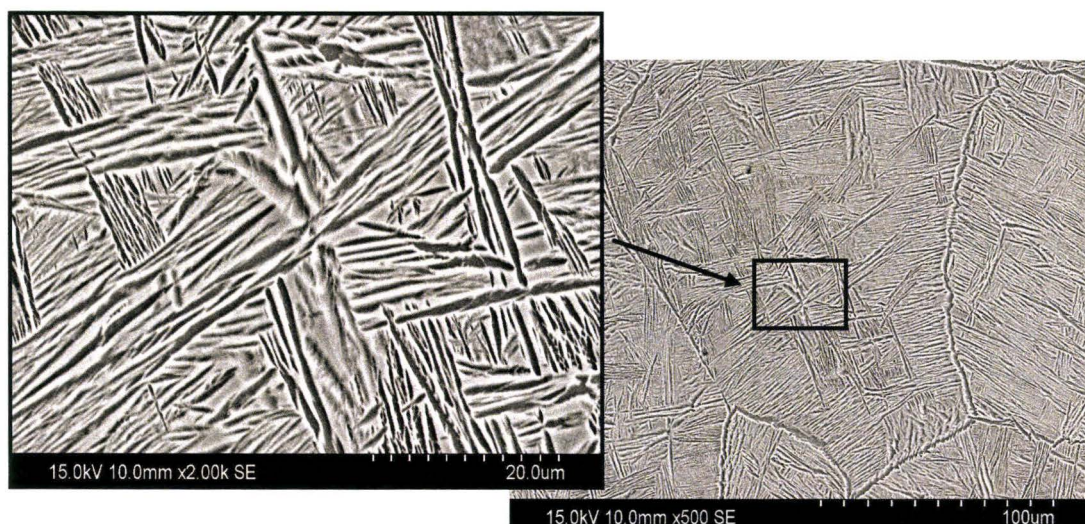
Figure 5.13: **SEM images of the microstructure after β annealing at 903°C, controlled cooling at 1°C/min. to 600°C and aged at 600°C for 8 hours, note the presence of fine acicular α amongst lamellar α. Etched in Kroll's reagent**

Analogous to the nomenclature used to describe steel microstructures, the microstructure is described as lamellar. This is because there is metallographic evidence that the α needles overlap abutting against one another. One likely explanation is that as the cooling rate is decreased, the scale of the α needles increases until needles of the same α variant interconnect forming undulating ribbon-like structures. Figure 5.14 presents a set of α platelets which intersect the specimen's polishing plane at a shallow angle. These intersecting α platelets appear as parallel bands, much wider than the adjacent α plates which intersect the polishing plane at steeper angles. Examination of these bands at higher magnifications revealed that they are in fact an arrangement of abutting α ribbons. A great number of similar occurrences were found throughout the specimen, confirming that the term lamellar is appropriate in describing the microstructure. Note also that a film α is present along the grain boundaries.
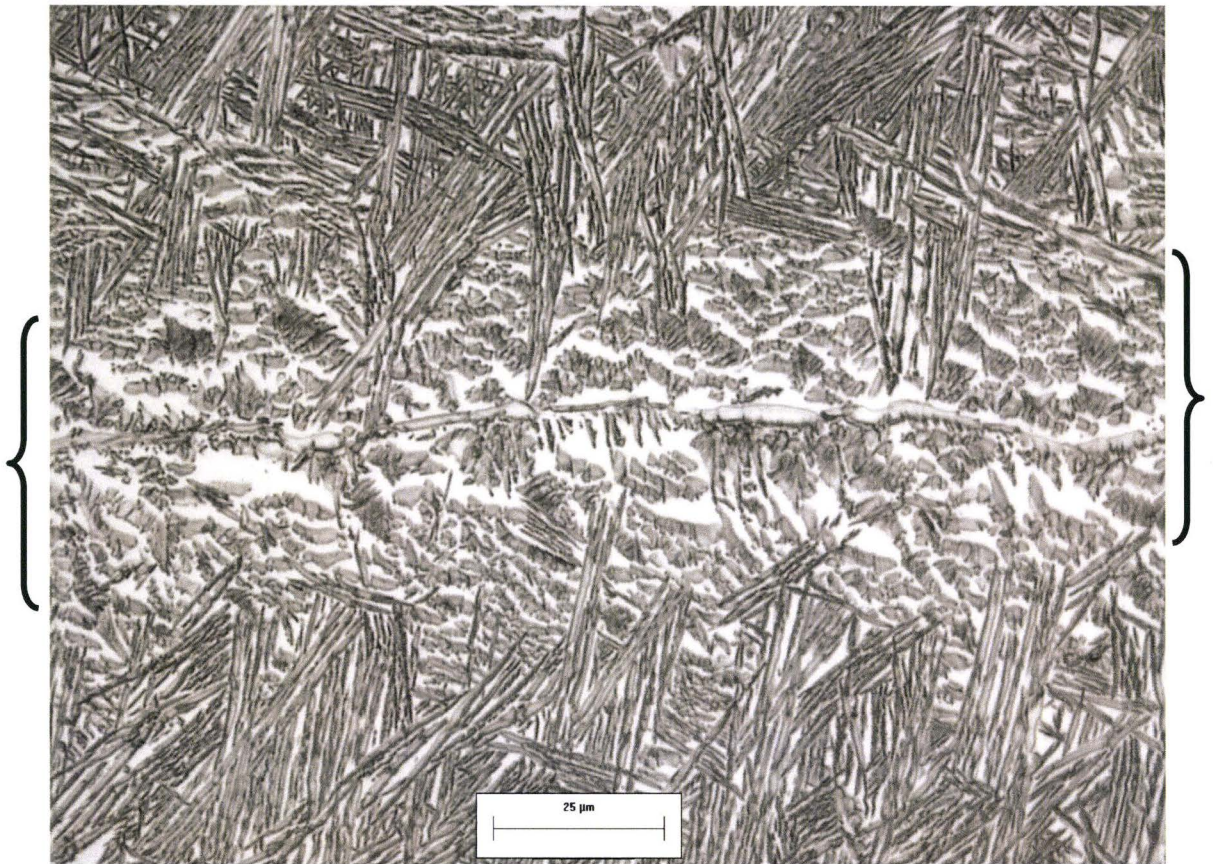
Figure 5.14: Optical image showing lamellar α; note that region surrounding the grain boundary (brackets) contains α platelets which are intersected at a shallow angle, rendering their appearance as parallel ribbons. The grain boundaries contain a film of α. Etched in Kroll's reagent

5.2 Microstructure after solution heat treatment in the α-β temperature range.

Section 5.1 dealt with solution heat treatment at approximately 50°C above the β transus temperature. Such heat treatment eradicates any α phase and causes complete re-crystallization after approximately 20 minutes. In contrast, solution heat treatment below the β transus preserves the character of the as-forged microstructure. The microstructure of the as-forged Ti-5553 consists of an uniformly dispersed globular α, in a matrix of aged β. Images of the as-forged microstructure have been presented in Figure 4.3. The globular α resulted from the extensive thermo-mechanical work received during forging in α-β temperature range, and is referred to as *primary* α. The detailed microstructure of the aged β can not be resolved by optical microscopy. It must be pointed out that the nature of the aged β in the as-forged condition is not controlled in the normal industrial practice; hence, high variability could exist depending on processing conditions. Since all the material used for these heat treatment experiments was from a single forged billet, this variability need not be considered.

Solution heat treatment in the α-β temperature range was carried out at 790°C ± 5°C, held at temperature for 3 hours and fan-cooled. This solution temperature is approximately 50°C below the β-transus and was selected on the basis of strength/ductility optimization studies which will be discussed in Chapter 6.0. For ease of reference, this heat treatment will be referred to as the ST condition; a schematic representation of this cycle is presented below:
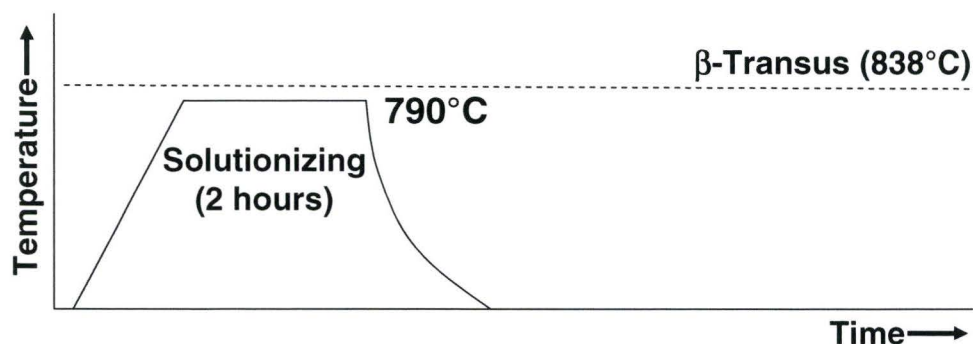
Diagram 5.8: Graphic Illustration of the ST Cycle.

The microstructure is presented in Figure 5.15, and consists of uniformly dispersed primary α in a matrix of retained β. Images (a) and (b) are optical micrographs taken at 400X and 1000X magnification, while (c) and (d) are backscatter SEM images. Comparing the ST microstructure to the as-forged microstructure, it is clear that the aged β matrix has been converted into retained β, while the scale of the primary α appears unaffected.

Figure 5.15 (a) and (b) show the globular morphology of the primary α particles and highlights the remarkably uniform distribution of these particles throughout the microstructure. At higher magnifications, a network of grain boundaries if found to span between the primary α particles, see Figure 5.15 (b). The scale of the primary α and the grain boundaries is roughly the same, with an average size of 2-5μm in diameter.

Under the SEM, it is apparent that the primary α exhibits facets, suggesting that a crystallographic relationship with the β matrix exists; furthermore, it is clear that the α particles have formed along grain boundaries or at triple points. Solution heat treatment for up to 18 hours

did not change the size or distribution of the primary α. This observation suggests that the grain boundaries are pinned at these particles and confirms that the volume fraction of α has reached equilibrium after solutionizing for 3 hours.

The globular character of the α particles and their arrangement at grain boundaries is consistent with a formation mechanism which minimizes the interfacial energy of the system.

(a)   (b)

c)   (d)
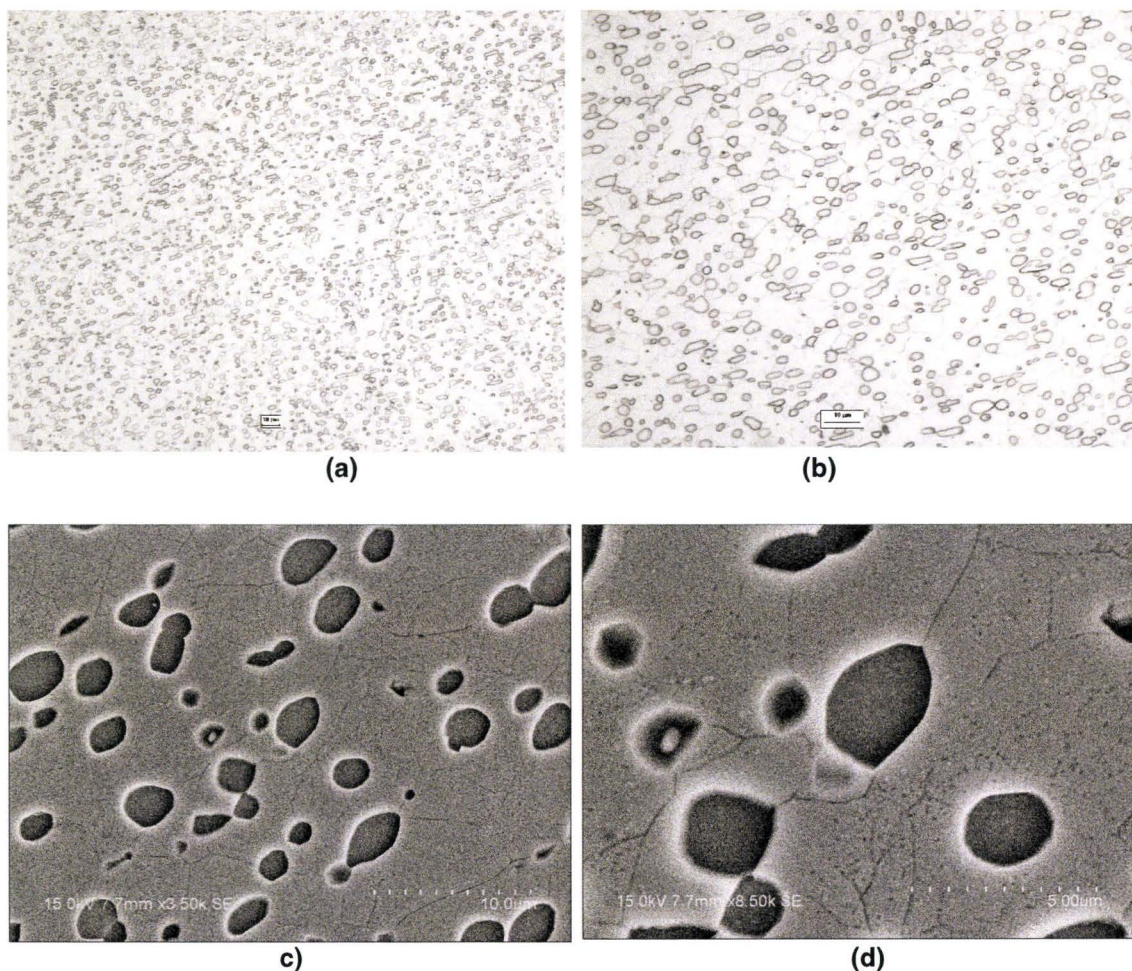
Figure 5.15: **Microstructure of Ti-5553 solution treated at 790°C and air cooled (ST condition) – (a) and (b) are optical images, (c) and (d) are SEM images. Etched in Kroll's reagent**

As described in the characterization of the as-forged billet (Section 4.3), the billet contains a macrostructure consisting of prior β grains which are relatively equiaxed in the transverse direction and elongated in the longitudinal direction. These grains have a diameter of roughly 0.5 to 1mm in the transverse direction, which is nearly two orders of magnitude larger than the scale of grain structures observed in Figure 5.15. Hence, the ST condition contains a macro and a micro - grain structure. To understand the character of the latter grain structure, EBSD analysis was performed on a ST and fan-cooled specimen.

Figures 5.16 a) and b) are EBSD acquired phase and contrast maps, respectively, corresponding to an area measuring 65x50μm. The dark bands to the top left side of the two images represent points for which there no solution to the Kikuchi patterns, and are likely due to subsurface scratches which were not visible even after fine polishing. Nonetheless, the overall proportion of successful solutions was greater than 83% which provides more than ample regions for detailed analysis.
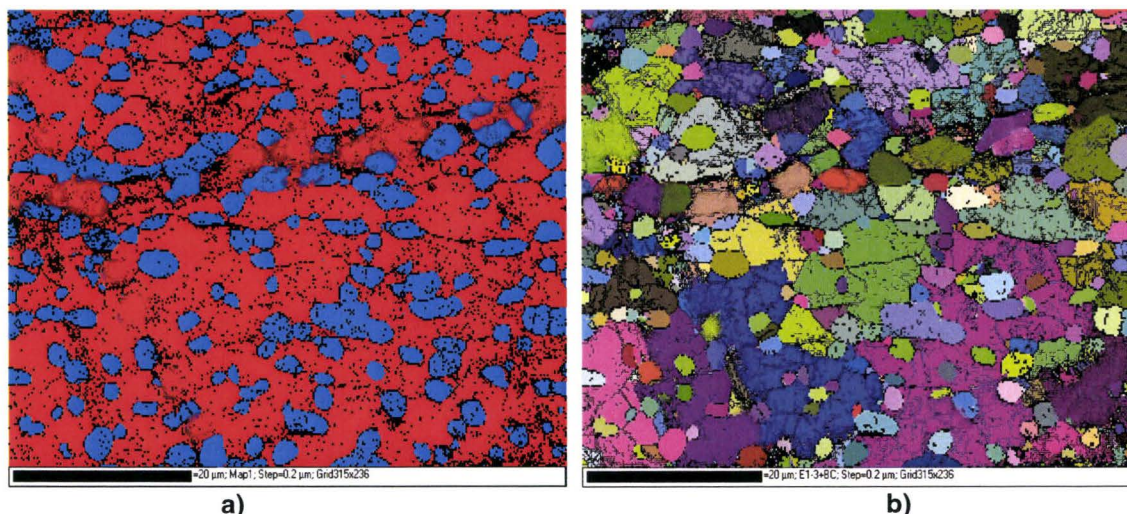
Figure 5.16: **EBSD acquired maps; a) is a phase map showing the α and β phases in blue and red, respectively; b) grain size distribution map, the different grains are randomly assigned colours for clarity.**

The images in Figure 5.16 illustrate clearly the distribution of primary α and retained β within the area analyzed and the numerous grain boundaries connecting the primary α particles. However, neither map provides insight into the character of the grain boundaries. Figure 5.17 is a grain misorientation map, accenting in different colours, the angular misorientation between each grain with respect to a reference grain - depicted by the symbol ⊗. It is clear from Figure 5.17 that the mapped region is made up of two large grains, with a high angle grain boundary traversing the image. Two large grains are clearly separated by one high angle grain boundary, one grain mainly blue, the other mainly lime yellow. Within each large grain, there are many low angle grain boundaries. As can be seen by the histogram showing the relative frequency at right, the majority of the grains boundaries within the blue grain, are misaligned approximately 5° with respect to the reference grain. The misorientation distribution within the lime green grain is somewhat larger and is centered about 39°. Furthermore, the number of blue sub-grains is much larger than the lime green sub-grains, this can be concluded by comparing the height of the peak at 5° with the peak at 30°.
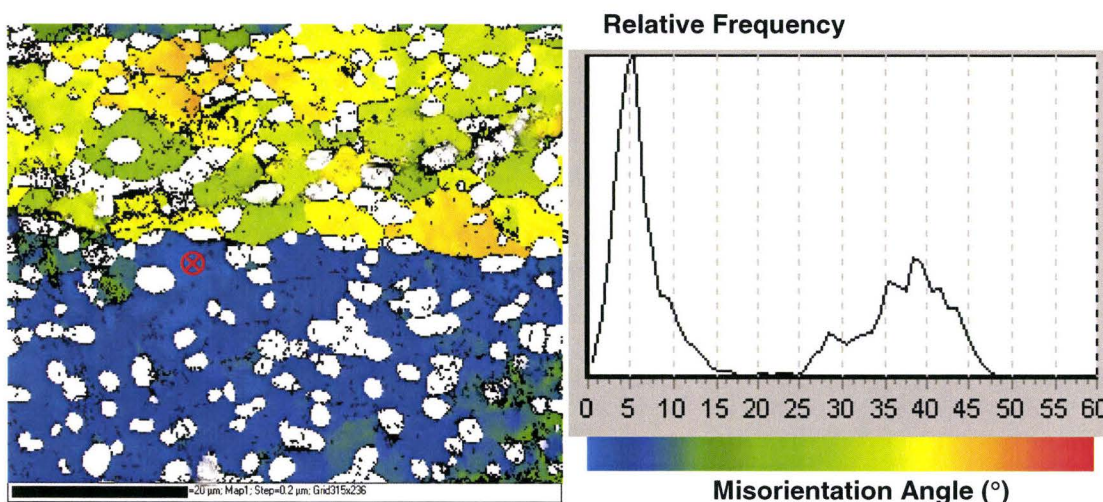
Figure 5.17: Grain misorientation map showing the relative frequency of grain misorientation angle (depicted by different colours per colour scale at bottom right) with the respect to the grain marked '⊗'.

A more precise analysis of the low angle grain boundaries can be conducted by taking a smaller, better mapped sub-region of the overall map, as that depicted in the contrast map presented in Figure 5.18 and labeled Region 1. The grain misorientation profile across three grain boundaries is shown as insets to the centre image. These profiles represent the changes in grain orientation along a straight line traversing the grain boundary. The profile plot displays changes in angle (°) in the ordinate versus distance in the abscissa (μm). The three grain boundaries analyzed provide further insight into their character; the large angle grain boundary is misaligned by 38°, while the low angle boundaries characterized are misoriented by approximately 3° and 5°, respectively.

The distribution of grain boundaries within Region 1 is presented as a histogram in Figure 5.19. This histogram portrays the relative frequency of misorientation angles encountered within Region 1. It is evident that the vast majority of the grain boundaries are misaligned by roughly 0.5° - 2°, with the highest misorientation being less than 10°.

The origin of the sub-grain structure observed is related to the thermo-mechanical work imparted onto the billet during forging. The last forging operations are carried out at a relatively low temperature in the α+β range. During this forging step considerable energy is stored in the material due to the increase in dislocation density. Upon further thermal steps, partial recovery gives rise to the fine-scale sub-grains structure observed.
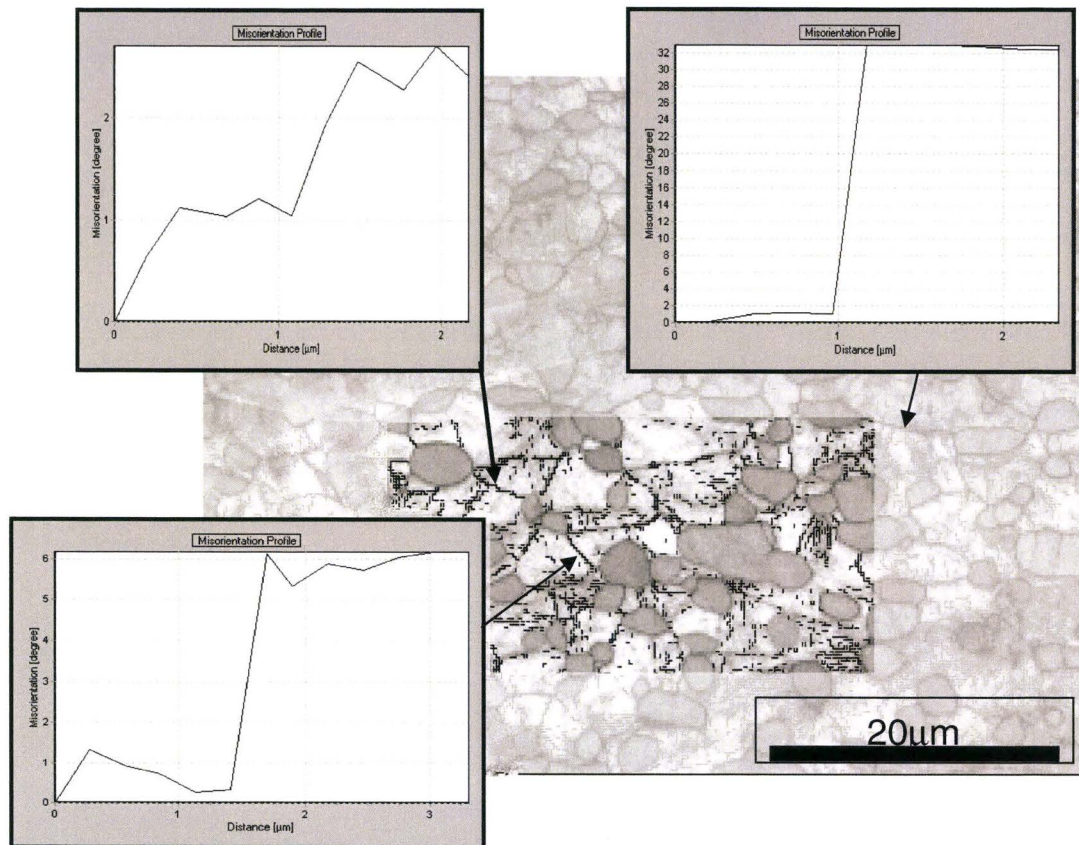
Figure 5.18: Contrast map; Region 1 is highlighted for clarity. The misorientation at three grain boundaries is shown.
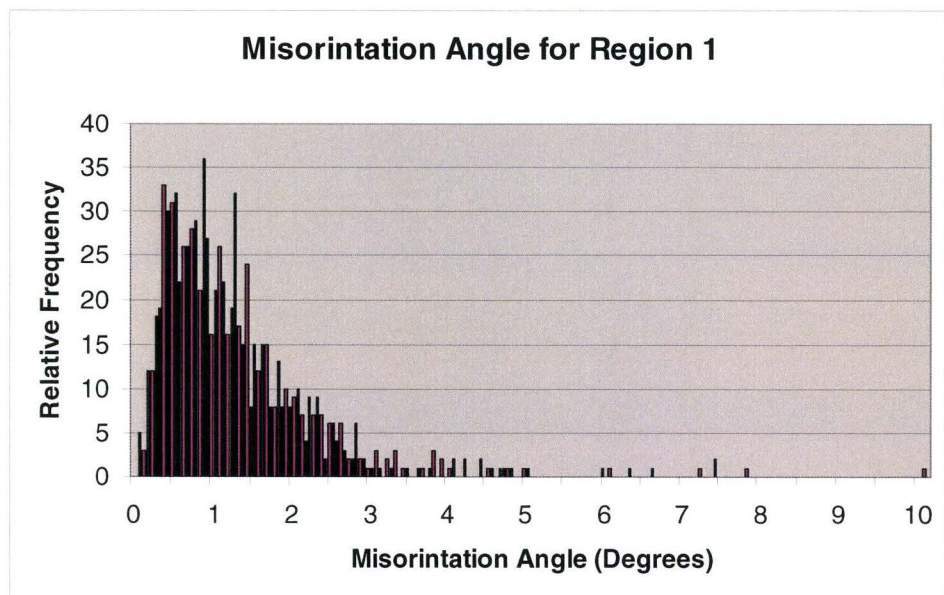
Figure 5.19: Histogram of grain boundary misorientation angles within Region 1.

A correlation between the primary α and retained β phase boundaries within Region was also characterized with respect to deviations from the Burgers' crystallographic relation:

$$(110)\beta \parallel (0001)\alpha,$$

This correlation function uses different colours to highlight phase boundaries which match closely the stated relationship. Figure 5.20 shows in red colour the boundaries which deviate 0 to 5° from the above relationship. This information suggests that the facets observed on the primary α particles could be the result of α/β grains surfaces aligned within small deviations from the Burgers relation. Accepting the above, these facets could be semi-coherent boundaries; however, additional crystallographic work would be required to confirm this point.

10μm
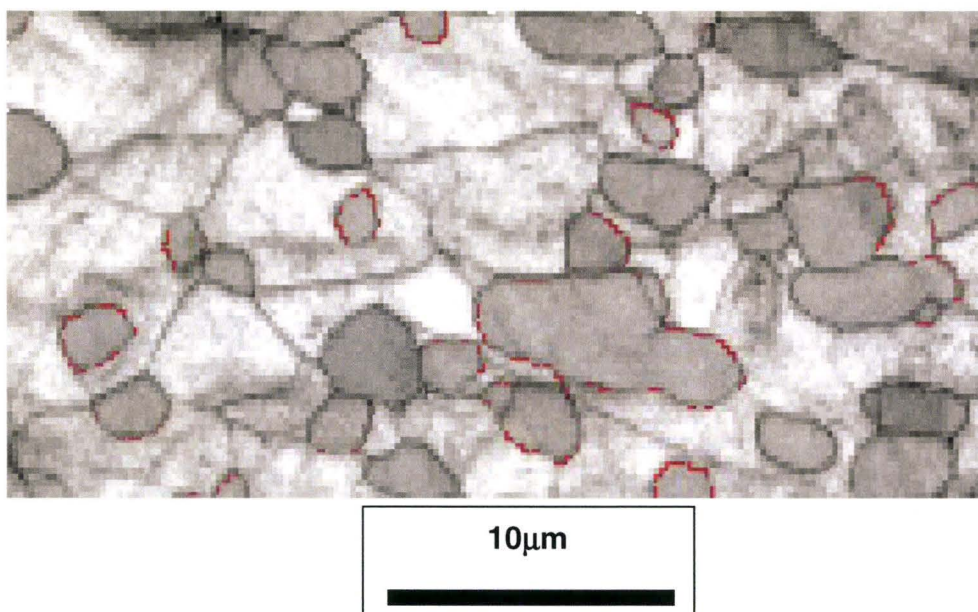
Figure 5.20:   Lattice correlation boundaries plot; red boundaries are those that are within a deviation of 5% from the Burgers' crystallographic relationship.

In summation, two salient microstructural features are resolvable by optical microscopy in the ST condition, these are: the globular primary α and the grain boundaries. Of the latter, there are high-angle prior β grain boundaries, and low angle grain boundaries.

Although ω-phase has been reported upon quenching from above the β transus, it is not clear from the Ti-5553 literature whether the ω-phase is present upon air cooling from the α-β temperature range. The following work is aimed at elucidating this important point.

5.2.1 Identification of the metastable ω-Phase

One of the most important aspects of the $\beta \rightarrow \alpha$ decomposition is the role played by metastable phases after solution heat treatment. In thermodynamic terms, metastable phases lower the energy barrier and ease the transformation of β to α by generally supplying nucleation sites. In doing so, the scale and distribution of the α precipitates can be profoundly affected. Electron transparent foils of the ST condition were prepared and examined in the TEM. Figure 5.21 is an image from jet polished foil depicting the primary α particles in a matrix of retained β, with the associated selected area diffraction (SAD) pattern from the [110]β zone axis.
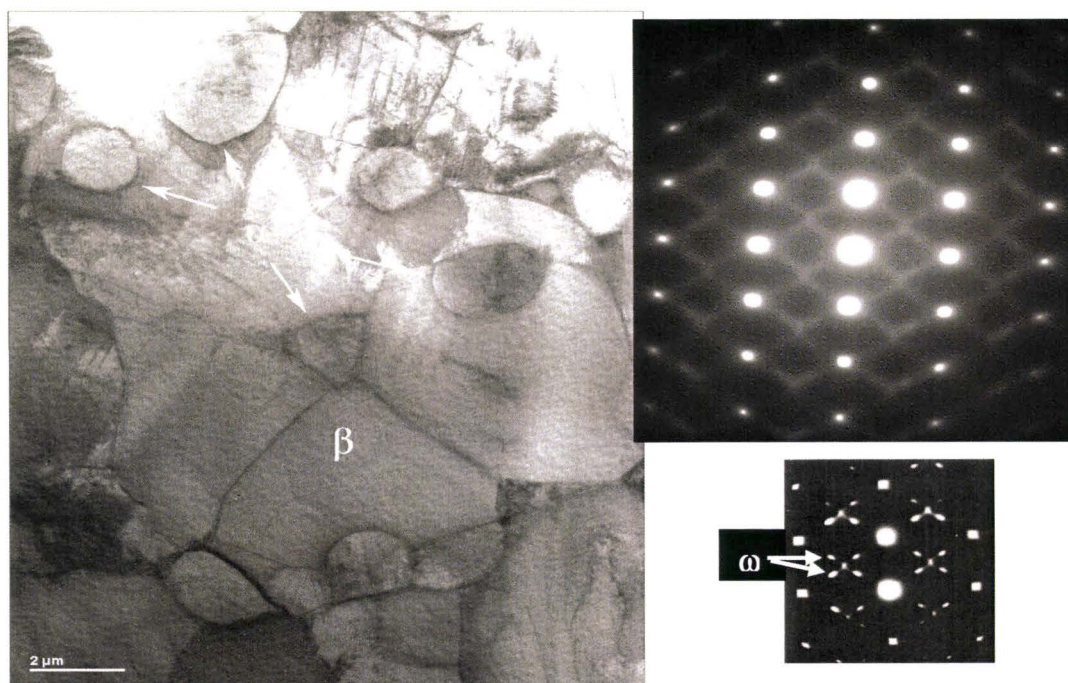
Figure 5.21:   TEM image of ST foil prepared by jet polishing, with associated SAD pattern for the β phase - [110]β zone axis, showing streaks between the primary reflections. SAD pattern at bottom right is from β-annealed Ti-10V-2Fe-3Al [36], showing locations of expected ω-phase reflections.

Although no discrete maxima reflections can be seen at the expected 1/3 and 2/3 points along the diagonal joining the β lattice plane diffraction maxima, diffuse streaking is evident along these directions. The presence of these streaks has been the subject of much investigation. Bowen [16], provides a concise explanation based on an extensive review of the literature. He states that there is consensus among researchers in that the streaking is the result of short-range correlated displacements due to (111)β plane collapse. The mechanism of ω formation was presented in Chapter 3.3.2, and involves a collapse of the pair of (111)β planes.

The streaking phenomenon is the result of the relatively small size and morphology of the ω-phase regions which create a short range modulation between the Hexagonal ω-phase regions and the BCC β matrix. The composition of the athermal ω is very similar than that of the quenched alloy. During ageing, noticeable changes in the lattice parameter of the β phase have

been reported [16]. These changes constitute solute partitioning involving solute enrichment of the β phase accompanied by a corresponding depletion on the ω phase. As the material characterized herein was fan-cooled from 790°C to ambient temperature within 15-20 minutes, the situation is closer to that encountered in the thermal ω. Although high resolution electron microscopy and chemical composition analysis would be required to confirm this effect in Ti-5553, a diffraction effect on the SADP of the β phase is consistently observed. It is reasonable to assume that this effect is due to solute partitioning, which would mean that the ω-phase regions are chemical and structural modulations in the β matrix lattice. Accounts of these modulations in the literature are often referred to as ω-precursor or diffuse ω. However, in this work the presence of these modulations will be referred to as ω-phase with an understanding that their size is relatively smaller in comparison to the thermally formed ω. Larger ω particles, as those normally associated with the thermally formed ω, present SAD patterns with discrete spots. [56] [4]

Patterns very similar to that presented in Figure 5.21 were reported by Jacques et al [44], in β-ST and quenched Ti-5553 and another β-titanium alloy, Ti-LCB (Ti-4.5Fe-6.8Mo-1.5Al), see Figure 5.22 (a) and (b).
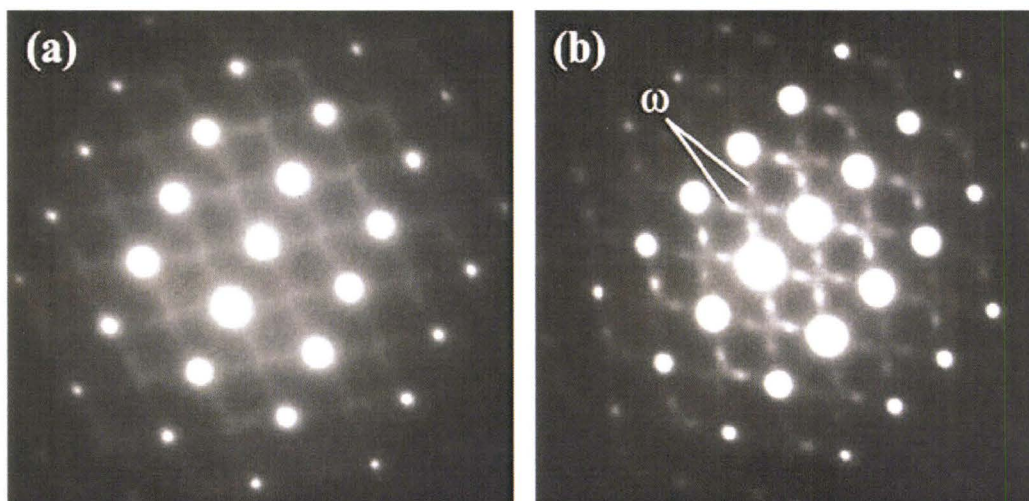
Figure 5.22: **Comparison of the [110]β zone axis SAD patterns for (a) Ti-5553 and (b) Ti-LCB in the β solution treated and quenched condition. Note the more distinct reflections from the ω phase on the Ti-LCB pattern.** [44]

Comparing the diffraction patterns for the β annealed condition, Ti-LCB displays discrete spots corresponding to the ω-phase, while Ti-5553 presents streaking. Jacques noted that although these two alloys have similar Mo-eq values, formation of ω phase in Ti-LCB is more "extended" than in Ti-5553. A rationalization for this variance was offered on the basis of the chemical composition differences between these alloys. Ti-LCB contains a higher Fe content (4.5 wt%) and much lower Al content (1.5 wt%). It is well accepted that formation of the ω phase is suppressed in alloys with significant Aluminum content. Williams et al. [48], showed that Al, O, Sn and Zr all suppress the formation of ω-phase. In the case of Al and O, their influence is to accelerate nucleation of the α phase, while Sn and Zr tend to stabilize the β phase. A more in depth account of the influence of these elements the ω phase in Ti-5553 is presented in the Discussion section at the end of this Chapter.

5.2.2   Microstructure evolution with ageing at 600°C

Mechanical property optimization studies conducted during this work demonstrated that ageing in the temperature range of 550-650°C provides a good balance of tensile strength and ductility. The following is a summary of the heat treatment cycles for which the microstructural changes will be presented:

- α-β solution treatment at 790°C for 2 hours
- Fan cooling to room temperature
- Ageing at 600°C for interval of:
  - 5, 10, 15, 20, 30, minutes;
  - 1 – 8 hrs with increments of 1 hr.
  - 13, 18, 24 and 48 hours.
- Air cooling to room temperature
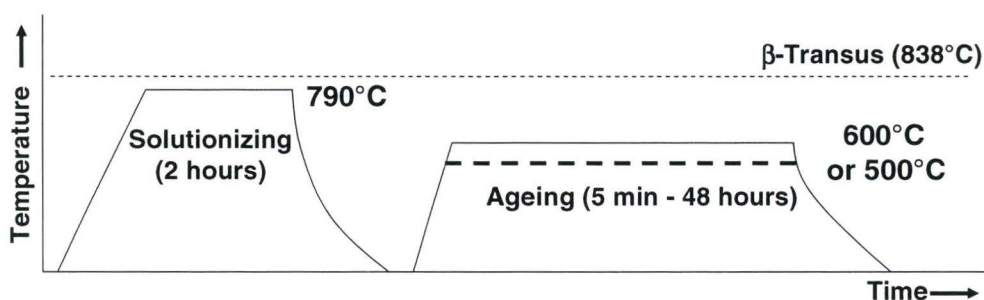
Diagram 5.9:   Graphic Illustration of the ST and Ageing Cycles.

In an effort to simplify the presentation of results, only the salient microstructures will be shown. Etching times can have a profound effect on the appearance of the microstructure; to minimize these effects, all specimens were etched at the same time for 7 seconds.

The microstructure resulting from ageing at 600°C for 15 minutes is presented in Figure 5.23.

Significant darkening of the retained β phase regions can be observed optically with etching, Figure 5.23 (a), but the transformation is non uniform with untransformed regions remaining. A better appreciation of the morphology and scale of the etched α precipitates can be gained from the SEM images, Figure 5.23 (b) and (c).

The slender, needle-like etched depressions correspond to the α precipitates dispersed among spherically-shaped depressions left by etching of the primary α particles. As noted for the microstructure of the ST condition, Figure 5.15 (c) and (d), the primary α contain facets becoming apparent at higher magnifications, see Figure 5.23 (c).
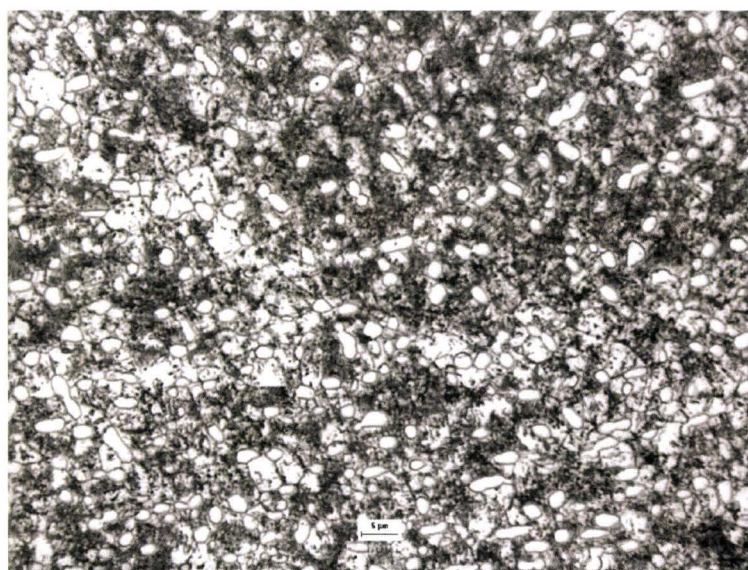
(a)
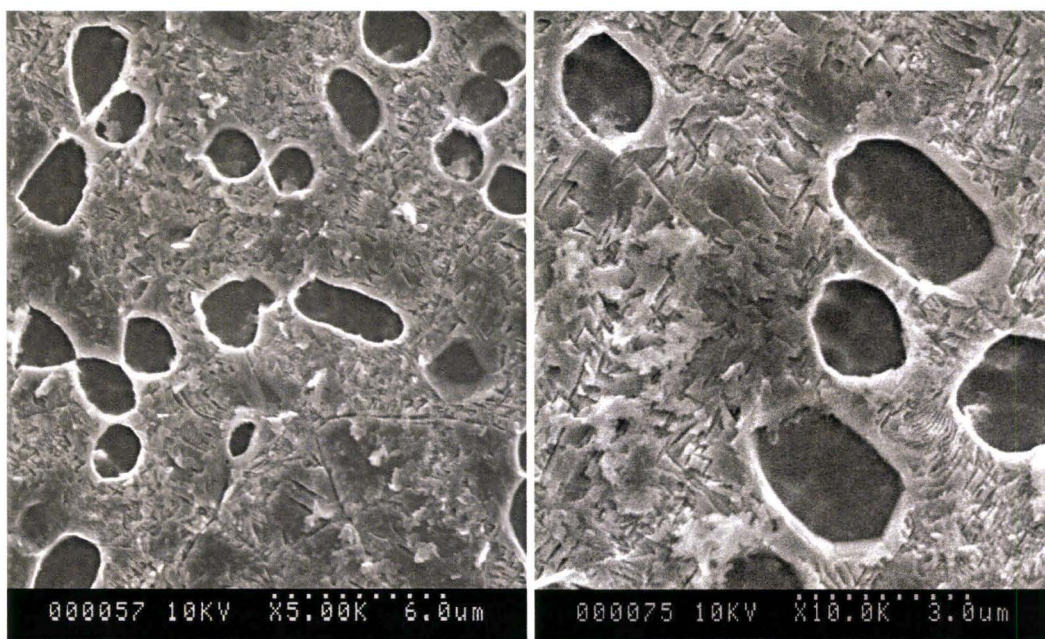
(b)

(c)

Figure 5.23: **Microstructure of ST specimen after ageing at 600°C for 15 minutes; (a) Optical image, (b) and (c) secondary electron images. Etched in Kroll's reagent**

In order to resolve the fine scale microstructure of the aged β, transmission electron microscopy of specimens aged for 20 minutes was conducted. Figure 5.24 presents the microstructure at two magnifications. The aged β matrix contains a number of α needles measuring several micrometers in length, but as highlighted by the dotted ellipse, a greater number of much smaller and closely spaced needles can also be resolved. At higher magnification, image at right, the larger α needles seem to contain internal structure. The nature of this structure will be addressed in the Discussion section.
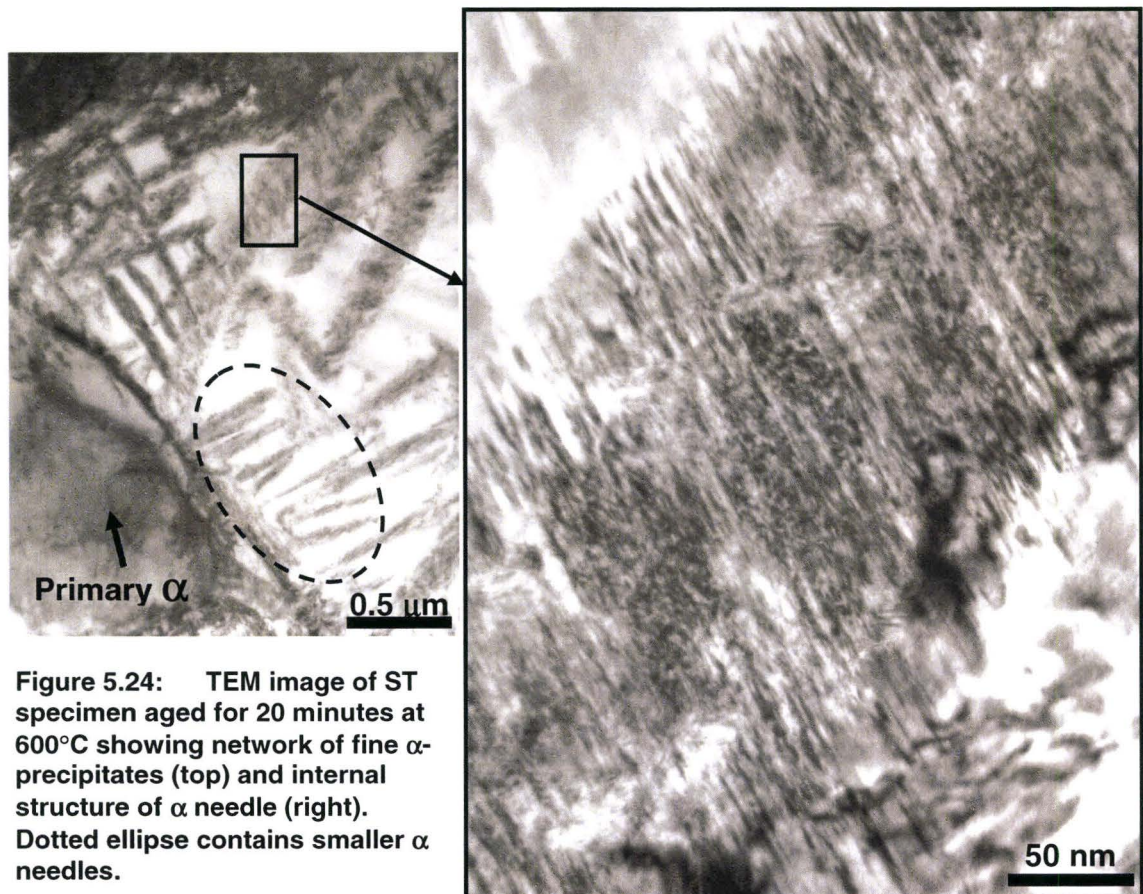
Figure 5.24: **TEM image of ST specimen aged for 20 minutes at 600°C showing network of fine α-precipitates (top) and internal structure of α needle (right). Dotted ellipse contains smaller α needles.**

After ageing for 60 minutes, darkening of the entire retained β phase regions is optically evident, indicating that complete transformation to α have occurred, see Figure 5-25 (a).
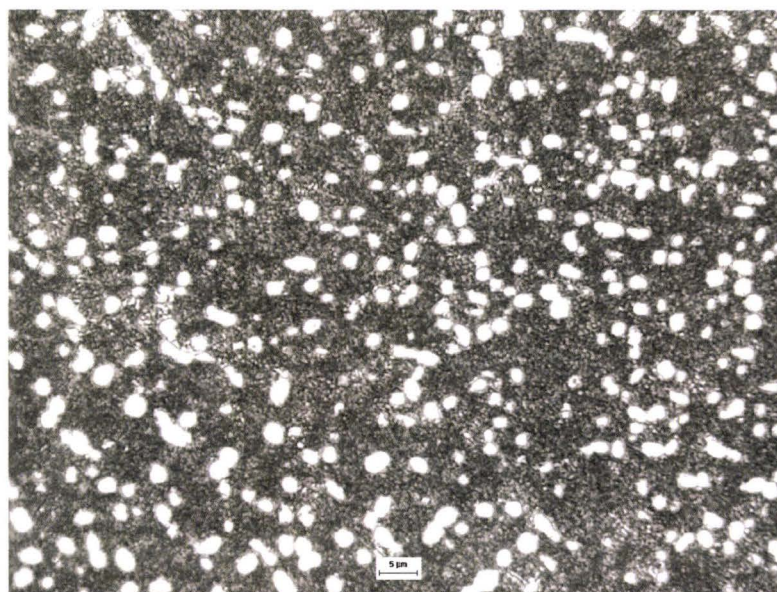
(a)
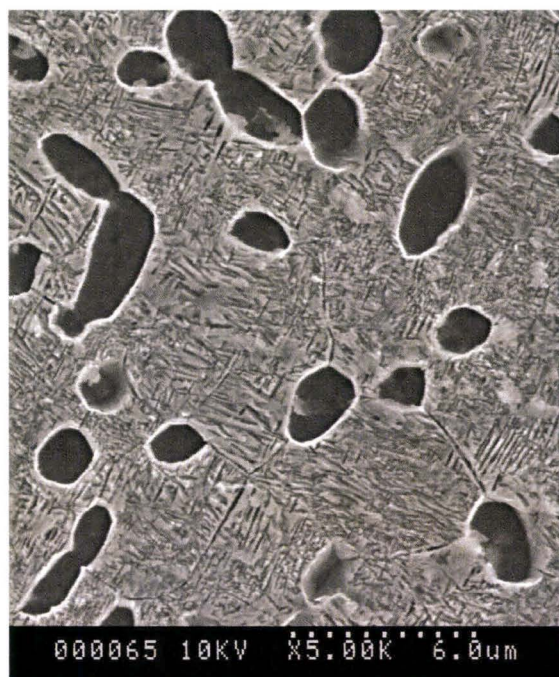
(b)

(c)

Figure 5.25: Microstructure of the ST specimen after ageing at 600°C for 60 minutes; (a) Optical image, (b) and (c) secondary electron images. Etched in Kroll's reagent

Under the SEM, Figure 5.25 (b) and (c), laths of fine scale, uniform α needles can be resolved. The grain boundaries appear as linear demarcations connecting the primary α globules, see Figure 5.25 (c).

The microstructure after ageing for 6 hours at 600°C is presented in Figure 5.26. Comparing Figures 5.25 (a) and 5.26 (a), it is evident that the microstructures are optically identical. However, under the SEM, coarser laths of precipitated lenticular α needles are evident and the grain boundaries appear as wider channels.

(a)

(b)

(c)
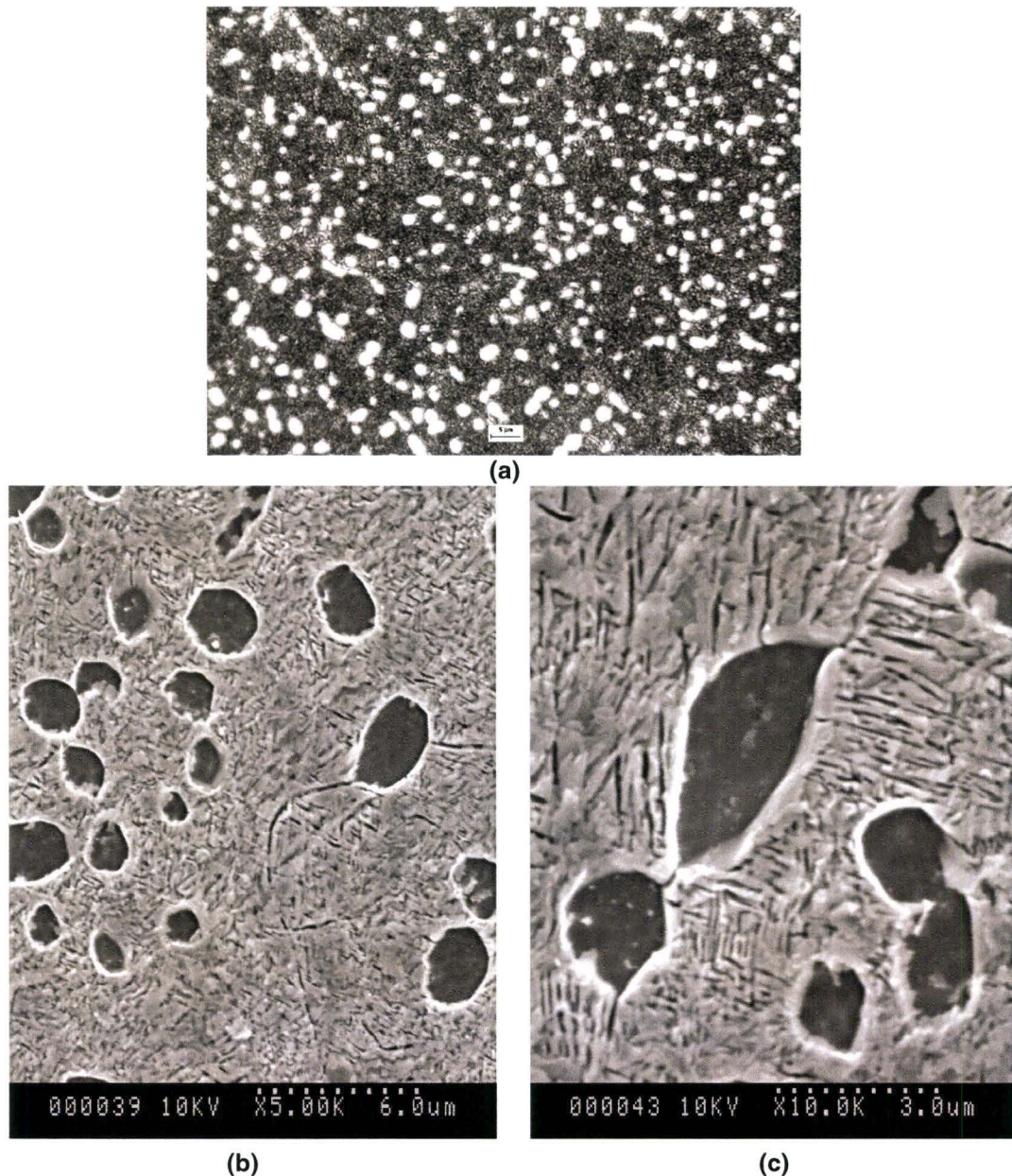
Figure 5.26:   Microstructure of the ST specimen after ageing at 600°C for 6 hours; (a) optical image, (b) and (c) secondary electron images. Etched in Kroll's reagent

TEM images of the microstructure at progressively higher magnifications are presented in Figures 5.27 and 5.28. It is clear from Figure 5.27 that a continuous α film is present along grain boundaries and surrounding the primary α particles. The appearance of these films explains why, after etching, the grain boundaries appear as grooves or channels which widen with increased ageing time.

Figure 5.28 presents the appearance of the matrix, with fully formed lenticular α needles in a lath arrangement. Note that the α needles are relatively uniform, measuring 1-3μm in length; furthermore, the smaller α needles present in the aged β matrix at 20 minutes ageing (see Figure 5.24) have totally disappeared. These observations suggests that evolution of the microstructure with increasing ageing time involves coarsening of the α needles and growth of α films along grain boundaries and around the primary α.
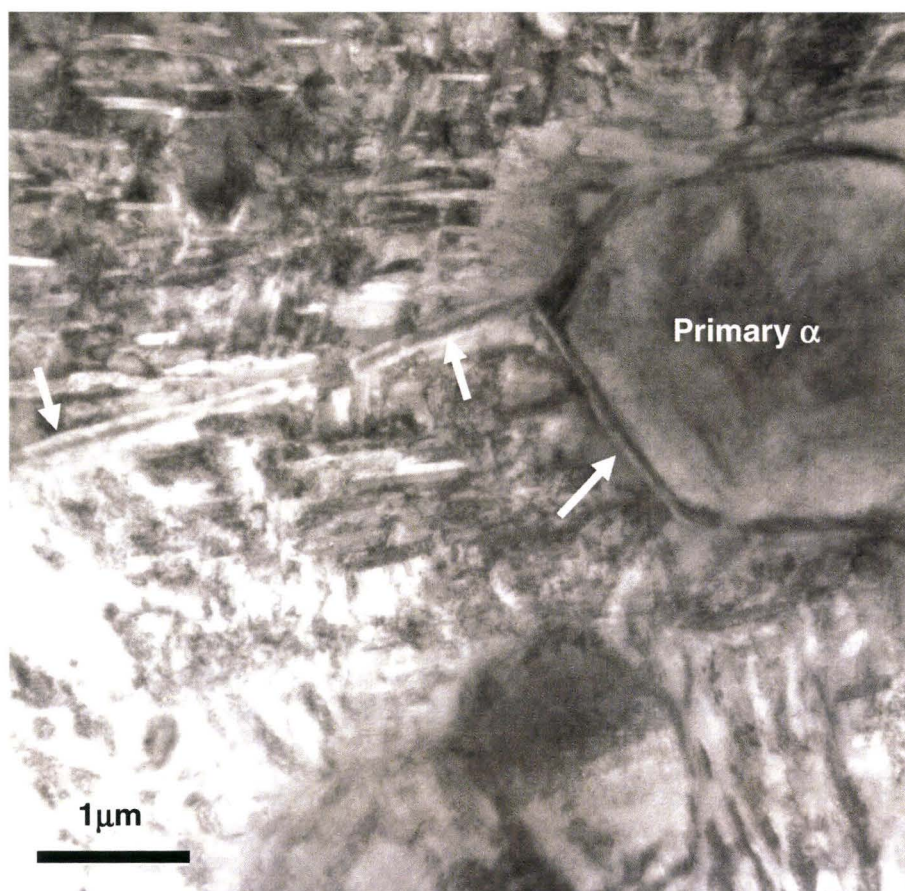
Figure 5.27: **Bright field TEM image of the ST specimen aged at 600°C for 6 hours showing a continuous α film along the grain boundaries and surrounding the primary α particles (white arrows).**
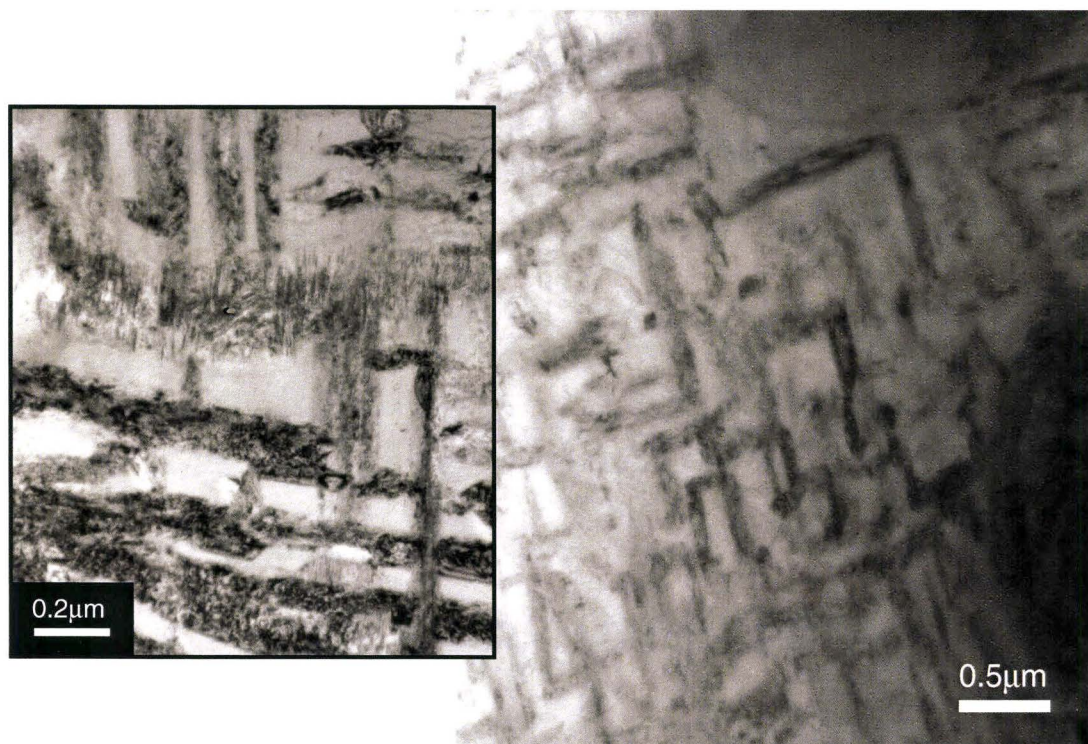
Figure 5.28: **Bright field TEM image of the ST specimen aged at 600°C for 6 hours showing the laths of lenticular α at two magnifications.**

With continued ageing the aged β microstructure continues to coarsen. Due to the inability to resolve the fine-scale α laths optically, only SEM images of the microstructure aged for 48 hrs are included. Relatively insignificant changes could be observed by doubling the ageing time from 24hrs to 48 hours.

Under the TEM, lenticular "stubby" α needles measuring 1-3μm in length and 0.2μm in width could be resolved and are shown in Figure 5.30. Continuous films of α, measuring approximately 0.2μm in thickness, are also visible along the grain boundaries, see arrows in Figure 5.30. The mechanism of formation of these films and a rationalization of the evolution of the ST microstructure will be discussed at the end of this Chapter.

Characterization of the microstructure after solution heat treatment and fan-cooling from the α-β temperature range has been presented. The microstructural changes which occur with ageing at 600°C were also characterized at time intervals ranging from 5 minutes to 48 hours. From these results, a clear pattern of β decomposition emerges: it begins with precipitation of fine scale acicular α throughout the retained β matrix; once the complete transformation to α has occurred, the α needles coarsen and α films grow along grain boundaries.

The following sections will explore the microstructural changes with annealing above the β transus temperature.
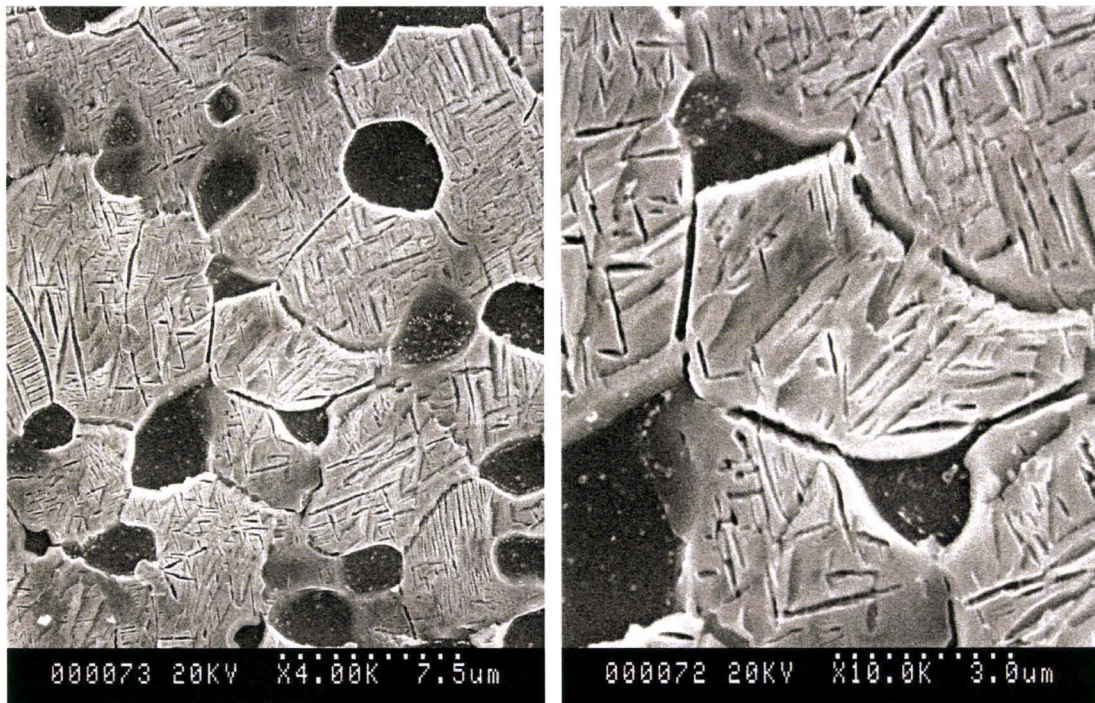
Figure 5.29: Secondary electron images of the ST specimen after ageing at 600°C for 48 hours, as viewed at 4,000 (right) and 10,000X (right). Etched in Kroll's reagent

Figure 5.30: Bright field TEM image of the ST specimen aged at 600°C for 48 hours. The white arrows point to continuous α films along grain boundaries (arrows).

The preceding sections explored the microstructural changes occurring with thermal cycles performed above and below the β transus temperature. Characterization of the as-cooled microstructure involved the identification of metastable phases. Subsequent to the characterization of the as cooled (fan-cooled) microstructures, various ageing cycles were performed and the evolution of the microstructure presented.

For the β annealed heat treatments, the rate of cooling from the annealing to the aging temperatures was varied from water quenching to a controlled furnace cooling. The nature and scale of the resulting α precipitates varied greatly. Sub-micron acicular α was predominant after fast cooling, while a much coarser microstructure consisting of lamellar α "ribbons" prevailed with controlled furnace cooling.

For the α-β solution cycles, the microstructure was characterized after solution heat treatment and after at various ageing times ranging from 5 minutes to 48 hours. Complete transformation of the retained β phase occurred after approximately 30 minutes, with coarsening of the precipitated α phase occurring commensurate to the ageing time. Continuous films of α are seen to form and grow along the grain boundaries and surrounding the primary α particles.

An in depth discussion of these results, focusing primarily with the nucleation and growth of the α phase during the various heat treatments is provided in the following section.

5.3   Discussion of the Microstructure Evolution

5.3.1   Thermodynamic-based equilibrium phase predictions

A description of the microstructure evolution, must first consider which phases are possible under equilibrium conditions. As discussed in Chapter 1, limited work has been published on phase transformations for Ti-5553, but even less phase equilibrium work has been published. Although equilibrium conditions rarely exist in an industrial context, a prediction of the possible phases which exist in equilibrium can be made by means of thermodynamic calculations. To accomplish this task, Thermo-Calc software using the TTTI3 - Thermotech Titanium database Version 3 were employed. The software uses the thermodynamic data in the TTTI3 database to calculate the mole fraction of each possible phase with changing temperature. Although the details of the calculations performed by the software are proprietary, the principle of the program is to establish the minimum Gibb's free energy under conditions of constant temperature, pressure and composition. [51]

Results of the thermodynamic predictions are presented in the form of % mole fraction of each possible phase versus temperature plots for a given alloy composition and are termed phase portraits. For all calculations the pressure was kept constant at one standard atmosphere or 101.325 kPa. Because the composition range for Ti-5553 is relatively wide and 5 principal alloying elements are involved, a sizable range of compositions would have to be considered. Nonetheless, for the purposes of predicting possible phases, three compositions were considered for the calculations. These compositions included all alloying elements at the low and high end of the compositional limits, as well as the composition for the heat of material characterized in this thesis (Heat 8-42-2034). Table 5.1 presents the three compositions studied and the accepted chemical composition range for Ti-5553.

Table 5.1:   **Chemical Composition Range for Ti-5553 and Compositions Used in Calculations.**

Element	Al	V	Fe	Mo	Cr	Zr	O2	C
Ti-5553 Weight % Range	4.4 - 5.7	4.0 - 5.5	0.30 - 0.50	4.0 - 5.5	2.5 - 3.5	0.30 max	0.18 max.	0.10 max.
Low Range Comp.	4.4	4.0	0.3	4.0	2.5	0.0001	0.1	0.001
High Range Comp.	5.7	5.5	0.50	5.5	3.5	0.3	0.18	0.1
Heat 8-42-2034 Comp.	5.38	5.01	0.32	5.04	2.79	0.002	0.15	0.007

The results of the Thermo-Calc calculations for the three compositions in Table 5.1 are presented in Figures 5.31, 5.32 and 5.33. For the Low Range Composition, the β phases (BCC) and liquid are prevalent at a temperature of approximately 1689°C, corresponding to the melting temperature of the alloy (lines 1 and 3). In the temperature range of 400 - 680°C the α(HCP) and β(BCC) phases are prevalent (lines 1 and 2). Small mole fractions of C15-FCC structure (line 4) and Ti$_3$Al (line 5) are present in the temperature range of 400 -500°C. Ti3Al, commonly known as α_2, has been found to posses the DO19 structure, a unit cell composed of 4 regular HCP cells apparently supported by covalent-like directional bonds connecting the aluminum and titanium atoms [23]. As for C15-FCC, this is the Strukturbericht designation, for an A$_2$B type phase having FCC structure, A and B representing Cr and Ti. [53].
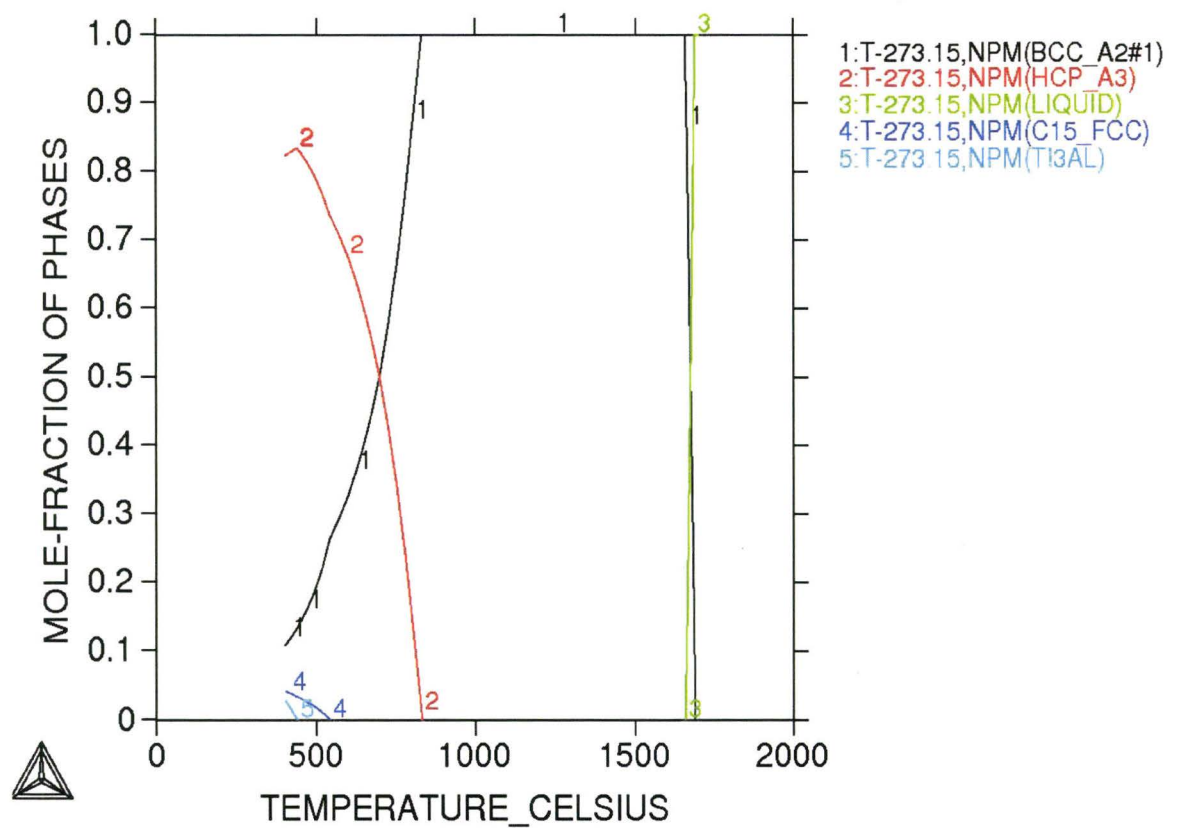
Figure 5.31:   Phase portrait for Low Range composition per Table 5.1.

A similar phase portrait was obtained for the High Range composition and is presented in Figure 5.32. The mole fractions of C15-FCC (line 5) and Ti_3Al (line 6) are higher and the are stable to higher temperatures, in the case of Ti_3Al, the phase is stable up to 720°C and a maximum mole fraction of 0.22% was calculated at a temperature of 400°C.
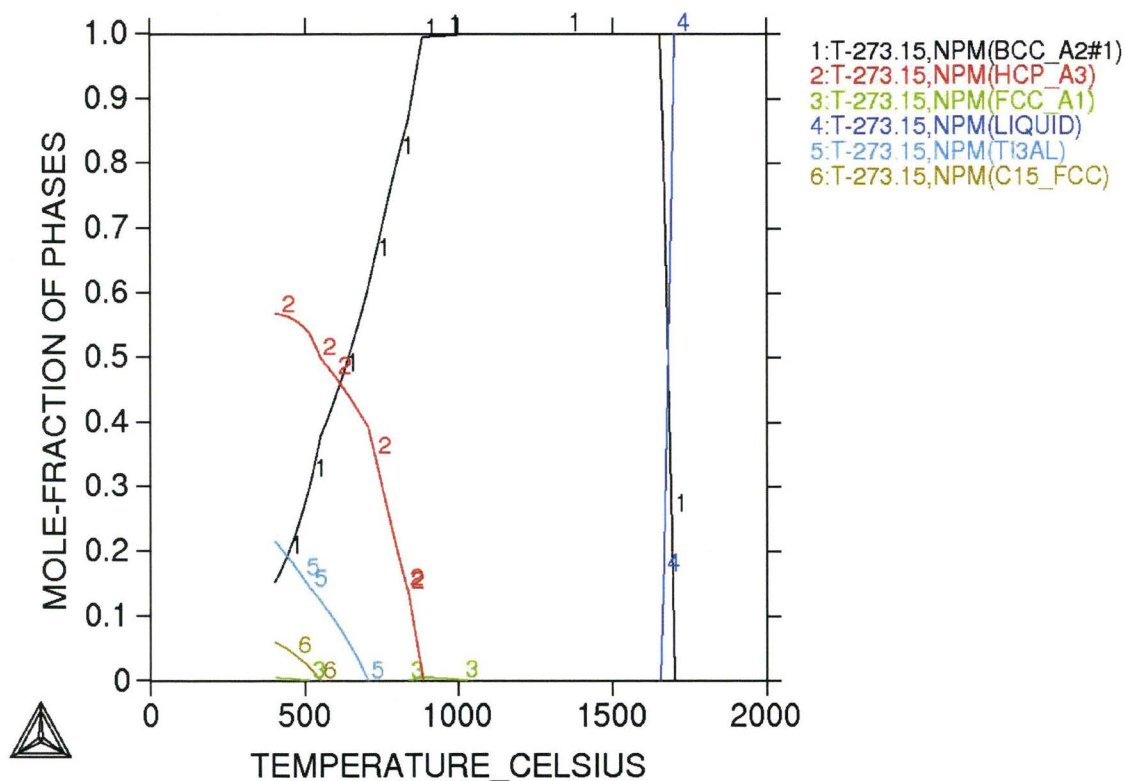
Figure 5.32:   Phase portrait for High Range composition per Table 5.1.

According to Figure 5.32, small amounts of Ti–FCC structure (line 4) are predicted for the 400-500°C and 800-1000°C temperature ranges. However, the mole fractions predicted are so small (>0.01%) that its presence under non-equilibrium conditions is extremely unlikely.
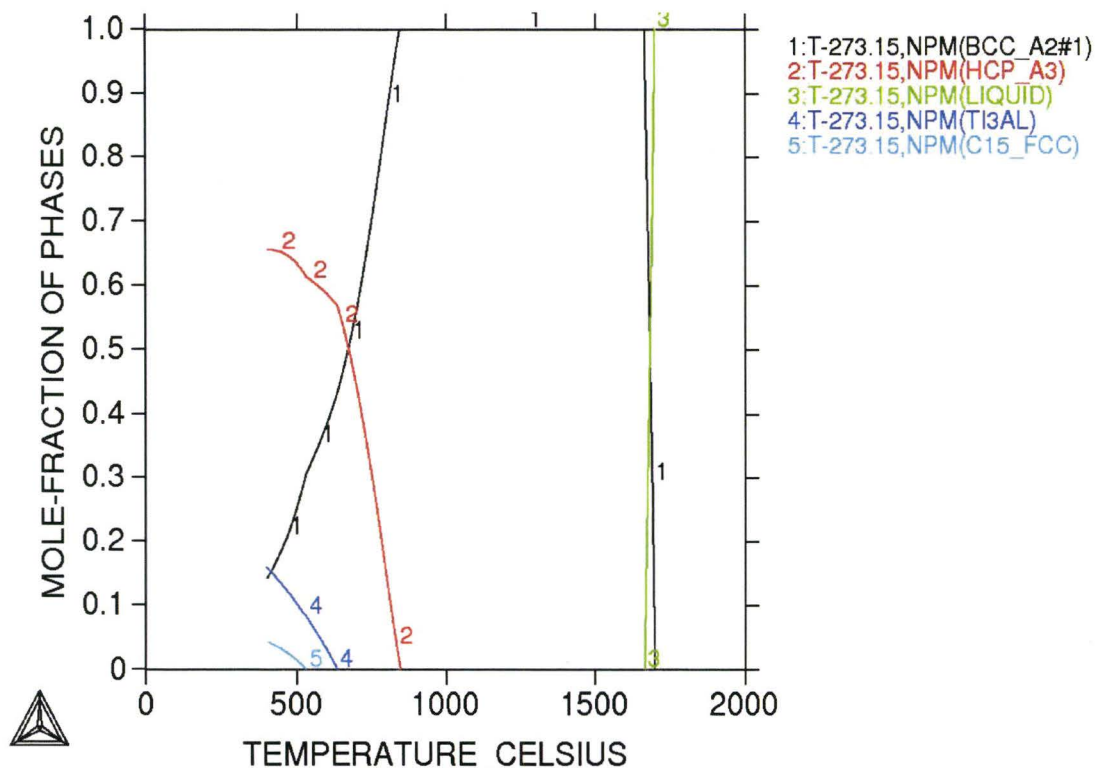
Figure 5.33: **Phase portrait for Heat Number 8-42-2034 per Table 5.1.**

The phase portrait for Heat 8-42-2034 is presented in Figure 5.33, which contains mole fractions of the C15 FCC and Ti_3Al phases between the Low and High Range compositions predictions. For the Ti_3Al phase a mole fraction of approximately of 1.7% is predicted at 400°C.

Two conclusions can be drawn from the above diagrams: 1) the Ti_3Al phase would be expected at relatively low cooling rates or conditions approaching equilibrium; and 2) the probability of the Ti_3Al phase formation is higher for compositions in the high end of the limits. The above predictions are consistent with recent reports of Ti_3Al formation in Ti-5553 in the literature. Cotton, et al.[31] reported small amounts of Ti_3Al phase precipitates when slow cooling in a furnace from above the β transus and ageing for several hours below 600°C. The presence of relatively high levels of Al in the alloy is also expected to favour formation of Ti_3Al precipitates.

The thermodynamic predictions presented above provide an insight into the possible phases for Ti-5553. Armed with this knowledge, it is now possible to begin to quantify the scale of the microstructural features in an attempt to relating them to the mechanical properties.

5.3.2   Quantification of Microstructural Features

In order to properly appraise the impact of the microstructure on mechanical properties, it is important to determine the scale of the microstructural features resulting from the heat treatments discussed earlier. A discussion of the considerations and assumptions in relation to the relative accuracy of the features measured is presented concurrently.

5.3.2.1 Heat treatments conducted above the β transus

Subsequent to β annealing the microstructure consists of re-crystallized β grains with a fine dispersion of ω and α precipitates. Upon ageing in the α-β temperature range, the retained β phase transforms to α, the scale of the precipitates varies with cooling rate and ageing time. The salient microstructural features for the β annealed and aged conditions have been characterized in detail; the grain size and scale of the precipitates are summarized in Table 5.2 for three conditions,

Table 5.2:   Scale of Microstructural Features for β Annealed and Aged Conditions.

Heat Treat Condition	Grain Size (μm)	Precipitates
β Annealed (903°C-75 min - fan-cool)	190	ω - >10 nm α - 10-20 nm
β Annealed (903°C-75 min – water quench)	190	ω - >10 nm
β Annealed and ST (903°C-75 min - fan-cool; 790°C 2 hrs – fan-cool)	190	Acicular α 0.5 - 2 μm long
β Annealed, Controlled Cool and Aged (903°C-75 min– cool at 1.0°C/min, aged at 600°C 8 hrs)	190	Lamellar α 2μm wide10-30 μm long

It can be deduced from Table 5.2 that the β grain size does not change with ageing time, however, a continuous grain boundary α film, similar in scale to the intra-grain α develops. The effect of this film on mechanical properties will be discussed in the next Chapter.

5.3.2.2 Heat treatments conducted below the β transus

Two microstructural features are predominant in the ST condition: the primary α particles and the grain boundaries. As confirmed by the EBSD work presented earlier, the great majority of the grain boundaries are low angle, many of which have a misorientation of 1° or less. Grains which are misaligned by less than 2° are likely to have limited contribution to the material strength and hence, grain size estimations have exclude these. A comparison between EBSD analysis of the grain misorientation and the optical micrographs, confirmed a good correlation between the optical detection of etched grain boundaries and a grain misorientation greater than 2°. Accordingly, calculations of grain size conducted by optical means are based on grain misorientations greater than 2°.

The size and aspect ratio of the primary α varied slightly between the longitudinal and transverse direction. However, in the transverse direction, the size of the α particles was in the range of 3-5μm, and the grain size was of the order of 2-4μm in diameter.

An attempt to measure the volume fraction of primary α by means of digital image manipulation resulted in values from 13.4 to 22.1%, depending on the criteria set to resolve the edge of the α particles and the error associated with grain boundaries. A "decoration" age step, which consisted in ageing at 600°C for 20 minutes, was used to darken the background and facilitate the area separation by pixel contrast. This technique yielded a primary α volume fraction of 16.5%. This value is in line with work by Fanning, et. al. *[24]*, which reported 16% primary α, also determined metallographically, after solution heat treating Ti-5553 at 804°C for 3 hours.

It is possible to calculate the % primary α from the pseudo binary phase diagram. Cotton, et al *[31]*, created an approximate pseudo-binary diagram for Ti-5553 by holding specimens at various temperatures for 40 minutes and air cooling. The samples were polished and the compositions of the primary α and the retained β were measured by electron microprobe analysis (EMPA) and converted to Mo equivalents. This diagram is reproduced in Figure 5.34. The concept of equivalent Mo and Al content is useful in terms of reference to a pseudo-binary phase diagram. As discussed in Chapter 3.1.1, the equivalent Mo and Al content for a multicomponent titanium alloy are given by the following formulae:

[Mo]-eq = [Mo] + 1/5[Ta] + 1/3.6[Nb] + 1/2.5[W] + 1/1.5[V] + 1.25[Cr] + 1.25[Ni] + 1.7[Mn] + 1.7[Co] + 2.5[Fe]

[Al]-eq = [Al] + 1/6[Zr] + 1/3[Sn] + 10[O]

The Mo and Al equivalencies of the heat of material used in this work are presented in Table 5.3.

Table 5.3   Composition of Ti-5553 Heat No 8-42-2034 Calculated Mo and Al Equivalents.

Sampling Location	Chemical composition for Ti-5553-Heat No 8-42-2034 (wt%)							Comp. Equivalents	
	Al	**V**	**Fe**	**Mo**	**Cr**	**Zr**	**O$_2$**	**Mo-eq**	**Al-eq**
Top	5.43	5.18	0.34	5.12	2.86	0.003	0.148	13.0	6.8
Bottom	5.34	4.84	0.30	4.96	2.73	0.008	0.151	12.4	6.9
Average								12.7	6.9

Placing the Mo-eq average from Table 5.3 in the diagram presented in Figure 5.34, it is possible to estimate the volume fraction of primary alpha by using the lever rule. At the solutionizing temperature, the predicted volume fraction of primary α is roughly 10%, which is significantly less than the 16.5% measured metallographically from the ST specimens. This discrepancy can be explained in terms of the inaccuracies associated with the EMPA technique, the errors with the Mo-eq approximations and the fact that the specimens were soaked for 40 minutes. Specimens in this work were soaked for 3 hours which would have allowed more time for diffusion of the α and β stabilizers. Although, the approximate diagram in Figure 5.34 is quite useful in illustrating the transformations taking place in Ti-5553, it must be used with caution when attempting to estimate the volume fraction of primary α. As the values derived from optical image analysis represent direct measurements on many fields of view, these values are deemed to be more accurate.
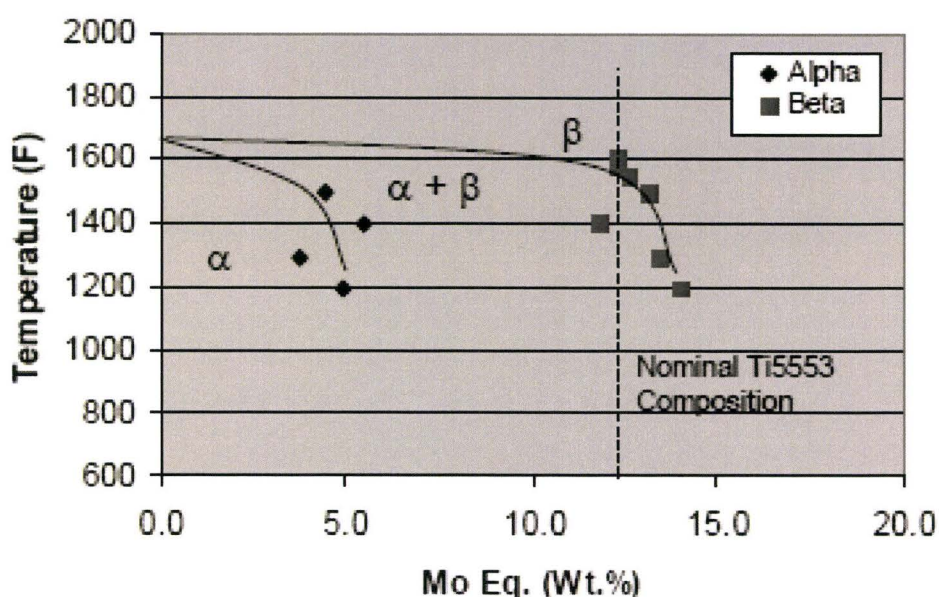
Figure 5.34:   Approximate pseudo-binary phase diagram for Ti-5553. *[31]*

With ageing, the retained β transforms to a fine scale acicular α precipitate, the size of this phase is dependent on ageing temperature and ageing time. For the purposes of quantifying this phase and relating it to the strength, the peak strength condition has been characterized in detail. Table 5.4 presents a summary of the relevant microstructural features in the ST and ST and aged conditions.

Table 5.4:   Scale of Microstructural Features for ST and ST +Aged Conditions.

Heat Treat Condition	Macro-Grain Size	Micro-Grain Size	Primary α		Lenticular α
	(Range in μm)	(Range in μm)	(Range in μm)	Vol.(%)	(μm)
ST condition (790°C-2 hrs, fan-cool)	500-800 (transverse)	2-4	3-5	16.5	No α (ω - >10 nm)
ST and Aged (Aged 20min at 600°C)	500-800 (transverse)	2-4	3-5	16.5	Diam. – 0.15 Length – 1-3
ST and Aged (Aged 6 hrs at 600°C)	500-800 (transverse)	2-4, GB α 0.1	3.2-5.5	17.5	Diam. – 0.2 Length – 1-3
ST and Aged (Aged 48 hrs at 600°C)	500-800 (transverse)	2-4, GB α 0.3	3.5-6.0	19.6	Diam. – 0.3 Length – 1-3

One characteristic common to both, the ST and β annealed heat treatments, is the abundance of nano-scale ω precipitates after cooling from near the β transus. Diffraction patterns with diffuse scattering due to ω and comparison to other β titanium alloys with similar Mo-eq *[44]* suggest that ω phase formation is suppressed in Ti-5553. As the precipitation of α is linked to nucleation at ω sites, a possible explanation for the suppression and scale of the ω phase in Ti-5553 is discussed next.

5.3.3   On the suppression and scale of the ω phase

The effect of Al additions on Ti-20%V alloy is presented in Figure 5.35, where the volume fraction of ω is shown to decrease with increased Al content. This graph illustrates that aluminum, a strong α stabilizer, suppresses formation of the ω phase. A similar trend of ω phase suppression is expected for increased levels of oxygen. It is important to note that the heat treatment for the material characterized in this work was done in air, which unavoidably results in elevated levels of oxygen. Approximately 50μm of oxygen-rich α case was observed on the periphery of all heat treated specimens, attesting to Oxygen pick up during heat treatment. Both, the relatively high Aluminum content in Ti-5553 and the effect of Oxygen pick up during heat treatment would account for a very fine scale ω precipitates and for the diffuse scattering observed in the diffraction patterns.

Given that the cooling time resulting from fan-cooling was approximately 15-20 minutes, the ω-phase can not be considered athermal, since considerable diffusion is expected during the cooling process.
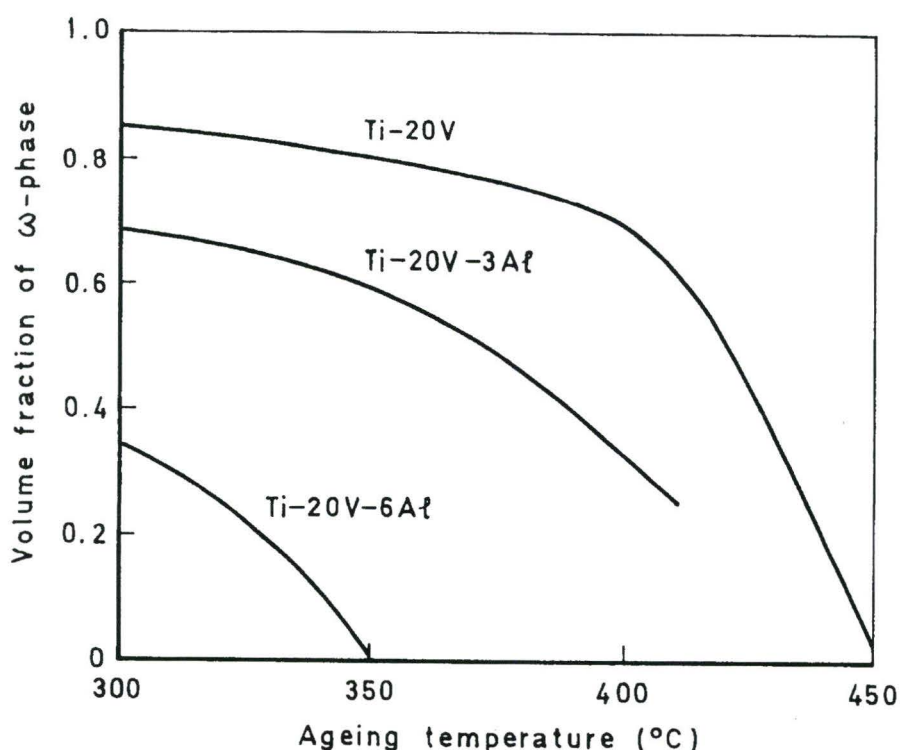
Figure 5.35:   Effect of the Al additions on the volume fraction of athermal ω-phase in Ti-20%V upon ageing between 300°C and 450°C. [16]

In summary, the diffraction pattern associated with the retained β phase resulting from sub-transus solution heat treatment displayed streaks rather than discrete spots. The streaks in the [110]β diffraction pattern were discussed extensively in Section 5.2.1, and are attributed to diffuse scattering from the nano-scale ω-phase. Imaging evidence of ω-phase resulting from β annealing and fan-cooling was presented in Section 5.1.1.

5.3.4 The Role of the ω Phase on the Nucleation of the α Phase

It has been confirmed in the literature *[47]* that the ω phase acts as nucleating sites for the precipitation of α. However, it must be noted the ω phase is unstable at high temperatures, quickly dissolving at temperatures above 500°C. Although evidence of ω has been found after a 5 minutes ageing at 600°C, these times represent heating times and not time at temperature. As the specimens had not yet reached 600°C after 5 minutes, the presence of ω may be short-lived or non existent at 600°C. Hence, it was not clear whether or not the ω phase plays a role on the number of nucleation sites and the final scale of the precipitated α.

To clarify this point, two sets of specimens were prepared by first solutionizing at 790°C: one specimen was fan-cooled to precipitate the ω phase, the other was cooled directly to the ageing temperature avoiding the ω phase altogether. The microstructures as viewed under the SEM for both specimens after 20 minutes ageing at 600°C are presented in Figure 5.36. It is clear from these images that the final scale of the precipitated acicular α is nearly identical. From the above, it can be concluded that the presence of ω phase after solution heat treatment and fan-cooling plays no role on the scale of the precipitated α - when ageing at 600°C. This finding is of importance as all industrial heat treatments for Ti-5553 involve ageing in this temperature range.

20.0kV 10.5mm x5.00k SE   10.0um   20.0kV 11.3mm x5.00k SE   10.0um

(a)   (b)
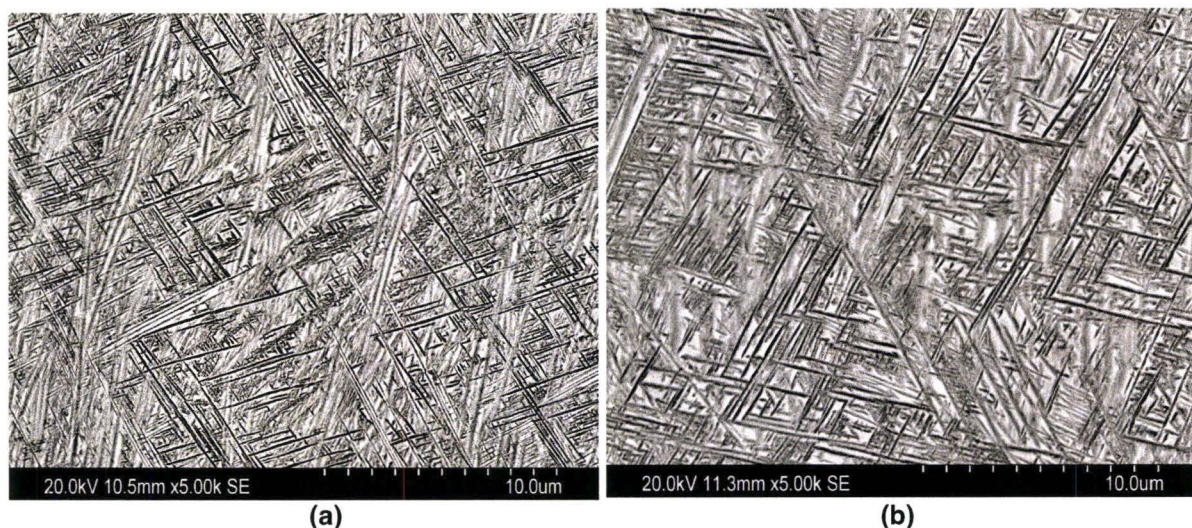
Figure 5.36: **SEM images of: (a) specimen fan-cooled from 790°C to room temperature and then aged at 600°C (20 mins), and (b)specimen cooled directly from 790°C to 600°C and aged for 20 minutes.**

5.3.5 Confirmation of the Heterogeneous Nucleation of the α Phase.

To confirm that nucleation of the α phase is heterogeneous in nature, a polished block of material in the ST condition was indented in a hardness testing machine. The plastic deformation caused by the indenter creates a gradient in the dislocation density away from the periphery of the deformed edge. After light polishing, the block was aged at 600°C for 10 minutes and etched to reveal the extent of transformation. The ageing response was obvious to the naked eye with dark rings of fully transformed structure surrounding the indentations in Figure 5.37 (A). Away from the indentation, the transformation was non uniform, see Figure 5.37 (B).
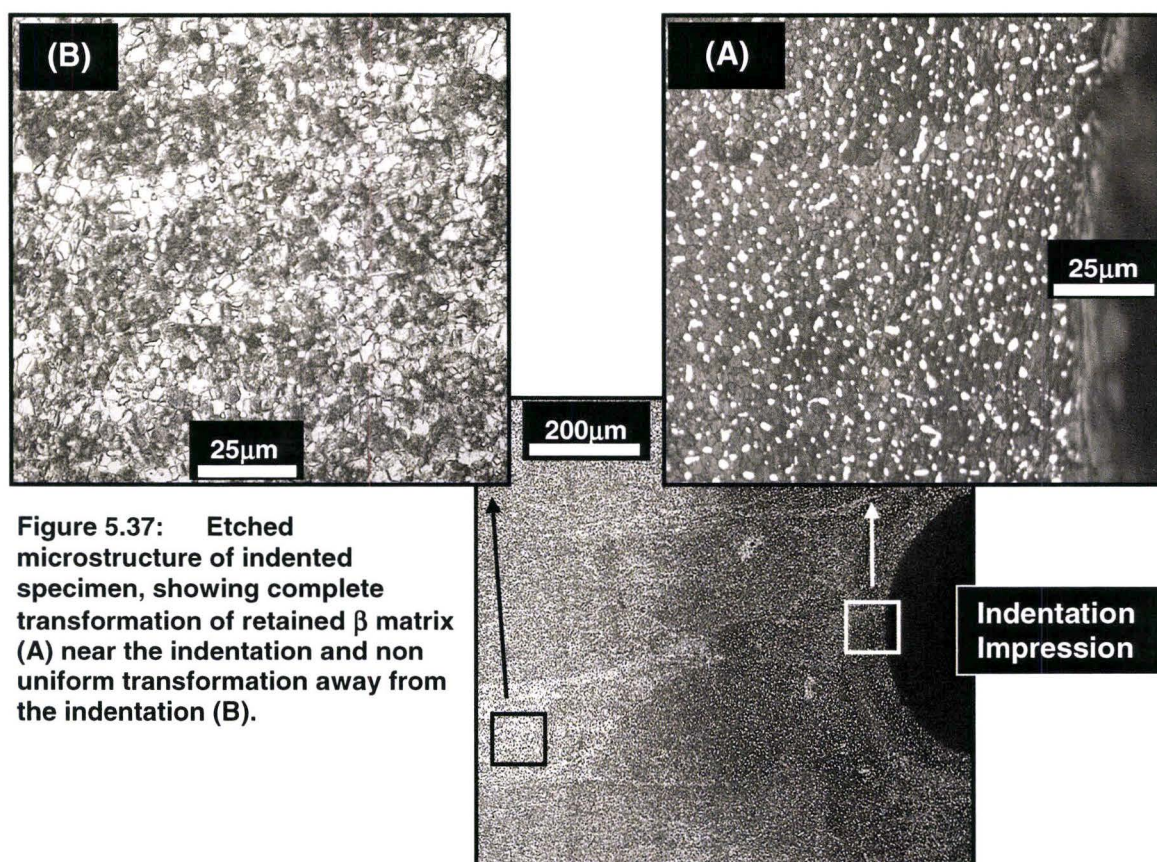
Figure 5.37: Etched microstructure of indented specimen, showing complete transformation of retained β matrix (A) near the indentation and non uniform transformation away from the indentation (B).

This simple experiment provides supporting evidence to the premise that nucleation of α is accelerated in the presence of dislocations. Moreover, the aged β structure near the indentation is of finer scale than that away from the indentation periphery. This suggests that the number of nucleation sites is greater, and the α precipitates are more closely packed in the regions of higher dislocation density. From the above observations it is concluded that α precipitation is heterogeneous and highly affected by the presence of dislocations. Since all the material tested was forged, differences in the dislocation densities are expected from grain to grain due to texture effects. This explains why the ageing response is non-uniform; with α precipitation beginning at the grains containing higher dislocation densities and percolating to other grains as ageing progressed.

5.3.6   Nucleation and Growth of the α Phase

It was established in the preceding pages that decomposition of the retained β is accelerated by the presence of dislocations, which provide nucleation sites for the α phase, and that a fine scale ω-phase exists upon fan-cooling.

Precipitation of α upon reaction times of only 1-2 minutes at an ageing temperature of 600°C have been reported by Cotton, et al. *[31]* However, the ω phase is reportedly unstable above 500°C, hence it is not clear whether this phase has dissolved or is still present at the onset of α nucleation. Thin foils of material aged for various times, were prepared and examined under the TEM. Observation of material aged for 5 minutes revealed that precipitation of α begins primarily within the grains is the form of discrete bands, approximately 0.1-0.2 μm in diameter, but some needles also nucleate at grain boundaries. The [110]β zone axis diffraction pattern is included in Figure 5.38 and it presents diffuse scattering and faint spots due to the ω phase, indicating that ω is still present. A depiction of the early stages of α precipitation is presented in Figures 5.38 and 5.39. Figure 5.39 - right, illustrates the outline of two such α needles traced from the bright field TEM image – left. By tracing the outline of the α regions, it is clear that these areas will develop into needles. In general, two types of needles are apparent: many randomly nucleated bands of α which become needles with continued ageing and fewer needles which begin as parallel discs of α. The latter type of needle will be discussed first. These needles begin as parallel slivers of α phase separated by retained β. These slivers are planar cross sections of disc-shaped volumes of α-phase. One likely scenario that would explain the remarkably uniform spacing of the α disks is that that their nucleation corresponds with dislocations arrays along low angle grain boundaries. As viewed at an oblique angle on a thin foil, a low angle grain boundary would manifest itself as a series of parallel dislocations. A similar mechanism of formation has been termed autocatalytic nucleation by G.R. Purdy, et. al.*[55]*, in which nucleation of arrays of plate-shape precipitates occurs at the stress and diffusion fields created by preceding precipitates. Low angle grain boundaries would facilitate the above conditions, by providing periodic stress gradients. Although additional work would have to be carried out to conclusively establish the exact mechanism, the frequency of observation of these arrays of α discs seems to correlate to the spacing of low angle grain boundaries reported previously in this Chapter.

The other seemingly random intra-granular α begins as bands containing linear arrays of α precipitates (discs) approximately 01-02 μm wide. It has been shown by Harper *[47]* and more recently Nag et al. *[54]*, that in Ti-5553, these α regions nucleate heterogeneously at ω sites. Furthermore, on the previous section it has been shown the nucleation of α is accelerated at heterogeneous sites such as dislocations.

Examination of these needles at higher magnifications revealed the presence of dislocations loops, these are shown at the inset in Figure 5.39 - bottom. The mechanism of formation for these needles seems to create dislocation loops, which in turn nucleate other α discs. It is surmised that the strain created by nascent HCP α discs within the BCC β matrix is accommodated by the dislocation loops observed.

Dark field observation suggests that these discs are not of the same α variant.

The density of the α discs varied from needle to needle and it increases with ageing time. After 20 minutes ageing, fully developed needles measuring 0.5-2μm are readily discernible, see Figure 5.40; a number of closely spaced, developing α needles can also be seen and are highlighted by the dotted ellipse. The preferential growth of α appears to be linked to self-accommodating and clustering of α variants.
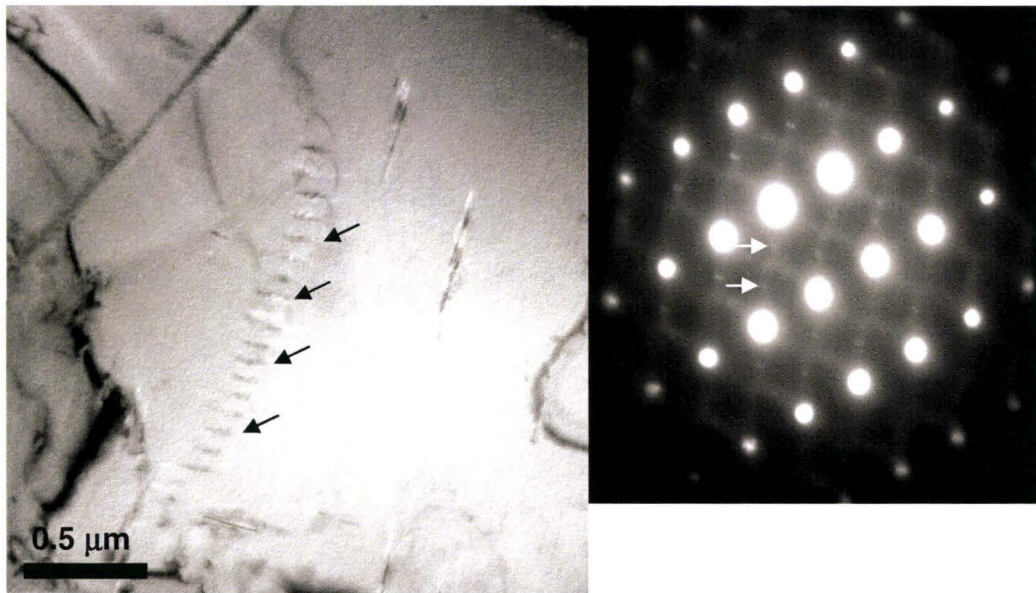
Figure 5.38: TEM foil of specimen aged at 600°C for 5 minutes, illustrating nucleation of linear arrays of α discs (arrows). At right [110]β zone axis SAD pattern showing streaking due to ω phase (white arrows).
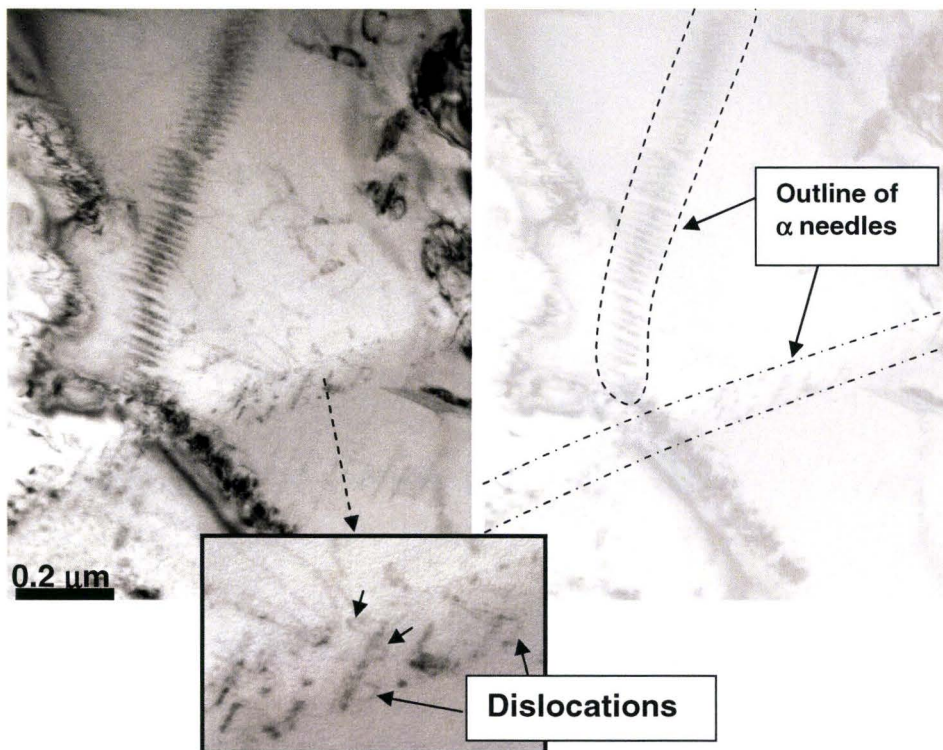
Figure 5.39: TEM image of nucleating α phase developing into needles, note the dislocation loops emanating from the α discs at inset bottom.

Similarly to the observations made by Williams [37] in other titanium alloys with high content of β stabilizers, the lenticular regions in Ti-5553 are seen to contain internal structure. An image of this substructure is presented in Figure 5.40 - right.
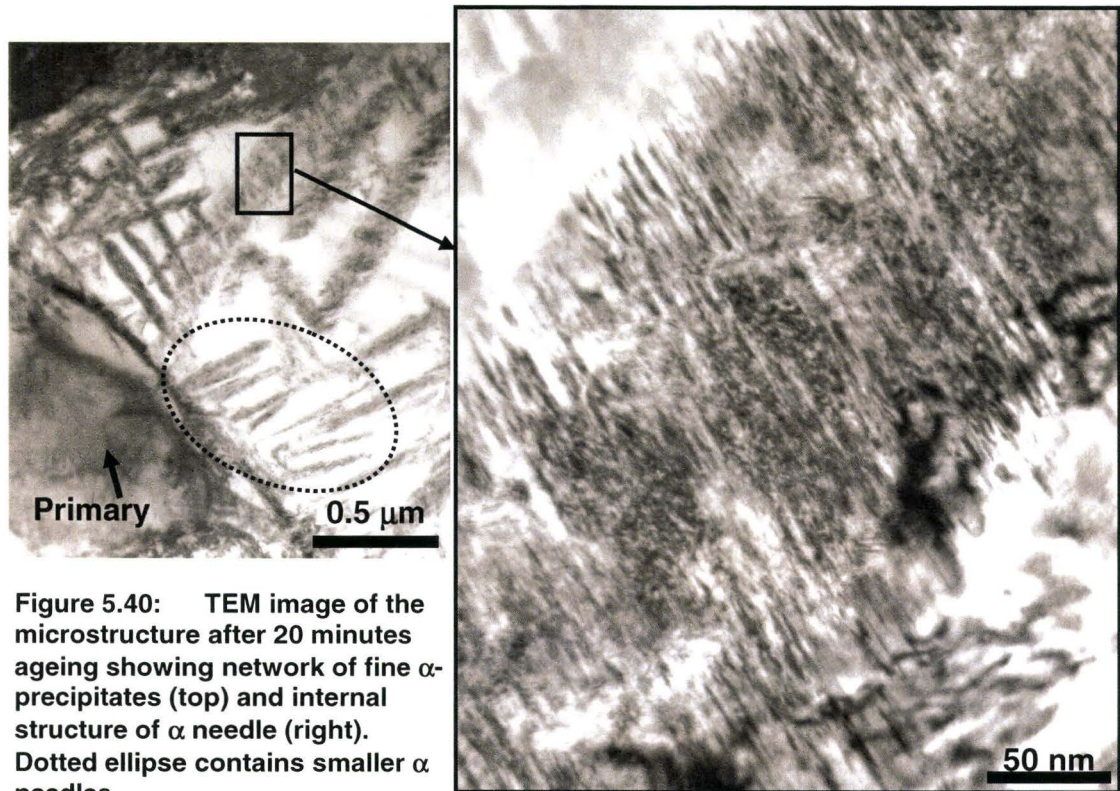
Figure 5.40:   TEM image of the microstructure after 20 minutes ageing showing network of fine α-precipitates (top) and internal structure of α needle (right). Dotted ellipse contains smaller α needles.

This substructure is said to be the result of the boundaries of individual particles contained within the needle. Williams describes two types of α precipitates from decomposition of the β phase; the first is a precipitate which follows the Burgers' relationship (type 1), as discussed in section 3.3 and 3.4, forming with Widmastätten plate or long needle morphologies. The second α type forms as very small "rafts" of lenticular regions and does not obey the Burgers relation (type 2). Selected area diffraction patterns of these two types of α are presented in Figure 5.41 (a) and (b), with the pattern from the region in Figure 5.40 presented at (c). It is clear that patterns (b) and (c) contain α reflections flanking the (110)β reflections and that these patterns are very different from that of the Burgers' α - pattern (a).   Furthermore, dark field imaging of the reflections flanking the (110)β reflection, suggest that these reflections belong to a different variant of α. Consequently, the substructure observed in Figure 5.40 is the result of different variants of alpha coexisting with an individual needle; see also Figure 5.42

(a)   (b)

$0\bar{2}0$	$\overline{1}10$	$\bar{2}00$
$1\bar{1}0$		$\overline{1}10$
200	110	020

(c)
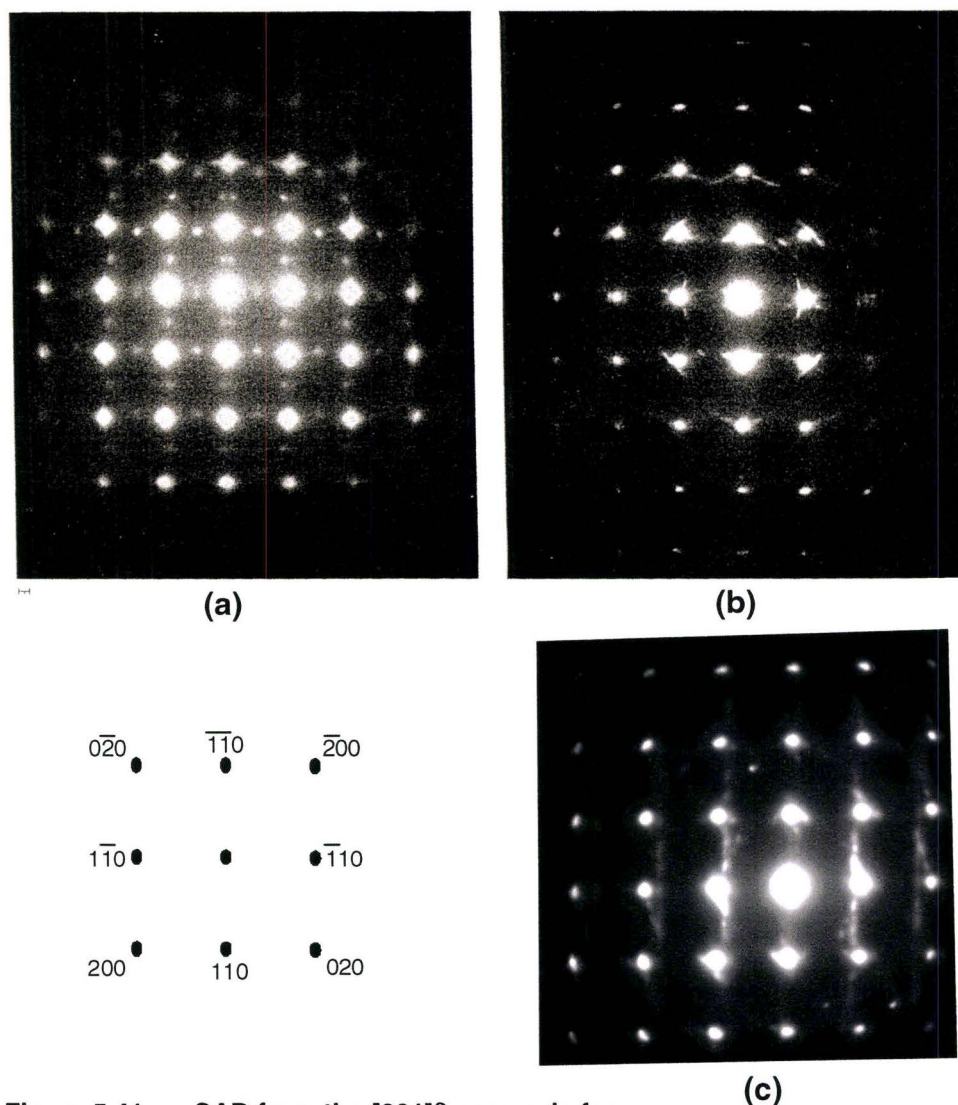
Figure 5.41: SAD from the [001]β zone axis for:
    (a) typical β+α pattern where α obeys the Burgers'
        orientation relation; *[37]*
    (b) atypical β+α pattern; *[37]*
    (c) Ti-5553 aged at 600°C for 20 minutes.

The presence of more than one α variant in such proximity could be explained by the generation of dislocation loops from the α discs, as shown earlier. These dislocation loops could nucleate another variant of α within a given needle. According to Nag et al.*[54]*, the preferential growth of a given α variant appears to be linked to self-accommodating and clustering of α variants morphologies. However, this particular aspect of α nucleation requires further study.
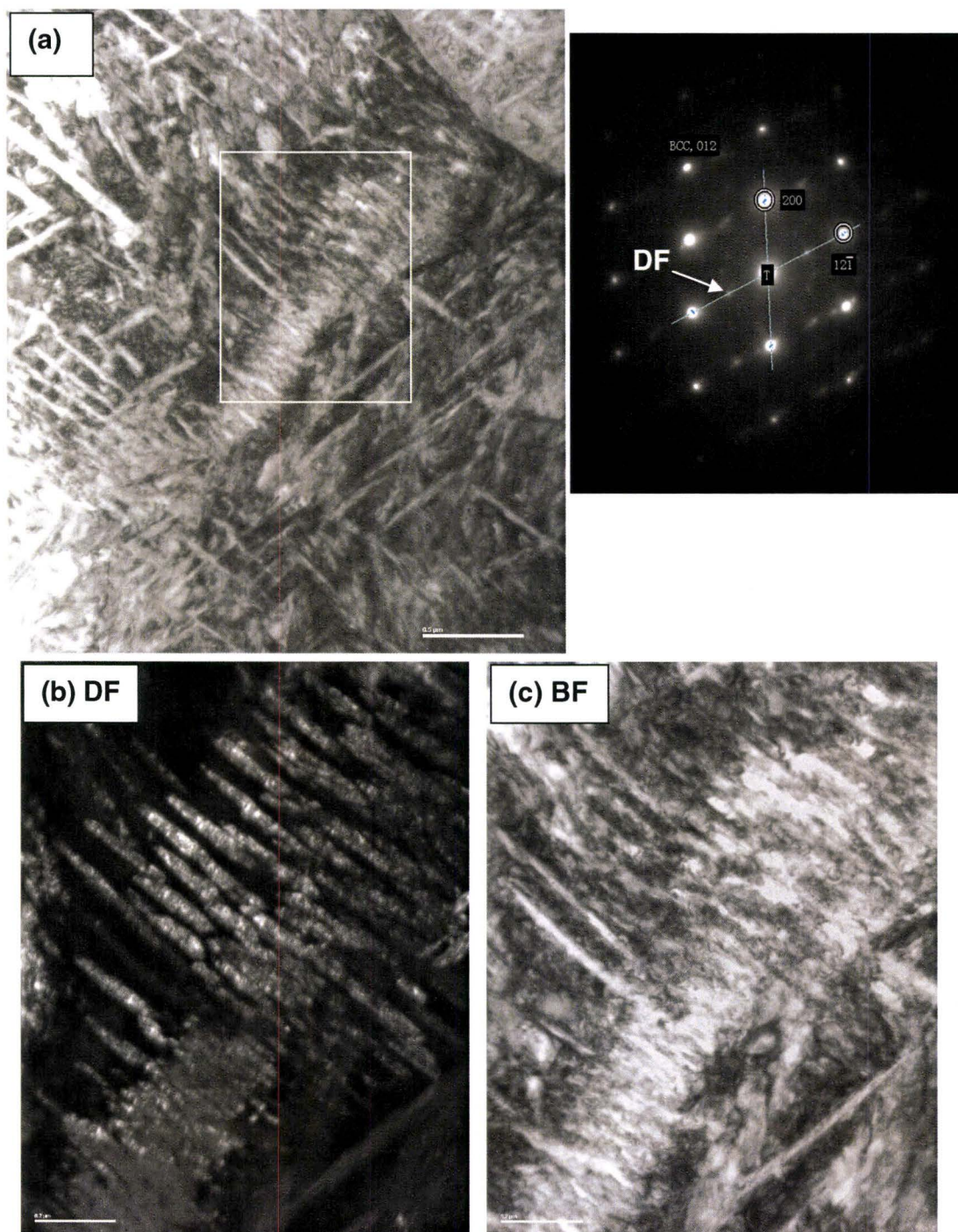
Figure 5.42: (a) TEM image of ST specimen aged for 20 minutes at 600°C, and [012]β zone axis diffraction pattern at top right. (b) and (c) are dark field and bright field images of central region, showing fine scale α precipitates of given α variant.

5.3.7   Progression of α Precipitation, α Agglomeration and GB Film Growth

Aging within the times for which the α volume fraction is still increasing causes the density of the α discs within the needles to increase. This time is of the order of 30-60 minutes for Ti-5553 at 600°C. Ageing beyond the time required for the volume fraction of α to reach equilibrium causes a gradual coarsening and agglomeration of the α needles. This point is illustrated by comparing the microstructure after 20 minutes and 6 hours ageing, see Figures 5.40 and 5.43, respectively. It is clear that the smaller needles present at 20 minutes ageing have agglomerated into coarser α needles measuring 1-3µm in length and 0.1-0.2µm in diameter.
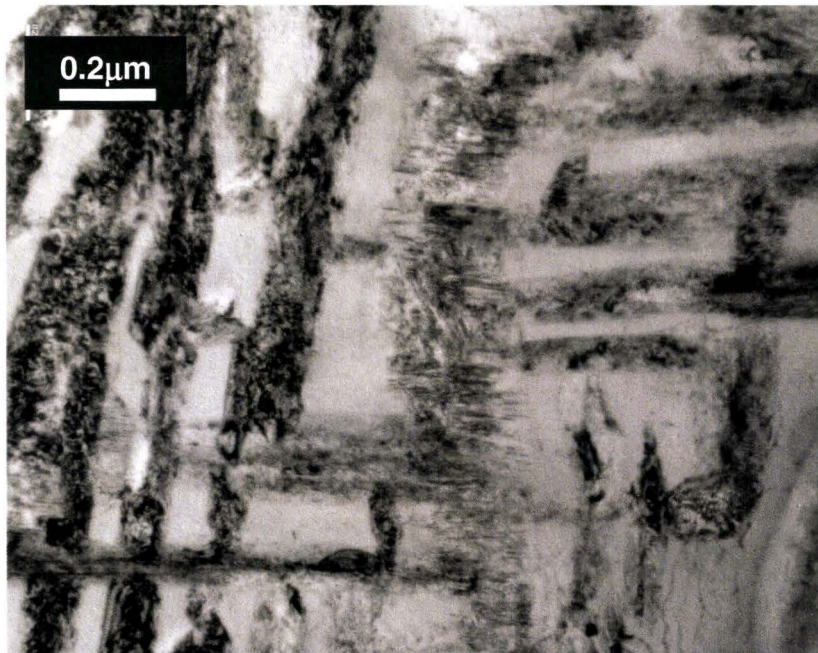
Figure 5.43:   Microstructure after ageing for 6 hours; note that the smaller α needles have agglomerated into a relatively uniform lath of needles.

Ageing for extended periods of time (i.e. over ageing to 48 hours), results in further coarsening of the individual α needles making up the laths depicted in Figure 5.44. The outline of the α needles is well defined and the apparent internal substructure noted in the early stages of precipitation under dark field conditions has essentially disappeared. This suggests that there has been a rearrangement of the α variants and the substructure has been "annealed out". Furthermore, there is a gradual coarsening of the grain boundary α films and a film circumscribing the primary α particles is also evident. The thickness of the grain boundary film is approximately 0.3µm, while the film around the primary α is roughly 0.2 µm.

Attempts at measuring the increase in primary α volume fraction by the optical technique described in section 4.9 were unsuccessful. Object separation by means of contrast is not feasible with the large number of α precipitates in the background. However, considering the increased diameter of the primary α particles due to the α film, it is possible to calculate the change in primary α volume fraction after an ageing time of 48 hours. Based on an average

primary α particle diameter of 0.35µm, and an average α film thickness of 0.17µm, the primary α volume fraction increased from 16.3% after solution treatment to 19.6% after ageing for 48 hours.
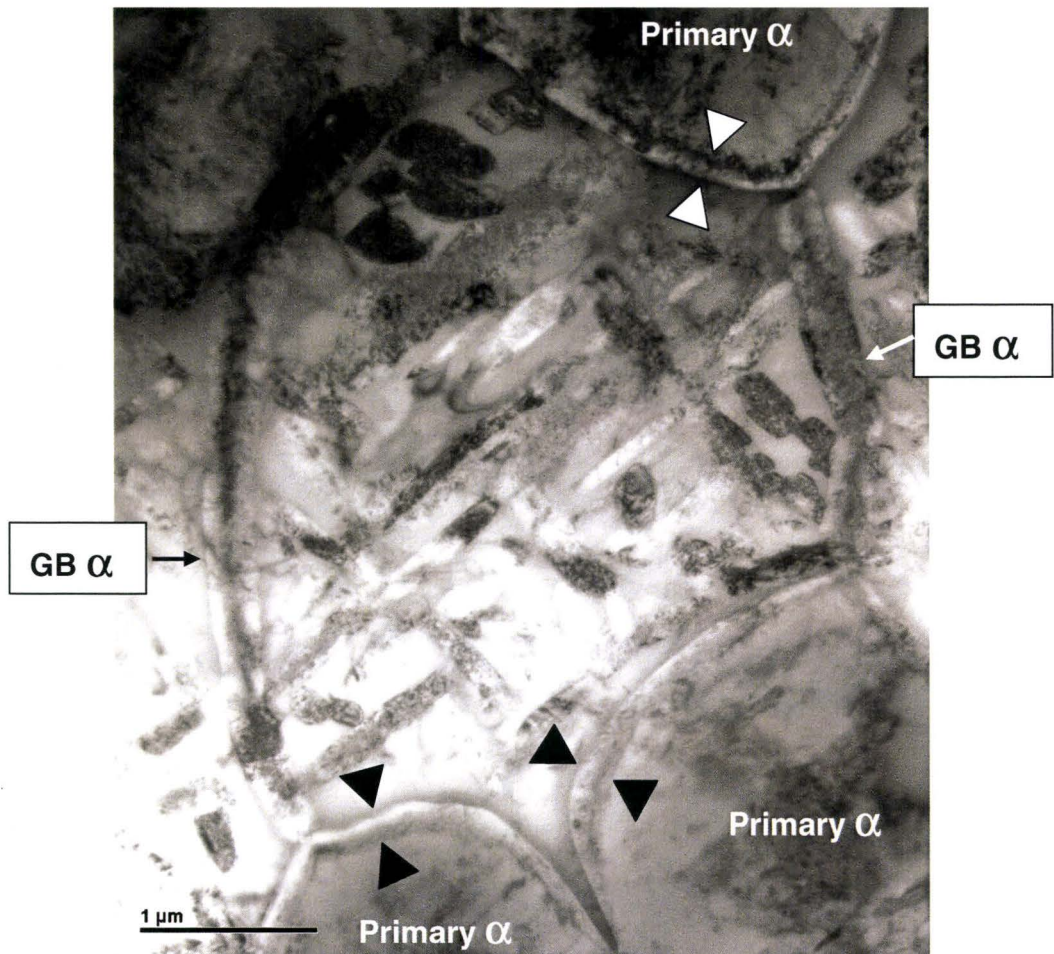
Figure 5.44:   TEM image of microstructure after ageing for 48 hrs. Note the continuous α film at grain boundaries and surrounding the primary α particles (black triangles). Fewer, coarser α needles fill up the matrix.

Since the chemical composition of the primary α and the α films are expected to be different due to solute partitioning, it is anticipated that the physical and mechanical properties of these phases will also vary. Moreover, the size and distribution of the precipitated α constituents is seen to change with ageing time, which would surely have impact on the alloy's mechanical properties. A more detailed discussion of the correlation between mechanical properties and microstructure will be presented in Chapter 6, where strengthening mechanisms and mechanical properties are addressed.

5.4   Rationalization of the microstructure evolution

An explanation of the $\beta \rightarrow \alpha$ transformation and evolution of the microstructure can be facilitated by invoking general thermodynamic principles. The succession of transformation steps follows competing processes which result in a lower free energy state for the system. This rationalization will be provided in the same order as the presentation of results, i.e., beginning with the β annealed heat treatments and following with the heat treatments performed below the β transus. To simplify this discussion, a pseudo-binary phase diagram for a typical β Titanium alloy and a semi-qualitative Time-Temperature-Transformation (TTT) diagram for Ti-5553 will be employed. Because of the familiarity with the Fe-C system and the similarities between Titanium and Iron phase transformation, analogues to the precipitation of Ferrite from Austenite will be drawn to clarify many points

5.4.1   Heat Treatments above the β Transus.

Beginning with the as-forged microstructure described in Chapter 4, heating above the β transus causes complete dissolution of the α phase and rapid recrystallization. This corresponds to Point 1 in Figure 5.45; this transformation is driven by the thermodynamic instability of the α phase above the β transus temperature.
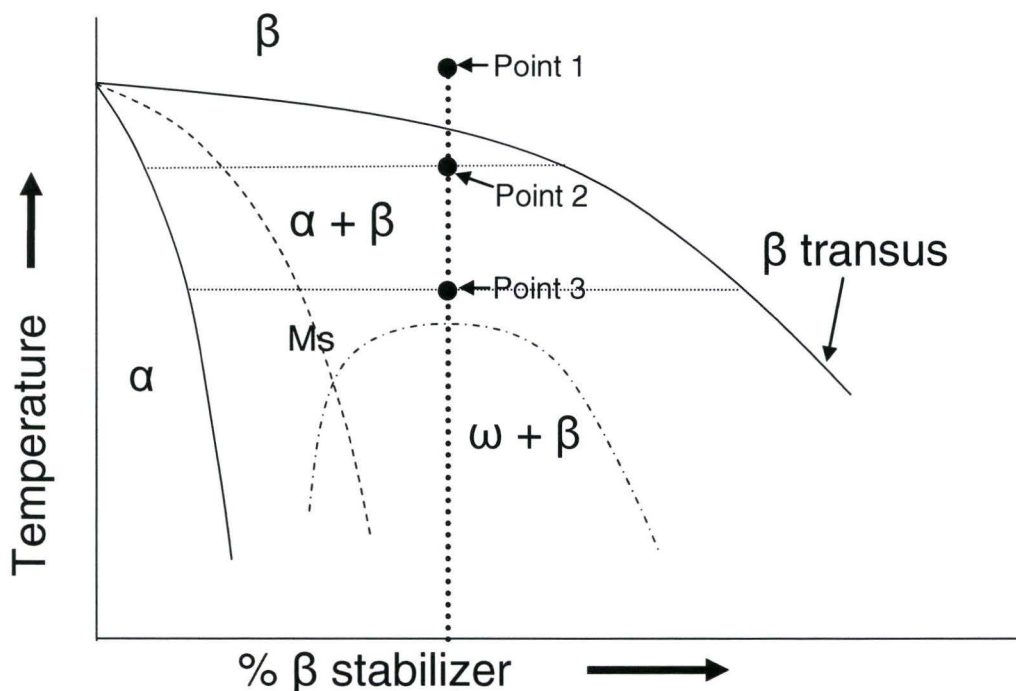
Figure 5.45:   Pseudo-Binary Phase Diagram for a Typical β Titanium Alloy.

The change in crystal structure is accompanied by recrystallization resulting in an equiaxed grain structure with an average grain size of ~190µm. Recrystallization is compulsory to lower the system's grain boundary free energy. Fan-cooling at an average rate of 1.7°C/sec is sufficient to retain the β phase at room temperature. However, as depicted in Figure 5.45, the retained β phase is metastable, seeing that α and β are the equilibrium phases at room temperature. Water quenching from above the β transus results in the formation of ω phase. Transformations involving the ω phase are typical of solute lean metastable titanium alloys such as Ti-5553, for which martensitic transformation is not favoured and the cooling rate is too fast to allow diffusion controlled precipitation of the equilibrium α phase. However, in Ti5553, fan-cooling results in formation of the ω phase and a fine scale dispersion of α precipitates. Formation of ω and ω+α are illustrated in the semi-qualitative TTT diagram depicted in Figure 5.46. Similarly to a Continuous Cooling Curve (CCT) diagram, two cooling curves labeled WQ (water quenched) and Fan-cool, respectively, have been plotted with dotted lines to illustrate the precipitation sequence for these cooling rates.
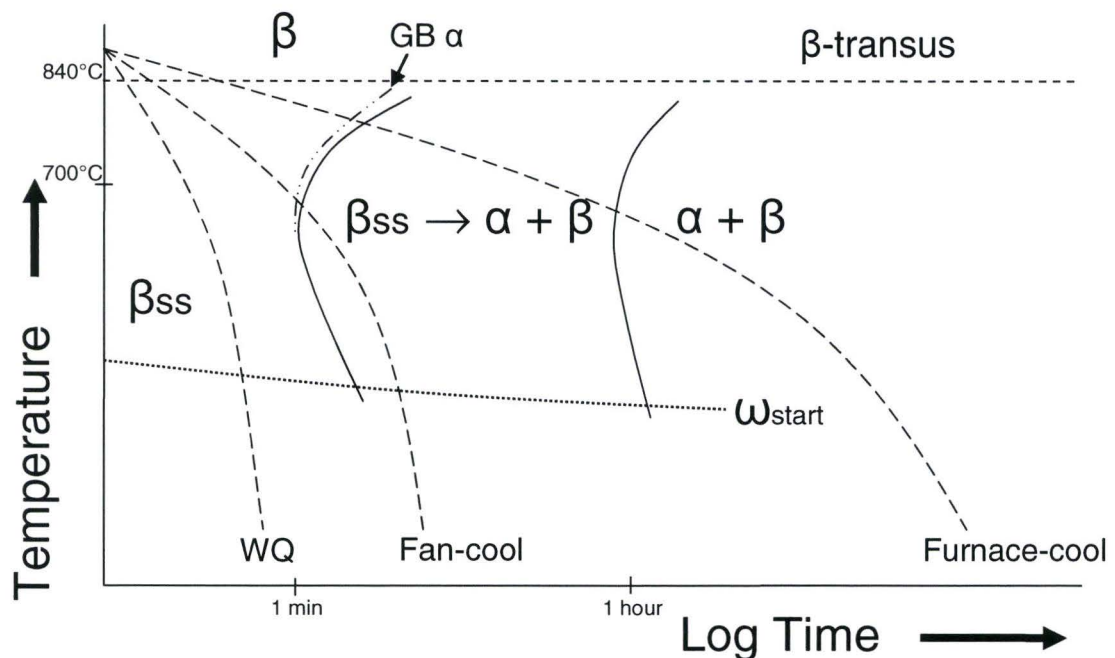
Figure 5.46:   Semi-Qualitative TTT diagram for Ti-5553.

Note that following the Fan-cool dotted line, the line labeled GBα is crossed first signifying that precipitation of grain boundary α will take place ahead of bulk α precipitation. The microstructure resulting from cooling in still air, rather than fan cooling, is presented in Figure 5.47. A series of grain boundary precipitates can be observed, some have plate morphology but some have "blockey" appearance similar to grain-boundary allotriomorphs observed in the precipitation of C-Ferrite from Austenite in steels. Cooling rates slower than the Fan-cool line favour nucleation at high surface energy sites such as grain boundaries. However, precipitation of blockey α within grains is also observed, most probably nucleated at other high energy defects such as inclusion interfaces, etc. Coexistence of grain boundary α with plate and allotriomorph morphologies indicates that this particular cooling regime is near the transition from

Widmanstätten-like plates to blockey morphology. Referring to the example of carbon steels, the different morphologies have been related to the growth velocity of incoherent and semicoherent interfaces at different undercoolings. Although this work did not specifically study the change in GB α morphology, observation of the β annealed fan-cooled versus slow cooled conditions showed Widmanstätten-like plates are favoured for fan-cooling. All specimens cooled at rates slower than fan-cooling displayed the blockey α at grain boundaries.
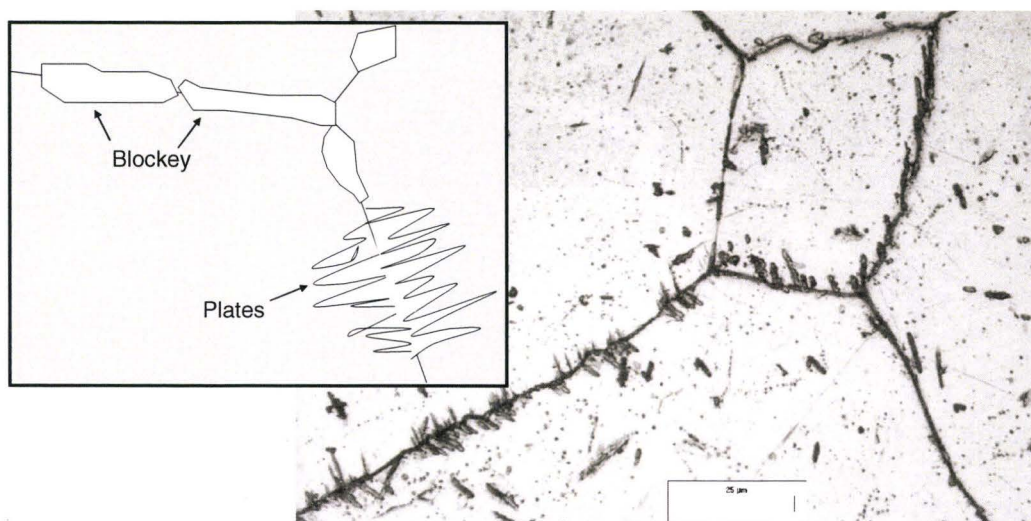
Figure 5.47. Microstructure of β annealed specimen cooled in still air; dark regions at grain boundaries and within grains are α precipitates. Inset is sketch of two types of grain boundary precipitates observed.

Heating the β annealed material to a high temperature in the α-β range (790°C), Point 2 on the Figure 5.45, precipitates a fine-scale (0.5-2µm long) acicular α. A subsequent ageing cycle for several hours at 600°C, Point 3 - in Figure 5.45, does not significantly alter the microstructure. The lack of change suggests that the transformation has proceeded to equilibrium after the solution cycle at 790°C. The driving force for α formation is the attainment of equilibrium volume fractions for α and β as predicted by the tie line at Point 2 in Figure 5.45. Once the metastable retained β phase has fully transformed to $\alpha+\beta$ at 790°C, further ageing at 600°C does not change the microstructure. This explains why the additional ageing cycle does not alter the microstructure.

Recent studies suggest that fine-scale α phase is nucleated heterogeneously at the ω phase present. Quenching from the β transus directly to the ageing temperature, thus avoiding the ω phase altogether caused no change in the scale of the acicular α microstructure. Consequently, although nucleation of α at ω sites has been reported in the literature [47] [54], it does not seem to affect the final scale of the α phase.

Furnace cooling from above the β transus to the ageing temperature, i.e. from Point 1 to Point 3 in Figure 5.45, labeled furnace-cool on Figure 5.46, results in much coarser acicular α (5-10µm long) and small clusters of lamellar α. The change in α morphology is related to the longer

diffusion times affected by the slow cooling and avoidance of the ω phase. A continuous grain boundary α film is also evident.

A further decrease in cooling rates (1°C/sec) results on a microstructure of lamellar α in a basket weave arrangement; as well, thicker grain boundary α films are noticeable. The lamellar α consists of side-by-side ribbons of α separated by bands of β. It is obvious that the scale of the microstructural elements becomes coarser with slower cooling rates. An explanation can be provided in terms of the longer transformation times, which allow solute diffusion over longer distances and sustains the growth of abutting α regions resembling ribbons.

Precipitation of α at prior β grain boundaries occurs due to the longer times through the high temperature range (GB α start), although the driving force for α nucleation is relatively low, the energy reduction due to α nucleation at grain boundaries is high.

The preceding discussion is aimed at providing insight into microstructure evolution for the β annealed heat treatments. Since the starting microstructure always consists of 100% retained β, it is relatively simple to follow the changes that occur by varying the thermal cycles. Except for the formation of the ω phase, the mechanism of β→α decomposition is a diffusion controlled process similar to that observed for carbon steels. The following discussion will deal with heat treatments below the β transus, which, by virtue of starting from a more convoluted microstructure, represent a more difficult task

5.4.2   Heat treatments below the β transus.

Since heat treatments in the α+β range do not totally eradicate the as-forged microstructure, it is essential to discuss the elements of the as-forged microstructure first. The as-forged microstructure consists of two types of α: i) uniformly distributed globular primary α 3-5μm in diameter and, ii) a dispersion of sub-micron lenticular α. The morphology of the primary α is globular, often containing facets, and is always located at the triple points or grain boundaries. Rationalization for the arrangement and morphology of the primary α can be provided by consideration of the heterogeneous nucleation of α in a matrix of supersaturated β during forging in the α-β temperature range. The change in Free Energy, G, of the system due to precipitation of the primary α is as follows.

$$\Delta G = -V\Delta G_v - \Delta G_d + A\gamma + V\Delta G_s$$

Where the term $V\Delta G_v$ is the volume free energy reduction due to formation of the α phase, ΔG_d is the reduction due to elimination of a defect, $A\gamma$ is the increase in free energy due to the creation of the α/β interface area, and $V\Delta G_s$ is the volume free energy associated with the misfit strain between the α/β interface.

Nucleation of α particles at triple points and grain boundaries is consistent with reducing the free energy associated with these defects. The globular morphology reduces the surface area and the free energy associated with the α-β interface.

Lattice correlation boundary work conducted by EBSD (Figure 5-20) showed that some primary α particles contained surfaces which maintain a crystallographic relationship with the β matrix while other particles did not. The illustration presented in Diagram 5.10 depicts the shapes of grain boundary primary α precipitates observed in solution treated Ti-5553 and the type of interfaces found.
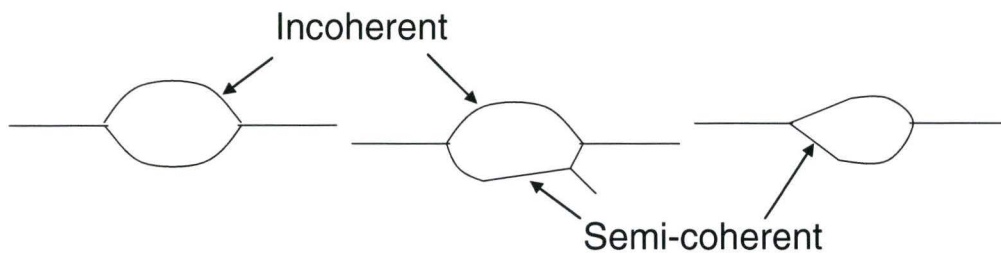
Diagram 5.10: Shapes of grain boundary primary α precipitates and types of interfaces observed in solution treated Ti-5553.

Semi-coherent interfaces reduce the strain energy associated with some interfaces, while lens-shaped incoherent interfaces are found when no relationship with the β matrix exists. These optimized shapes reduce the interfacial strain.
Hence, the overall arrangement and morphology of the primary α particles is consistent with a state of minimized free energy for the primary α retained β system at a given temperature.

Solution heat treatment of the as forged microstructure at temperatures close to the β transus transforms all the lenticular α to β. However, at 50°C below the β transus the primary α and the grain boundaries appear largely unaffected. Even after hours at the solution temperature the volume fraction of primary α does not change. This means that the volume fractions of α and β are in equilibrium - as given by the tie line at Point 2 in Figure 5.45. Preferential dissolution of the lenticular fine α during solution heat treatment is due to their smaller size and large interfacial energy when compared to the large globular primary α particles. Once the lenticular α is dissolved, increasing the solution temperature to the β transus causes dissolution and eventual disappearance of all the primary α.

When the solution heat treated microstructure is fan-cooled the β phase is retained at room temperature. The retained β also contains nano-scale ω phase precipitates. However, much like the retained β in the preceding section, this phase is metastable with a tendency to decompose to an equilibrium mixture of α and β upon ageing.

When heating the solution treated material in the range 500-600°C, Point 3 in Figure 5.45, the volume fraction of α increases significantly and a fine scale lenticular α needles are seen to precipitate within minutes. Furthermore, at this temperature, the respective compositions of the α and β are quite different than that at Point 2. Hence, the lenticular α is of different composition than the pre-existing primary α. Due to the presence of near equilibrium composition primary α, the super-saturation of the retained β is lower than that after β annealing. Consequently, the driving force for α nucleation is also expected to be lower than after β annealing. As demonstrated earlier in this Chapter, nucleation of the lenticular α is heterogeneous at dislocations and grain boundaries.

With continued ageing, the scale of the lenticular α continues to coarsen, as does the grain boundary α. This coarsening is due to the drive for attainment of equilibrium composition and the reduction of interfacial free energy ($A\gamma$).

Doubling the ageing time from 24 hours to 48 hours does not significantly alter the scale of the lenticular and grain boundary α, suggesting that near equilibrium conditions are attained at

24 hours. This behaviour is quite desirable from a practical heat treatment point of view - as the resistance to over aging is an important consideration when heat treating components with thin and thick cross sections.

The preceding pages provide a thorough examination of microstructural response of Ti-5553 with heat treatments above and below the β transus and after ageing. Furthermore, a rationalization of these changes in terms of thermodynamic principles has been presented. The effect of the ω phase and dislocations on nucleation of the α phase has been investigated. Decomposition of the retained β phase and growth of the α have been followed to the attainment of near equilibrium conditions.

These results have focused on the microstructural changes but make no inference into the effect of these changes on the alloy's mechanical properties. The following Chapter deals with the mechanical properties of Ti-5553, and how the deformation and fracture processes are affected by the microstructure.

6.0   MECHANICAL PROPERTIES IN HEAT TREATED Ti-5553

A conventional approach to evaluating the response to heat treatment for a novel alloy system would entail characterizing of the mechanical properties as a function of ageing temperature and time. Often, the chemical composition of the materials studied can be altered and the changes in properties investigated. In some cases, it is possible to vary the heating and cooling rates, and thermo-mechanical processing to explore the effect of processing parameters on mechanical properties. Since the nature of this project and ultimate goals are related to a commercial alloy in the context of industrial practices, the approach followed in this thesis diverges from the standard method.

The work presented through this thesis is aimed at gaining an understanding of the heat treatment response of a new titanium alloy for which the composition and thermo mechanical processing are fixed. The heat treatments conducted involve solution heat treatment above or below the β transus, followed by cooling and ageing. Although there is flexibility in the heat treatment parameters, the heating and cooling rates chosen and the heat treatment practices were in line with those of commercial heat treatments. The temperatures chosen for ageing were selected on the basis of preliminary screening tests for this alloy. Furthermore, the material cross sections selected were representative of typical landing gear components.

A rationalization of the alloy's strength and fracture behaviour is presented by means of simple models used to illustrate the relative contribution of microstructural changes occurring after each heat treatment. This semi-quantitative approach attempts to highlight the role of specific features of the microstructure on tensile properties. The effect of the ω phase on the properties of the β annealed and the solution treated group of heat treatments will be clarified. The rationalization considers the differences in plastic behaviour and strain hardening rates for the primary α and β phase to explain deformation and fracture modes. Moreover, the mechanism of void formation, which ultimately limits the strength of the material, will be conclusively identified.

As mentioned in the introduction to this thesis, a central criterion in materials selection for airframes is the strength to density ratio. Resistance to fatigue and elastic modulus are sometimes key for many airframe components, however, landing gear design is still dominated by static strength considerations. With this in mind, the mechanical property evaluations for Ti-5553 have focused on strengthening mechanisms and their dependence on the alloy's microstructure. As for other β titanium alloys, the competition between plasticity and fracture draws interest to obtaining the proper balance between strength and ductility. To this end, optimization of tensile properties for the STA condition was conducted by systematically varying the solution treatment and ageing temperatures. Recommendations on volume fractions of primary α as well as ageing temperatures and times will be presented.

A great deal of reliance is placed by industry in the knowledge of the strength and resistance to fracture, although primarily in simple tension. In view of the fact that the stress state in actual components involve more than tensile stresses, deformation and fracture evaluation will be accomplished by means of tension, compression and shear tests.
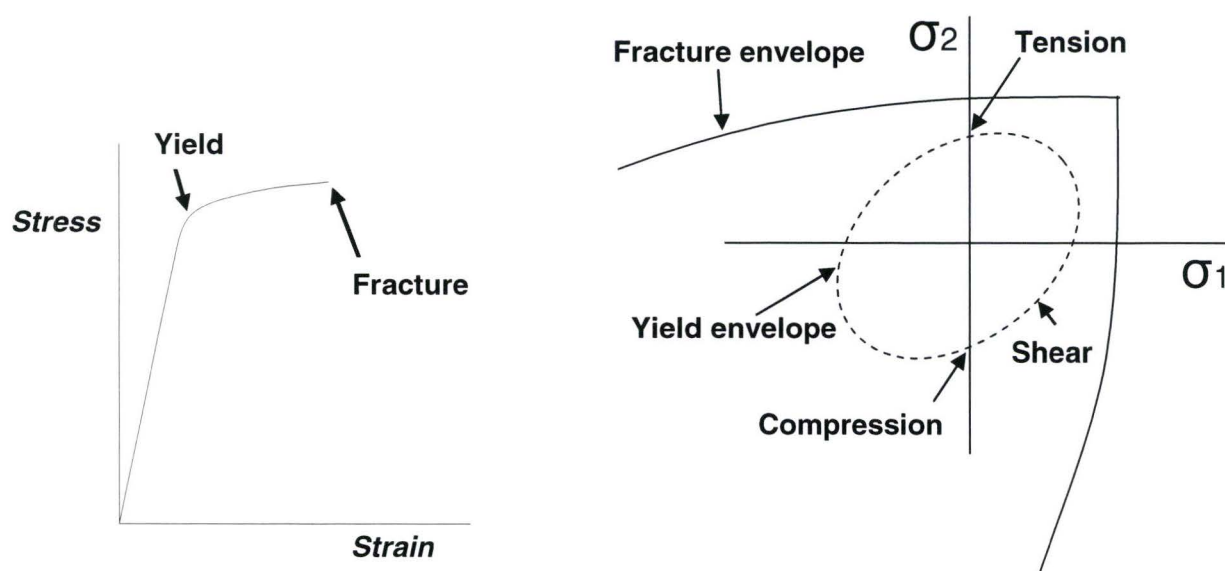
Diagram 6.1. Diagram Depicting Representative Yield and Fracture Envelopes (right), Constructed from Stress-Strain Evaluation (left).

As illustrated in Diagram 6.1, the measurements of the uniaxial strength in tension ($\sigma_{tension,}$),

compression ($\sigma_{comp.}$) and pure shear (τ), will be used to construct the biaxial yield and fracture envelopes for Ti-5553.

Knowledge of critical yield and fracture properties is essential to reduce the risk of component failure. However, other considerations such as the fracture toughness and resistance to stress corrosion cracking are equally important if a new alloy is to be adopted. To this end, the fracture toughness and SCC resistance will be evaluated and compared against currently used titanium alloys. In the case of the stress corrosion cracking, the alloy's resistance to crack initiation and crack propagation under harsh environmental condition will be investigated

6.1   Mechanical Properties with Heat Treatments Above the β Transus

Presentation of the mechanical property results will be in the same order as for the microstructure, addressing the heat treatments conducted above the β transus temperature first. In general, these heat treatments involve β annealing at approximately 50°C above the β transus (903°C) for 75 minutes. The cooling rate ranged from water quenching to controlled furnace cooling. Some specimens were re-solution treated in the α-β temperature range and some were cooled directly from the β annealing temperature to the ageing temperature to avoid formation of the ω phase. Ageing was always carried at 600°C, which represents the mid point of the recommended ageing temperature range for this alloy. The selection of this ageing temperature will be discussed near the end of this Chapter where mechanical property optimization results are presented.

6.1.1   Tensile Properties of the β Annealed Group of Heat Treatments

A description of each heat treatment cycle and the labels applied to simplify reference are presented in Table 6.1. The engineering tensile property results are provided in Table 6.2, with a plot of the Engineering Stress-Strain curves for representative curves in Figure 6.1.

Table 6.1:   Summary of Heat Treatments with Corresponding Labels

Label	Description of Heat Treatment
BAFC	β annealed at 903°C for 75 min, fan-cooled
BAWQ	β annealed at 903°C for 75 min, water quenched
BAST	β annealed at 903°C for 75 min, fan-cooled, solution treated at 790 for 2 hrs.
BASTA	β annealed at 903°C for 75 min, fan-cooled, solution treated at 790 for 2 hrs, aged at 600°C for 3 hrs.
BACCA	β annealed at 903°C for 75 min, furnace cooled at 1.0°C/sec to 600°C, aged at 600°C for 8 hrs.

Table 6.2:   Engineering Tensile Properties For The Various Heat Treat Cycles

Label	YS (MPa)	UTS (MPa)	% Elongation*	% R of A	Hardness HRC
BAFC	783	855	6.0	15.0	28.9
BAWQ	728	810	5.0	11.0	28.6
BAST	GF	1010	GF	GF	46.9
BASTA	GF	979	GF	GF	46.3
BACCA	1020	1100	12.0	20.0	43.0

*GF = Grip Failure - all specimens failed at grip; * = % elong. in 25mm gage length.*
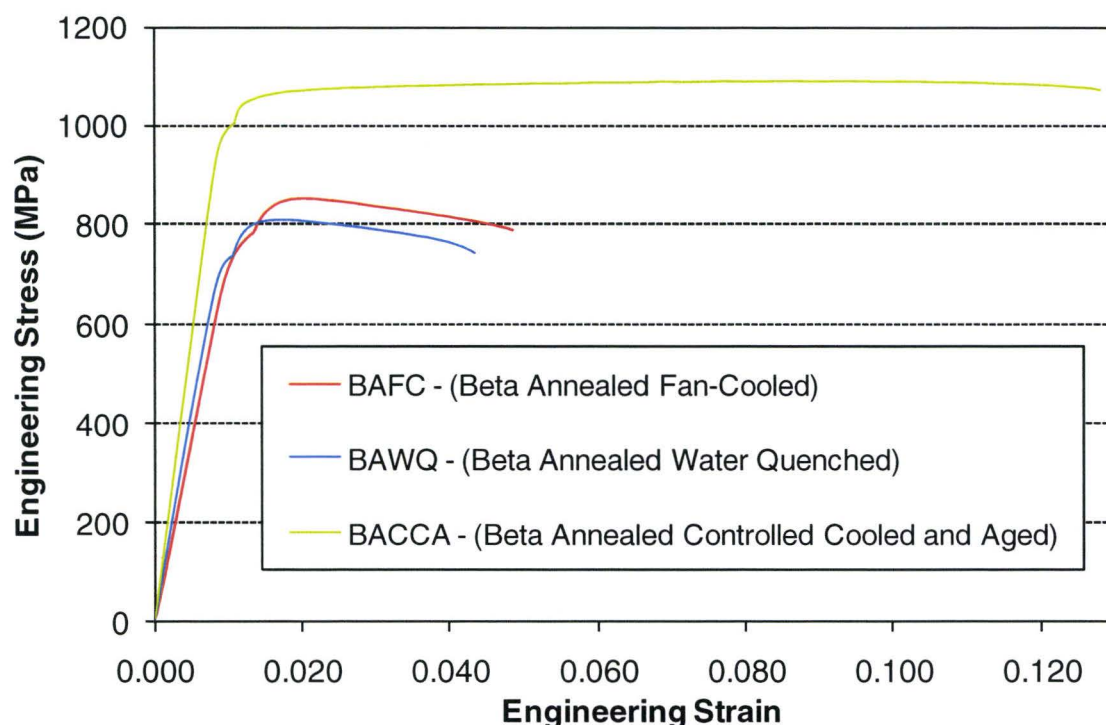
Figure 6.1:   Engineering Stress-Strain Curves for Selected β Annealed Cycles

Comparing the properties of the fan-cooled and water quenched conditios in Table 6.2 provides insight into the effect of cooling rate from above the β transus. The tensile yield and ultimate strengths for the water quenched material are slightly lower than those for the furnace-cooled material. The measures of ductility, namely % Elongation and % R of A, are also lower. Both of these conditions display a maxima in their stress-strain behaviour shortly after yield with a negative slope in the stress strain curve up to the specimen's fracture. A comparison of the respective microstructures for these two conditions in Table 6.1 reveals that the only difference is that the BAFC condition contains nanometer-scale α precipitates in addition to the ω phase. Hence, it is surmised that the presence of the α precipitates increases ductility and strength by retarding fracture process, however, a more in depth analysis of the reasons for this variance will be provided in the Fracture Mode Evaluation section of this chapter.

A meaningful evaluation of the tensile properties of the BAST and BASTA conditions was not possible as all specimens in these two conditions failed prematurely at the threaded grips. Similar tensile behaviour in all these specimens is not surprising, as the microstructures are essentially identical. As presented in Chapter 5, and despite the added ageing cycle for the BASTA condition, both microstructures consisted of sub-micron acicular α precipitates. No necking or plastic deformation was obvious in any of the specimens, which is symptomatic of the brittle nature of this condition.

The BACCA condition exhibited considerably higher strength and ductility than the prior β annealed conditions, however it is evident from Figure 6.1 that the ultimate tensile strength is only 80MPa higher than the yield strength. This near-plateau regime in the stress strain curve after the onset of plasticity points to a very low work hardening rate. The microstructure for this condition is 100% lamellar - composed α "ribbons" separated by β bands; these ribbons are organized in a basket weave arrangement. Similar microstructures have been associated with moderate strength but high ductility in other titanium alloys such as Ti-6Al-4V, as is the present case for Ti-5553.

The true stress-true strain curves for three selected conditions are presented in Figure 6.2. Dotted lines indicate extrapolated data between the point of instability and the true fracture stress for which instantaneous cross section measurements are not available. The strain hardening rate, $d\sigma/d\varepsilon$, has been taken to be the slope of this dotted line. The fracture strains, fracture stresses and strain hardening rates are presented in Table 6.3. As expected, the work hardening behaviour for the fan-cooled and the water quenched material are very similar, while the BACCA condition has of higher strain hardening rate. Nonetheless, compared with low alloy steels, these work hardening rates are considered to be low.

The strain hardening rate at the transition region from elastic to plastic behaviour has been characterized by plotting the rate of change in stress and strain beyond the onset of plastic deformation. A detail of the area of the curve studied and the corresponding $d\sigma/d\varepsilon$ versus ε are presented in Figure 6.3.
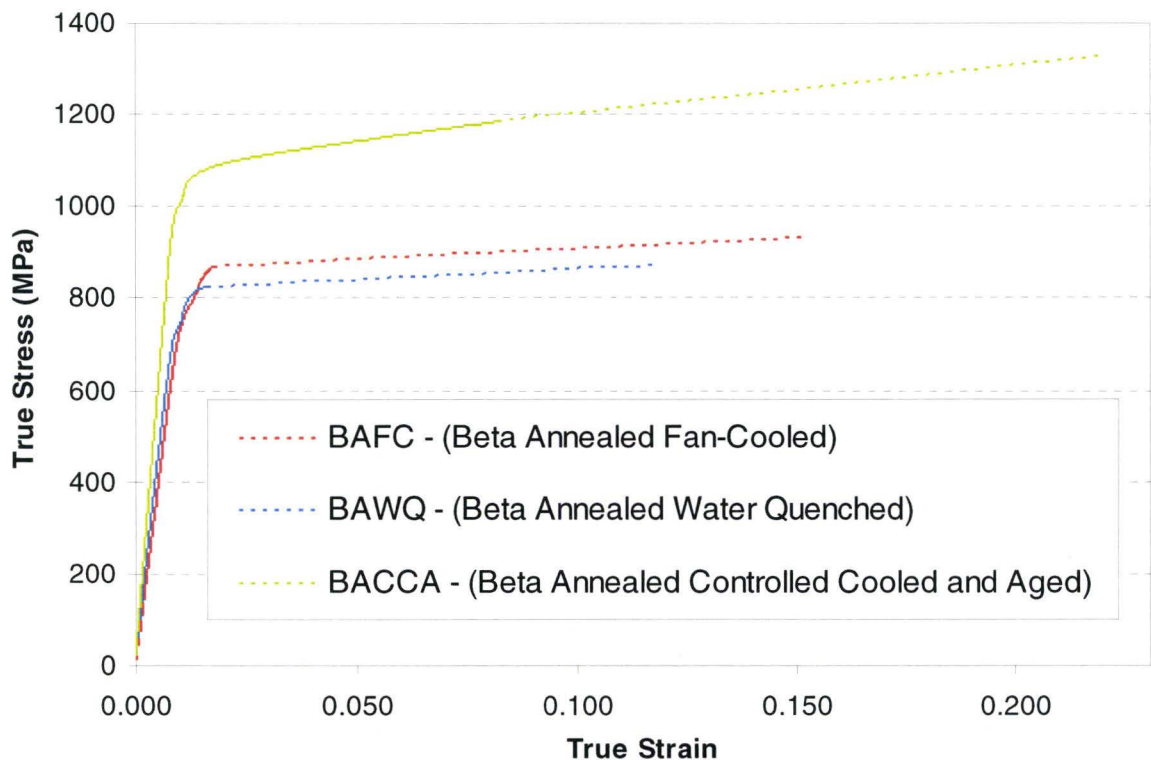
Figure 6.2: **True Stress-True Strain Curves for Selected β Annealed Cycles.**

Table 6.3: **Tensile Fracture Strain, Fracture Stress And Strain Hardening Rates For The Various Heat Treat Cycles**

Label	Fracture strain	Fracture stress (MPa)	Slope of line, $d\sigma/d\varepsilon$ (MPa)
BAFC	0.15	938	503
BAWQ	0.12	859	481
BAST	GF	1010	GF
BASTA	GF	979	GF
BACCA	0.22	1333	1096

Note: GF = Grip Failure - all specimens failed at threaded grip
$d\sigma/d\varepsilon$ = is the slope of the strain-strain line from maximum load to fracture

Figure 6.3: **Top – Portion of the True Stress-True Strain curves analyzed; Bottom – Plot of hardening rate, $d\sigma/d\varepsilon$ versus ε for the BAFC and BACCA conditions**

The data plotted in Figure 6.3 - bottom has been fitted with a polynomial function to more clearly show the rates of change. Note that despite the scatter in the data, at strains above 0.015 the data becomes asymptotic approaching the fracture stress for the two conditions, but it is not zero. This plot illustrates that the work hardening rate for the BACCA condition is greater than that of the BAFC condition; at a strain of 0.010, the rate of change of the BACCA is double that of the BAFC. A similar trend has been found for the strain hardening rate in the linear portion of the curve. The effect of the strain hardening rate on the mechanisms of deformation and fracture will be addressed in the Discussion section of this Chapter.

6.1.2   Effect of Grain Size

Whether water-quenched or furnace-cooled, the dominant features in the β annealed microstructure are the grain boundaries. To assess the effect of the grain boundaries on yield and ultimate tensile strengths, specimens of different grain sizes were tested. These specimens were produced by annealing at progressively higher temperatures and longer times than those used for the BAFC condition. It is assumed that the grain size is the major microstructural feature changing during these heat treatments. In this manner, the grain size was increased from approximately 0.2mm to 1mm. Table 6.4 presents the Engineering tensile property results for the various grain sizes tested. All specimens were fan-cooled from the annealing temperature.

Table 6.4:   Tensile Properties for β Annealed and Fan-Cooled Material with Different Grain Size

Annealing Temp/Time	Grain Size (μm)	YS (MPa)	UTS (MPa)	True-FS (MPa)	% Elongation*	% R of A
900°C/90min	187	779	855	943	6	16
950°C/3hrs	195	786	855	932	7	14
1000°C/6hrs	363	745	848	915	5	15
1050°C/15hrs	698	758	807	835	2	1.5
1100°C/7hrs	898	765	827	867	2	5.5

*Note: True-Fracture Stress is noted as "True-FS"; * = % elong. in 25mm gage length.*

The following conclusion can be drawn from the results in Table 6.4: the yield strength, fracture stress and ductility decrease with increasing grain size. This trend was presumed to be in line with the Hall-Petch law, obeying a relationship of the type:

$$\sigma = \sigma_i + K\, d^{-1/2}$$

Where σ_i = Friction Stress, K = Locking Parameter and **d** = Grain Size.

To confirm this observation, the yield and true-fracture stresses were plotted against $d^{-1/2}$; these results are presented in Figure 6.4. Two straight lines, in good agreement with the Hall-Petch relationship, could be fitted through the data.
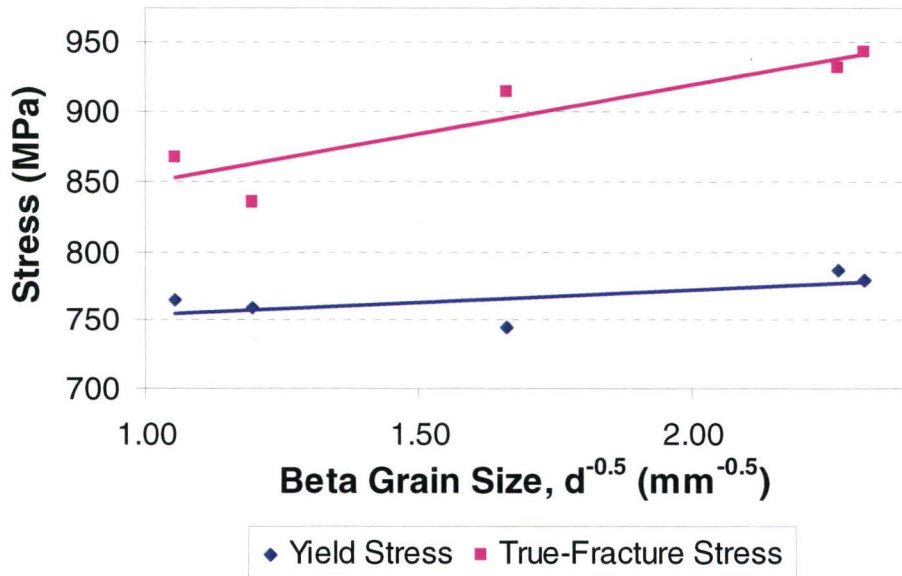
Figure 6.4: **Plot of Yield Stress and True-Fracture Stress against β Grain Size**

From the two straight lines in Figure 6.4, the following relationships between the β grain size and the yield and fracture stresses were established:

$$\sigma_Y = 736 + 17.9 \, d^{-\frac{1}{2}} \quad \text{(eq. 6.1)}$$

$$\sigma_{FS} = 776 + 71.7 \, d^{-\frac{1}{2}} \quad \text{(eq. 6.2)}$$

The slope of the yield stress (eq. 6.1) line is much smaller than that of the true fracture stress line (eq. 6.2), indicating a weak dependence of the yield stress on grain size. However, the fracture stress has a stronger dependence on the scale of the grains, the reasons for this will be addressed in more detail at the end of this Chapter.

6.1.3 Compression Properties of the β Annealed Condition

By and large, the tensile behaviour of the β annealed condition can be described possessing low strength and brittle in nature. Although limited tensile data has been published for Ti-5553, no compression data to be available for this alloy. Cylindrical rods were machined from the β annealed and fan-cooled material, excised adjacent the tensile specimens. The results are tabulated in Table 6.5; the tensile properties are also included for ease of comparison. Although all the properties are very similar, the most remarkable aspect of this data comparison is that the true-fracture stresses in tension and in compression are effectively identical. This implies that although the direction of load application is reversed, the failure mechanisms are the same. A more complete explanation will be provided later in this Chapter.

Table 6.5: **Comparison of Properties in Tension and Compression for β Annealed Fan-Cooled Heat Treat Cycles**

Label	YS (MPa)	UTS (MPa)	True-FS (MPa)	% Elongation*	% R of A
BAFC Tens.	783	855	938	6.5	15.0
BAFC Comp.	834	-	942	-	11.0

*Note: * = % elong. in 25mm gage length.*

Compression specimens of the BACCA condition were also manufactured and tested, however, due to their much higher ductility; the specimens underwent extensive plastic deformation (barreling) but did not fail. As the deformation at the core of the specimen was substantially less than at the specimen's outside diameter, it was not possible to establish meaningful values such as yield and fracture stresses. The same behaviour was encountered when testing the specimens for the STA condition.

Nonetheless, the important characteristic to note about Ti-5553 in the β annealed condition is that, its tensile and compressive fracture stresses are the same. Compression testing of the solution treated and aged conditions will be presented in the next section.

6.2 Mechanical Properties with Heat Treatments Below the β Transus

As described in Chapter 5, specimens heat treated above the β transus undergo a phase change, which results in complete recrystallization and grain growth after 20 minutes. One ensuing disadvantage is that the mechanical property benefits associated with the smaller grain size inherent in the as-forged microstructure are lost. It is for this reason that industrial heat treatments requiring peak strength are conducted below the β transus. As demonstrated in the preceding Chapter, solution heat treatment at 790°C, approximately 50°C below the β transus, does not alter the as-forged grain size as well as the size and distribution of the primary α. All specimens were fan-cooled, which provides a cooling rate sufficiently fast to retain the β phase at room temperature. The retained β is metastable and will decompose to the equilibrium α and β upon ageing. In order to establish the kinetics of the ageing process, a survey of the changes in hardness with ageing time was conducted.

6.2.1   Hardness Changes with Ageing Time at 600°C

Published reports on Ti-5553 in the literature *[24]* have shown that a desirable balance of strength and ductility is achieved with ageing the sub-transus solution treated material in the range of 550-650°C. Prior to a detailed investigation of the mechanical properties with ageing time, the kinetics of the hardening process were characterized by tracking the hardness change with ageing time at 600°C. Aside from aiding in the selection of ageing times for detailed property determination, the hardness measurements provide a prediction of the tensile properties changes for ageing up to 48 hours. Figures 6.5 (a) and (b) present the Rockwell C hardness against aging time. It is clear from Figure 6.5 (a) that an increase of 12 HRC points occurs within 30 minutes of aging start, and hardness remains relatively constant with additional ageing up to 48 hours. A more detailed account of the hardness changes occurring over the first 60 minutes can be seen in Figure 6.5 (b). From the rapid hardening response it can be inferred that the bulk of the β decomposition, in terms of α precipitation, are essentially complete within the first 30 minutes. This inference is confirmed by the investigation of the microstructure evolution already presented in Chapter 5.0.

It is important to consider that the additional aging time which resulted from cool down subsequent to solution treatment in unaccounted for in Figure 6.5. For example, the cool down time from 800°C to 300°C which is roughly 7 minutes, should be added to the total aging time. This cool down time would have contributed to diffusion driven nucleation and growth of the α phase preempting the ageing cycle.

Another observation from Figure 6.5 a) is the apparent decrease in hardness that occurs between 5 and 10 hours ageing. Although the accuracy of the testing method is ± 1HRC, it may appear that the change in hardness is within the instrument accuracy. Nonetheless, the measurements were repeated and the trend confirmed for a second time. Furthermore, the hardness survey was repeated using the Vickers (500grs) hardness scale, to rule out the possibility of artifacts due to indenter differences. Hardness surveys using both scales confirmed a temporary drop in hardness for ageing times between 5 and 10 hours, the possible reasons for this drop will be addressed with the presentation of mechanical property results.

Based on the hardness information, ageing times of 20 minutes, as well as 1, 3, 6, 13, 18, 24 and 48 hours were selected for determination of the tensile properties.

To eliminate variability, all specimens were solution treated and fan-cooled at the same time. The ageing cycles were carried out in the same furnace, with the only interruption being the opening of the furnace door to remove specimens at the prescribed times. Machining and testing of specimens was done as a group using the same equipment.
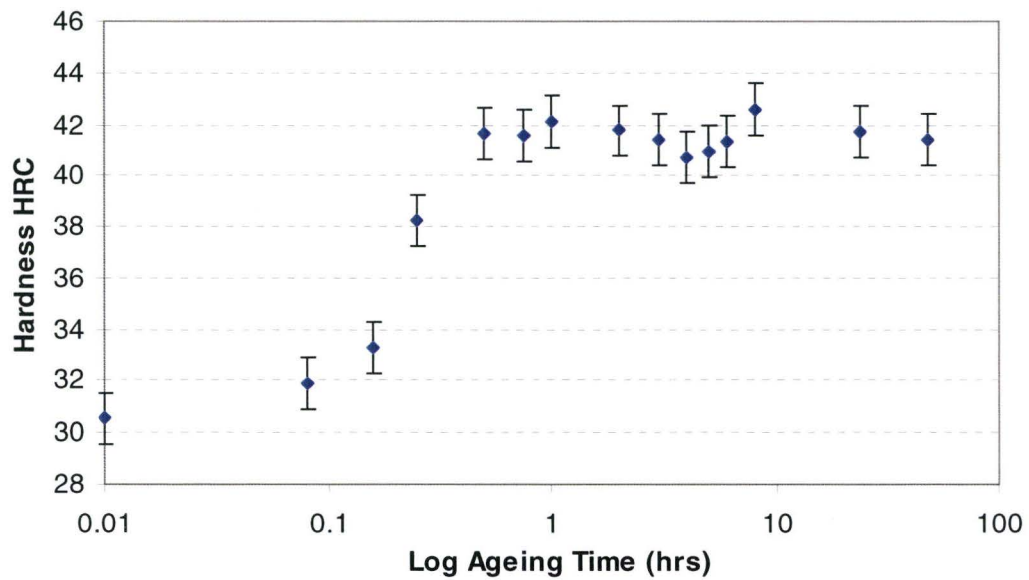
(a)
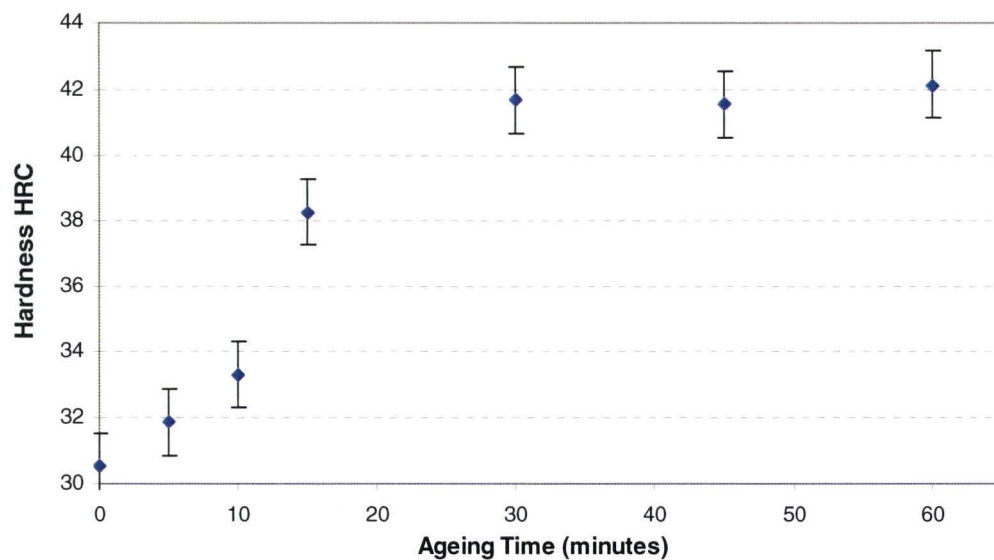
(b)

Figure 6.5   (a) Plot of Hardness versus Log of Ageing Time (ageing at 600°C);
(b) Plot of Hardness versus Ageing Time (ageing at 600°C).

6.2.2   Tensile properties after solution treatment and ageing at 600°C

As with the β annealed heat treatment cycles, a brief description of each heat treatment cycle and the corresponding labels are provided in Table 6.6. This label is composed of the letters STFC or STA, to differentiate the solution treated fan-cooled and the solution treated, fan-cooled and aged cycles, followed by a hyphen and one or two digit numbers, referring to the ageing time in hours. Tensile specimens were machined from plates of 20mm thick material which were solution treated, fan-cooled and aged for the times noted; the average tensile properties are summarized in Table 6.7. The cooling rates resulting for fan-cooling are in line with those presented in Figure 4.7.

The Engineering Stress-Strain curves for four representative specimens are shown in Figure 6.6; curves for the other conditions were very similar and have been omitted for clarity. In the solution heat treated condition, Ti-5553 has a yield strength of ~860 MPa and an ultimate tensile strength of ~900 MPa. These values are comparable to annealed Ti-6Al-4V.

After ageing for 20 minutes, the yield strength increases to ~1200 MPa and the tensile strength reaches ~1300 MPa. This rapid increase in tensile properties is in line with the hardness versus time measurements presented earlier, and with the massive precipitation of lenticular α needles observed and discussed in the Microstructure Evolution - Chapter 5.0. Beyond the yield point, all engineering stress-strain curves reach a maxima and display either a plateau or decreasing slope up to fracture.

However, the most striking observation derived from Table 6.7 is the constancy in the yield and ultimate tensile strengths with ageing time greater than 20 minutes. The tensile properties remain more or less constant from 20 minutes up to 48 hours. This result has important practical implications for heat treatment of industrial structures such as landing gears, since ageing times can vary significantly within the thick and thin sections of a given component.

In terms of ductility measurements, the % elongation and % reduction of area are relatively high after solution treatment - higher than those for annealed Ti-6Al-4V. However, these values decrease rapidly after aging for 20 minutes, and then gradually increase, reaching a peak at approximately 6 hours. The peak in ductility is in line with the hardness drop depicted in Figure 6.5 (a) – where the hardness response was plotted against aging time. With over-aging, the ductility decreases gradually to levels similar to those observed after ageing for 0.3 to 1 hour.

Table 6.6:   **Summary of heat treatments with corresponding labels**

Label	Description of Heat Treatment
STFC	ST at 790°C for 2hrs, fan-cooled
STA-0.3	ST at 790°C for 2hrs, fan-cooled, aged at 600°C for 20 min.
STA-1	ST at 790°C for 2hrs, fan-cooled, aged at 600°C for 1hr
STA-3	ST at 790°C for 2hrs, fan-cooled, aged at 600°C for 3hrs
STA-6	ST at 790°C for 2hrs, fan-cooled, aged at 600°C for 6hr
STA-13	ST at 790°C for 2hrs, fan-cooled, aged at 600°C for 13hrs
STA-18	ST at 790°C for 2hrs, fan-cooled, aged at 600°C for 18hrs
STA-24	ST at 790°C for 2hrs, fan-cooled, aged at 600°C for 24hrs
STA-48	ST at 790°C for 2hrs, fan-cooled, aged at 600°C for 48hrs
STA5-1	ST at 790°C for 2hrs, fan-cooled, aged at 500°C for 1hr
STA5-3	ST at 790°C for 2hrs, fan-cooled, aged at 500°C for 3hrs

Table 6.7:   **Engineering tensile properties after ageing at 600°C for various times**

Label	Age time (hrs)	YS (MPa)	UTS (MPa)	% Elongation*	% R of A
STFC	0	858	900	16.0	46.0
STA-0.3	0.3	1234	1310	5.0	13.0
STA-1	1	1234	1307	6.0	12.5
STA-3	3	1241	1289	7.0	20.0
STA-6	6	1245	1310	8.0	22.0
STA-13	13	1214	1258	8.5	22.0
STA-18	18	1224	1262	5.0	18.5
STA-24	24	1279	1307	5.5	13.0
STA-48	48	1279	1307	5.5	13.0

*Note: * % elong. in 25mm gage length.*
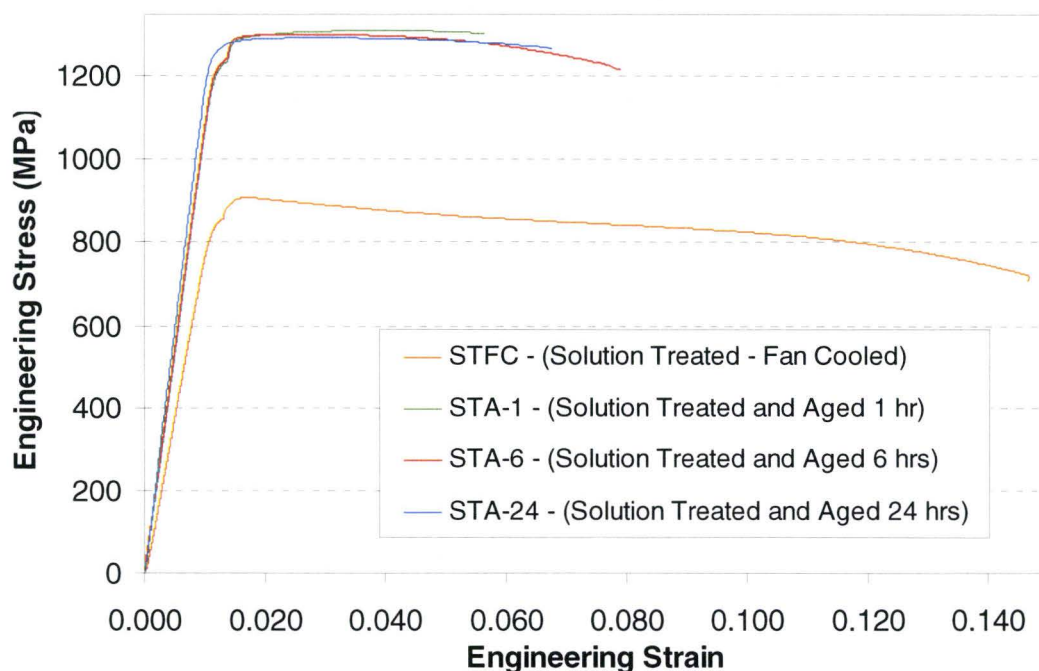
Figure 6.6:   Engineering stress-strain curves for selected ST cycles

The true stress-true strain plots for four selected heat treat conditions are presented in Figure 6.7. These 4 curves are deemed representative of the spectrum of tensile properties; plots of the other ageing conditions are very similar and have been omitted for clarity. Dotted lines indicate extrapolated data between the point of instability and the true fracture stress for which instantaneous cross section measurements are not available.

The fracture strain, fracture stress, and strain hardening rate $d\sigma/d\varepsilon$, from maximum load to fracture, have been calculated for the curves shown in Figure 6.6 and are presented in Table 6.8. Several important observations can be made from the data presented in Tables 6.7 and 6.8:

i)   there is a marked increase in the flow stress from the un-aged to the aged conditions:

ii)   despite the microstructural changes occurring with ageing, the fracture stress remains relatively constant between the aged and un-aged conditions.

iii)   in general, the strain hardening rate, $d\sigma/d\varepsilon$, is inversely proportional to the fracture strain.

One conclusion that can be deduced from the constancy of the fracture stress is that fracture mechanism must also be invariant between these conditions. Furthermore, the damage and fracture processes must be related to a microstructural feature common to the un-aged and aged conditions. As the solution treated condition has been shown in the previous Chapter to have a different microstructure that the aged condition, the fracture process appears to have little to no dependence on the microstructural changes occurring during ageing. It follows that the transformation of the retained β matrix to lenticular α plus β which occurs with ageing, has a

drastic effect on the strength and ductility, but does not affect the fracture mechanism. Analysis of the fracture mode will be addressed in a separate section.
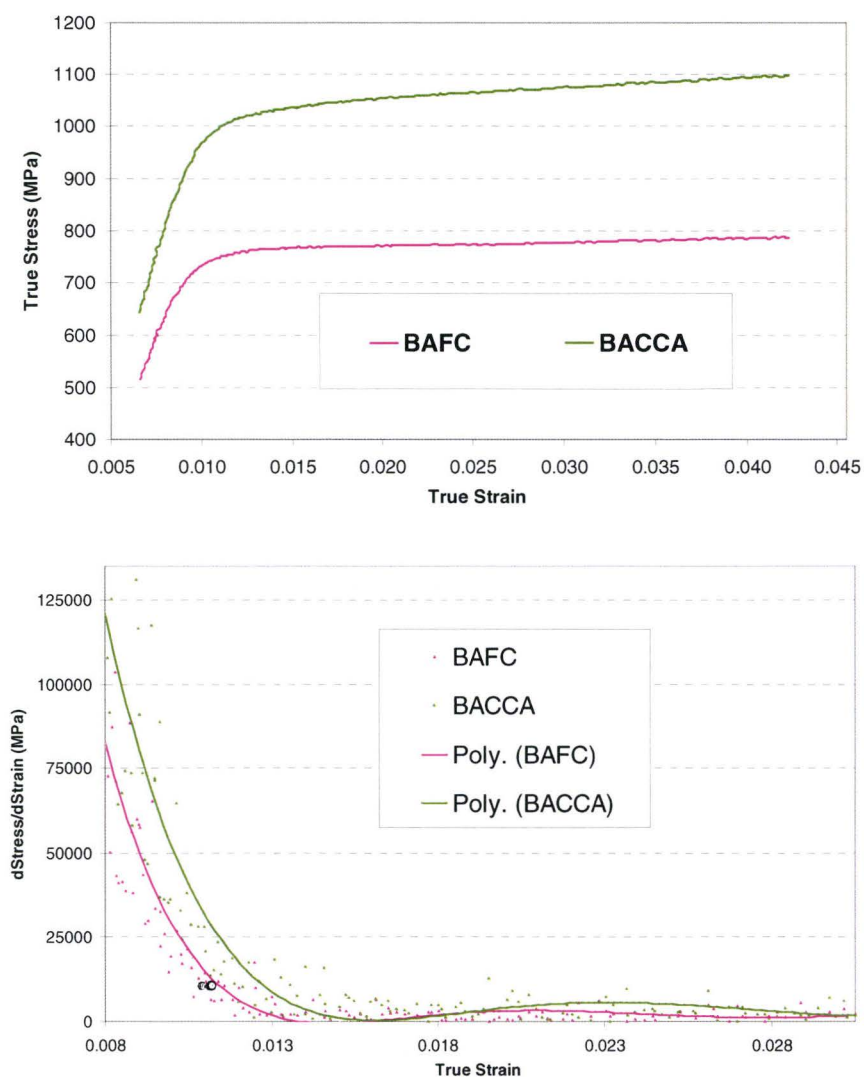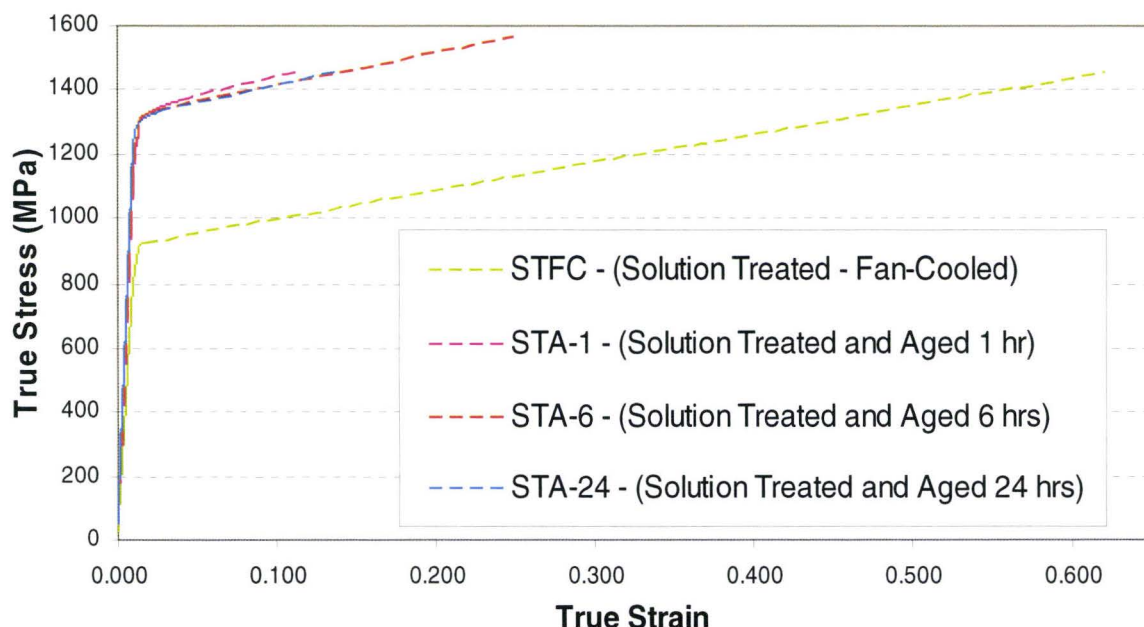

Figure 6.7:   True Stress-True Strain curves for Selected ST Heat Treat Conditions

Table 6.8:   Tensile Fracture Strain, Fracture Stress and Strain Hardening Coefficients for the Various Heat Treat Cycles

Label	Fracture strain	Fracture stress (MPa)	Slope of line, $d\sigma/d\varepsilon$ (MPa)*
STFC	0.63	1453	888
STA-1	0.12	1460	1255
STA-6	0.25	1566	1039
STA-24	0.14	1457	1153

$d\sigma/d\varepsilon$ = is the slope of the strain-strain line from maximum load to fracture

Although somewhat higher than those for the β annealed group of heat treatments, the strain hardening rates are relatively low when compared to steels and point to low work hardening behaviour.

Analysis of the strain hardening rate on the transition from elastic to plastic behaviour has been characterized by plotting the rate of change in stress and strain beyond plasticity. The regions of the curves studied and the corresponding $d\sigma/d\varepsilon$ versus ε are presented in Figure 6.8.
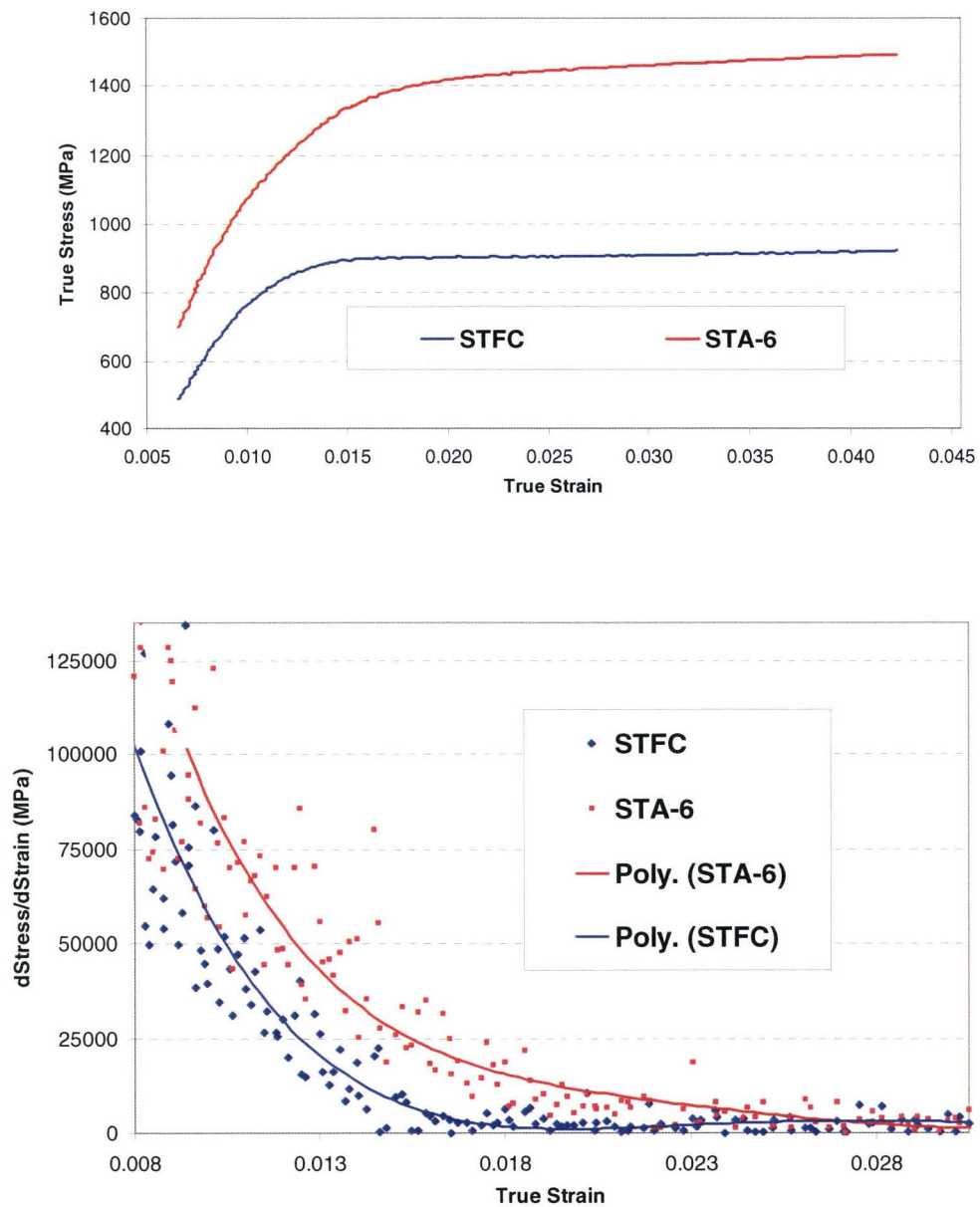
Figure 6.8:   Top - Portion of the True Stress-True Strain Curves Analyzed; Bottom – Plot of $d\sigma/d\varepsilon$ versus ε for the STFC and STA-6 Conditions

A polynomial function has been fitted to the data plotted in Figure 6.8 – bottom to help visualize the rates of change. Note that the data becomes asymptotic at a value of approximately 1500MPa, which represents the true stress at maximum load for the two conditions. This plot illustrates that the work hardening rate for the STA-6 condition is greater than that for the STFC condition; at a strain of 0.0125, the rate of change of the STA-6 is double that of the STFC. This observation and the higher strain hardening rate in the linear portion of the curve imply that transformations during ageing increase both, the strength and the work hardening capability of the material. A more detailed discussion of the effect of the work hardening rate on the deformation and fracture mechanisms will follow in the Discussion section of this Chapter.

6.2.3 Tensile Properties After Solution Treatment and Ageing at 500°C

Based on observations of the microstructure in similar β titanium alloys, ageing Ti-5553 at lower temperatures should result in finer-scale α precipitates leading to higher tensile strengths. To asses the effect of lower temperature age cycles, specimens were aged at 500°C for 1 hour and 3 hours. These specimens were labeled STA5-1 and STA5-3, respectively; a full description of the heat treatment cycle is contained in Table 6.6. The tensile results are presented in Table 6.9; for comparison, results of specimens aged at 600°C for the same times (STA-1 and STA-3) are also presented.

Table 6.9:   Engineering Tensile Properties after Ageing at 500°C and 600°C

Label	Age Temp. (°C)	Age Time (hrs)	YS (MPa)	UTS (MPa)	True-FS (MPa)	% Elong.*	% R of A
STA5-1	500	1	1289	1410	1512	2.5	4.5
STA5-3	500	3	1469	1513	1611	3.0	4.0
STA-1	600	1	1234	1307	1473	6.0	12.5
STA-3	600	3	1241	1289	1535	7.0	20.0

*Note: True-Fracture Stress is noted as "True-FS"; * = % elong. in 25mm gage length.*

As anticipated, ageing at 500°C increases the yield and ultimate tensile when compared to material aged at 600°C. This increase in strength is accompanied by a reduction in ductility, namely the % elongation decreases by a factor of two, while the % reduction of area decreases by a factor of roughly four. However, the true fracture stresses for materials aged at 500°C is higher that those for material aged at 600°C. Nonetheless, these values vary by less than 5%, which implies that the fracture mechanisms must also be similar. Comparing the results of the un-heat treated material to those after ageing at 500°C and 600°C, it can be concluded that the scale of the retained β decomposition products, i.e. lenticular α, does not significantly affect the damage and fracture processes.

6.2.4   Compression properties of the solution treated and aged condition

Compressive properties are important criteria for component design. To measure the properties in compression and to understand the effect of loading direction on the fracture process, compression specimens 10mm in diameter by 15mm in length were compression tested to failure. These rods were machined from the same material block and axial orientation as the tensile specimens that had been aged for 6 hours at 600°C. The results are presented in Table 6.10 together with the tensile results for comparison. Figure 6.9 presents the stress-strain curves for rods tested in compression. Comparing the average fracture stress in tensile and compression for the same condition we find that the fracture stresses are virtually identical (σf (tension) = 1581MPa, σf (comp.) = 1582 MPa). From this data a conclusion similar to that for the β annealed condition can be drawn, the fracture mechanism must be the same in tension as it is in compression.

Table 6.10:   Comparison of Properties in Tension and Compression for theSTA-6 Condition

Label	YS (MPa)	UTS (MPa)	Fracture Stress (MPa)	% Elongation*	% R of A
STA-6 Tens.	1245	1566	1581	6.5	15.0
STA-6 Comp.	1266-	-	1582	-	16.0**

*Note: * % elong. in 25mm gage length. ** based on barreling diameter*
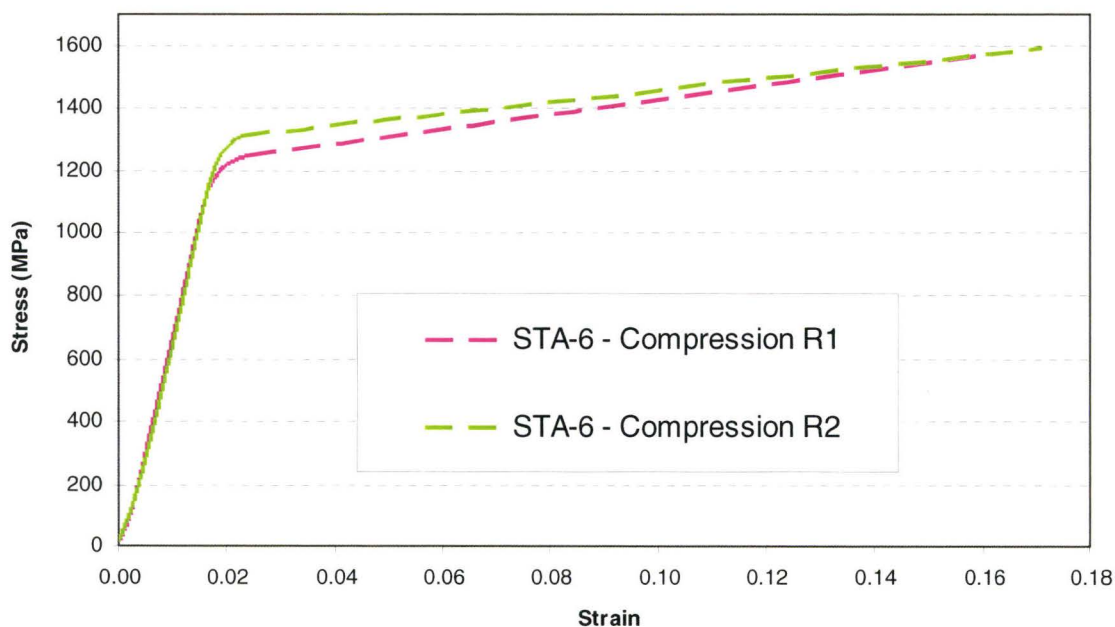
Figure 6.9:   Plot of Stress–Strain for Rods Aged For 6 Hrs at 600° C Tested In Compression

6.2.4.1 Tensile and Compression Properties for Ti-10-2-3 in the STA Condition

In order to ascertain whether this behaviour is also observed in other β titanium alloys or unique to Ti-5553, tension and compression tests were conducted for Ti-10V-2Fe-3Al specimens. Ti-10-2-3 is the most commonly used alloy for landing gear structures today. The properties in tension and compression for Ti-10-2-3 in the solution treated and "peak" aged condition are presented in Table 6.11, the label applied is STA1023. Note that the yield stress in compression could not be determined due to unavailability of a working compressometer.

It is evident that Ti-10-2-3 in the STA condition also exhibits the same fracture stresses in tension and in compression.

Table 6.11:   Comparison of Properties in Tension and Compression for Ti-10-2-3 in the STA Condition

Label	YS (MPa)	UTS (MPa)	Fracture Stress (MPa)	% Elongation*	% R of A
STA1023 Tens.	1179	1251	1474	7	21.0
STA1023 Comp.	-	-	1421	-	20.5

*Note: * % elong. in 25mm gage length.*

The tensile and compression properties for Ti-5553 in the BAFC and the STA conditions, as well as those for Ti-10-2-3 are summarized in Table 6.12. It is clear that the fracture stresses in tension and compression are the same, which is unlike the behaviour of the majority of engineering materials. A rationalization for of this behaviour will be presented in the Discussion section of this chapter.

Table 6.12:   Comparison of Properties in Tension and Compression

Label	YS (MPa)	UTS (MPa)	Fracture Stress (MPa)	% Elongation*	% R of A
STA-6 Tens.	1245	1566	1581	6.5	15
STA-6 Com.	1266	-	1582	-	16
STA1023 Tens.	1179	1251	1474	7	21.0
STA1023 Comp.	-	-	1421	-	20.5
BAFC Tens.	783	855	938	6.5	15
BAFC Com.	834	-	942	-	11

6.2.4.2 Shear Properties of the Solution Treated and Aged Condition

The shear properties are also an important consideration in design of engineering structures. Measurement of shear properties can be more complicated than the standard tension and compression properties. Often, the shear strength of a material is determined by a specimen subject to torsion tests, however, pin and punch tests are sometimes used. The results will depend on specimen size and configuration. The fracture stress in shear for the STA condition was determined using a top hat specimen described in the Experimental section of this thesis. Attempts at measuring the fracture stress in shear for other conditions such as the STFC condition resulted in excessive error. This error was associated with the high ductility of the material and the dimensions of the specimens. All specimens showed some degree of buckling and consequently were found to be subject to bending instead of pure shear loading. Nonetheless, the results for the STA condition were deemed accurate as no buckling was found upon analysis of the cracked specimens.

The fracture stress for the STA-6 condition in shear was found to be: τ_f = **890 MPa**.

6.2.5   Additional Properties of the Solution Treated and Aged Condition

Consideration of a new alloy for design must take into account a comprehensive review of material behaviour. The properties of the β annealed group of heat treatments, particularly those attained with controlled cooling, are attractive when higher ductility is required. As demonstrated in the previous sections, Ti-5553 in the solution treated and aged condition is capable of higher tensile strengths than in the β annealed condition. Furthermore, Ti-5553 has a higher tensile strength than Ti-10-2-3 for an equivalent ductility (see Tables 6.10 and 6.11). In spite of the attractive tensile, compressive and shear strengths, other properties such fracture toughness and resistance to environmental degradation are essential to complete the assessment. An ever present consideration is the alloy's resistance to stress corrosion; typically these properties are assessed in an aggressive environment such as salt water fog or alternate immersion in salt water. The following sections present fracture toughness and stress corrosion cracking results for variations of the STA condition.

6.2.5.1 Fracture Toughness for the Solution Treated and Aged Condition

A significant difference can be found in the fracture toughness of β titanium alloys depending on heat treatment condition. For example, values between 30 and 100MPa√m have been reported in the literature for various alloys and conditions. *[10]*

Although fracture toughness is not a primary design requirement in Landing Gear stress calculations, this property is always kept in mind by designers to assess the ability of an alloy to resist fracture in the presence of a crack. The fracture toughness of Ti-5553 in two heat treated conditions was assessed using the compact C-type specimen and methodology described in Chapter 4. The heat treatments used were variations in the STA conditions characterized earlier and are labeled as STA-X and STA-Y, and were recommended by the material supplier. The STA-X cycle involved a single solutionizing step at 820°C for 3 hours followed by ageing at 600°C for 8 hours. The STA-Y heat treatment consisted in two solutionizing steps, one at 820°C and 804°C each for 3 hours, followed by ageing at 600°C for 8 hours. These heat treatments represent slight variations of the STA-6 condition. The material supplier anticipated that a double solution heat treatment would increase Fracture Toughness as reportedly observed in similar alloys. The results are presented in Table 6.13, the test orientations are noted.

Table 6.13:   Fracture Toughness Values for Two Heat Treated Conditions

Test Orientation (as defined in Chapter 4)	STA-X K_{IC} (MPa√m)	STA-Y K_{IC} (MPa√m)
C-L	33.0	31.3
C-L	38.3	31.5
R-C	36.6	34.1
R-C	29.2	31.3
Average	34.3	32.1

It is evident from the results that the double solution heat treatment cycle does not offer any improvements in fracture toughness, which would be expected, based on the similarity of the microstructures. Nonetheless, these results are included to increase the data pool and obtain an overall appraisal of the fracture toughness capability of Ti-5553. Industry specifications for Ti-10-2-3 require a minimum of 44 MPa√m in the STA condition, but values closer to 50 MPa√m are typical. The average of all results for Ti-5553 in the STA condition is 33.2 MPa√m, which is roughly 1/3 lower than the typical value for Ti-10-2-3. The microstructural basis for the lower fracture toughness is presented in the Discussion section of this Chapter.

6.2.5.2 Resistance to Stress Corrosion Cracking

Determination a material's resistance to stress corrosion cracking (SCC) is normally assessed in two ways, each dealing with a different failure mode:

1) - initiation of a stress corrosion crack and specimen failure in the absence of a flaw or crack, and
2) - propagation of an existing flaw or crack under conditions conducive to stress corrosion or K_{ISCC}.

Based on these separate processes, two different types of SCC tests were conducted. The specimens were excised from forged bar in the STA-6 condition with the grain orientations noted. The environments used for the evaluations involve NaCl, which is considered the benchmark for the aerospace industry.

The specimen used for the onset of SCC was the "C" ring specimen per ASTM G38, as described in Chapter 4.0. The specimen's axis was oriented perpendicular to the bar's forging direction; this orientation is referred to as the short transverse direction. The test conditions are summarized in Table 6.14.

Table 6.14:   Summary of "C" Ring Stress Corrosion Results

Heat treat cycle	Stress (MPa - 85% of YS)	Specimen orientation/duration
STA-6	1090	**Short transverse/60 days**

The applied stress was 1090MPa (85% of YS) in an alternate exposure consisting of 10 minutes immersion in the salt water (3.5% NaCl), followed by 50 minutes drying cycles. The specimen passed 60 days without failure. The test environment and test duration were in line with requirements for titanium alloys and considered to be severe for most materials.

As explained in detail in Chapter 4.0, the resistance to crack propagation by SCC was determined by means of the 1.0-C(T) Modified WOL K_{ISCC} specimen. The load was applied by a fine-threaded bolt, implying constant displacement conditions. The specimens were pre-cracked in fatigue and subjected to stress intensity levels corresponding to 75% of the K_{IC} value. The stress intensity was later increased to the higher levels shown in Table 6.14 due to the negligible crack growth observed at the initial stress levels. Four specimens, two longitudinal and two transverse, were tested for 100 hrs at a temperature of 24°C.

Determination of K_{ISCC} was in accordance with ASTM E1681, by the following:

$$K_{ISCC} = P / [(BW)^{\frac{1}{2}}] * f(a/W)$$

Where P is the load, B is the specimen thickness, W is the specimen width, a is the crack length and the term $f(a/W)$, is available from tables in ASTM E399 - for each ratio of a/W.
The test results are provided in Table 6.15.

Table 6.15: **Summary of K_{ISCC} Results**

Specimen Orientation	Stress Intensity (MPa√m)	K_{ISCC} (MPa√m)
Longitudinal	35.1	29.0
Longitudinal	34.5	29.1
Transverse	32.5	29.6
Transverse	32.4	28.5
Average	33.6	29.1

A number of validity checks apply to the determination of the K_{ISCC}, two out of the four specimens tested failed the validity criterion in terms of the perpendicularity of the crack to the specimen sides. However, the degree of crack misalignment was relatively small and the results still provide useful information on the alloy's resistance to SCC.

Comparing Ti-5553 to other β alloys such as, Ti-10-2-3 and Beta C, Ti-5553 has a relatively high resistance to K_{ISCC}. However, as the method of determination of K_{ISCC} is based on the K_{IC} specimens, and since Ti-5553 has a relatively low K_{IC}, its average K_{ISCC} value is lower than for other β alloys.

In general terms, Ti-5553 has a high resistance to crack initiation and crack propagation by means of stress corrosion, which is characteristic of all titanium alloys in the environments assessed here [4] [12].

6.2.6   Optimization of Mechanical Properties

Although the heat treatments conducted above the β transus provided higher ductility, the strength levels achieved were similar to those obtained in Ti-6Al-4V. For example, a tensile strength of 1100MPa was determined for the BACCA condition. The strength levels are deemed too low for weight efficient design of landing gear components. The industrial interest in Ti-5553 is in the heat treatments below the β transus, where tensile properties superior to those of Ti-10-2-3 have been demonstrated. In has been shown in Table 6.9 that tensile strengths between 1300MPa and 1500MPa can be achieved by solution treating at 790°C and ageing between 600°C and 500°C, respectively.

As a final step in the investigation of the tensile properties of Ti-5553, a heat treat optimization study was conducted; this study involved a combination of two solution heat treatment temperatures and four ageing temperatures. In this manner, eight distinct heat treatment cycles were produced, with three tensile specimens tested for each cycle. This investigation was done in conjunction with TIMET Corporation, some of this work has been published in the literature [24]. The material employed was in the form of discs 178mm in diameter by 89mm thick from a Ti-5553 round bar produced by TIMET Corporation. The β-transus for this bar was 852°C, as determined metallographically. The mechanical properties resulting from solution treatment and ageing at various temperatures are presented in Table 6.16. For ease of comparison, the tensile strength and % elongation versus ageing temperature have been plotted as bar charts for the two solution temperatures, see Figure 6.10.

Table 6.16:   Tensile Properties after Solution Heat Treatment at the Specified Temperature for 3.0 hrs, Followed by Air Cooling and Ageing for 8 hrs at the Temperatures Specified

Solution Temp.(°C)	Ageing Temp.(°C)	UTS (MPa)	YS (MPa)	% Elongation*	% Red. of Area
804	610	1292	1217	9.0	22.6
804	627	1257	1171	10.3	22.4
804	643	1200	1131	10.3	26.9
804	660	1176	1099	11.7	26.8
832	610	1335	1236	5.3	11.1
832	627	1288	1186	6.0	10.3
832	643	1249	1155	8.3	18.7
832	660	1198	1103	9.3	20.8

*Note: * % elong. in 25mm gage length.*
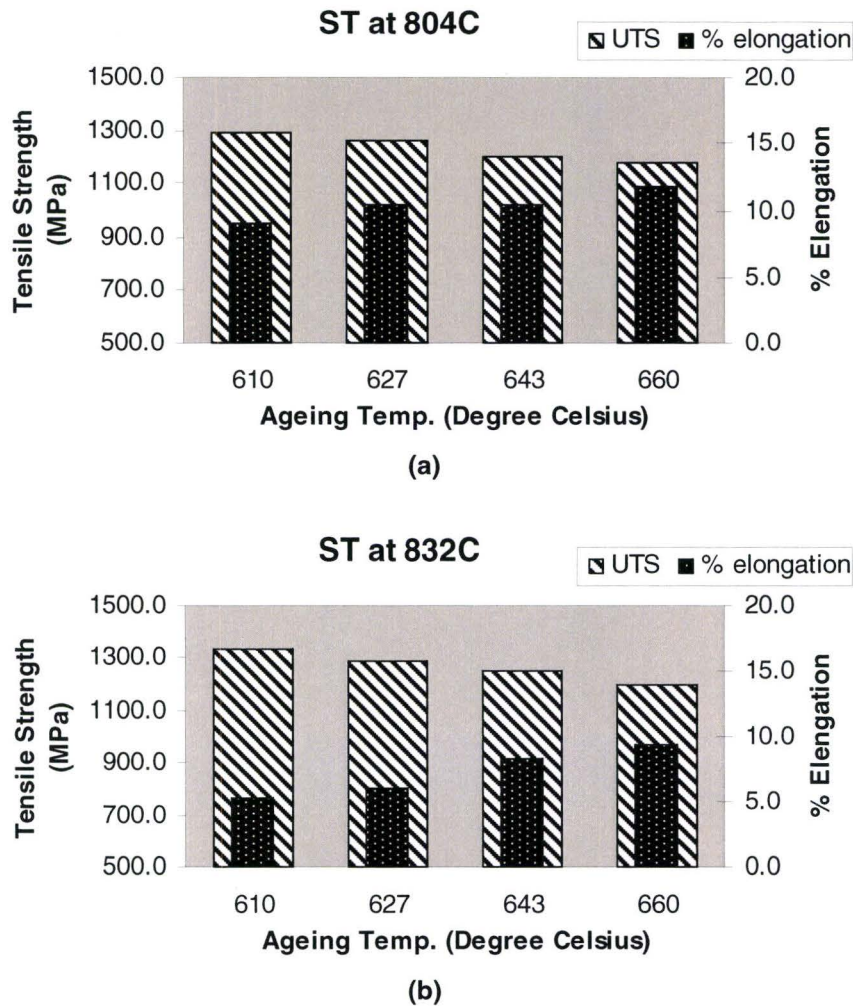
Figure 6.10   Bar Plot of Tensile Strength and % Elongation versus Ageing Temperature for: (a) Solution Treatment At 804°C; (b) Solution Treatment at 832°C

Comparing the tensile results, it is clear that increasing the solution heat treatment temperature has a small incremental impact on strength, but a large reduction in ductility. The reasons for this disproportionate ductility reduction can be understood by comparing the microstructures. Figure 6.11 presents the microstructures of the material solution treated at 804°C and 832°C and aged at 610°C. The volume fraction of primary α resulting from solution heat treatment at 804°C was found to be approximately 16%, while 6% primary α was found after solution heat treatment at 832°C. Hence, for any ageing temperature selected, reducing the volume fraction of primary α, or alternatively, increasing the volume fraction of aged β, has the effect of increasing the strength to some extent - but reducing ductility significantly. In other words, the primary α phase plays the dominant role in controlling the ductility by accommodating a higher degree of plastic deformation than the aged β phase.
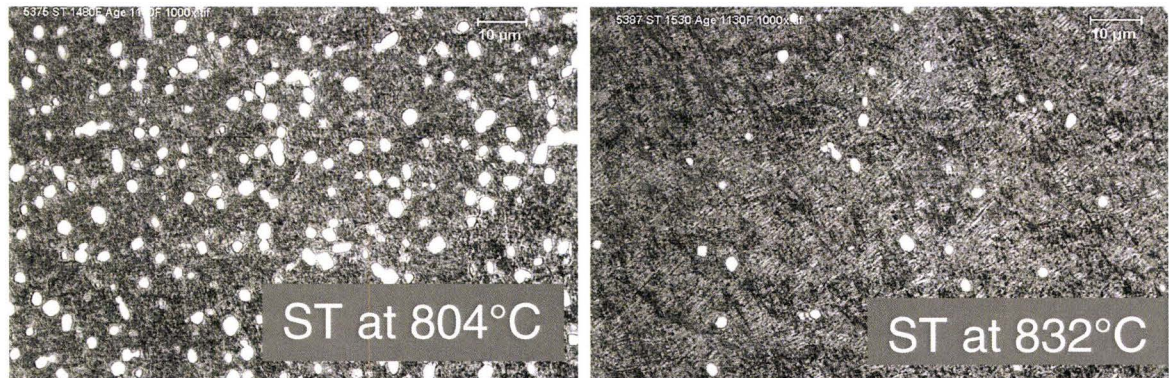
Figure 6.11: **Microstructures Of Material Solution Treated At 804°C (Left) And 832°C (Right), and Aged At 610°C. Etched in Kroll's Reagent**

The second important trend that can be deduced from analysis of the data is that increasing the ageing temperature decreases the tensile strength and increases ductility. Since the ageing response is related to the volume fraction of retained β, this strength/ductility trend effect is more pronounced for the material solution treated at 832°C, which contains 10% more retained β.

After consideration of the above data, the preferred solution heat treatment temperature was determined to be 50°C below the β-transus, which provides for higher ductility with no loss of strength. In terms of primary α volume fractions, a target range between 15-20% provides the optimal balance between strength and ductility.

Selection of the ageing temperature is related to strength/ductility targets and varies for specific applications. Typically, a minimum elongation target of 6% is stipulated in landing gear designs, which would suggest an ageing temperature of 610°C or lower. However, because of chemical composition variability between heats of material, the ageing temperature must be carefully selected for each material heat. To simplify this process, Table 6.16 provides useful guidelines for ageing temperature selection.

6.3   Fracture Mode Evaluation

In general terms, three salient points can be made from analysis of the mechanical properties:

(i)   The range in tensile properties varies significantly between the BA and ST group of heat treat cycles - a similar range is observed within each heat treatment group.

(ii)   The true-fracture stresses in tension and in compression are of similar magnitude for a given heat treatment group – these stresses are identical for a given heat treat condition.

(iii)   All conditions displayed a relatively low strain hardening behaviour. It is clear from the differences in mechanical properties between the heat treatment cycles characterized that plastic deformation and fracture processes must be greatly influenced by the microstructures. Starting with the β annealed group of heat treatments, the following sections will delve into the deformation and fracture mode in an effort to rationalize the impact of the microstructure on properties.

6.3.1   Deformation and Fracture for the β Annealed Group of Heat Treatments in Tension

In summation, the BAFC condition displays low strength and low ductility; the BAST and BASTA are essentially so brittle in nature, that a meaningful determination of properties could not be made using the standard specimen configuration. In comparison, the BACCA condition possesses moderate strength and, elatively high ductility. Figure 6.12 presents a compilation of low magnification SEM images of the fracture surfaces of tensile specimens. A general, comparison of the macro-scale fracture for the four conditions will be conducted jointly. However, since the mode of fracture for each condition was quite different, a detailed assessment for each condition will be presented separately.

General comparison:

The fracture surface of the BAFC condition contains flat faceted features separated by regions containing dimples indicative of ductile tearing. As shown in Figure 6.12 (a), limited necking and absence of a shear lip are evident, which are consistent with the low ductility results obtained.

All the BAST and BASTA specimens failed at the threaded grips, see Figure 6.12 (b) and (c), and displayed a relatively flat fracture surface with no shear lip features.

In contrast, the BACCA fracture surface exhibited extensive shear lip features and dimple morphology throughout the fracture face. The fracture topology was jagged and rough textured, based on the smaller cross section at fracture - it is clear that extensive necking had taken place.

(a) BAFC

(b) BAST
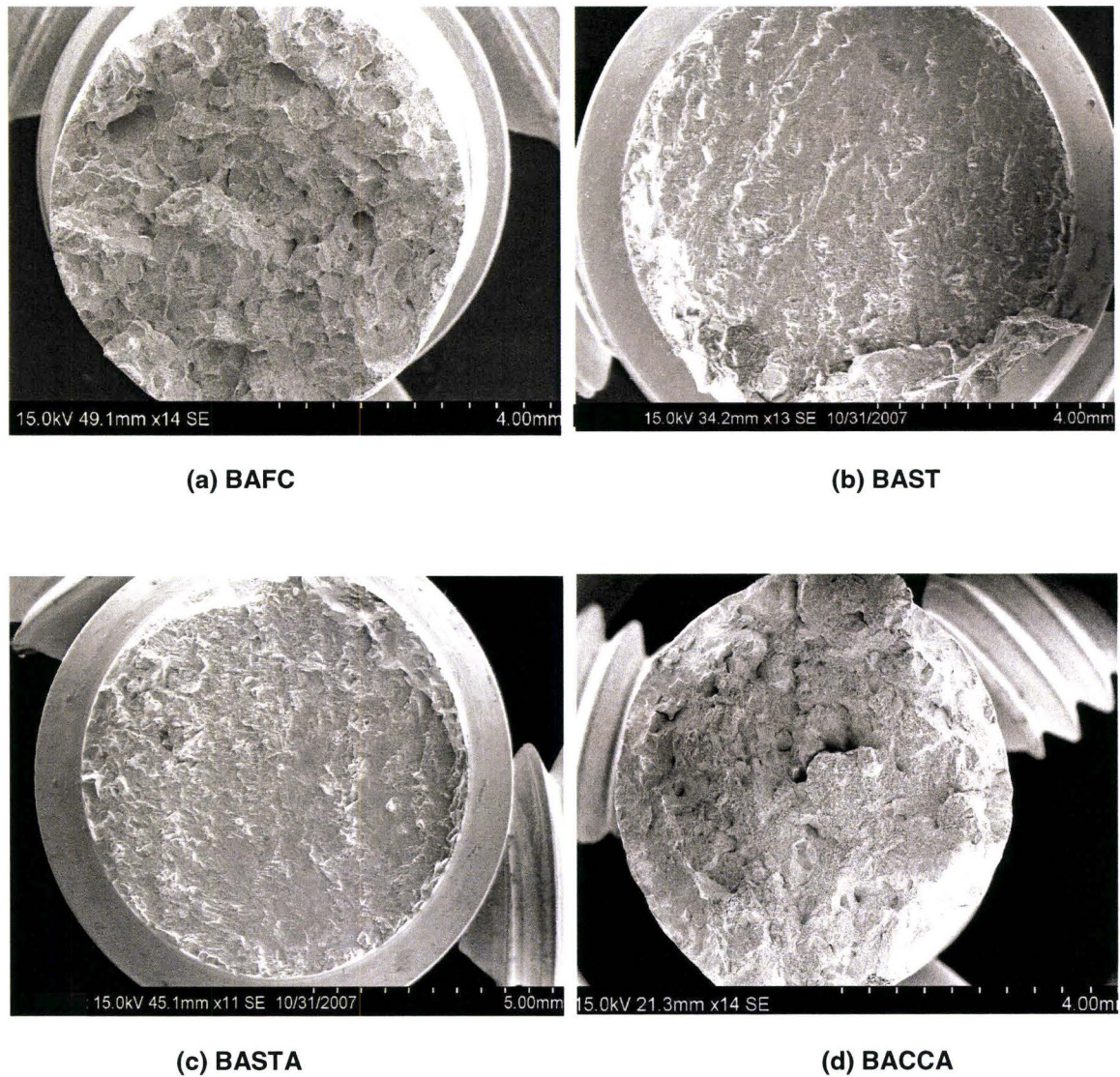
(c) BASTA

(d) BACCA

Figure 6.12:   SEM images of fractured tensile specimens for the following conditions: (a) BAFC; (b) BAST; (d) BASTA; (d) BACCA.

6.3.1.1 Deformation and Fracture of the BAFC Condition

Under the SEM, the overall fracture morphology consisted of large flat facets separated by dimple regions, see Figure 6.13. The facet features were not unlike those characteristic of intergranular fracture as their span was in line with the specimen's grain size. However, at high magnifications, these facets were covered in arrays of shallow dimples with linear ridges of larger sized dimples. As depicted in Figure 6.13, some of the ridges were parallel to one another, but many intersected across the flat facets.

To better understand this peculiar fracture morphology, a fractured specimen was sectioned longitudinally and metallographically prepared for observation. Figure 6-14 is a collage of optical images of the specimen's cross section; note that 10-20μm of nickel have been deposited over the fracture surface for better edge retention. These images provide a clear explanation for the features observed on the fracture surface; the entire cross section contained clearly defined slip lines, some of which have developed into trans-granular cracks.

Figure 6.13: SEM images of fracture surface for a BAFC specimen. Fracture morphology contains facets, separated by regions containing dimples (top left). At high magnifications, (top and bottom right), the facets contain parallel and intersecting ridges made up of shallow dimples. The facets also contain a periodic pattern of very shallow dimples.
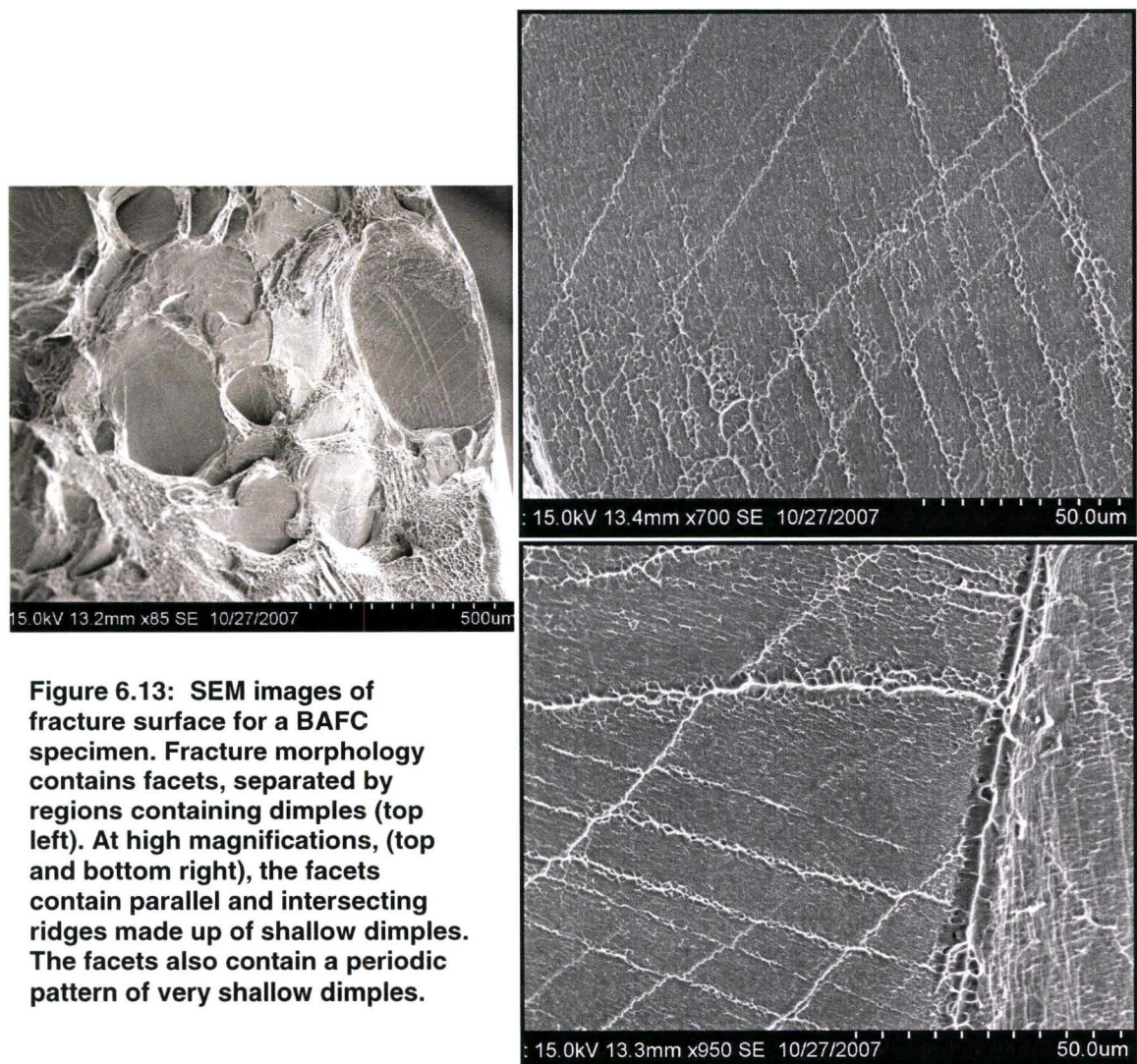
The fact that the slip lines are visible at low magnification is indicative of a highly localized slip process. Scanning the fractured edge, see Figures 6.14 and 6.15, it is evident that the fracture is transgranular - along the cracks created by the localized slip mechanism. The dimple regions in Figure 6.13 are the 'ligament' regions, were the trans-granular cracks failed to connect resulting in ductile-tearing and dimple rupture. A plausible explanation for the localized slip phenomenon observed will be addressed in the Discussion section of this chapter.
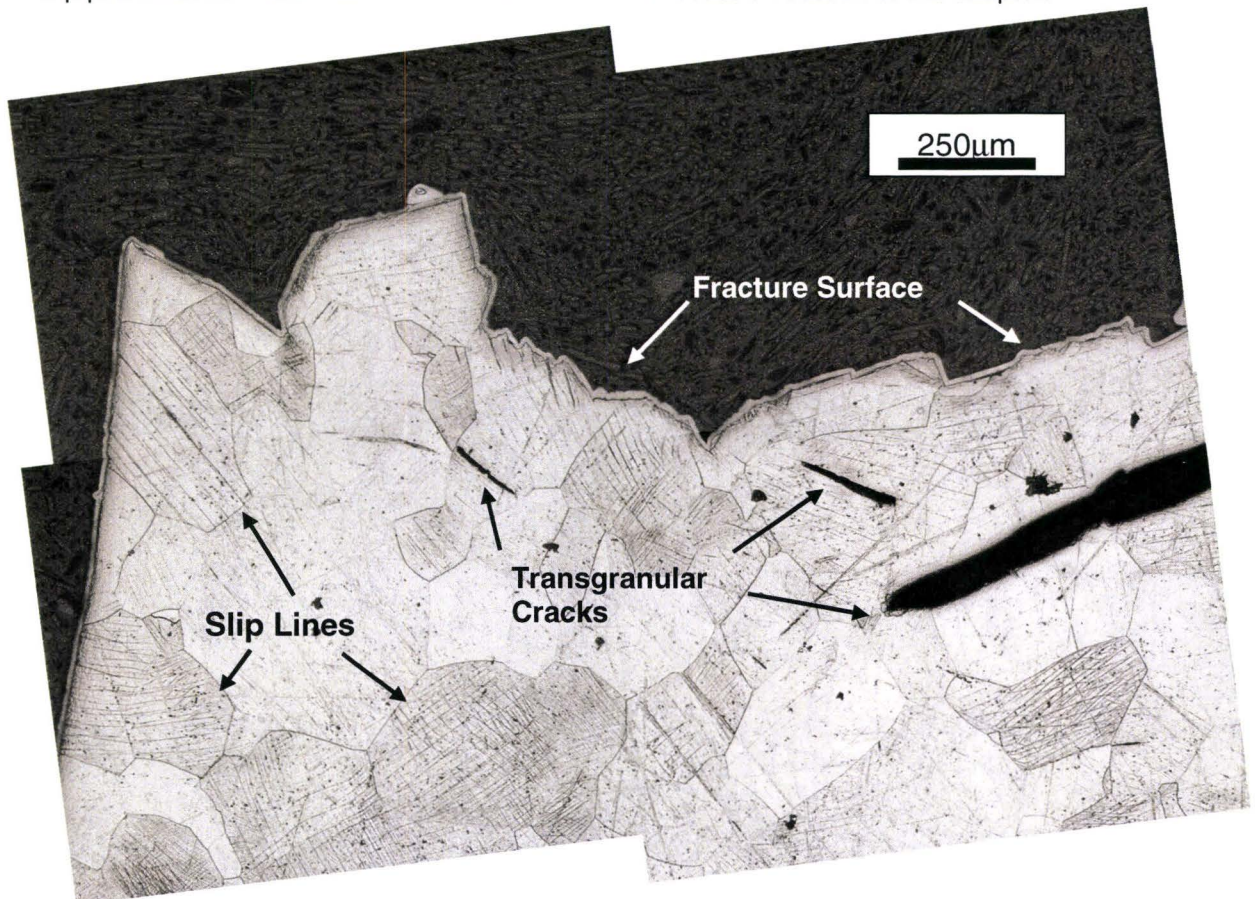
Figure 6.14: Collage of optical images of fractured specimen's cross section. Etched in Kroll's reagent.
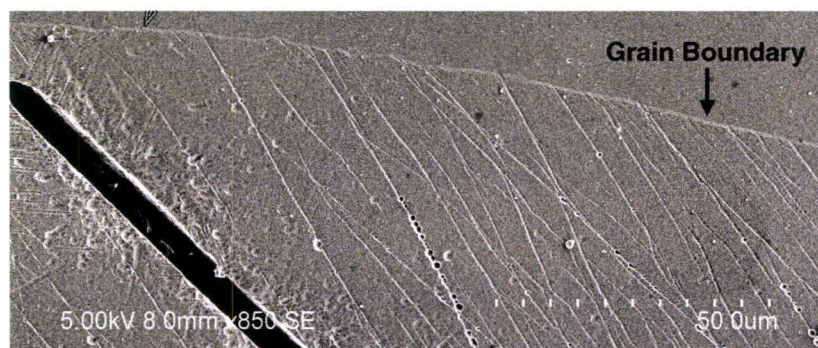
Figure 6.15: SEM image of slip bands and crack

6.3.1.2 Deformation and fracture of the BAST and BASTA conditions

Both of these conditions possessed very similar microstructures, and displayed very similar fracture behaviour, consequently they will be addressed jointly. As depicted in Figure 6.12 (b) and (c), the BASST and BASTA specimens failed at the threaded grips, signifying that the stress intensity factor associated with the thread was larger than that of the reduced gage section of the specimen. The fractured specimens were cross sectioned and metallographically prepared. Figure 6.16 is and optical image of such cross section, note the layer of nickel at the surface which was deposited to allow better edge retention.

The failure is transgranular, with no evidence of a shear lip or gross plastic deformation. Some specimens contained secondary cracks at the thread's root radius adjacent to the fracture plane. Failures of this nature are more often than not associated with a brittle material behaviour and low fracture toughness. Typical behaviour during tensile testing would allow for some plastic deformation of the first loaded thread within the grips, hence redistributing the load to the second thread, and so on - thus lowering the stress concentration due to the thread's profile. The hardness of the BASST and BASTA conditions were 46.9 and 46.3, respectively. These values represent the highest hardness measured for Ti-5553 in any condition and imply that the yield strength for this condition is also high. Consequently, the high yield strength and low fracture toughness indicate that deformation of the first threads within the grip does not occur readily. As a result, load redistribution to the other threads does not take place and cracks develop at the thread.

The material's expected low fracture toughness renders it susceptible to premature fracture from the small cracks at the thread root. Although the yield strength and fracture toughness were not measured, the above scenario is consistent with the forensic evidence gathered from the fractured specimens.
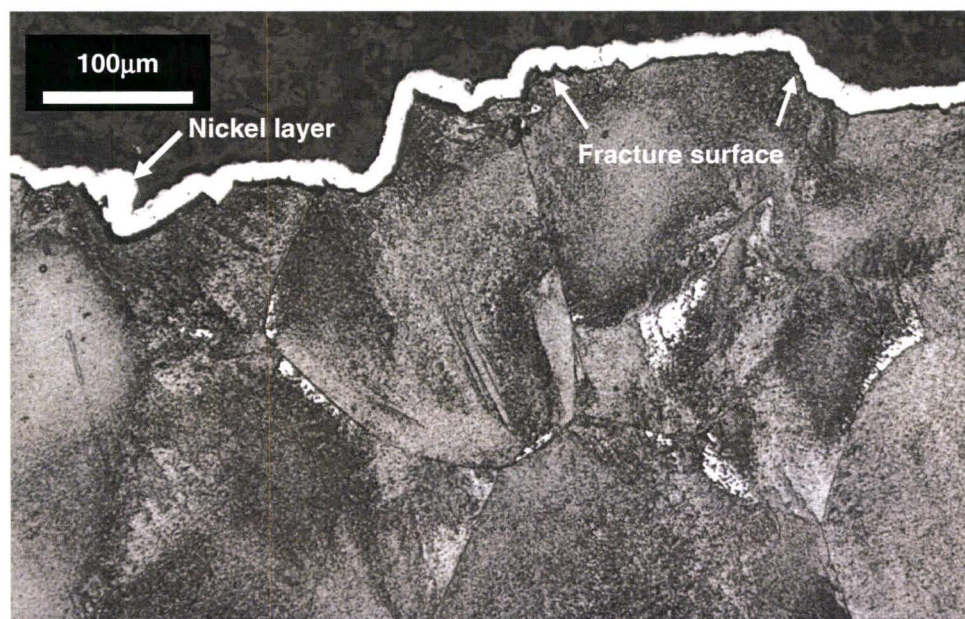
Figure 6.16:   Optical Image of Tensile Specimen Cross Section. Etched in Kroll's Reagent.

SEM examination confirmed the observations of the cross sectioned specimen, the fracture surface presents relatively smooth plateaus, devoid of the typical dimple features indicative of ductile rupture. The flat fracture surfaces contained arrays of grooves of the same scale as the rafts of acicular α characteristic of the microstructure. It appears that the cracks causing final fracture cut through these rafts of acicular α leaving relatively smooth plateaus. Some regions containing shallow dimples are evident, as highlighted by ellipse in Figure 6.17.
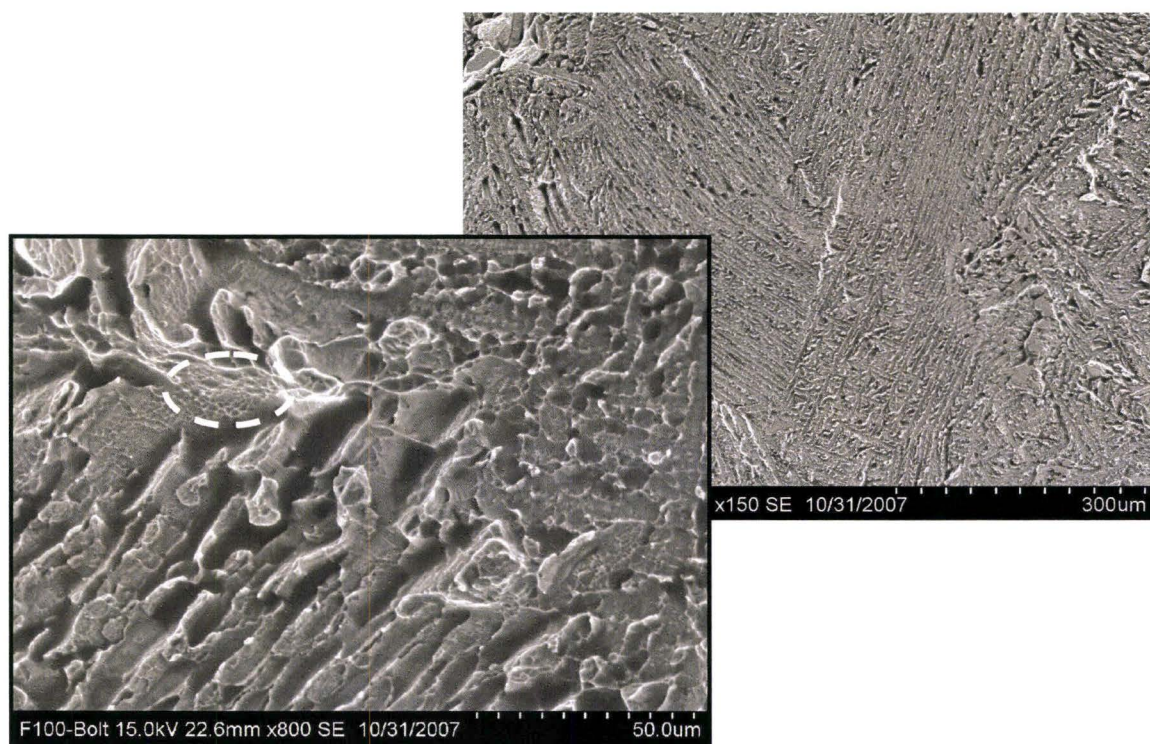
Figure 6.17:   SEM Image of Fractured BASTA Specimen, Showing Smooth Plateaus with Parallel Grooves; Ellipse Highlights Region with Shallow Dimples

6.3.1.3 Deformation and Fracture of the BACCA Condition

Fracture of the BACCA specimens involved considerably more plastic deformation and necking than for the other specimens in this group of heat treatments. The fracture surface was topographically rough, with a shear lip circumventing the specimen. Under the SEM, dimples features indicative of ductile fracture and secondary cracking were the dominating characteristics for these specimens; typical areas of a specimen are shown in Figure 6.18. The size of the dimples was roughly 5μm in diameter.
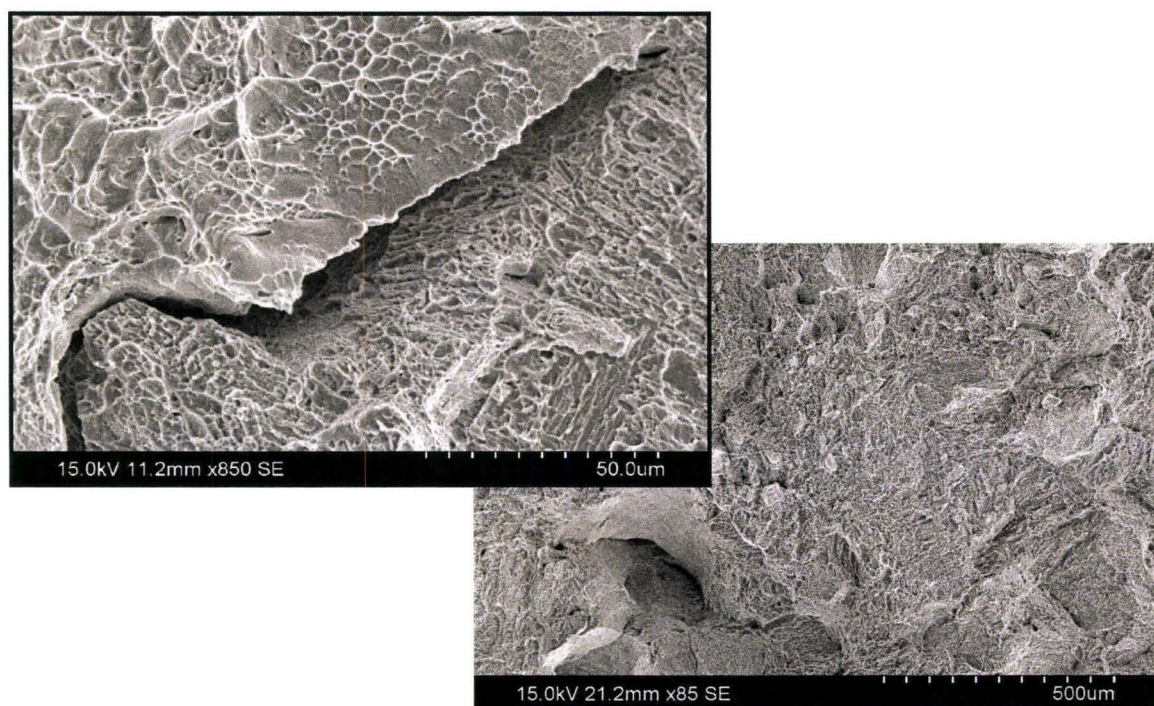
Figure 6.18: **SEM image of fractured BACCA specimen, showing dimple features. Inset at top left shows dimples and a secondary crack.**

The above results suggest that very different deformation and fracture modes are operative within the β annealed group of heat treatments. It is clear that this behaviour has a microstructural basis; an attempt at relating the microstructure to the deformation and fracture mechanisms will be provided and the Discussion section at the end of this chapter.

6.3.1.4 Deformation and fracture of the BAFC condition in compression

Compression specimens exhibited non-uniform plastic deformation (barreling) and failed due to cracks oriented at approximately 45° to the load axis. This mode of failure is consistent with shear fracture along the plane of maximum stress oriented at 45° to the load direction. Figure 6.19 shows the appearance of the fractured specimen and a cross section through the centre of the specimen.

After testing, the specimen's general appearance was rough, with an orange peel texture on its outside diameter. At low magnification, the rough texture was attributed to steps associated

with the slip bands projecting onto the surface and the step difference between deformed grains. The cross section image depicts extensive grain deformation along the large diagonal crack traversing the specimen. At higher magnifications, these deformed grains contained clearly visible slip lines; Figure 6.20 is an example of a typical region away from the centre crack. Unlike the numerous secondary cracks observed on the tensile specimen, no smaller cracks could be resolved aside from the large centre crack. This is likely due to the closing action ensuing from the compressive loading. In general, the mode of failure is the same as that of the tensile specimens, with highly localized planar slip as the damage mechanism.
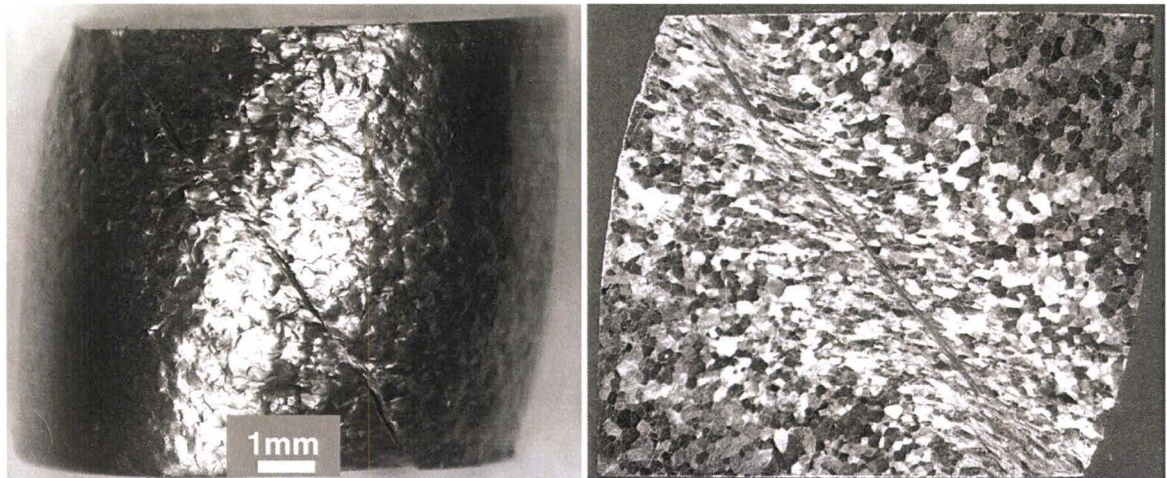
Figure 6.19:   Optical Images Of BAFC Specimen Fractured In Compression; Left Image Shows General Appearance, Right Image Shows Etched Cross Section.

Figure 6.20:   Optical Image of BAFC Compression Specimen Taken Away From the Centre Crack; Note the Clearly Visible Slip Lines. Etched in Kroll's Reagent

6.3.2   Deformation and Fracture for the Solution Treated Group of Heat Treatments in Tension.

In contrast with the β annealed group, the solution treated group of heat treatments shows the highest ductility after fan-cooling from the solution temperature (STFC). Although the BAFC and STFC conditions have similar strengths, the % R of A of the former is roughly 1/3 that of the latter. Obviously, the microstructural factors affecting the yield and ultimate tensile strengths must be very different that those affecting the fracture process.
Figure 6.21 presents a compilation of low magnification SEM images of the fracture surfaces of tensile specimens for the four representative conditions within this group.

Comparing the four fracture surfaces in Figure 6.21, it is clear that the STFC specimen is smaller in diameter than the others. This difference is due to the higher degree of necking undergone by this specimen. All specimens displayed a shear lip circumventing a relatively flat-plateau region at the centre of the specimens. Since the mode of failure was essentially the same, the deformation and fracture analysis for the entire group of heat treatments will be addressed jointly.

At higher magnifications, every specimen exhibited dimple rupture features indicating that they failed in a ductile manner by a mechanism of micro-void growth and coalescence.
Figure 6.22, (a), (b), (c) and (d) are images of the typical fracture morphology for conditions STFC, STA1, STA6 and STA24, respectively. In general, the four fracture surfaces were very similar in appearance with very similar dimple sizes between 3-5μm is diameter.

The mechanism of dimple formation is better illustrated in Figure 6.23, where a secondary crack was examined under the SEM. In these images, dimples, measuring approximately 5μm, are being formed between the two separating surfaces of the crack. Nonetheless, it is not obvious whether the void formation process involves de-cohesion at the primary α to aged β interface, within the primary α or within the aged β itself. It is important to note that the size of the primary and the grain size are all between 2-6μm. As the dimple size is very similar for all specimens, and the dimple diameter is of the same scale as the mentioned microstructural features, establishing the weak link is crucial to understanding the fracture mode.

(a) STFC
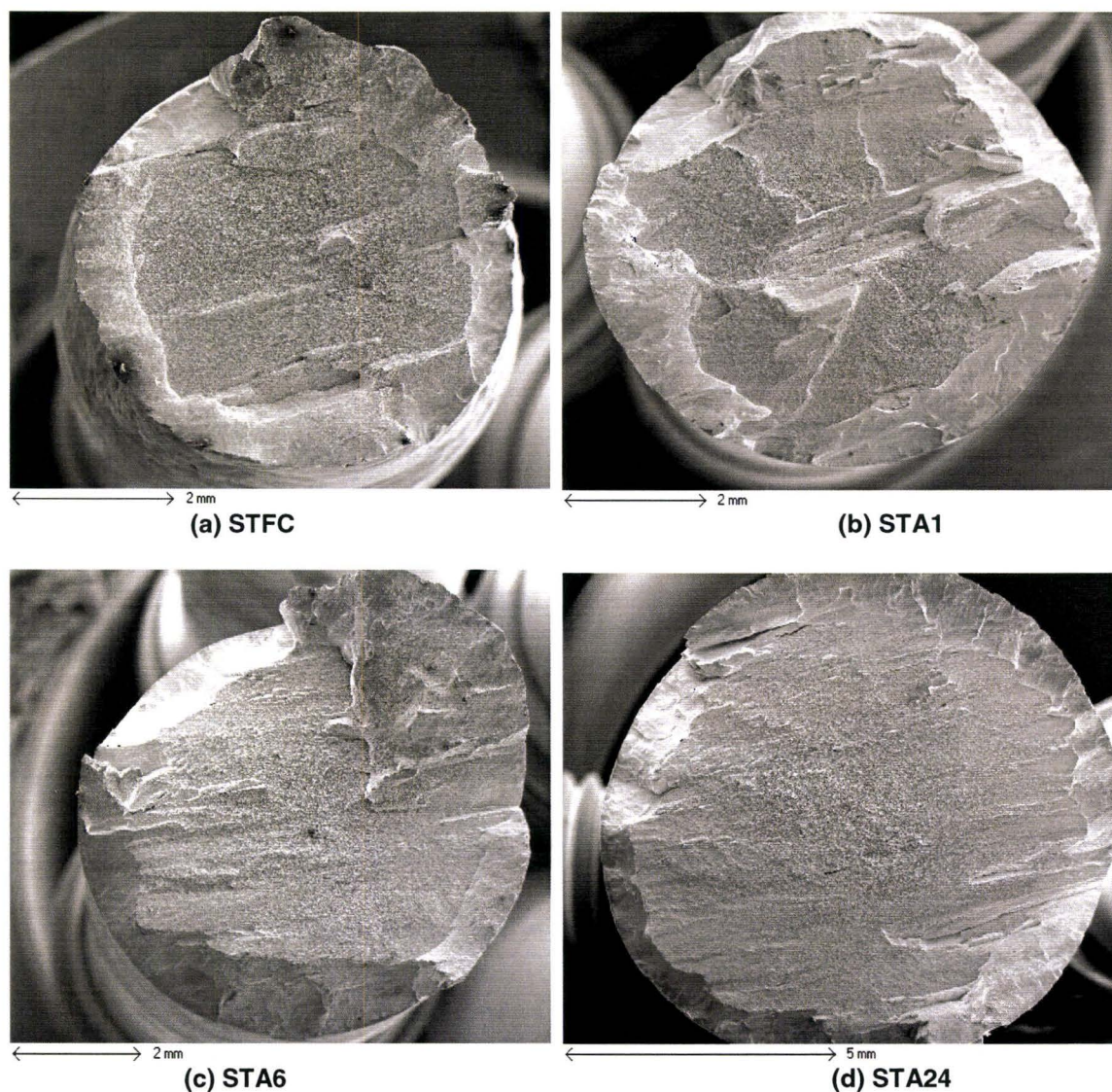
(b) STA1

(c) STA6

(d) STA24

**Figure 6.21:   SEM images of fractured tensile specimens for the following conditions:
(a) STFC; (b) STA1; (d) STA6; (d) STA24**

(a) STFC
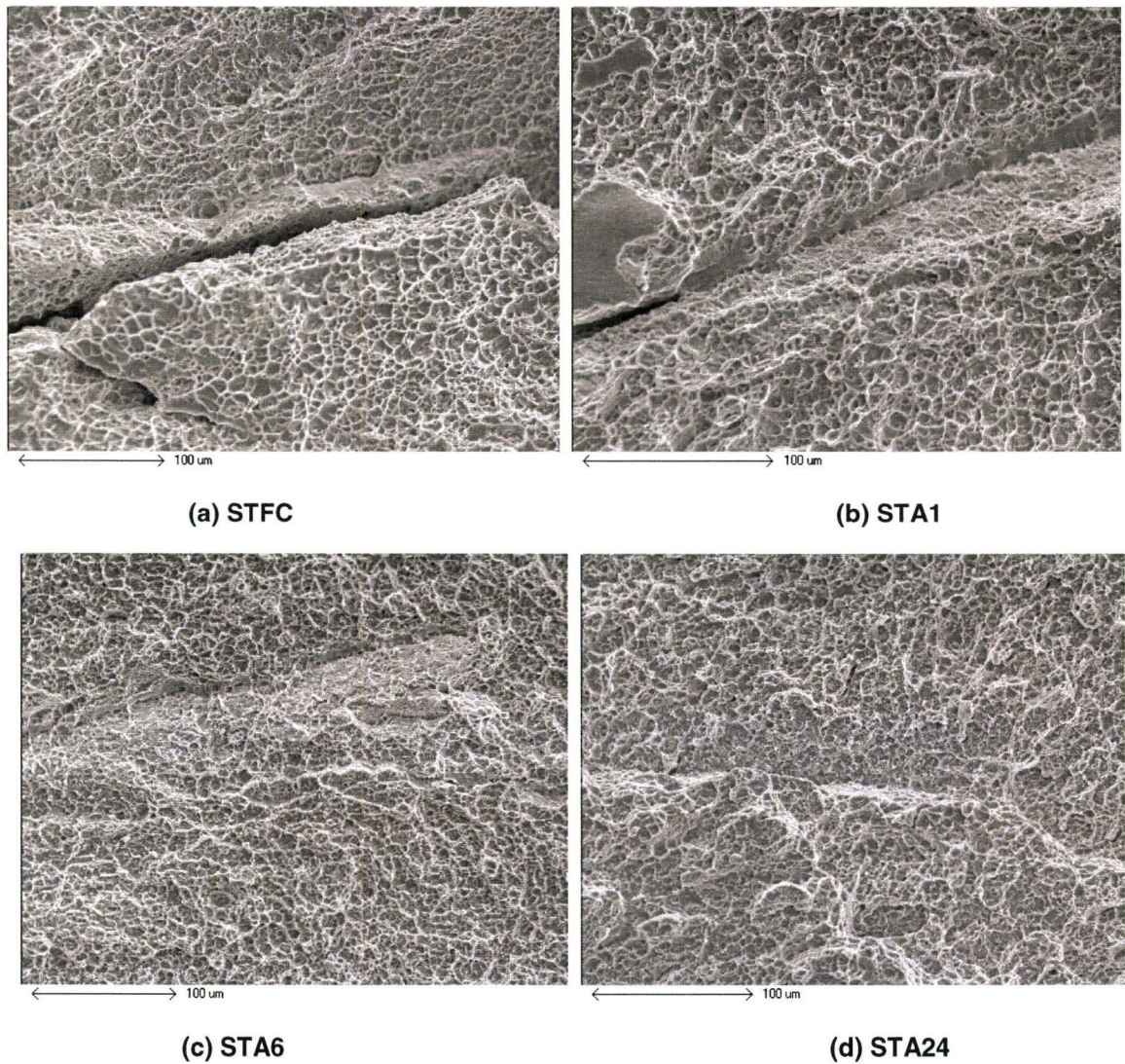
(b) STA1

(c) STA6

(d) STA24

Figure 6.22:   SEM image of fractured tensile specimens for the following conditions: (a) STFC; (b) STA1; (d) STA6; (d) STA24; all specimens displayed dimple rupture features of roughly the same dimple diameter.
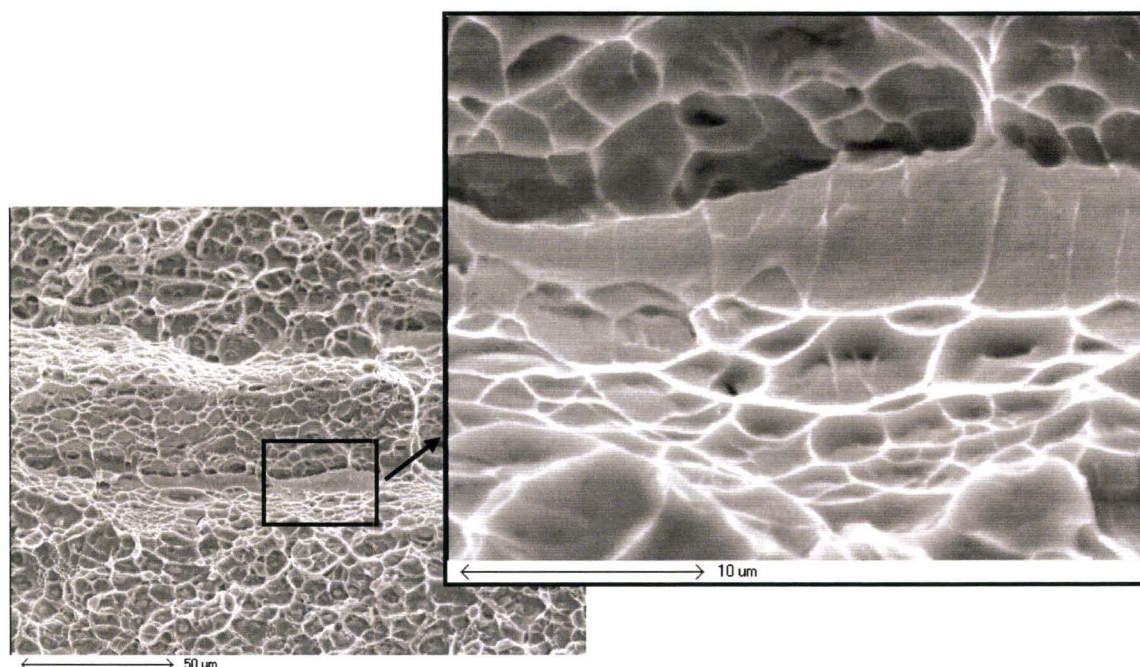
Figure 6.23: **SEM image of secondary crack showing dimples formation between the separating cracks surfaces.**

To answer this important question, the representative fractured tensile specimens for each heat treatment condition were cross sectioned and metallographically prepared. Figure 6.24 is an optical image of a secondary crack below the fracture surface of the STFC specimen. The microstructure surrounding the crack shows evidence of extensive plastic deformation; the originally globular primary α particles have become stretched and lens-shaped.

Careful examination of the un-etched cross sectioned specimens just below the fracture surface, revealed evidence of void formation by de-cohesion at the primary α to β interface. As shown in Figure 6.25, there is also extensive evidence that some of the primary α particles deform plastically and eventually fracture within themselves. Cracks within the primary α were typically associated with particles which had become elongated and "necked", rather than those spherically shaped. Nonetheless, the great majority of these small voids were found at the primary α to β interfaces, this observation applies to all specimens.

Based on the observations above we can conclude that the damage and eventual fracture process is closely linked to the interfacial strength between the primary α and aged β. The lenticular α that makes up the aged β does not appear to play a direct role in the void formation and fracture processes. This finding explains why the STFC specimens, which are devoid of lenticular α within the retained β, and the STA specimens, which are packed with lenticular α after ageing, fail by the same mechanism. A more detailed explanation of the mode of failure is contained in the Discussion section of this Chapter.
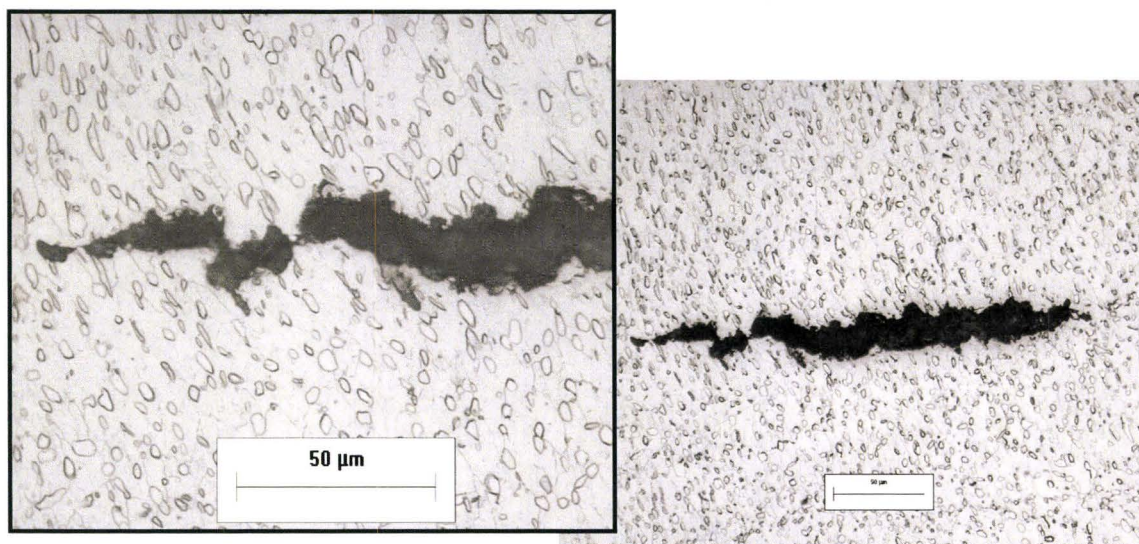
Figure 6.24: Optical image of cross sectioned STFC specimen, showing secondary crack below the fracture surface of specimen. Note the elongated primary α.
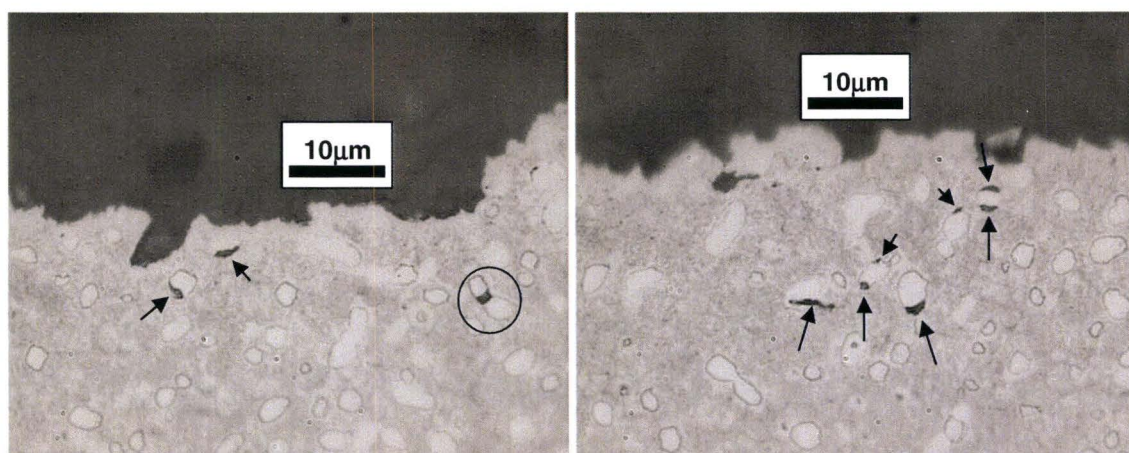
Figure 6.25: Optical image of cross sectioned STA6 specimen, depicting mechanism of void formation at primaryα to aged β interface (arrows) and within the primary α itself (circle). Lightly etched in Kroll's.

6.3.3   Fracture Mode in Compression

Compression specimens, heat treated to the STA-6 condition failed due to cracks oriented at approximately 45° to the load axis. The cracks are consistent with fracture along the direction of maximum shear stress. Figure 6.26 shows a side view of a cracked specimen and a view of the fracture surfaces. The fracture faces were smooth and extremely reflective due to the extensive smearing that occurred as the fracture surfaces slid over one another. Many secondary cracks, also oriented at approximately 45° to the load axis were observed on a specimen cross section. One such crack is depicted in figure 6.27, with an SEM image of a crack tip on the inset at right. Although plastic deformation can be observed along the cracks path, the trajectory of the crack involves propagation along the primary α to β interfaces. This observation is consistent with the mode of crack propagation observed in tension.

Figure 6.26:   Optical images of STA6 specimen fractured in compression; left image shows general appearance, right image shows etched cross section.
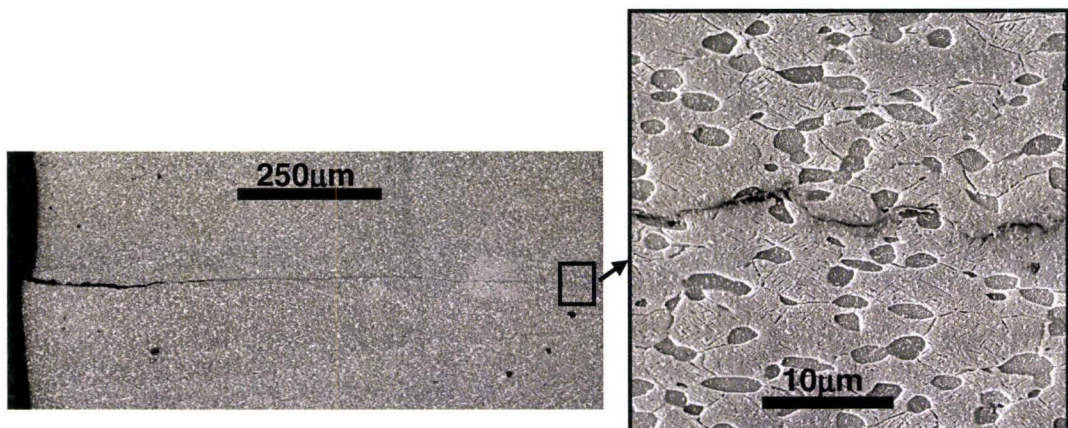
Figure 6.27:   Right – Optical image of secondary crack; Left – SEM image of crack tip.

6.3.4   Fracture Mode in Shear

The fractured "top hat" specimens contained cracks propagating from the corners, as depicted in Figure 6.28. These cracks were examined under the SEM, where elongated primary α particles could be observed surrounding the primary cracks. Because of the extensive deformation, and the closing action of the planar shear, it was not possible to trace whether the cracks followed a path along the primary α to β interfaces. However, many instances of elongated and severed primary α particles were observed along the crack path.
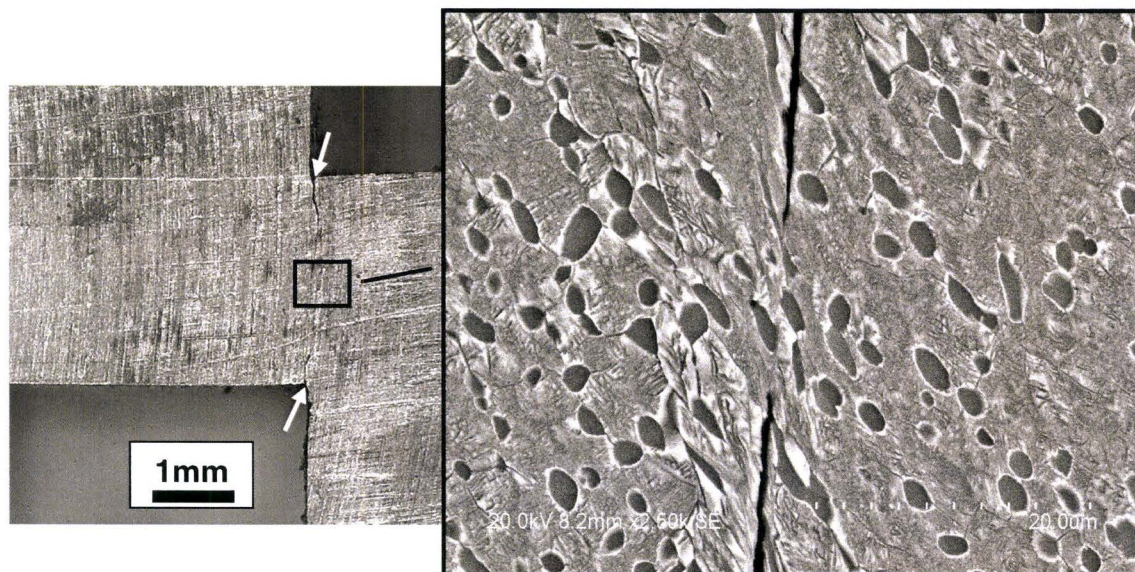
Figure 6.28:   Left – Optical image of cracked shear specimen, arrows point to cracks. Right - SEM image of crack tip.

Regrettably, the deformation processes inherent in the compression and shear tests tend to bring any crack surfaces close together, consequently, these two tests provided less insight into the damage and fracture mechanisms than the tensile test.

In summary, the primary damage process for the ST group of heat treatments is by deformation and eventual rupture at the primary α to β interfaces. In the STFC condition, there is evidence that the plastic deformation process is accommodated uniformly by both, the retained β and the primary α. The overall plasticity is extensive, which explains the higher ductility measured in tension.

For the STA conditions, the primary α appears to deform to a higher extent than the aged β (acicular α in β matrix) and the overall deformation is more localized.

In any case, the primary damage process for the ST group of heat treatments is by deformation and eventual separation at the primary α to β interfaces. This separation creates voids which coalesce and result in specimen fracture. A rationalization of the plasticity and resistance to fracture for each of the heat treatments characterized is presented in the following section.

6.4   Discussion

The strength of titanium alloys can be attributed to four basic hardening mechanisms:

I)   Grain boundary strengthening

II)   Solid solution strengthening

III)   Strengthening due to high dislocation density

IV)   Precipitation strengthening

For the β titanium alloys, the strengthening derived from cold working is not typically important, since the heat treatment temperatures involved preclude high dislocation densities. However, the other three mechanisms are effective in all commercial β titanium alloys.
A great range of mechanical properties can be obtained by varying the heat treatment; nevertheless, the strength is usually limited by the competition between ductility and fracture.

The theoretical shear strength of most metals has been roughly approximated to be of the order of:

$$\tau_{th} \approx G/2\pi.$$

However, more realistic estimates of τ_{th} are in the range of G/30.

In a tension test the maximum shear stress is along a plane oriented 45° to the axial direction and is half as large as the tensile stress. Consequently, the theoretical estimate of shear failure in tension is:

$$\sigma_{th} = 2\tau_{th}$$

Since G is of the order of E/2 to E/3, this estimate gives a value of $\approx$ E/10 for σ_{th}. Below is a table comparing the ratio of the elastic modulus to tensile strength for three common aerospace alloys:

Alloy	Elastic Modulus (GPa)*	Ultimate Strength (MPa)*	Ratio E/σ
7175-T74 – Alum.	70	524	134
300M – Steel	200	1862	107
Ti-10-2-3 - STA	110	1193	92

Values from MMPDS - 04 Design Handbook.

Although these values are roughly one tenth that of the theoretical strength estimate, the strength value for titanium alloy Ti-10-2-3 is the closest to the theoretical strength, i.e. $\approx$ E/92.

Because of the high strength levels possible with β titanium alloys, understanding the role of the microstructure on the competition between plasticity and fracture is of utmost importance. The end goal of this chapter is to provide a correlation between the microstructures observed after the various heat treatments and the properties measured. This is be achieved by exploring the influence of the various microstructural features on the resistance to deformation and fracture. To begin, the role of the ω phase on deformation mechanisms for the various heat treatments is

discussed. The dependence of the fracture stress on the grain size is examined for the β annealed conditions. In the case of the solution treated conditions, the role of the primary α and the character of the grain boundaries are considered in the rationalization of the deformation and fracture processes. The results of a property optimization study for the solution treated and aged condition is discussed; the effect of the solution and ageing temperatures on properties is explained on the basis of the scale of the microstructure.

Rationalization of the strength is carried out using a semi-quantitative approach, considering the incremental contribution of each microstructural features. In order to provide a meaningful correlation, the characteristics of the microstructure are used in various models to link the microstructural feature and the measured property. Assessment of the properties in tension, compression and shear are employed to develop the yield and fracture envelopes for Ti-5553 in two dimensional stress. Finally, the theoretical the practical consequences of these results are briefly discussed.

6.4.1 Rationalization of the Mechanical Properties for the β Annealed Group Of Heat Treatments

In general, the β annealed group of heat treatments had lower ductility than the solution treated conditions. This is attributed to the much larger grain size intrinsic to the β annealing heat treatments. Controlling the cooling rate from above the β transus can improve both strength and ductility by increasing the scale of the α precipitates.

Both the water-quenched and fan-cooled β annealed conditions have relatively low strength and also low ductility. An explanation for this brittle behaviour is provided in the next section.

6.4.1.1 The role of ω phase and the localization of slip process

Deformation and fracture of the BAFC an BAWQ structures occurred by the formation and propagation of transgranular cracks. The fracture mode was by microvoid coalescence and growth and not cleavage. It was suggested that a mechanism of intensely localized slip is responsible for clearly visible slip bands and shearing within the grains. An image of such observation is presented in Figure 6.29.
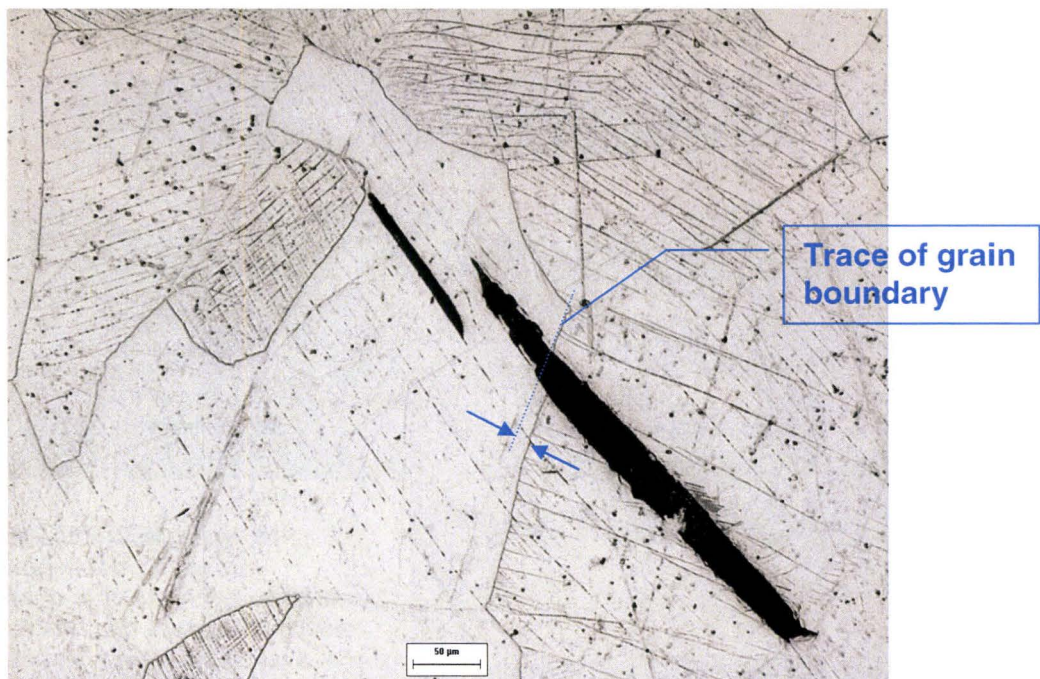
Figure 6.29:   Optical image of fractured BAFC tensile specimen's cross section -uniform elongation ~ 6%. Etched in Kroll's reagent.

The specimen in Figure 6.29 had undergone tensile testing and exhibited a uniform plastic deformation of approximately 6%. In this image, many parallel and intersecting slip lines can be seen and two cracks (dark bands) are evident. One of the cracks has arrested at a grain

boundary, the other has extended into an adjacent grain. The continuation of slip lines across grain boundaries is also evident. Nonetheless, it is obvious from the shift at the grain boundaries trace that a significant shear strain is concentrated at these regions, and that the grain boundaries are the main impediment to slip line movement. However, the nature of the crack formation process and the shallow dimples observed on the fracture mode section is not obvious. Furthermore, curious dimple patterns were observed on the facets of the fractured tensile specimens. These patterns consisted of parallel ridges of larger dimples in background of periodic patterns of finer-scale dimples.

To better understand the damage mechanism and the peculiar dimple morphology observed on the facets in Figure 6.13, a three point bend test was conducted. The specimen was a rectangular plate 20mm by 10mm by 2mm thick, with highly polished sides. After bending the specimen to failure, the polished sides were examined in the SEM near the fracture. Figure 6.30 is an image of the deformed bend specimen showing several step cracks and an oblique view into one of the crack surfaces. It is clear from this image that the shallow dimples observed between the crack's surfaces are due to voids that form by a combined shear/tension loading mechanism.

Figure 6.30: SEM image of polished of 3 point bend specimen side showing steps due to localized slip and cracks. Note the shallow dimples on crack surface.
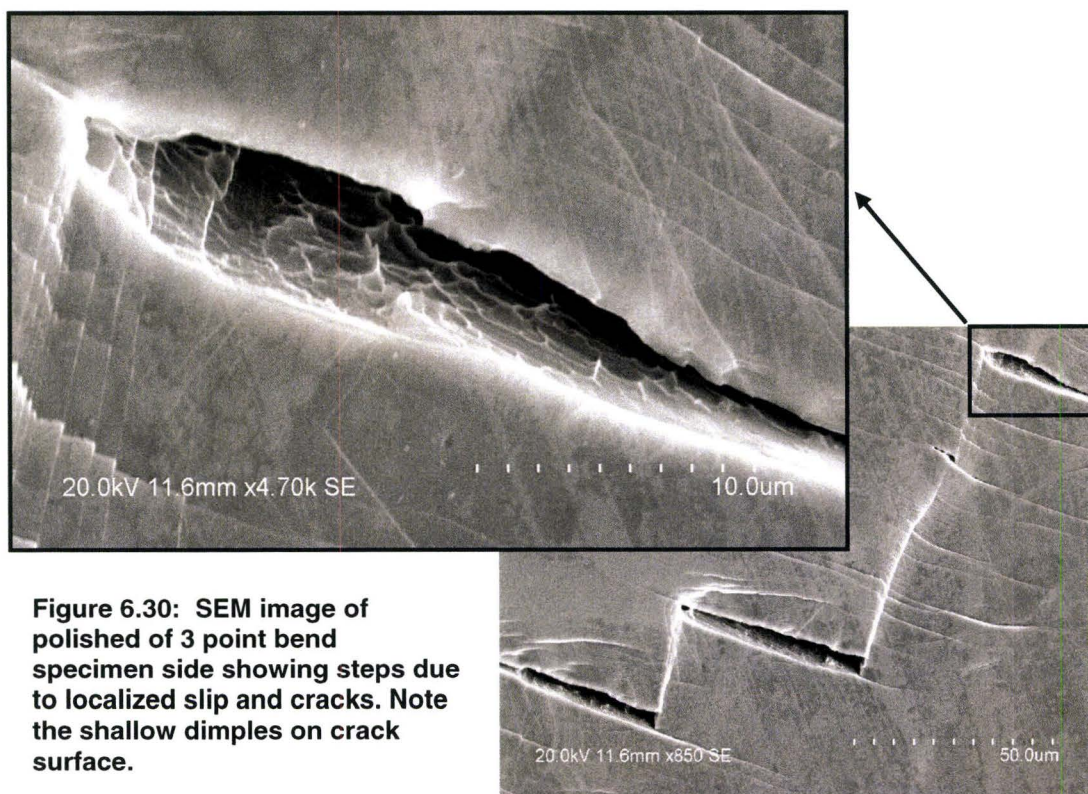
To characterize the nature of the slip bands, thin foils of the same fractured specimen were prepared and examined under the TEM. At low magnification, Figure 6.31 (a) two sets of parallel bands of dislocations can be observed. Two trace lines coloured blue and red are superimposed for clarity, these bands show that at least two slip systems are involved.
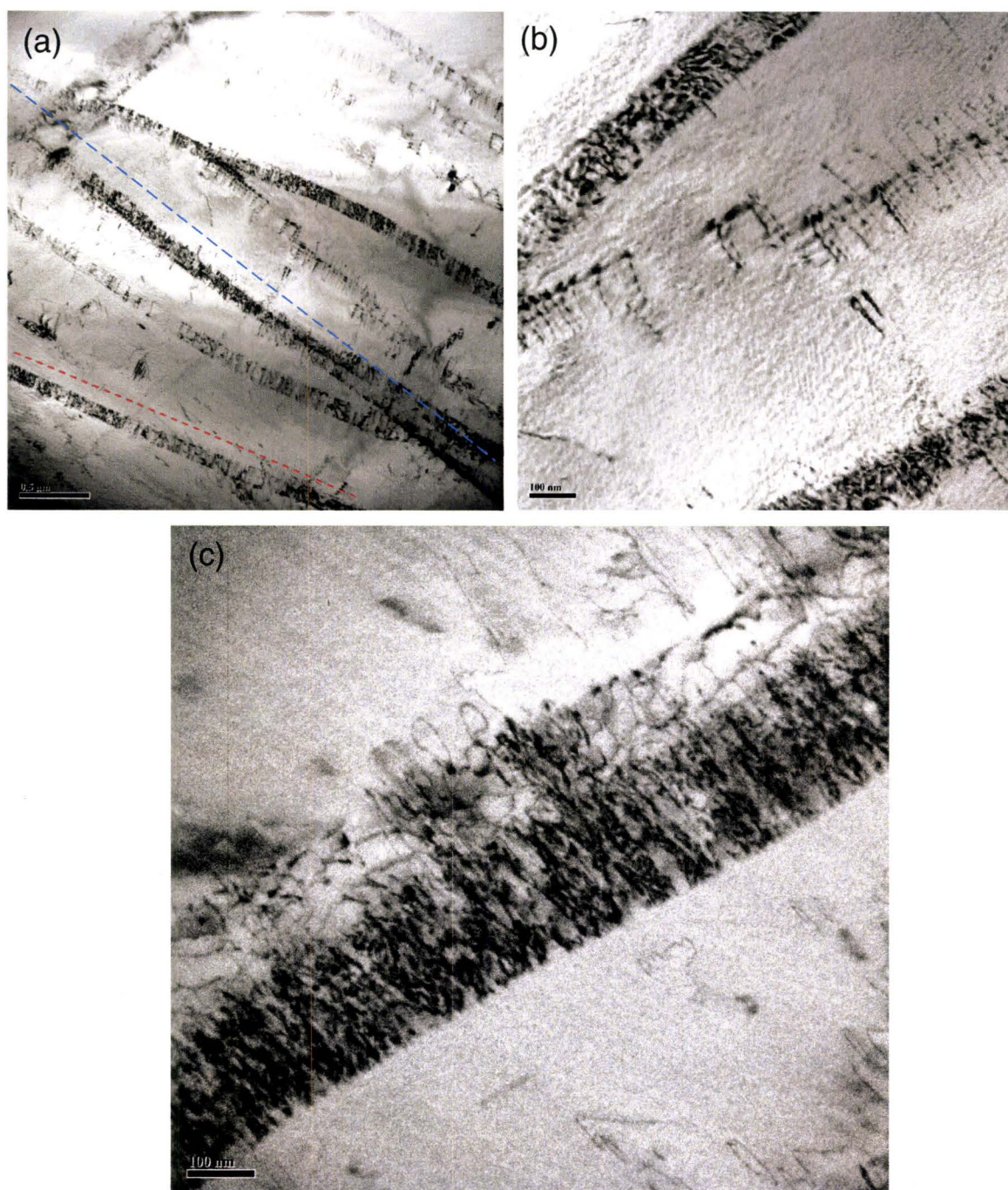
Figure 6.31: **TEM images of fractured BAFC tensile specimen - uniform elongation ~ 6%, showing slip bands indicative of intensely localized slip at three magnifications (a), (b), (c).**

These bands represent zones of dark contrast due to collections of dislocations which traverse the foil thickness at an oblique angle. Some of these bands contain jogs and dislocation dipoles, which are associated with immobile dislocation segments Figure 6.31 (b). At higher

magnifications, see Figure 6.31 (c), the dark bands are densely packed with dislocations. The dislocation-to-dislocation interactions along these narrow zones lead to dislocation multiplication and the formation of voids. In the absence of secondary particles or other dislocation obstacles, continued plastic deformation results in dilation within the slip band giving rise to voids. These voids grow, coalesce and become transgranular cracks. The above process explains the ductile nature of the fracture process along the slip bands, as evidenced by dimples on the fracture facets. Upon close observation of these facets, two distinct patterns became apparent: i) parallel ridges of larger dimples and, ii) a periodic arrangement of shallow dimples on the background; Figure 6.32 shows a typical region containing these patterns.
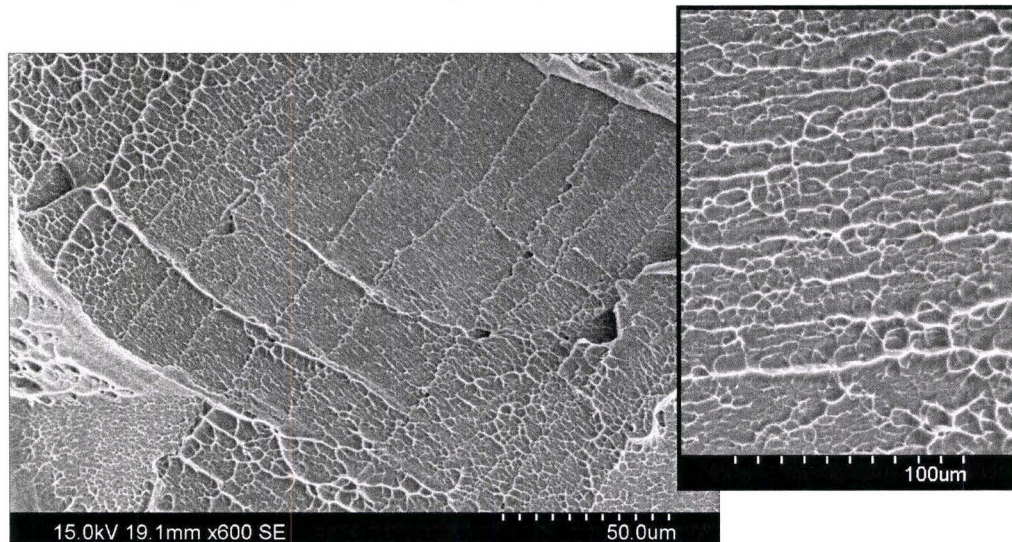
Figure 6.32:   Fracture Surface of BAFC Tensile Specimen, Showing Dimple Pattern on Fracture Facet; Higher Magnification View at Right.

A rationalization for the periodic arrangement of dimples observed on the fracture facets can be visualized with the aid of Figure 6.33.
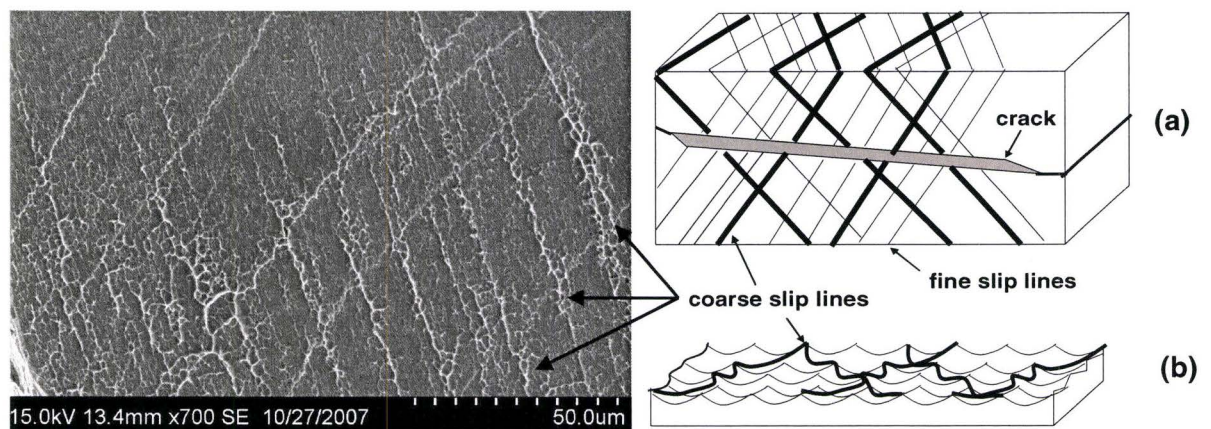
Figure 6.33   Sketch Illustrating the Origin of Ridges of Dimples Observed on Facets of Tensile Specimen Fracture Surface. (a) Volume of Deformed Material Containing a Crack; (b) Morphology of Crack Surface.

Observation of the deformed specimens under the optical microscope revealed that the distance between parallel coarse slips bands is occupied by many finer slip lines. The parallel alignment of these coarse and fine slip lines suggest that they belong to a single slip system. However, numerous intersecting slip lines, almost certainly belonging to a second slip system, were also a common observation. Consider a volume of material containing at least two sets of localized slip bands each involving a different slip system as sketched in Figure 6.33 (a). The coarse bands are depicted by thick lines, while the finer slip lines are shown by thinner lines. As the trace lines from the two slip systems encounter an intragranular crack, there will be a larger shear displacement from the coarser slip bands (larger dimples) than for the finer lines (smaller dimples. As shown in Figure 6.33(b), the shear displacements from coarse and fine lines belonging to two slip systems can be traced on the surface of the crack.

This explains the parallel ridges and periodic pattern arrangement of dimples traversing the fracture surface facets. However the question as to why the slip process is localized remains unanswered.

Earlier in this chapter, evidence was presented of the formation of nano-scale ω phase upon cooling from above the β transus. Even after cooling from high in the $\alpha+\beta$ phase field, nano-scale ω precipitates were found to be present. Considering that the ω phase can have four variants, precipitation along specific BCC -β planes is preferred. It has been demonstrated that precipitates of this small size, have a diffuse coherent interface in an elastically distorted BCC lattice [18]. Furthermore, planar slip of the BCC lattice has been observed in many systems. Planar slip has been linked to the stacking fault energy (SFE); the lower this energy, the higher the tendency for planar slip. More fundamental work would be required to measure the SFE in Ti-5553. Nonetheless, as dislocations move through the BCC lattice they can cut through all four variants of the ω precipitates. Cutting of the small ω precipitates along the slip direction would tend to weaken this plane and bring about a channeling effect for similar dislocations travelling in the vicinity. This channeling effect localizes the slip process to a narrow band of planes. Many instances of localized planar slip being attributed to the presence of ω phase in the quenched β microstructure have been reported in the literature. In particular, Ohyama, et al. studied the effect of athermal ω phase on the tensile properties of Ti-15V-3Cr-3Sn-3Al [59]. Localized planar slip attributed to ω phase of very similar characteristics to that observed in Ti-5553 were reported. Hence, deformation and fracture process observed for Ti-5553 in the β annealed condition is consistent with dislocations cutting through the nano-scale ω precipitates. On the other hand, the STFC condition microstructure also contains ω phase precipitates, however, the ductility values, deformation and fracture modes are quite different than that of the BAFC conditions. This difference is discussed in the following section, where the effects of the grain size and grain boundaries are explored.

6.4.1.2 The role of grain boundaries and the grain size on the strength, deformation and fracture

A cross section of the fractured BAFC specimen, displaying optically evident slip lines, was examined in the SEM. Figure 6.34, is an image of the slip lines at high magnification showing many slip lines that have arrested at the grain boundaries. At high magnifications, some of the slip lines contained etching pits which were more pronounced near the grain boundaries, suggesting that dislocation pile-ups occur at these features. This evidence indicates that the grain boundaries are effective barriers to this slip deformation process.
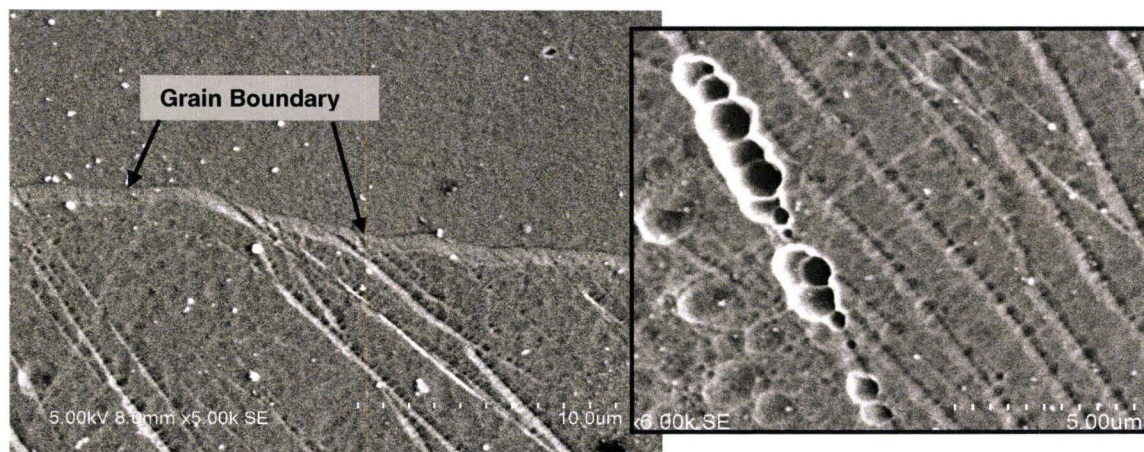
Figure 6.34: SEM Image of Fractured BAFC Tensile Specimen - Uniform Elongation ~ 6%, Showing Slip Bands Near the Grain Boundaries. Etched in Kroll's Reagent

As presented in Table 6.4, reducing the grain size produces a small increase in yield strength, but a more noticeable effect on fracture stress and reduction of area. This observation is reasonable if we consider that the yield stress is the stress required to begin moving dislocations through the bulk microstructure which includes cutting through the ω precipitates. It is for this reason that the plot of grain size versus Yield stress results in a line which is almost horizontal - as depicted in Figure 6.4 (Hall-Petch plot). It follows that no significant increase in yield strength would be expected by decreasing the grain size. However, as the length of the total dislocation displacement, d, is increased by increasing the grain size, (see Diagram 6.2) the damage accumulated by the dislocation travel length is greater. Consequently, more microcracks would tend to form in the specimens with larger grain size, which in turn will suffer from premature crack formation and fracture.

β annealed microstructure　　　　　**Solution treated microstructure**
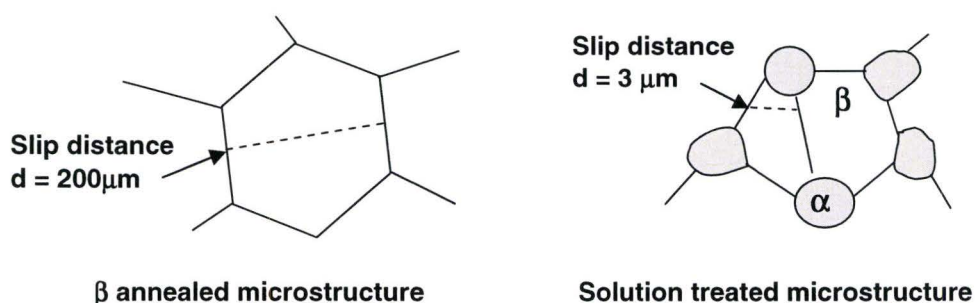
Diagram 6.2. Sketch Illustrating the Scale of the Slip in the β Annealed and the Solution Treated Conditions.

Although, the BAFC and STFC conditions have similar yield strengths (783 and 858 MPa, respectively), their fracture stress and reduction of areas are very different (938 and 1454 MPa; 15% and 46%, respectively). As depicted on the diagram above, the grain size of the BAFC specimens is of the order of 200μm, while the scale of the primary α and sub-grains in the STFC condition is of the order of 2-5μm. It is expected that the primary α phase boundaries would behave akin to the β grain boundaries. This prediction is supported by evidence gathered on

deformed STFC specimens deformed in compression by 19%. The specimen was finely polished and solution heat treated in Argon and then deformed in compression. Figure 6.35 presents SEM images from the secondary (left image) and backscatter detectors (right image). Shear bands are observed to extend as straight lines through the retained β matrix but loop around the primary α. Microcracks are also observed at the primary α to β interface.
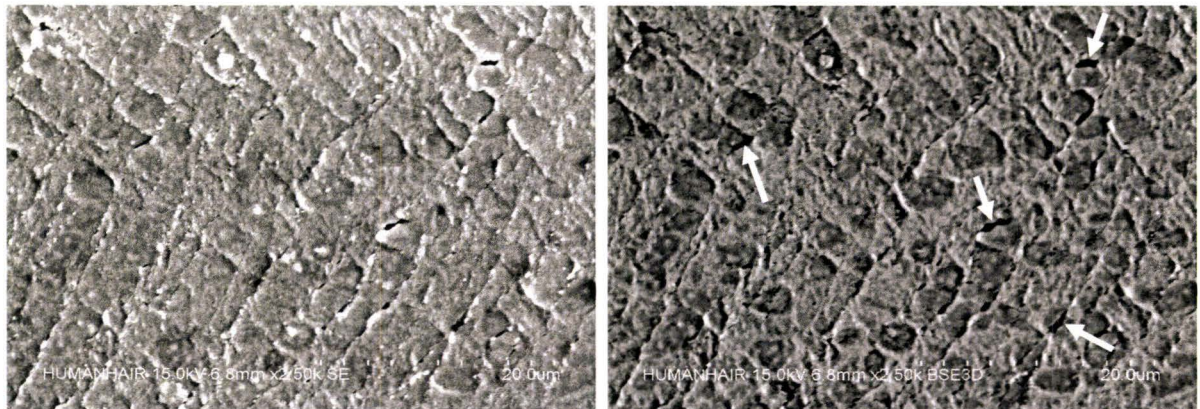
Figure 6.35:   Secondary (Left) and Backscatter (Right) Image of STFC Specimen Deformed 19% in Compression. Arrows Point to Microcracks

Accordingly, the proximity within these particles represents a slip path roughly two orders of magnitude smaller for the STFC condition. Although ω particles may be cut by dislocations in both conditions, the much shorter dislocation slip distance for the STFC condition greatly reduces the amount of damage and the tendency to form cracks. This rationale suggests that the embrittling effect of the ω phase is curtailed by the close proximity of the dislocation barriers, which limit the damage due to localized slip. Consequently, the four fold increase in fracture strain of the STFC condition over the BAFC condition is the direct result of shortening the scale of the total slip.

6.4.2   Rationalization of Mechanical Properties for the Solution Treated Group of Heat Treatments

Of the heat treatments studied, the BAST and BASTA conditions exhibited the highest strength. Although the actual tensile strength could not be determined due to fracture at the grips, hardness measurements place the strength at roughly 1600MPa.
However, the material did not plastically deform, indicating that material fractured prior to yielding:

$$\sigma_f = \sigma_y$$

We know from forensic analysis of the fractured tensile specimens that the microstructure consists of a dispersion of sub-micron acicular α in β grains approximately 200μm in diameter. In this condition, there is no ductile phase within the microstructure to accommodate plastic deformation and the material fails in a brittle manner. Consequently, the BAST condition is not practically appealing. On the other hand, the solution treated and aged condition displayed relatively high strength and ductility, with an ultimate tensile strength of ~ 1300MPa and an elongation of ~ 8%. Starting with the solution treated and following with the aged condition, the mechanism of plastic deformation will be discussed next. This discussion takes into account the nanohardness and stress strain behaviour of the microstructural constituents to explain the bulk properties.

6.4.2.1 Interpretation of the Effect of the Microstructure on Properties

The microstructure of the solution treated group of heat treatments is made up of two phases: α and β. Before ageing, the microstructure consists of globular primary α and retained β; after ageing, the retained β is transformed to fine-scale lenticular α in a matrix of β. A qualitative explanation of the distribution of strain will be provided on the basis of the microstructural features' hardness and the stress-strain behaviour. Table 6.17 presents the average nano-hardness of the salient microstructural features in Ti-5553, expressed in GPa. Plots of the True Stress-True Strain, and the work hardening rates, $d\sigma/d\varepsilon$, versus σ and versus ε are provided in Figure 6.36 - (a), (b) and (c), respectively. Figure 6.36(c) shows an expanded view of $d\sigma/d\varepsilon$ for strains of 0.014 to 0.04, highlighting that the strain hardening rate becomes asymptotic but it is not zero.

Table 6.17:   Nano-Hardness of Important Microstructural Features

Phase	Average Nanohardness (GPa)
Primary α (STFC)	2.1
Retained β (STFC)	3.0
Aged β (STA)	4.3
Aged β (STA5-3)	5.0
Annealed β (BAFC)	3.6
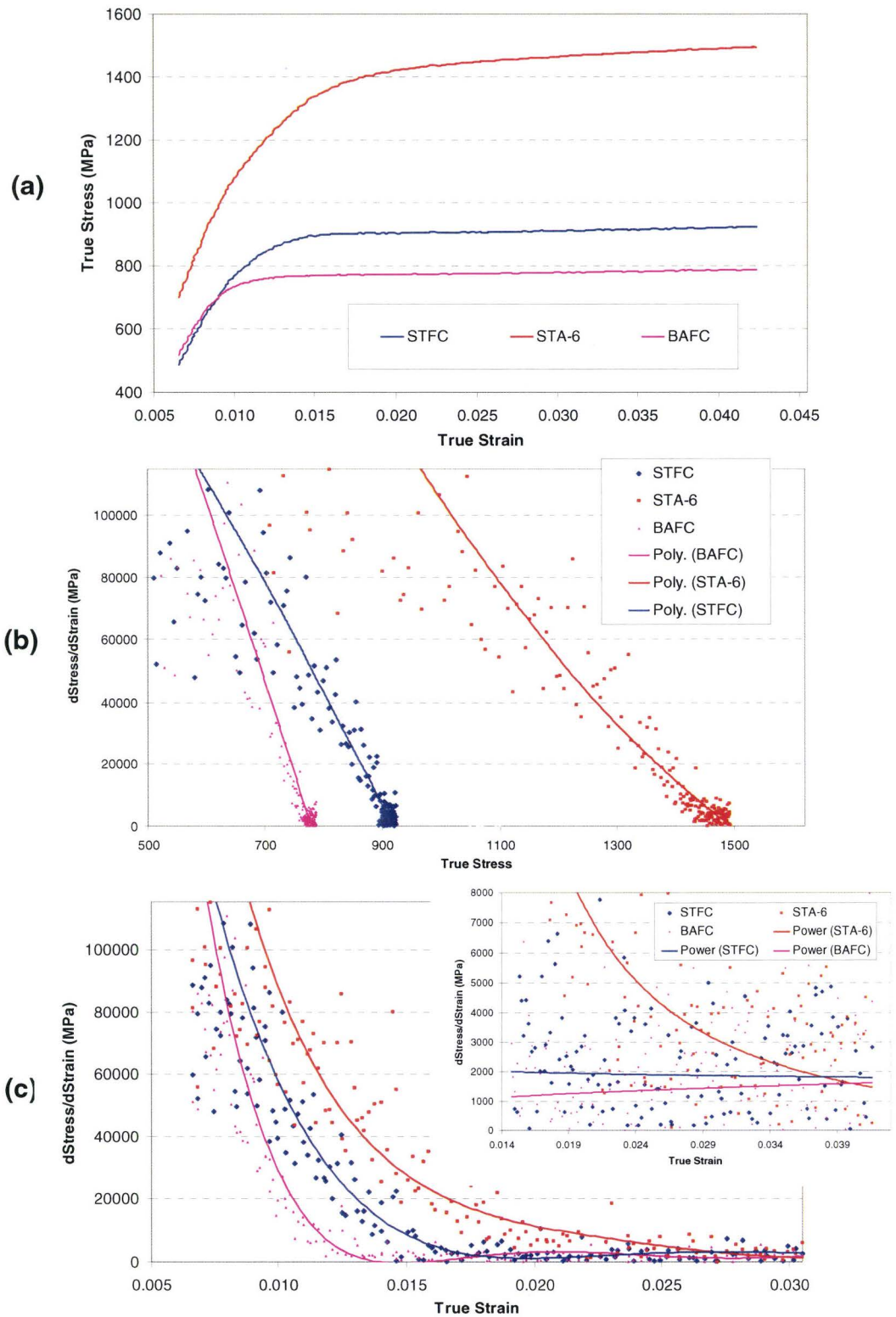
Figure 6.36: (a) True Stress-True Strain Curves For BAFC, STFC, STA-6 Between Strains 0.006 And 0.042; (b) Plot Of dσ/dε Versus True Stress, (c) Plot Of dσ/dε Versus True Strain; Inset Expanded Plot For Strains Of 0.014 To 0.04.

The size of the primary α particles and retained β grains are too small for conventional determination of their respective tensile properties; accordingly, nano-hardness measurements were obtained for each. Since the size of the lenticular α is too small to be measured with a nano indenter, the aged β hardness reported corresponds to the composite value of the fine-scale lenticular α and β matrix together. In terms of the stress-strain behaviour, the retained β phase in the STFC condition is always associated with some amount of primary α. This makes determination of the strain hardening characteristics for the retained β difficult. Although the compositions of the retained β in the BAFC and in the STFC conditions are not the same, the strain hardening behaviour of this phase in the two conditions is expected to be similar. For this reason, the stress strain and $d\sigma/d\varepsilon$ curves the BAFC conditions are also included in Figure 6.36.

6.4.2.2 Deformation of the STFC Condition

One of the remarkable attributes of forged Ti-5553 is the uniformity of shape and distribution of the primary α particles within the retained β matrix. From this observation, isotropic deformation behaviour is expected. The softest feature in the microstructure is the primary α with a hardness of 2.1GPa, followed by the retained β at 3.0GPa. The difference in hardness between the primary α and retained β is roughly 30%, which will impose a constraining effect on deformation of the primary α.

The lower nano-hardness suggests that the primary α has the lowest yield stress. As the strain hardening rate of the primary α is not available, it is not possible to remark on its precise strain hardening behaviour. Nonetheless, with loading beyond the elastic limit of the primary α an initial high rate of strain hardening will ensue while the retained β is still elastic. Although the extent of strain for which β is still elastic is relatively small, strain hardening of the primary α will reduce the initial strength contrast between the two phases.
The % elongation and % reduction of area for the STFC condition are 16% and 46%, respectively, which represents the highest ductility measured for Ti-5553. The extent of uniform deformation for the STFC condition suggests that the α and β phases deform cooperatively. In other words, the plastic deformation is accommodated fairly evenly between the two phases. This suggests that the strain hardening behaviour for the primary α must be comparable to that plotted in Figure 6.36 (b) and (c) for the retained β (BAFC). Still, the difference in yield strength between the two phases, which we will refer to as mechanical contrast, is primarily accommodated at the α/β interfaces. Eventually, the strain at the primary α to β interface exceeds the interfacial strength resulting in de-cohesion. Small voids will appear, grow and coalesce, leading to specimen fracture.

It is important to note that the mechanical contrast between the primary α and retained β is relatively small, leading to a cooperative deformation between the two phases and a high degree of uniform deformation prior to specimen rupture. Upon ageing, the retained β will transform to a fine scale mixture of lenticular α in β, with a drastic increase in strength. This leads to a much larger mechanical contrast between the two phases which will be discussed next.

6.4.2.3 Deformation of the STA Conditions and the Role of the Primary α

With ageing at 600°C, the aged β matrix hardness increases to 4.3GPa, which is more than double that of the primary α. This suggests that the yield strength of the aged β is also significantly higher than that of the primary α. Consequently, a high mechanical contrast between the primary α and aged β exists. Following a similar argument to that of the preceding section, this high mechanical contrast will have a much higher constraining effect on deformation of the primary α. Loading beyond the yield point of the primary α will cause plastic deformation within this phase while the aged β is still elastic. Although the range of strain over which this elasto-plastic behaviour prevails is relatively small, the very high initial strain hardening rates lead to dislocation pile ups and added strain at the α/β interfaces.

Another important observation from the strain hardening behaviour depicted in Figure 6.36, is the steep decline in the work hardening rates over the elasto-plastic regime. This rapid decline can not be explained by way of usual dislocation density storage arguments typical for single phase materials. Consider for example a ductile single phase material such as copper. Tensile loading of a copper specimen beyond the elastic limit results in uniform plastic deformation. In contrast to Ti-5553, the strain hardening rate for copper declines slowly with increasing strain. This effect is due to ability of the material to store dislocations throughout the microstructure, a process which is not localized to any particular microstructural feature. In the case of the STA condition, the initial and increasing mechanical contrast between the two phases leads to dislocation agglomeration at a narrow band near the α/β interfaces. As a result, the strain hardening capacity of the material is limited and the strain hardening rate declines steeply.

The change is strain at the α/β interfaces over the elasto-plastic regime is dependent on the initial mechanical contrast and the strain hardening behaviour of the constituent phases. To help visualize these changes, the strain hardening rate versus true strain plotted in Figure 6.36 (c) will be used. At a strain of 0.01 the strain hardening rate of the STA-6 condition is ~87,000MPa, while that of the STFC is ~59,000MPa. Although the exact strain hardening behaviour of the primary α is not known, its strain hardening rate is expected to be lower than that exhibited by the STFC and the BAFC (~28,000 MPa) materials. This deduction is based on the arguments presented in 6.4.2.2, the lower hardness of the primary α and the absence of strengthening precipitates within the primary α particles. More importantly, with increasing deformation the difference in work hardening rates is more pronounced - see Figure 6.36 (b) and (c). This means that the aged β within the STA-6 microstructure continues to harden at a higher rate than the primary α further increasing the mechanical contrast. The higher constraining factor of the aged β over the unaged β conditions is responsible for a greater degree of localization of the strain to the interfaces for the former condition. The strain contrast between the two phases increases until the shear strain at the α-β interface is exceeded and microcracks are created. Hence, the fracture process is controlled by the degree of the strain localization at the α/β interfaces which fail at a critical shear stress.

Based on the above argument, increasing the number of α/β interfaces should decrease the effective interfacial strain and lead to less strain localization and greater uniform deformation. In fact, this expectation is confirmed by the results presented in Table 6.16, where increasing the primary α volume fractions from 6% to 16%, more than doubles the % reduction of area. Hence, the role of the primary α can be envisaged as the phase providing plasticity to the microstructure. The above rationalization also explains why the ductility and strength remain constant with ageing time, since the volume fraction of primary α and the constraining ability of the matrix are also constant.

It is clear from the above discussion that the deformation and fracture processes for the ST heat treatments are sharply affected by the high mechanical contrast between the relatively weak primary α and the stronger β phase, and the volume fraction of the primary α. Based on these observations, a simpler way to rationalize the mechanical behaviour of the STA condition, is to consider the alloy as being a composite of a strong constituent (aged β matrix) and a discontinuous weak constituent phase (primary α). An illustration of such material is presented in Diagram 6.3 (a). In this manner, the relationship between plasticity and fracture can better be better explained by a meso-scopic composite model where strain localization at the α/β interfaces occurs - and by the existence of a critical shear stress for fracture.

Generally speaking, the stress-strain behavior of continuous fiber reinforced composite can be simplistically described as depicted in Diagram 6.3 (b), where the mechanical response of the fiber, the matrix and the composite are shown. For simplicity, the Young's modulus of the fiber, the matrix and the composite are assumed to be the same. For this type of composite, the strength is dependent on the volume fraction of the fibers, as follows:

$$\sigma_c = \sigma_f \, V_f + \sigma_m \, (1 - V_f)$$

Where: σ_c ; σ_f; σ_m = composite, fiber and matrix strengths, and V_f = Volume fraction of fibers

Considering that the material being studied herein contains a hard matrix and soft discontinuous particles, the description of the mechanical behaviour upon loading is much more complex.

(a)   **(b)**
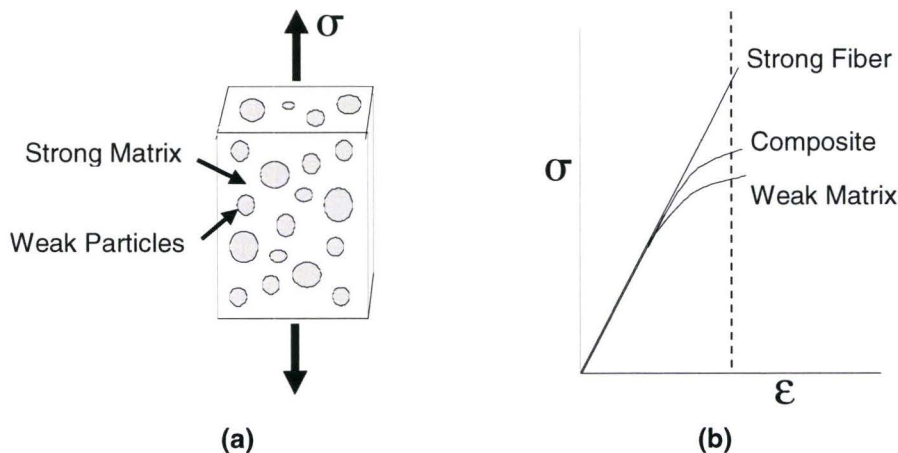
Diagram 6.3. (a)Strain-Strain Behaviour for a Composite with a Strong and Weak Constituent; (b) Element of Two Phase Material Uniaxially Stresses in Tension.

A model to predict the composite strength would require characterization of the strain distribution between the phases and the effect of the volume fractions of α and β. This work is beyond the scope of this thesis, however some work has been carried on other metal matrix composite (MMC) systems.

For example, Wang, et.al. [62], analyzed the localized distribution for particle reinforced metal-matrix composites and showed that a strong three dimensional stress state develops due to the

deformation incompatibility between the matrix and particles. In the case of an Aluminum matrix composite, reinforced by SiC particles, the soft aluminum matrix is strengthened by the constraining effect of the hard particles. Such behaviour is named Stress Enhancement Effect and leads to a very high strain hardening rates during the early stages of plastic deformation. For the present case however, the precise strengthening effect will depend on factors such as: a) the strength contrast between the matrix and the particles, b) the volume fraction of each constituent phase and c) the size, shape and distribution of the phases. [62]

For the case illustrated in Diagram 6.3 (a), the matrix, being the stronger constituent with the larger volume fraction, would have a more pronounced constraining effect on the primary α particles. As explained earlier, this mechanical contrast leads to high initial strain hardening rates and a steep strain hardening decline for the elasto-plastic regime. The constraining effect of the constituents and the high strain hardening rates have been used by Wang and Margolin [63] to explain the composite behaviour and the strong Bauschinger effect observed in 70-30 Alpha-Brass single crystals. The parallels in behaviour studied for similar systems, reinforce that for the STA condition, the constraining effect of the hard β matrix results in localization of the strain to the regions near the α/β interfaces and leads to shear decohesion at the interfaces.

In summary, there are two essential features of the mechanical response of the titanium alloy described in this thesis: the mechanical contrast between the α and β phases and the tendency to strain localization. These two characteristics account for the salient features of the mechanical response and the connection between plasticity and fracture; the difference in yield strength of the α and β phases was inferred from their differences in microhardness and gives rise to a mechanical contrast which varies with heat treatment. The mechanical contrast gives rise to a long elasto-plastic transition and extremely high apparent initial work hardening rates which decay rapidly with plastic strain. The hardening rates arise from the yielding of the constrained α phase and the subsequent spread of plasticity to the β phase. The high apparent hardening rates are given by the product of the volume fraction of the β phase times its Young's modulus; this rate decays as the volume fraction of elastically loaded β decreases rapidly since plasticity spreads into this phase. However, the effects of the mechanical contrast continue during the co-deformation of the α and β phases giving rise to large internal stresses at the α/β interfaces; these stresses lead to decohesion of the interface at a critical imposed strain. Joining of the voids created by decohesion is controlled by the strain localization. Many of the fracture processes observed in the alloys investigated here follow a critical stress criterion. This appears to arise from the strong strain localization in both the β alloys with large grain sizes and the α-β alloys.

A full explanation of the mechanical behaviour of Ti-5553, requires consideration that the strength and ductility properties are strongly affected by the scale of the precipitates which result from ageing. After all, ageing increases the ultimate tensile strength by 45% and reduces ductility by 50%. However, rationalization in terms of the usual dislocation to particle interactions does not provide a clear description of the constant strength with long ageing times and role of the primary α volume fraction on deformation and fracture. As the tensile properties in STA condition are seen to increase within 20 minutes of ageing and remain constant for long ageing times, a meso-scopic approach to describing the structure property relationship is more fitting.

Using this meso-scopic composite approach the strength and ductility are directly related to the relative volume fractions of the two constituent phases. However, some changes in tensile strength are observed by ageing at different temperatures, the following section deals with the changes in scale that occurs within the microstructure by ageing at a lower temperature and for long ageing times.

6.4.2.4 The Effect of Ageing Temperature and Ageing Time

Decreasing the ageing temperature from 600°C to 500°C increases the yield, ultimate and true fracture stresses, while decreasing material's ductility, see Table 6.9. Although the volume fraction of primary α remains constant, the scale of the lenticular α precipitates decreases. This suggests that for a given primary α volume fraction, the more finely spaced lenticular α precipitates act as more effective barriers to dislocations. Based on the hardness differences between the aged β microstructures, the 500°C aged microstructure will deform to a lesser extent, hence transferring more strain to the primary α/β interface leading to fracture.

With ageing beyond the optimal 6-13hrs, the size of the lenticular α increases by agglomeration and coarsening. As presented in Table 6.7, over-ageing reduces the ductility while a slight increase in the yield and ultimate strengths is observed. Microstructurally, a continuous film of α phase develops around the primary α particles and along the grain boundaries. As the diameter and volume fraction of the primary α increases, a commensurate increase in reduction of area would be expected; however, the opposite is observed. This behaviour is not completely understood, however, it is hypothesized that this change is due to the 0.3μm thick grain boundary α film. It has been observed in many β alloys that continuous grain boundary α films are detrimental to ductility [18]. In alloy Ti-10-2-3, continuous grain boundary α films are reason for rejection based on quality control of forged products. One possible mechanism for the decrease in ductility may be related to preferential plastic deformation of the soft α film, which leads to grain boundary sliding and the appearance of microcracks, see Figure 6.37. Even for thin films, the preferential plastic deformation can be thought of as dislocation pile ups at triple points in adjacent grains. The displacement between grains will produce microcracks and result in relatively low plastic deformation overall. [18]

Based on this hypothesis, the negative impact of the grain boundary α film would outweigh the positive impact of the higher primary α volume fraction. Nonetheless, more work would be required to positively confirm this mechanism in Ti-5553.
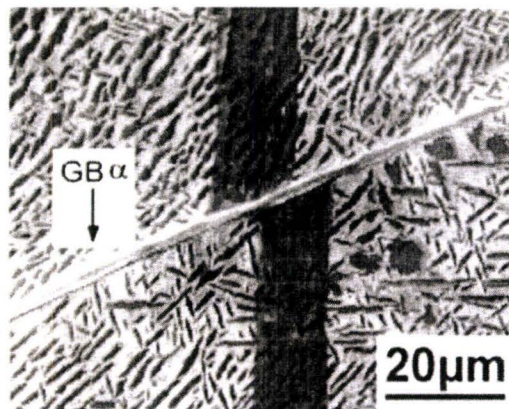
Figure 6.37   **Preferential plastic deformation (see displaced marker) at thin α films on β grain boundaries; stress direction is horizontal.** [18]

The qualitative discussions presented earlier are aimed at providing information of the character of the microstructural features and their contribution to the strength, deformation and fracture. The following section considered the feature's character to select a representative model and assumptions to rationalize the strength in a quantitative or semi-quantitative manner.

6.4.3   Rationalization of the Yield Strength Based on the Microstructure

The models used to rationalize the strength of an alloy involve various terms which account for the relative contribution of a microstructural characteristic to the strength. An overall model for an alloy possessing several strengthening contributions is presented below:

$$\sigma_y \propto \sigma_i + K_y/\sqrt{d} + K^*\sqrt{c_i} + K\sqrt{r}\,f + Gb/L + \alpha Gb\sqrt{\rho} + \pi r\,\gamma_s/b$$

| Peierls Stress | Solid Solution Strengthening | Orowan Strengthening | Precipitate Strengthening |

| Grain-Boundary Strengthening | Second Phase Strengthening | Strain Hardening |

Where:

σ_y = Yield Stress; G = Shear Modulus

σ_i = Peierls Stress - Lattice resistance to dislocation movement

K_y, K^*, K, α, π = Constants

d = grain size; ρ = Dislocation density

c_i = concentration of a given element i

r, f = Radius, and volume fraction of second phase

b, L = Burgers vector, and average length between precipitates

γ_s = surface precipitate/matrix interface energy

These models offer a simplistic description of the dislocation - microstructure interactions, nonetheless they are useful in providing an appreciation of the extent of strengthening provided by a given feature. Many of the constants required for accurate calculation are not available for Ti-5553, hence assumptions will be made based on values from the literature for other alloys. In order to simplify the rationalization, some models are presented in simple form and the results compared against measured values. The intent of this semi-quantitative exercise is to provide greater insight into the role of the microstructure and not to predict with precision the measured values.
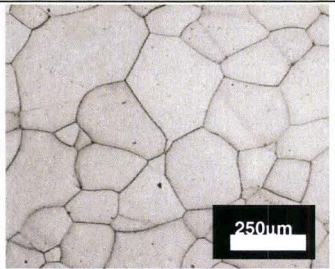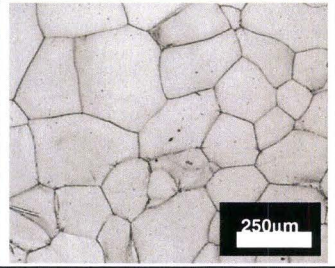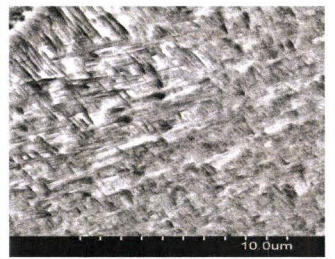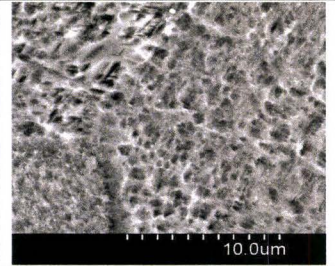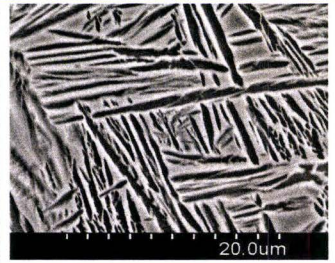
Note that the terms for Solid Solution, Orowan and Precipitate strengthening all describe contributions due to second phase particles; each of these will be used as deemed appropriate based on the size and character of the particles involved.

6.4.3.1 Strengthening Mechanism for the Heat Treatments above the β Transus

To aid in the calculations, the salient microstructural features summarized in Table 6.18.

Table 6.18:   Summary of Representative β Annealed Group of Heat Treatments and Corresponding Microstructures

Heat Treatment	Label	Microstructure Description	Microstructure
β annealed at 903°C for 75 min, fan-cooled	BAFC	Grain structure: 100% retained β, equiaxed, grain size 190μm diameter average Precipitates: ω - >10nm α > 20nm	
β annealed at 903°C for 75 min, water quenched	BAWQ	Grain structure: 100% retained β, equiaxed, grain size 190μm diameter average Precipitates: ω - >10nm	
β annealed at 903°C for 75 min, fan-cooled, solution treated at 790 for 2 hrs.	BAST	Grain structure: equiaxed, prior-β grain size 190μm diameter average Acicular α 0.5-2.0μm long in a β matrix	
β annealed at 903°C for 75 min, fan-cooled, solution treated at 790 for 2 hrs, aged at 600°C for 3 hrs.	BASTA	Grain structure: equiaxed, prior-β grain size 190μm diameter average Acicular α 0.5-2.0μm long in a β matrix	
β annealed at 903°C for 75 min, furnace cooled at 1.0°C/sec to 600°C , aged at 600°C for 8 hrs.	BACCA	Grain structure: equiaxed, jagged prior-β grain boundaries, 190μm diameter average Lamellar α 2μm thick, 10-30μm long in a β matrix	

6.4.3.2 Estimation of the Strength after β Annealing

The β annealed microstructure, whether fan-cooled or water quenched, can be described simplistically as - 100% retained β phase with β grain boundaries. At a much smaller scale, the water quenched microstructure contains nano-scale ω phase, while the fan-cooled microstructure contains nano-scale ω and α precipitates.

Hence, the microstructural elements contributing to the yield stress are:

   a)   solid solution strengthening from alloying elements including interstitials
   b)   precipitate strengthening due to the ω an α phases (shearable precipitates)
   c)   grain boundary (Hall-Petch) strengthening

Given that annealing is carried out above the β transus temperature resulting in complete recrystallization, strengthening due to strain hardening is likely to be negligible and is consequently ignored.

An expression that would account for these terms is of the form:

$$\sigma_y = \sigma_i + K^*\sqrt{c_1} + K_y/\sqrt{d} + 2x\,\pi r\,\gamma_{s(\alpha)}/b + 2x\,\pi r\,\gamma_{s(\omega)}/b$$

Since $2x\tau \approx \sigma$, a factor of 2 X has been applied the $\pi r\,\gamma_s/b$ term to convert the shear stress to tensile stress.

The actual composition of the material heat used for these experiments was presented in Chapter 4.0. All of the alloying elements contribute to solid solution strengthening of Ti-5553. The number of alloying elements, and in particular the notable effect of interstitials, makes calculation of the yield stress quite difficult. Complex factors such as lattice misfit and other microstructure interactions are difficult to assess independently and much more so in a collective manner. However, an approximation to the relative contribution of alloying elements might be of

the form: $\sigma_y = \sigma_i + K_1\sqrt{c_1} + K_2\sqrt{c_2}$ ....,

Where: σ_i = Peierls stress, K_i = constants, c_i = concentration of alloying element i

As the necessary constants for the above expression are not available, an empirical estimation may perhaps prove more appropriate.

Consider the increase in the yield strength by additions of elements as presented in Table 6.19. A summation of these contributions results in a gross overestimate of the yield strength. Consequently, it appears that the effect of the combined additions is much less than the sum of the individual element contributions. Due to the extreme difficulties in accounting for the solid solution strengthening, this contribution will be accounted for as part of Peierls stress.

Table 6.19:   Effect of additions to the yield strength of titanium. *[30]*

Element	Addition to Base, %	Yield Strength Annealed* MPa	Annealed* ksi	Heat Treated* MPa	Heat Treated* ksi
Base Ti		241	35	...	...
Alpha-stabilizer:					
N	0.1	483	70	...	...
O	0.1	365	53	...	...
C	0.1	324	47	...	...
Al	4	496	72	...	...
Neutral stabilizer:					
Zr	4	331	48	...	...
Sn	4	310	45	...	...
Beta-stabilizer:					
Fe	4	593	86	703	102
Cr	4	510	74	655	95
Mn	4	503	73	634	92
Mo	4	490	71	620	90
W	4	483	70	572	83
V	4	400	58	496	72
Nb	4	310	45	324	47
H	0.1	241	35**	...	...
Si	1	448	65	...	...

An expression was derived for the grain boundary strengthening in section 6.1.2 (eq. 6.1) for the characterized material in the BAFC condition:

$$\sigma_{y\,GB} = 736 + 17.9/\sqrt{d}$$

The calculated Peierls stress was 736 MPa, considering the average grain size of 0.190mm, we obtain a yield stress of 780 MPa.

The average yield stress for the BAFC and for the BAWQ material are 783 MPa and 728 MPa, respectively - see Table 6.2.

The calculated values are in good agreement with the measured yield strengths, which is expected - as equation 6.1 was derived from the same body of data. Nonetheless, the Peierls stress, which accounts for solution strengthening and the strengthening due to ω and α phases, is much higher than that reported for a similar β alloy in the literature. Niinomi and Kobayashi *[57]* reported a Peierls stress of 500 MPa for Ti-15V-3Cr-3Sn-3Al in the β annealed condition. These Ti-5553 and Ti-15333 have very similar [Mo]eq. and [Al]eq, but ω phase was not reported for the latter. Hence, if we assume this value for solid solution strengthening and the Peierls stress in Ti-5553, the difference would account for the effect of the ω and α precipitate strengthening.

$$736 - 500 \propto 2x\,\pi r\,\gamma_{s(\alpha)}/b + 2x\,\pi r\,\gamma_{s(\omega)}/b$$

236 MPa = Strength due to solid sol., α and ω precipitates

Since the only microstructural difference between the BAWQ and the BAFC microstructures is the presence of nano-scale α precipitates, the difference in strength must the contribution due to the α precipitates, as shown below:

$$783 - 728 = 55 \text{ MPa} \propto 2x\ \pi r\ \gamma_{s(\alpha)}/b \quad - \quad \text{(contribution due to } \alpha\text{)}$$

And subtracting the contribution due to the α phase:

$$236 - 55 = 181 \text{ MPa} \propto 2x\ \pi r\ \gamma_{s(\omega)}/b \quad - \quad \text{(contribution due to } \omega\text{)}$$

Based on the assumptions above, the strengthening due to the ω phase is roughly three-fold that of the α phase. Qualitative TEM evaluations of the microstructure revealed that the volume fraction of ω appeared to be significantly larger than that of α, which is consistent with the above estimates.

The strength of the BAST and BASTA conditions could not be established due to their brittle nature. An explanation of the fracture mode and possible reasons for the brittle behaviour was provided in section 6.3.1.2, thus, these conditions will not be discussed further.

6.4.3.3 Estimation of the Strength after β Annealing, Controlled Cooling and Ageing

It was shown in the microstructure evolution chapter that slowing the cooling rate results in coarser α precipitates. The microstructure of the BACCA condition consists of fully aged β matrix; the aged β is made up of lamellar $\alpha + \beta$. These lamellae resemble ribbons of α separated by β, in a basket weave arrangement. The ribbons have a thickness 2μm and are 10-30μm long. The ribbons are abutted together, making it difficult to determine their average width.

Hence, the microstructural elements contributing to the yield stress are:

a) solid solution strengthening from alloying elements including interstitials
b) strengthening due to the lamellar $\alpha + \beta$ structure
c) grain boundary (Hall-Petch) strengthening

Accounting for the strengthening contribution due to the lamellar $\alpha + \beta$ structure is not a trivial task due to the basket weave arrangement and the complex aspect ratio of the ribbons. In view of the above, assessing the effective interlamellar spacing or mean free path for dislocation travel is problematic. Langford proposed empirical expressions for pearlitic steels of the form:

$$\sigma_y = \sigma_i + K_1\ S^{-1/2} + K_2\ S^{-1}$$

Lamellar Strengthening

Where S = inter-lamellar spacing, and K_1, K_2 = constants

From Table 6.2, the yield strengths of the BACCA and the BAFC conditions are 1020 MPa and 783 MPa, respectively. As the grain size has not changed, the difference in the two microstructures is in the matrix, which has transformed from retained β to lamellar $\alpha+\beta$. Assuming

that the overall solid solution strengthening is not affected by the solute partitioning to the α and β a phases, the difference in strengths is due to the lamellar matrix:

$$1020 - 783 = 237 \text{ MPa} = K_1 S^{-1/2} + K_2 S^{-1}$$

The contribution to the strength due to the lamellar matrix is at least 237 MPa.
However, the yield strength for the BAFC (783MPa) includes the contributions due to the ω phase (181MPa), which will not have formed by the controlled cooling; adding this contribution:

Strength due to lamellar matrix + contribution of ω phase = 237 + 181 = 418MPa

Consequently, the contribution to the strength due to the lamellar matrix is closer to 418MPa.

Unfortunately, the constants for Ti-5553 are not available a confirmation of the above model is not possible. Nonetheless, the contribution due to the transformation of the matrix is estimated to be between 237 and 418MPa, or roughly 25-40% of the yield strength.

6.4.4 Strengthening Mechanism for the Heat Treatments below the β Transus

To aid in the discussion and calculations, the salient microstructural features are summarized in Table 6.20.

6.4.4.1 Estimation of the Yield Strength after Solution Heat Treatment

From inspection of the microstructure, the important microstructural features that contribute to the strength of the STFC condition are:
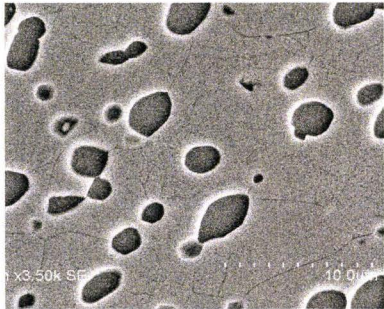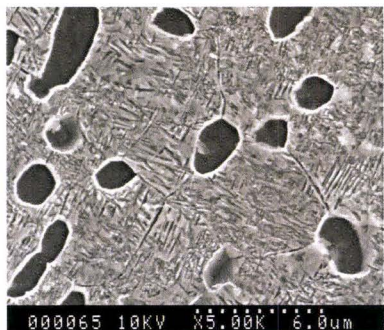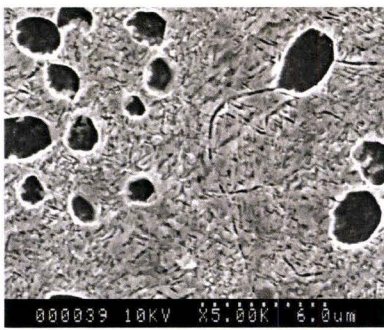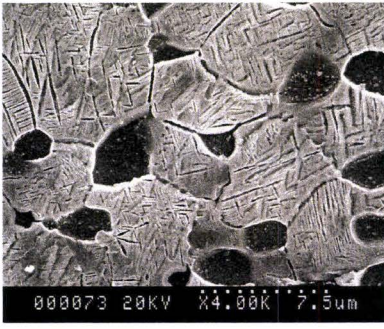
a) solid solution strengthening from alloying elements including interstitials
b) second phase strengthening (primary α size and volume fraction)
c) grain boundary strengthening (high angle and low angle grain boundaries)

As the material has undergone thermal treatments at relatively high temperatures, a relatively low dislocation density is expected, hence, the strengthening due to strain hardening on the onset of plastic deformation will be ignored. A general expression for the terms described above is of the form:

$$\sigma_y = \sigma_i + K^*\sqrt{c_1} + K_y/\sqrt{d} + K\sqrt{r}\,f$$

Accounting for the solid solution strengthening for this condition is as difficult as for the β annealed condition; the same can be said for the assessment of the Peierls stress. Although solute redistribution would have occurred between the primary α and retained β phases, the overall solute content is the same. As for the β annealed condition, the combined strength contribution due to solid solution and Peierls stress will be assumed to be 500MPa [57].

Table 6.20: **Summary of Representative Solution Treated Group of Heat Treatments and Corresponding Microstructures**

Heat Treatment	Label	Microstructure Description	Microstructure
ST at 790°C for 2hrs, fan-cooled	STFC	Globular primary α in a matrix of retained β; grain size 0.5-0.8mm; sub-grain size 2-4μm, diam. Primary α vol. fraction 16.5%	
ST at 790°C for 2hrs, fan-cooled, aged at 600°C for 1hr	STA-1	Globular primary α in a matrix of aged β; grain size 0.5-0.8mm; sub-grain size 2-4μm. diam. Lenticular α, diam. 0.15μm, length 1-3μm. Primary α vol. fraction 16.5%	
ST at 790°C for 2hrs, fan-cooled, aged at 600°C for 6hrs	STA-6	Globular primary α in a matrix of aged β, grain size 0.5-0.8mm; sub-grain size 2-4μm. diam. Lenticular α, diam. 0.2μm, length 1-3μm. Primary α vol. fraction 17.5%	
ST at 790°C for 2hrs, fan-cooled, aged at 600°C for 24hrs	STA-24	Globular primary α in a matrix of aged β, grain size 0.5-0.8mm; sub-grain size 2-4μm diam.. Lenticular α, diam. 0.3μm, length 1-3μm. Primary α vol. fraction 19.6%. Grain boundary α films 0.3μm thick.	

$$\sigma_i + K^* \sqrt{c_1} \approx 500 \text{MPa}$$

The yield strength for the STA condition is 858MPa, which can be described as the sum of the contributions due to the primary α and the grain boundaries. Subtracting the contribution due to solid solution and Peierls stress:

$$858 - 500 = 358 \text{MPa} = K_y / \sqrt{d} + K \sqrt{r}\; f$$

Characterization of the grain boundaries in chapter 5 revealed two distinct types of boundaries, high angle (β grain size 500-800μm in diam.) and low angle (sub grains 2-4μm diam.). The low angle boundaries correspond to misalignments of less than 5°, and although more numerous, their contribution to strength is likely to be smaller than the high angle boundaries. The contribution due to the low angle boundaries will be accounted for with the primary α term.

Using the locking parameter (K_y) derived from the β annealed condition .

$$\Delta\sigma_{y\,GB} = K_y / \sqrt{d} = 017.9 / \sqrt{0.65} = 22 \text{MPa}$$

As expected, the contribution due to the re-crystallized β grains is relatively small. Subtracting the β grain boundary contribution from the overall strength we obtain the strengthening due to the primary α and the low angle grain boundaries.

$$358 - 22 = 336 \text{MPa} = K\sqrt{r}\; f$$

Although the size and volume fraction of the primary α particles and the low angle grain boundaries are known, the proportionality constant is unknown. The contribution due to the low angle grain boundaries is accounted for by increasing the primary α radius by 33% and leaving the volume fraction unchanged.

Based on the above assumptions, the value of K has been calculated at 45.5 GPa/mm$^{-1/2}$.

Using the above value to estimate the increase in strength due to the change in primary α volume fraction which occurs with over-ageing (16.5% to 19.6%), provide increases of ~63MPa, which to a first order approximation, correlates well with the measured yield strengths. It is evident from the semi-quantitative analysis presented above that the most important feature are the primary α particles, the relatively large β grain size contribute little to the strength.

6.4.4.2 Estimation of the Yield Strength after Ageing

After ageing for 20 minutes the yield strength increases from 858MPa to more than 1200MPa. This increase is directly related to precipitation of fine-scale lenticular α throughout the retained β microstructure. In simple terms, the yield strength after ageing can be described as the sum of the strength after solution heat treatment and the increase in strength due to the lenticular α precipitation:

$$\sigma_{y\,STA} = \sigma_{y\,STFC} + \Delta\sigma_{y\,ageing}$$

Considering the strength after ageing for 6 hours (STA-6 = 1245MPa):

$$\Delta\sigma_{y\ ageing} = \sigma_{y\ STA\text{-}6} - \sigma_{y\ STFC} = 1245 - 858 = 387MPa$$

The size and character of lenticular α particles is such that dislocations would not be expected to cut through them. Hence, an Orowan-type strengthening relationship is anticipated, as follows:

$$\Delta\sigma_y \propto Gb/L$$

Taking the $\vec{a}$-type Burgers vector ($<11\bar{2}0>$ direction) for α titanium to be 0.295nm, a shear modulus of 44GPa (α) and an average spacing between needles (edge to edge) of 0.075μm, we obtain:

$$\tau_y = 44 \times 0.295 \times 10^{-9} / 0.075 \times 10^{-6} = 173MPa$$

Since $$2 \times \tau_y \approx \Delta\sigma_y \Rightarrow 2 \times 173 = 346\ MPa$$

To a first order approximation, the above results correlate very well with the measured values. It must be pointed out that small changes in the inter-needle spacing, **L**, have a drastic influence on the yield strength. This explains the increase in tensile strength observed when ageing at 500°C, for which the lenticular α needles are spaced closer together. However, it does not explain the slight increase in strength observed with overageing depicted in Figure 6.38. Ageing for 24 to 48 hours results in agglomeration and coarsening of the lenticular α with a corresponding increase in the **L** value. This increase in strength and decrease in ductility is believed to be due to growth of continuous α films at the grain boundaries. As shown in Table 6.20, α films measuring 0.3μm thick are observed after ageing for 48hrs. These films change the character of the low angle grain boundaries by acting as more effective barriers to dislocations, thus reducing the path length.
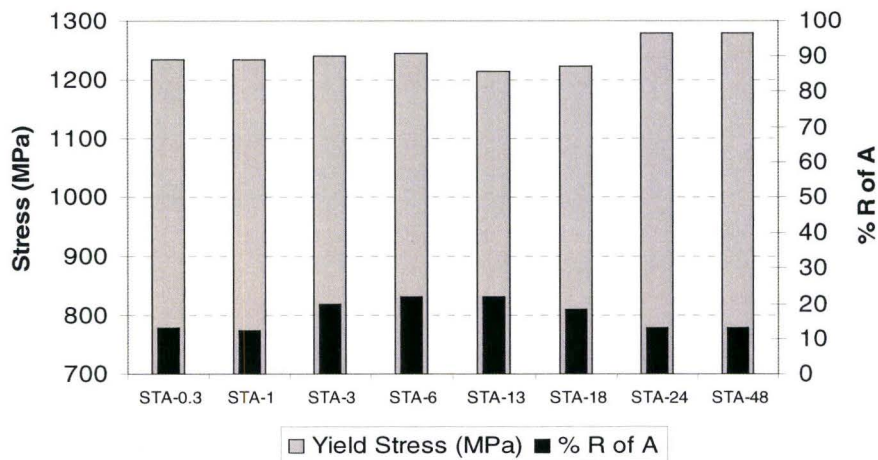
Figure 6.38:   Yield Strength and % Reduction of Area for the Solution Heat Treated and Aged Conditions

This study indicates that the optimum balance between strength and ductility is achieved by ageing between 6-13 hours, where reductions of area values greater than 20% are achieved without loss of strength. More importantly, this lengthy window of invariant ageing response of ti-5553 is quite desirable from an industrial perspective, as it implies uniform properties for components with thin and thick sections.

6.4.5   Comparison of True-Fracture Stresses

As presented in Table 6.7, the engineering tensile properties for the solution treated and the solution treated and aged conditions were found to vary significantly. After ageing, the yield and ultimate tensile strengths increase by roughly 400MPa, and the ductility is reduced by two to three times. These changes were rationalized earlier on the basis of the transformation of the retained β matrix into a fine-scale dispersion of lenticular α. However, the true-fracture stress is found to remain relatively constant for all ageing times.

The true-fracture stress and the reduction of area, for the STFC and all the STA group of heat treatments are presented in bar form in Figure 6.42. Although a large change is observed in the % R of A, the true-fracture stress shows little change. Moreover, ageing at 500°C results in an average fracture stress of approximately 1560MPa; this value is in line with the average fracture stress after ageing at 600°C (~1490MPa).
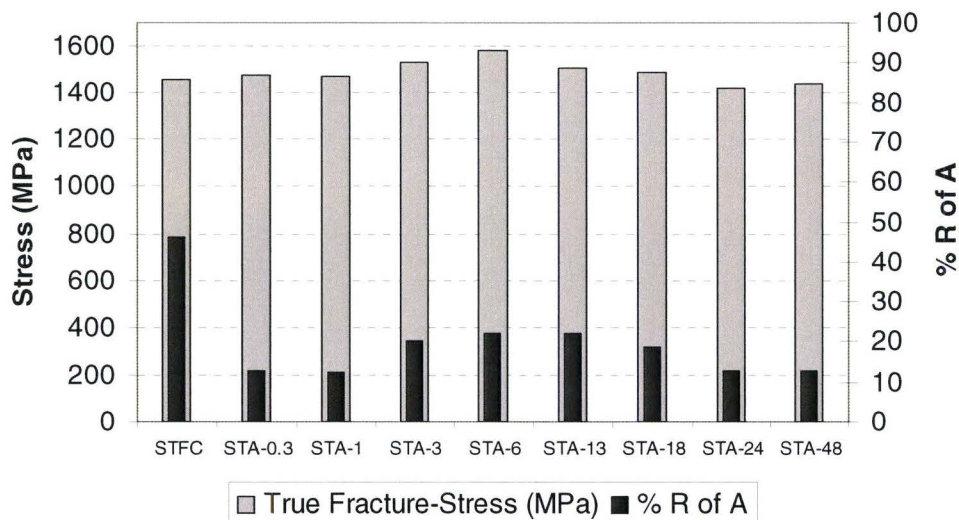
Figure 6.39:   True-Fracture Stress and % Reduction of Area for the ST Group of Heat Treatments

Therefore, despite the vast differences in microstructure and tensile properties between the STFC and STA conditions, the fracture process must be the same and it must be related to the same microstructural feature common to both conditions. Indeed, in section 6.3.2 the weak link in the microstructure was found to be the primary α to β interfaces that introduce voids which coalesce and lead to failure. This explanation is further substantiated by the similarity in dimple morphology and size between all the fractured tensile specimens, regardless of ageing time. The same can be said for the material aged at 500°C.

6.4.6 Comparison of fracture stresses in tension and compression

The fracture stress in tension and in compression for the STA-6 and the BAFC conditions were presented in Table 6.12. For comparison, this Table also includes the tensile and compressive properties for Ti-10V-2Fe-3Al.. The results for the true-fracture stress and % reduction of area are plotted in bar form in Figure 6.40.
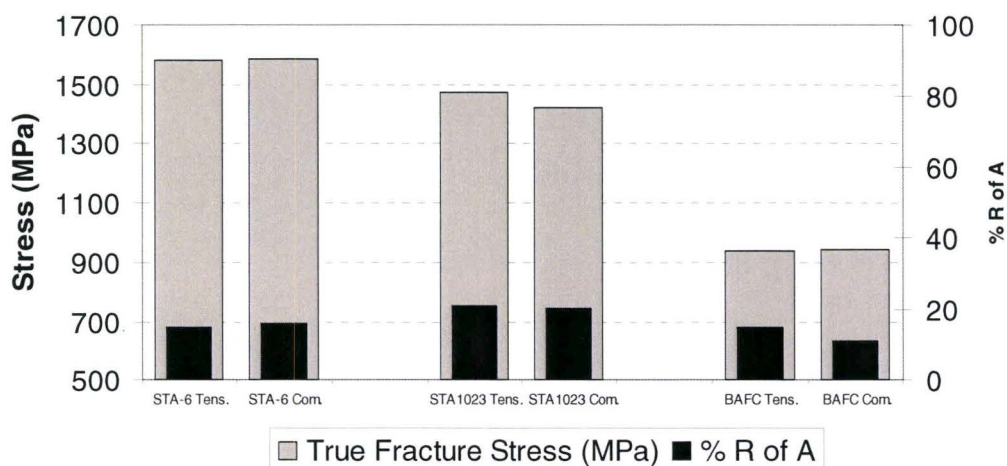
Figure 6.40:   **True-Fracture Stress and % Reduction of Area in Tension and Compression for: STA-6 (left), STA1023 (centre) and BAFC (right) Conditions**

This chart clearly illustrates that regardless of loading direction, the fracture stresses and % Reduction of Areas are essentially the same. This characteristic is quite uncommon for most engineering alloys, which typically exhibit a much higher fracture stress in compression than in tension. This effect is attributed to the void closing action which are inherent to compression loading. Formation of internal voids and microcracks in tension is often associated with weak interfaces or fracture of brittle phases such as inclusions. Propagation of cracks arising from such defects is much more difficult in compression than in tension. Thus, for relatively brittle materials, the fracture stresses in compression are larger than those in tension.

However, the principal shear stresses are at an oblique angle and reach a maximum at 45° to the loading direction. It is important to note that reversing the loading direction from tension to compression merely causes a reversal in the direction of the shear couple but does not alter the mechanics of shear loading. Consequently, if the fracture is originated due to shear rather than tension, than the direction of loading is inconsequential to the damage and fracture processes. Based on the above, we can conclude that the mechanism of void formation must be related to fracture at the primary α to β interface in shear. The fact that the various ageing times have the same fracture stress in the solution treated heat treatments is connected to the same critical shear strength at the primary α to β interface. Reversing the loading direction and changing the matrix microstructure do not affect this critical shear strength and the fracture stress remains constant.

On the other hand, the mechanism of damage and fracture for the β annealed condition is related to highly localized slip along preferred crystallographic directions within the BCC grains. Although this mechanism is intrinsically different from that of the ST heat treatments, a similar

argument applies. Damage is accumulated in shear along slip planes within the β grains. When the damage exceeds a critical value, shear rupture along these slip planes result in cracks which coalesce and specimen fracture ensues. This process is dependent on grain size which controls the average slip length. As this process also involves shear stresses, compression or tensile loading merely reverses the directions of the stresses in the shear couples. Consequently, the fracture stress in tension and compression are the same.

6.4.7 The Fracture Envelope for Ti-5553 in the BAFC Condition

A brief review of the concept of yield and fracture envelopes, and the most widely used models to predict these surfaces were presented in the Literature Review section of this thesis. Furthermore, it was stated that for relatively brittle engineering materials, the fracture stresses in compression tend to be larger than those in tension. Specially, for materials such as cast iron, ceramics or alloys produced by powder metallurgy, the fracture stress in compression is several times larger than that in tension. Solution treated and aged Ti-5553 would be considered a relatively brittle engineering alloy, for which a high compressive fracture stress would be expected.

To develop the failure envelope, the magnitude of the yield and fracture stresses obtained in tension and compression for the BAFC condition have been plotted in Figure 6.41. The values have been plotted as coordinates in a two principal-stress set of axis, σ_1 and σ_2.
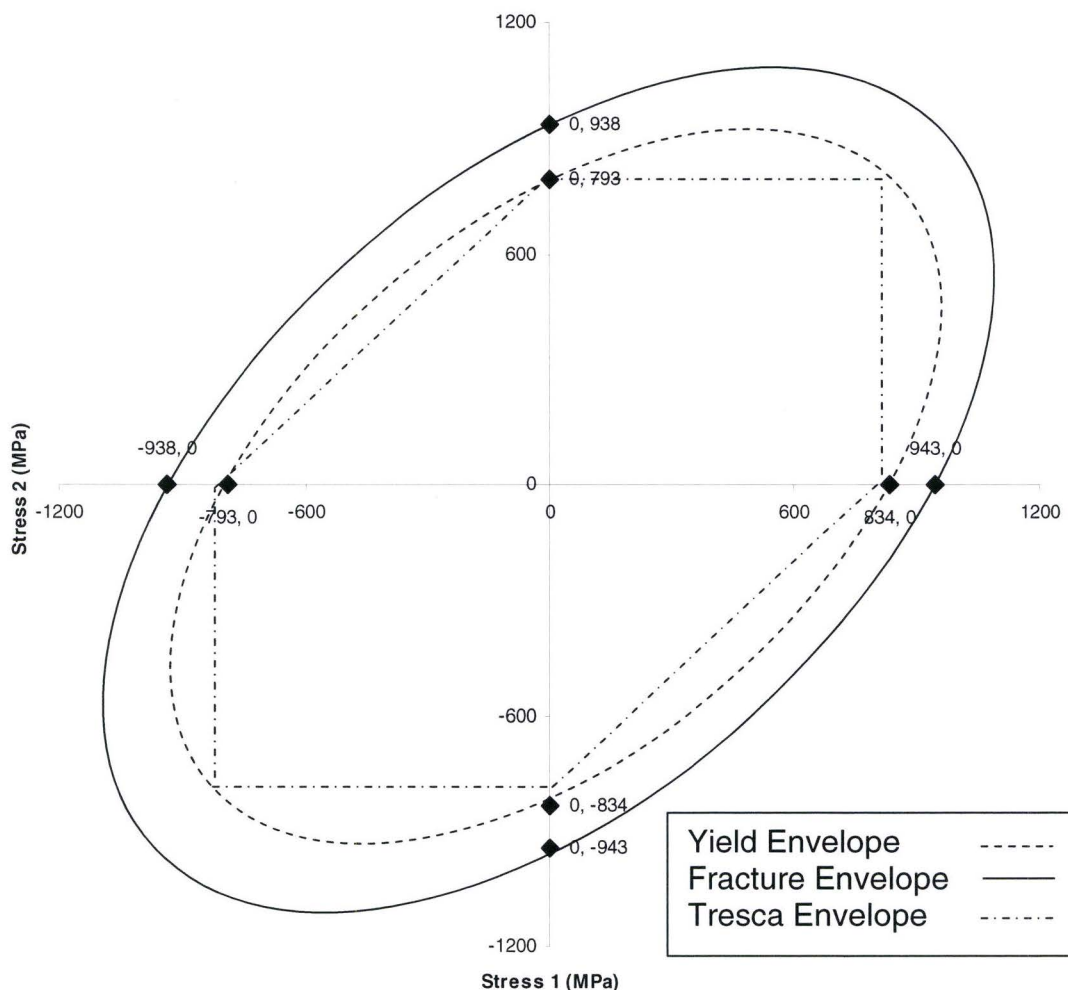
Figure 6.41: **Failure Envelope for Ti-5553 in the STA-6 Condition; Fracture Envelope Shown by Solid Line, Yield Envelope Shown by Dotted Line, Tresca Failure Criteria Shown by Semi-Solid Line.**

Note that the data plotted in Figure 6.41 is reasonable agreement with that predicted by the Tresca failure criteria as the tensile and compressive values on the σ_1 and σ_2 axis lay very close to the predicted values. The yield and fracture stresses in tension and compression are practically the same, due to their identical fracture mode. As explained earlier, the fracture mechanism for the BAFC condition is by transgranular shear resulting from localization of the slip process. Since the fracture mode is due to shear stresses, the tensile and compressive fracture stresses are the same. Consequently, the yield and fracture envelopes are described by two concentric ellipses.

6.4.8 The Fracture Envelope for Ti-5553 in the STA-6 Condition

The magnitude of the yield and fracture stresses obtained in tension and compression, as well as the fracture shear stress for the STA-6 condition have been plotted in Figure 6.42. The values have been plotted as coordinates in a two principal-stress set of axis, σ_1 and σ_2. The value of shear stress τ is plotted along the 45° line, since $\sigma_1 = \left|-\sigma_2\right| = 2\tau$.

Due to the symmetry of the shear stress along the 45° line, the two shear values on two diagonally opposed quadrants have the same magnitude.

The plot indicates that the fracture stresses in tension and in compression are identical; consequently, the fracture envelope is an extension of the yield envelope.

As explained earlier in this chapter, the basis for this fracture characteristic is that failure occurs by decohesion at the primary α to β interface in shear. Since the reversing the loading direction does not alter the magnitude of the shear stress, but only reverses the direction of the shear couple, this failure mechanism is insensitive to loading direction.

For reference, the Tresca failure criteria have also been plotted inside the yield envelope. As the Tresca criteria for failure falls entirely within the yield envelope, adopting these criteria for design would result in a more conservative approach, at the expense of added weight.

It is clear from Figure 6.42 that the fracture envelope for Ti-5553 in the STA-6 condition is in excellent agreement with the shear strain energy (von Mises) model for failure. Although the failure mode of the STA-6 condition is different than that of the BAFC condition, the failure envelopes are similar in that the fracture stresses in tension and compression are the same. Stress calculations tend to ignore the possibility of compressive failure, seeing that for most engineering materials the fracture stress in compression is larger that that in tension.

The consequence of this finding is quite significant for design of landing gear structures. It indicates that the fracture stresses in tension and compression are essentially identical and the possibility of compressive failure must be considered during analysis.
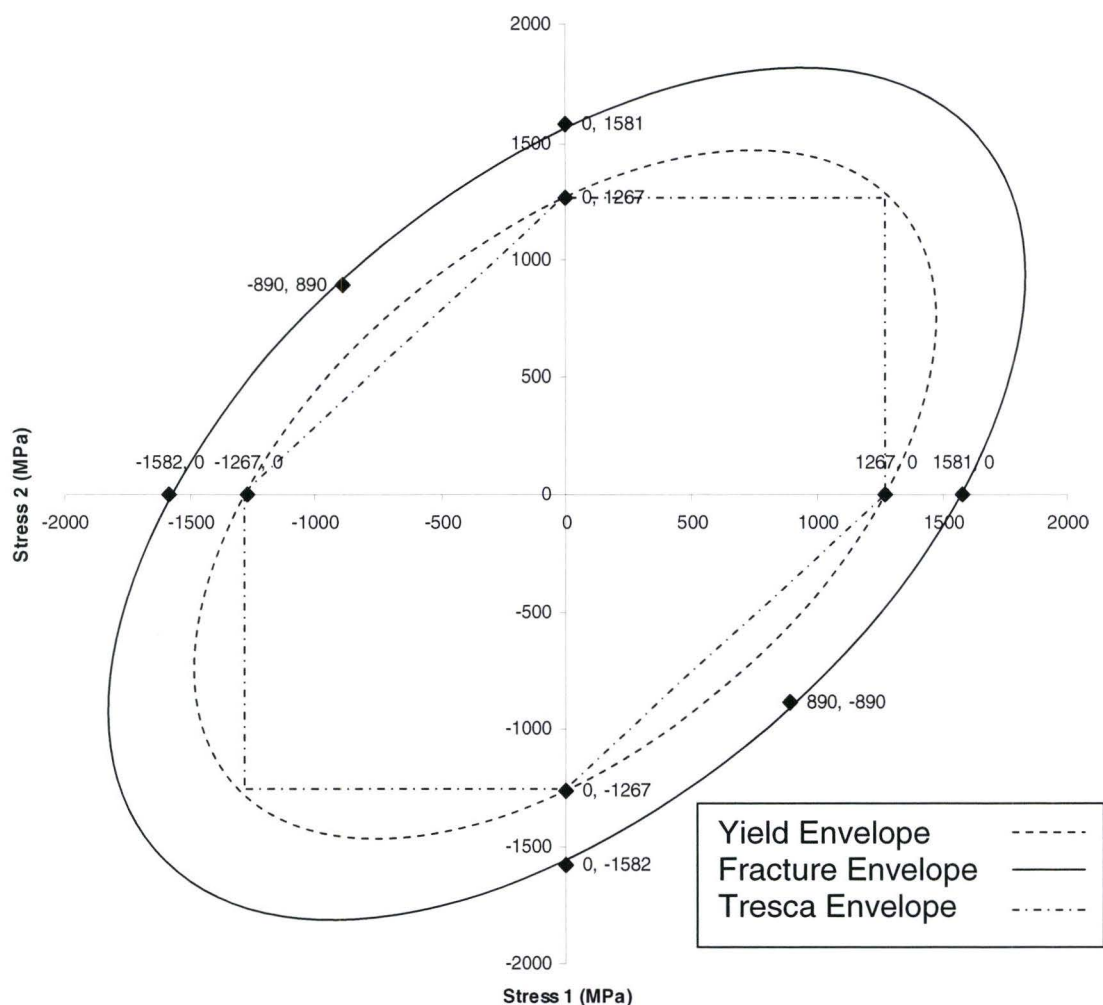
Figure 6.42:   Failure Envelope for Ti-5553 in the STA-6 Condition; Fracture Envelope Shown by Solid Line, Yield Envelope Shown by Dotted Line, Tresca Failure Criteria Shown by Semi-Solid Line.

7.0   MAJOR FINDINGS, CONCLUSIONS AND FUTURE WORK

The work presented in this thesis is aimed at providing a more thorough metallurgical understanding of a new alloy, Ti-5Al-5V-5-Mo-3Cr, through the investigation of its microstructure and properties.

The order of presentation of results for the characterization of the microstructure and properties was in accordance with the two types of industrial heat treatments prescribed for β titanium alloys:

1) Heat treatments above the β transus, (β annealed group of heat treatments)

2) Heat treatments below the β transus, (α-β solution treated group of heat treatments)

A series of major findings and conclusions from this work are presented below following the same order.

7.1   Heat Treatments Above the β Transus

i)   Heat treatment above the β transus temperature causes complete recrystallization of the as-forged microstructure. The as-cooled microstructure consists of equiaxed β grains with an average grain size of 200µm. Water quenching from above the β transus results in precipitation of a dispersion of nano-sized ω phase; while the fan-cooled microstructure contains nano-sized ω and α precipitates. The cooling times from the β transus to 400°C for water quenching and fan-cooling were of the order of less than 1 minute and 4 minutes, respectively. This suggests that α precipitation begins within 1 and 4 minutes.

ii)   Ageing of the fan-cooled microstructure at 790°C or 600°C precipitates sub micron acicular α throughout the β grains. The tensile properties of this condition could not be determined using standard tensile specimens due to brittle failure at the grips. However, hardness measurements suggest that the material has an ultimate tensile strength of ~ 1600MPa.

iii)   When ageing at 600°C, the presence of ω phase after fan-cooling plays no role on the final scale of the precipitated α. This was established by ageing retained β specimens with and without the ω phase. It is believed that the ω phase disappears during heat-up to the ageing temperature, however more work is needed to prove this hypothesis.

iv)   Controlled cooling from above the β transus to the ageing temperature at slower rates produces a coarser α+β microstructure. Acicular α laths are produced with cooling rates of 1°C/min, while lamellar α develops at cooling rates of 3.4°C/min.

v)   The β annealed and fan-cooled condition is characterized by relatively low strength (~850MPa) and low ductility (~6% elong.).The fracture mode is by intensely localized slip and the creation of transgranular cracks. Localization of slip is attributed to shearing of the nano-scale ω precipitates by dislocations. The grain boundaries are the major impediment to dislocation motion by controlling the slip distance. A linear

relationship between the grain size, $\mathbf{d}^{-1/2}$, and the yield and fracture stresses was established, as described by the Hall-Petch relation. With controlled cooling, the strength and ductility improve by precipitation of lamellar α within the β matrix. Improvements in ductility and strength are achieved by reducing the slip length; this can be accomplished by reducing the grain size or introduction of other dislocation barriers such as α precipitates.

vi) The fracture stress was found to have the same magnitude in tension and in compression. This characteristic is attributed to the common fracture mode, which involves localized shear along discrete slip planes. The localized slip produces accumulation of dislocations, lattice dilation and the generation of voids within the narrow slip bands. With continued shear deformation the voids grow and coalesce resulting in transgranular cracks.

vii) Plotting the yield and fracture stresses on a two-principal stress axis coordinate system results in two concentric ellipses in good agreement with the von Mises model of failure.

7.2 Heat Treatments Below the β Transus

i) Solution heat treatment below the β transus and fan-cooling results in complete dissolution of the as-forged acicular α phase within the aged β matrix. Solutionizing at 50°C below the β transus yields a volume fraction of 16.5% primary α in a matrix of retained β. Low angle grain boundaries and globular primary α, each measuring 2-4μm average in diameter, are uniformly distributed throughout the retained β matrix.

ii) The retained β contains a nano-scale dispersion of ω phase. Although the ω phase has a propensity to localize the slip process, the finely spaced grain boundaries and primary α limit the slip length and prevent premature void formation.

iii) The tensile strength in this condition is relatively low, i.e. ($\sim$ 900MPa) and the ductility relatively high ($\sim$ 16% elongation.). The high ductility is attributed to cooperative α-β deformation of the primary α to β matrix, due to their comparable strain hardening behaviour. Deformation of the retained β matrix is dominated by localized slip, however the scale of slip is greatly reduced by the presence of the primary α and the grain boundaries. Fracture occurs by shear decohesion at the primary α to β interface.

iv) With ageing in the 500°C to 600°C temperature range, precipitation of α within the retained β begins within 5 minutes of the start of ageing. Precipitating is heterogeneously nucleated at dislocations and grain boundaries. The final scale of the precipitated α is not affected by the presence of the ω phase, it is believed that this phase disappears during heat-up to the ageing temperature.

v) A drastic increase in hardness and tensile strength occurs within 20 minutes of ageing. The yield and ultimate tensile strengths reach values of roughly 1200 and 1300MPa, respectively, and remain relatively constant for up 48 hours ageing.

vi) The increase in tensile strength observed after ageing for 20 minutes is caused by precipitation of lenticular α, measuring 0.15μm in diameter and 1-3μm in length. With

continued ageing, agglomeration and coarsening of the lenticular α is observed. However, the overall change in scale of the lenticular α phase does not change significantly which accounts for the constancy in the yield and tensile strengths.

vii) The fracture stresses for the solution treated condition and for material subsequently aged at 500°C and 600°C are quite similar in magnitude. This similarity is due to the fact that the fracture mechanism, which controls the fracture stress, is the same for all these conditions. The fracture mechanism for all the solution treated conditions is begins with shear decohesion of the primary α to β interfaces.

viii) Additionally, the fracture stress in tension and compression are exactly the same. This characteristic is also due to the fact that the fracture mechanism in tension and compression occurs by shear fracture at the primary α to β interfaces. The fracture mechanism is insensitive to loading direction since reversing the loading direction does not alter the magnitude of the shear stress, but only reverses the directions of the shear couple.

ix) In the aged condition, increasing the solution treatment temperature reduces the volume fraction of primary α and the ductility. The role of the primary α during plastic deformation can be envisaged by considering the differences in yield strengths and strain hardening rates between the primary α and the aged β. As the primary α is much softer than the aged β, it begins to yield ahead of the aged β; its lower strain hardening rate indicates that it continues to accommodate the larger share of plastic deformation upon loading. Consequently, the primary α plays a ductilizing role within the aged microstructure.

This investigation has been aligned with the requirements associated with the aerospace industry, in particular with the needs of the landing gear design community. The approach for material characterization and investigation of the mechanical properties has taken into consideration these interests. In light of this, a series of practical remarks and recommendations for future work are also presented.

7.3 Practical Remarks and Recommendations for Future Work

Introduction of a new alloy to the aerospace design community is a lengthy and arduous process. This is justifiable since the criticality of the applications involved demands care and rigorous scrutiny.

With an understanding that this alloy had been fully developed by the material supplier and that the chemical composition and thermo-mechanical processing were fixed, full adoption of this alloy in new designs required the closing of certain gaps in the state of knowledge. These gaps were primarily related to the alloy's response to heat treatment and its deformation and fracture properties. The work presented herein has endeavored to bridge these gaps.

Seeing that the high strength associated with the solution treated and an aged condition constitutes a competition between plasticity and fracture, the following are practical guidelines for optimizing the balance between ductility and strength:

i)   The solution heat treatment temperature should be selected to achieve a volume fraction of primary α between 15-20%. Based on the optimization work presented earlier, a suitable starting temperature would be 50°C below the β transus.

ii)   Increasing the volume fraction of primary α improves ductility with a small impact on tensile strength.

iii)   Ageing in the range of 600-630°C, for periods of 5-10 hours represent a window of peak strength and ductility for Ti-5553.

Comparing the fracture toughness of Ti-5553 to that of other β titanium alloys we see that its K_{IC} values are lower. Although, K_{IC} this is not a primary consideration in Landing Gear design, it represents a higher risk. This risk can be mitigated by reducing the probability of surface and internal defects through increased inspection. Designing to a lower fatigue damage allowance, as well as shot peening of all fatigue critical features would also lower the risk of component failure.

In regards to the threshold of crack initiation and propagation under conditions of stress corrosion cracking, these values appear lower than those for similar alloys. In particular the K_{ISCC} value is lower than that for Ti-10-2-3 in the STA condition. This is not surprising since the SCC evaluation approach is based on the fracture toughness approach. Nonetheless, failures of titanium components due to SCC in normal aircraft operating environments are rare, and the risk of this mode of failure is low.

On the other hand, the significance of the fracture behaviour of Ti-5553 in tension and compression is of great importance to structural design. It means that checks for compressive failure, so called "residual strength" calculations, must accompany the analysis for failure in tension. The limited comparative work done on Ti-10-2-3 also suggests that a similar fracture envelope is applicable, thus, similar comments apply to this alloy.

This work has highlighted areas for continued research and identified a number of points which need further study and clarification, these are:

I. Since the majority of the property optimization work was focused on the solution treated and aged (high strength) conditions, optimization of the β annealed condition would be needed to fully understand its potential for other application. As stated in the Introduction, a primary criterion for material selection in some landing gear components is resistance to fatigue and not strength. Recently, improved toughness and fatigue life has been reported for the β annealed slow cooled and aged Ti-5553. [31] Work on optimizing the β annealed slow cooled condition may show attractive properties for future designs.

II. A more thorough understanding of the microstructural factors affecting the fracture toughness of Ti-5553 in the STA condition is needed in order to improve this property.

III. Although inferences have been made about the strain hardening behaviour of the primary α on the basis of its deformation behaviour, the precise strain hardening rate is unknown. Because of the relatively small sizes involved, this behaviour could be investigated by measuring the nano-hardness changes as a function of strain.

IV. Evidence has been provided that the presence or absence of ω phase in the retained β does not change the final scale of α precipitates upon ageing. This is believed to be due to dissolution of the ω phase during heating to the ageing temperature (600°C). Hence, nucleation of α is unaffected by the ω phase, as this phase is no longer present. This hypothesis is based on the instability of ω phase at high temperatures in similar alloys. Nonetheless, TEM work would be required to confirm this hypothesis.

V. Although this work has clarified the microstructure evolution and role of many microstructural features on the properties, the impact of the microstructure on fatigue properties has been outside of the scope of this thesis. Considering the critical importance of fatigue analysis is the design process, a thorough understanding of the fatigue properties of Ti-5553 is needed.

VI. Plotting the yield, fracture and shear stresses on a two-principal stress axis coordinate system results in two concentric ellipses in excellent agreement with the shear strain energy (von Mises) model for failure and not the Mohr's modified shear stress model - as first expected. The practical consequences of this finding are significant to structural analysis and are discussed in the next section.

VII. It should be emphasized that the models developed in this thesis are mesoscopic in nature. In the future, a more definitive view could be developed by studying the Bauschinger effect during the elasto-plastic transition or studying the internal stresses in the two phases by neutron diffraction. Furthermore, at a more microscopic level, a detailed study of the co-plasticity of the hexagonal and BCC phases by detailed TEM studies would be of great value. Thus the titanium alloy studied in this thesis remains a rich source for future study.

References

[1] Ashby M.F., Materials Selection in Mechanical Design, Pergamon Press, ISBN 0 08 0419707 0, 1992.

[2] Fanning J.C., S.P. Fox, Recent developments in Metastable β Strip Alloys, Journal of Materials Engineering and Performance 14 (2005), 703-708.

[3] Yu K.O., E.M. Crist, R. Pesa, N. Cecchini and C.M. Bugle, Single Melt beta C for Spring and Fastener Applications, Journal of Materials Engineering and Performance 14 (2005), 697-702.

[4] Boyer R.R, G. Welsch, E.W. Collings, Materials Properties Handbook, Titanium Alloys, ASM International, ISBN 0-87170-481-1

[5] Boyer R.R. and R.D. Briggs, The use of β titanium alloys in the aerospace industry, Journal of Materials Engineering and Performance 14(2005) 681-685

[6] Tetyukhin V.V, Current State of the Russian Titanium Industry and VSMPO; Development of New High Strength Alloys for Aircraft and Civil Engineering, Proceeding of the 13th Annual Titanium Conference; ITA, 1997.

[7] Metallography, a study on the metallographic structure and constitution of Titanium alloys; prepared by the RMI Titanium company.

[8] An Update on Properties and Applications for Ti-5Al-5Mo-5V-3Cr, presented at the International Titanium Association, Scottsdale 2005, presented by VSMPO staff.

[9] Molchanova E.K., Phase Diagrams of Titanium Alloys, 1965 Israel Program for Scientific Translations Ltd.

[10] Nyakana S.L., J.C Fanning, R.R. Boyer, Quick Reference Guide for β Titanium Alloys in The 00s, Journal of Material Engineering and Performance, JMEPEG (2005), 14:799-811.

[11] Alloy Phase Diagrams, ASM Handbook - Volume 3, ASM International, ISBN 0-87170-381-5 (v.3).

[12] Donachie, Matthew J. Jr. - Editor, Titanium, a Technical Guide, ASM international, ISBN: 0-87170-309-2, (1988).

[13] Duerig T.W. and J.C. Williams, Overview: Microstructure and Properties of Beta Titanium Alloys, Beta Titanium Alloys in the 1980's ed. by R. R. Boyer and H. W. Rosenberg, AIME, New York, (1984).

[14] Polmear I.J, Light Alloys, Metallurgy of Light Metals,., Publishers - Edward Arnold Ltd, 1981, ISBN 0-7131-2819-4

[15] Ankem S., S.R. Seagle, Heat Treatment of Beta Titanium Alloys, Beta Titanium Alloys in the 1980's ed. by R. R. Boyer and H. W. Rosenberg, AIME, New York, (1984).

[16] Bowen A.W., Omega Phase Formation in Metastable β-Titanium Alloys, Beta Titanium Alloys in the 1980's ed. by R. R. Boyer and H. W. Rosenberg, AIME, New York, (1984).

[17] Baggerly R.G., Determination of the Omega Phase Volume Fraction in Single Crystals of Beta Titanium Alloys, Metallography, 8, 361-373, American Elsevier Publishing Comp, Inc. (1975)

[18] Lutjering G., J.C. Williams, Titanium, Springer-Verlag, Berlin, Heidenberg, New York, ISBN 3-540-42990-5.

[19] Williams D.B. & C. B. Carter, Transmission Electron Microscopy, Plenum Press, N.Y., 1996, ISBN: 0-306-45324-X.

[20] Headley T.J. & H.R. Rack Phase, Transformations in Ti-3Al-8V-6Cr-4Zr-4Mo, Metallurgical Transactions A, Volume 10A, July 1979, pp 909-920.

[21] Quantification of Grain Boundary Segregation in the Analytical Electron Microscope, V.J. Keast & D.B. Williams, Journal of Microscopy, Vol. 199, Pt1, July 2000, pp 44-55.

[22] Ladd M.F. & R.A. Palmer, Structure Determination by X-ray Chrystallography, Second Edition, 1985 Plenum Press, N.Y., ISBN: 0-306-42295-6.

[23] Harper M.L., R. Banerjee, D.J. Evans and H.L. Fraser, Microstructural evolution in TIMETAL 555, Internal presentation (report), The Ohio State University, 2002.

[24] Fanning J., TIMET Report SR 2343, Tensile Mechanical Properties of 7 inch, TIMETAL 555 Billet, Heat H2597, TIMET Henderson Technical Lab. Later published in JMEPEG (2005) 14:788-791 Properties of TIMETAL 555 (Ti-5Al-5Mo-5V-3Cr-0.6Fe).

[25] AMS 2380 (Aerospace Material Specification), Approval and Control of Premium-Quality Titanium Alloys, SAE International.

[26] del Prado J., A. Huang, X. Song, D. Hu and Xinhua Wu, Influence of Carbon and oxygen on the Hardening Response of Ti-15-3; IRC in Materials, The University of Birmingham, Edgbaston, B15 2TT, UK. Paper not yet published, provided by Michael Loretto, University of Birmingham.

[27] Ishunkina T., V. Rodionov (VILS, Russia), The Nature of Phase Transformations, Optimization of Structure and Properties of High Strength Titanium Alloys. Russian Publication "Metallurgy and Metals Heat Treatment", pp 13-19.

[28] Williams J.C., Phase Transformations in Ti-alloys – A Review of Recent Developments, Titanium and Titanium Alloys, Scientific and Technological Aspects, Edited by J.C. Williams, and A.F. Belov, 1982, ISBN 0-306-40191-6, pp 1477-1498.

[29] Utevsky L.M., A.B. Notkin, N.N. Semyenova, N.Z. Pertsovsky and A.S. Fainbron, Investigation Into the Internal Structure of α-phase Crystals in Complex Titanium alloys, Titanium and Titanium Alloys, Scientific and Technological Aspects, Edited by J.C. Williams, and A.F. Belov, 1982, ISBN 0-306-40191-6, pp 1531-1542.

[30] Seagle S.R., P.A. Russo, Principles of Alloying Titanium, Titanium and Its Alloys, , Material Engineering Institute-ASM international Course Material, Course 27, pp. 8-12.

[31] Cotton J. D., R. R. Boyer, R. D. Briggs, R. G. Baggerly, C. A. Meyer, M. D. Carter, W. Wood, G. Tewksbury, V. Li and X. Yao: Phase Transformations in Ti-5Al-5Mo-5V-3Cr-0.5Fe, Presented at, and to be published in the Proceedings of, Titanium 2007 in Kyoto Japan, June 3-7, 2007

[32] Hall, J.A., Primary Processing of Beta and Near Beta Titanium Alloys, Beta Titanium Alloys in the 1980's ed. by R. R. Boyer and H. W. Rosenberg, AIME, New York, 1984

[33] Burgers W.G.; Physica 1, 1934, p.561

[34] Newkirk J.B., Geisler A.H., Acta Met. 1, 1953, p.370

[35] Otte H.M., The Science, Technology and Application of Titanium, Pergamon Press, Oxford, UK, 1970. p. 645.

[36] Duerig T.W., Terlinde G.T., Williams J.C., Phase Transformations and Tensile Properties of Ti-10V-2Fe-3Al, Metll Trans A, Vol. 11A, Dec. 1980.

[37] Jaffe R.I., Burtle H.M., Titanium Science and Technology, Critical Review by Williams J.C., Kinetics of Phase Transformations, p.1433-1493., 1973

[38] Seagle S.R., Bania P.J., Principles of Beta Transformation and Heat Treatment of Titanium Alloys, Material Engineering Institute-ASM international Course Material, Course 27, 1994.

[39] Hickman B. S., Omega Phase Precip[itation in Alloys of Titanium with Transition Metals, *Met Soc of AIME-Trans*, v 245, n 6, June, p 1329-36, 1969.

[40] Furuhara T., Nakamori H., Maki T., Chrystallography of α Phase Precipitated on Dislocations and Deformation Twin Boundaries in a β Titanium Alloy, Material Transactions, JIM, Vol. 33, No. 6, pp. 585-595, 1992

[41] Aaronson H.I., Spanos G., Masamura R.G., Vardiman D.W., Monn D.W., Menon E.S.K.,Hall M.G., Sympathetic Nucleation: an overview, Materials Science and Engineering B32, pp. 107-123, 1995

[42] Menon S.K., Aaronson H.I., Acta Metallurgica, v35, n3, p.549-563, 1987.

[43] Rosenberg H.W., Titanium Alloying in Theory and Practice, in "The Science, Technology and Application of Titanium", (Proc. 1st Int. Conf. on Titanium, London), R.I Jaffe and N.E. Promisel, Ed. Pergamon Press, 1970.

[44] Clément N., Lenain A., Jacques P.J., Mechanical Properties Optimization via Microstructural Control Of New Metastable Beta Titanium Alloys, JOM, January 2007, pp.50-53, 2007.

[45] Leyens C., Peters M., Titanium and Titanium Alloys, Fundamentals and Applications, Wiley-VCH, 2003, ISBN 3-527-30534-3.

[46] Ankem S., D. Benerjee, D.J. McNeish, J.C Williams and S.R. Seagle, Silicide Formation in Ti-3Al-8V-6Cr-4Zr-4Mo, RMI Company internal report, February, 1985.

[47] Harper M.L., A study of the Microstructural and Phase Evolutions in TIMETAL 555, M.Sc. Thesis, Ohio State University, 2004.

[48] Fan, Z., Miodownik, A.P., TEM study of metastable β-phase decomposition in rapidly solidified Ti-6Al-4V alloy, *Journal of Materials Science*, v 29, n 24, p 6403-6412, Dec 15, 1994.

[49] Rhodoes C. G., J. C. Williams, Metallurgical Transaction A, 6 (1975) 2103-14

[50] Gammon L. M., R.D. Briggs, J.M. Packard, K.W. Batson, R. Boyer, C. W. Domby, Metallography and Microstructures of Titanium and its Alloys, ASM Handbook, Volume 9, G.F VanderVoort, editor, P899-917, 2004

[51] Hillert M., Some viewpoints on the use of a computer for calculating phase diagrams, Physica B, 103B, n1, p. 31-40, 1981.

[52] Boyer R.R, G. Welsch, E.W. Collings, Materials Properties Handbook, Titanium Alloys, ASM International, ISBN 0-87170-481-1, p. 23.

[53] Alloy Phase Diagrams, ASM Handbook - Volume 3, ASM International, ISBN 0-87170-381-5 (v.3), Introduction to Phase Diagrams, Crystal Structure Nomenclature.

[54] Nag S., R. Banerjee, R. Srinivasan, J.Y. Hwang, M. Harper, H.L Fraser, ω-Assisted nucleation and growth of α precipitates in the Ti-5Al-5Mo-5V-3Cr-0.5Fe β titanium alloy, Acta Materialia, 57, p. 2136-2147, 2009

[55] Perovic V., G.R. Purdy, L.M. Brown, Autocatalytic Nucleation and Elastic Stabilization of Linear Arrays of Plate-shaped Precipitates, Acta Metallurgica, Vol 29, Issue 5, p. 889-902, 1981

[56] Collings E.W. The Physical Metallurgy of Titanium Alloys, American Society for Metals, 1984, ISBN 0-87170-181-2.

[57] Niinomi M., Kobayashi T., Fracture characteristics analysis related to the microstructures in titanium alloys, Materials Science and Engineering, A213, p. 16-24, (1996)

[58] Ohyama H., Ashida Y., Nishimura T., Maki T, Effects of deformation temperature on deformed and aged microstructures and tensile properties in Ti-15V-3Cr-3Sn-3Al, ISIJ International, Vol.33, No. 8, p. 889-897. (1993).

[59] Mechanics of Materials 1, E. J. Hearn, Third Edition, ISBN 0 7506 3265 8.

[60] Dowling N.E., Mechanical Behaviour of Materials, Engineering Methods for Deformation, Fracture, and Fatigue, Second Edition, ISBN 0-13-905720-X.

[61] Mc Clintock, Argon A., Mechanical Behavior of Materials, Library of Congress Catalog Card No 64-16906, Addison-Wesley Publishing, 1966.

[62] Zhirui Wang, Tzi-Kang Chen and D.J. Lloyd, Stress Distribution in Particulate Metal Matrix Composites under External Load, Metal. Trans., Vol. 24A, pp. 197-207, 1993.

[63] Zhirui Wang and Harold Margolin, The Interaction of Surface and Interior to Produce Bauschinger Behavior in 70-30 Alpha-Brass Single Crystals Oriented for Easy Glide, Res Mechanica, 21, pp. 249-286, 1987.